BEHAVIOR OF REFRACTORY LININGS FOR SLAGGING GASIFIERS

by

En-Sheng Chen

B.Sc. (Eng.) (Civil), National Taiwan University (1977)
M.Sc. (Eng.) (civil), Massachusetts Institute of Technology (1982)

Submitted to the Department of
Civil Engineering
in Partial Fulfillment of the
Requirements of the Degree of

Doctor of Philosophy

at the

Massachusetts Institute of Technology

May 1984

Signature of Author _____
Department of Civil Engineering

Certified by _____
Oral Buyukozturk, Thesis Supervisor

Accepted by _____
Francois M. M. Morel, Chairman
Civil Engineering Departmental Committee

BEHAVIOR OF REFRACTORY LININGS FOR SLAGGING GASIFIERS

by

En-Sheng Chen

Submitted to the Department of Civil Engineering
in partial fulfillment of the requirements
for the Degree of Doctor of Philosophy
in Civil Engineering, May 1984

ABSTRACT

Coal gasification in a slagging gasifier unit is an efficient process in converting coal into economic gaseous fuel. In the gasifier, the operating temperatures are high with simultaneous presence of highly corrosive slags and gases. A refractory lining system is usually adopted as a thermal barrier to maintain the high operating temperature in the gasifier and as a potective layer for the gasifier vessel against corrosion attack. The refractory linings are generally in the form of composite cyclindrical walls composed of layers of bricks, mortar joints and cooling systems. Due to critical design conditions that exist in the gasification environments, a safe and economic design of the lining system and the determination of proper operational control involve challenging engineering problems which require a thorough understanding of the lining behavior in the high temperature, highly corrosive environments.

Generally, high-Al_2O_3 and high-Cr_2O_3 refractories have been considered as candidate materials for the primary layers of the lining systems in the slagging gasifiers. These materials have relatively high resistance to corrosion and thermal attack. The material and systems behaviors of the linings adopting these materials are quite complex, and a thorough behavioral understanding is essential for achieving an optimal design and for the determination of proper operational schemes. It is the purpose of the present work to develop predictive material models and analysis capability to study the lining system behavior in gasification environment, and through analytical/numerical simulations to reach specific guidelines for the design and the operation of the lining systems.

Temperature dependent material models are developed to represent the thermophysical and thermomechanical behaviors of the candidate refractory materials. Special emphasis is on the development of a time-independent, damage-type constitutive model for brittle materials. This model adopts the bounding surface concept in stress space to characterize material strengths in various stress paths, and, in

conjunction with the adoption of a damage parameter in strain space, to represent the material degradation due to damage accumulation. This model is general, and has the capability to predict the material response to multiaxial, nonproportional, and cyclic loads.

In addition to the time-independent constitutive model, a creep model, a conductivity model for cracked media, and polynominal representations of thermophysical properties are proposed for the candidate materials. A special finite element program incorporating these models is developed. The computer package developed provides a unique and powerful tool for the thermomechanical analysis of refractory lining systems.

A predictive corrosion model is proposed to study the long-term corrosion process of lining systems in slagging gasifiers. The corrosion process is considered as the interactive results of different corrosion mechanisms (dissolution and spalling), and temperature distribution in the lining systems. Based on this model, sensitivity study, including various lining materials, lining geometries, and operating conditions, is performed to identify the important factors characterizing the long-term corrosion behavior of the linings.

In high-temperature environments, the transient heat-up period represents a critical structural stage in the lining system. During this period the linings experience severe structural conditions, due to the high temperature gradient, high confining stresses, and the less effective stress relaxation. A proper design and operational control in reducing the damage in the lining during the heat-up periods is of great concern. In the present work, the thermomechanical behavior of linings with various combinations of lining material and lining geometry (single layer, multiple layer, and the adoption compressible layers and expansion joints) , and under various heating schemes (various combination of different heating rates, and holding periods) is studied. The results from these studies provide a basis for the determination of proper design and operational control for the linings in slagging gasification.

Finally, based on the findings from the thermomechanical and corrosion analyses, recommendations are made for the design and operation of reliable and durable lining systems.

Thesis Supervisor: Dr. Oral Buyukuzturk
Title: Associate Professor of Civil Engineering

ACKNOWLEDGEMENTS

The author wishes to express his sincere appreciation to Professor O. Buyukozturk for his supervision of this thesis, his continued interest and encouragement, and valuable suggestions throughout the course of this work. His pioneering efforts in the development of a general thermomechanical analysis methodology for structural systems with brittle materials have contributed to a great extent to this research.

The author would also like to acknowledge the support, encouragement and cooperation of a number of individuals. In particular, the author would like to thank Mr. R. Bradley of Oak Ridge National Laboratory for his moral and intellectual support, and continuous encouragement; Mr. W. T. Bakker of Electric Power Research Institute; Professor T. D. McGee of Iowa State University; Mesrs. M. E. Washburn, K. R. Costen and L. Trostel of Norton Company for kindly sharing their valuable experience and spending many hours in discussing problems of this research with me; Professors D. Veneziano, J. H. Slater and V. C. Li who were the thesis committee members of the author. The author particularly expresses his appreciation to Professors D. Veneziano and J. H. Slater for their helpful criticisms and countless help in reading and improving this thesis.

The author wishes to extend his gratitude to Mrs. S. L. Weiner, for her excellence, expertise and patience in typing the manuscript, and for her numerous and consistent help.

Finally, the author would like to express his deepest appreciation to his parents and his wife, Judy, for their continuous support and encouragement throughout the years of his education.

This work was supported by the U.S. Department of Energy through Advanced Research and Technology Development Fossil Energy Materials Program, under contract No. 7862.

TABLE OF CONTENTS

LIST OF FIGURES

Figure No. Page

Figure No. Page

Figure No. Page

Figure No. Page

Figure No. Page

Figure No. Page

Figure No. Page

LIST OF TABLES

LIST OF SYMBOLS

Chapter 3

A, a, b, n, T_o	model parameters in creep model
A_L, A_u, λ_1	model parameters in time-independent constitutive model
a_T	temperature shift factor
C_p	specific heat
D	normalized distance
E	Young's modulus
e^c_{ij}, de^c_{ij}	deviatoric creep strain tensor, and its increment
$\bar{e}^c$	equivalent deviatoric creep strain
e_{ij}, de_{ij}	deviatoric strain tensor, and its increment
e^e_{ij}, de^e_{ij}	deviatoric strain due to elastic response, and its increment
e^p_{ij}, de^p_{ij}	deviatoric strain due to plastic response, and its increment
F	bounding surface
$F_1, F_{1,max}$	normalization factor, and its maximum value
f_p	material strength in uniaxial compression
H^e	generalized elastic shear modulus
H^p	generalized plastic shear modulus
H^*	generalized modulus between dD and dK
$I_1, dI_1, I_{1,max}$	first stress invariant, its increment, and its maximum value
J_2, J_3	second and third deviatoric stress invariants

J^D	deviatoric creep function
J^V	volumetric creep function
K, dK, K_{max}	damage parameter, its increments, and its maximum value
k_g	thermal conductivity of gas
K_R, K_u	associated K value at the beginning of recent loading and unloading process, respectively
k_s	thermal conductivity of solid
K_t	tangent bulk modulus
R	distance of bounding surface from the hydroaxis along S_{ij} direction
r	distance from the projection of current stress point on the deviatoric plane to the hydroaxis
R_g	universal gas constant
S_{ij}, dS_{ij}	deviatoric stress tensor, and its increment
T	temperature
$t, \Delta t$	time parameter, and its increment
α	coefficient of thermal expansion
β	shear compaction-dilatancy factor
β_1	shear compaction factor
β_2	shear dilatancy factor
ε^c_{ij}	creep strain tensor
ε^c_v	volumetric creep strain
$\varepsilon_{ij}, d\varepsilon_{ij}$	strain tensor, and its increment
$\varepsilon_{kk}(\varepsilon_v), d\varepsilon_{kk}, \varepsilon^p_v$	volumetric strain, its increment, and its plastic component

$d\varepsilon^{o}_{kk}$, $d\varepsilon^{d}_{kk}$	volumetric strain increment due to isotropic and deviatoric stress/strain increments, respectively
ε_p	associated axial strain to f_p in uniaxial compressive load
λ, μ	Lame's constants
ν	Poisson's ratio
ν_c	Poisson's ratio of creep
ρ	density of material
$\gamma^{p}_{o}, d\gamma^{p}_{o}$	plastic octahedral shear strain, and its increment
θ	angle between projections of position vector of principle stress and that of any tensile semi-axis on deviatoric plane
$\sigma_{ij}, d\sigma_{ij}$, $\sigma_I, \sigma_{II}, \sigma_{III}$	stress tensor, its increment, and its principal value
$\Delta\sigma_i$	stress increment in i^{th} principal direction
$\tau_o, d\tau_o$	octahedral shear stress, and its increment

Chapter 4

A, B, T_o	parameters of corrosion model
a_i	parameters of conductivity model
D_c	depth of corrosion
D_p	depth of slag penetration
E_o	initial Young's modulus
F_X	distribution function of random variable X
h	coefficient of heat convection
k_s	thermal conductivity of solid
m_X	mean of random variable X

r	radius
r_o	inner radius of gasifier
T	temperature
T_c	critical temperature for slag penetration
T_H	hot-face temperature
T_1	temperature in the gasifier
T_2	cold-face control temperature
t	time parameter
V_X	coefficient of variation of random variable X
Y, Y_o	lining thickness, and its initial value
α	mean occurrence rate in unit time
Φ	generalized normal distrubition
σ_X	standard deviation of random variable X
Δt	the interval between two adjacent events
δ	Direc delta

Chapter 5

$\underline{B}^i$	Strain-displacement transformation matrix of i^{th} element
$\underset{\sim}{b}$	body force vector
$\underline{C}$	heat capacity matrix
C_p	specific heat
$\underline{D}, \underline{D}^i$	material rigidity matrix, and that associated with element i
$\underline{D}_{UC}, \underline{D}^*, \underline{D}_{CR}$	material conductivity matrix of uncracked medium, of cracked medium at local coordinate system, and of cracked medium at global coordinate system

$\underset{\sim}{F}$	nodal force vector
F_{ℓ}	concentrated load at point ℓ
$\underset{\sim}{f}, \underset{\sim}{f}_j$	generalized force vector, and its value at j^{th} time step
$\underset{\sim}{f}_T$	boundary traction vector
$\underline{H}$	coordinate transformation matrix
h	coefficient of heat convection
$\underline{K}$	system assemblage stiffness matrix
$\underline{K}_s$	heat conductivity matrix
k_x, k_y, k_n	thermal conductivity in x and y directions, and in the direction normal to the boundary of a domain
k_{CR}	equivalent thermal conductivity of a cracked medium
k_g	thermal conductivity of gas
$\underset{\sim}{N}, \underset{\sim}{N}^i$	interpolating function, and that associated with i^{th} element
$\underset{\sim}{P}$	heat supply vector
$T, \bar{T}, T_o, T_\infty$	temperature, its prescribed value, its initial value, and ambient temperature
$T^i, \underset{\sim}{T}^i_n$	temperature in i^{th} element, and temperature vector at nodes of i^{th} element
$\underset{\sim}{T}_n, \underset{\sim}{T}_{n,j}$	temperature vector at nodes of a system, and its value at j^{th} time step
$t, \Delta t$	time parameter, and its increment
X, Y, Z	system coordinates
$\underset{\sim}{u}, \underset{\sim}{u}_n, \underset{\sim}{u}^i_n$	displacement vector, its values at nodes, and its values at the nodes of i^{th} element
V_a	crack volume fraction
$\underset{\sim}{\varepsilon}, \underset{\sim}{\varepsilon}^i$	strain vector, and that associated with i^{th} element

ε_f, ε_a	initial tensile strain at crack formation, and post-failure strain
$\underset{\sim}{\varepsilon}_o^i$, $\underset{\sim}{\varepsilon}_{oo}^i$, $\underset{\sim}{\varepsilon}_{oc}^i$, $\underset{\sim}{\varepsilon}_{oT}^i$	initial strain vector of i^{th} element, and its component due to system initial state, creep effets, and temperature effects, respectively
Ω	domain of field problem
ρ	density of material
Γ_1	boundary on which temperature is specified
Γ_2	boundary on which the convective heat loss is specified
$\underset{\sim}{\sigma}$, $\underset{\sim}{\sigma}_i$	stress vector, and that associated with i^{th} element
σ_n	normal stress over joint interface
τ	shear stress over joint interface
$\Delta\underset{\sim}{\varepsilon}$	strain increment
π	functional representation of a field problem

Chapter 6

E	Young's modulus of compressible material
L,W	length and width of expansion joint
X,Y,Z	system coordinates

CONVERSION FACTORS

Parameter	English to SI Conversion
Length:	1 in = 25.4 mm
Mass:	1 lb = 435.9 g
Temperature:	$T\ (°F) = (9/5)\ T\ (°C) + 32°F$
	$T\ (°F) = (9/5)\ T\ (°K) - 459.7°F$
Density:	$1\ lb/in^3 = 2.768 \times 10^{-2}\ g/mm^3$
Pressure, Stress:	$1\ lb/in^2$ (PSI) $= 6895\ Pa\ (N/m^2)$
Specific Heat:	1 Btu/lb-°F = 1.055 Cal/g-°C
Thermal Conductivity:	1 Btu/hr-in-°F = 2.077×10^{-2} Watt/mm-°K

Prefixes most often used with SI units

10^9	giga	G
10^6	mega	M
10^3	kilo	K
10^{-3}	milli	m
10^{-6}	micro	μ

CHAPTER 1

INTRODUCTION

§1.1 COAL GASIFICATION - A REVIEW

Coal gasification is the process of manufacturing gas from coal by heating the coal while reacting it with air, hydrogen, steam, and other various mixtures. The early process of producing coal-gas can be traced back to late 18th century when the gas was obtained by heating coal in the absence of air [69]. In the early 19th century, when coal-gas producers started distributing their product for lighting in London, it became widely adopted in Europe and U.S. In fact, nearly every major city in the eastern U.S. once had its gashouse where gas was manufactured for lighting and cooking.

The early methods of coal gasification involved a destructive distillation process and a gasification process [69]. In the distillation process, the coal was heated until it decomposed chemically, releasing gas with a heating value of from 475 to 560 Btu/cft (B.T.U. per cubic foot). In this step over 70 percent of the original coal remained as a solid residue, and as a result, a second stage gasification process was adopted to further utilize the coal. In the gasification process the solid residue reacted with air, oxygen, and steam to produce a gas consisting essentially of a mixture of hydrogen and carbon monoxide. The heating value of this final gas was only about 300 Btu/cft.

The technology for producing gas from coal has improved substantially since the 19th century. The use of coal-gas declined after World War II due to the emergence of low-cost, high heating-value (1000 Btu/cft) natural gas. Natural gas is clean, easy to distribute by pipelines, and convenient to use, and therefore has become the preferred candidate for residential and commercial use.

In recent years the shortage of natural gas and petroleum made the prospect of commercial production of synthetic fuels from coal attractive once again. In the United States, for example, the energy generated by the use of available coal would exceed that of all forms of petroleum and natural gas combined. With the improved gasification technology for producing high-Btu gas and improved technology for building durable gasifier vessels, the installation of commercialized gasification plants seems feasible.

In general, there are two broad categories of coal gasification: low and medium-Btu gasification (200 ~ 400 Btu/cft), and high-Btu gasification (about 1000 Btu/cft) [64]. The low and medium-Btu gasification processes inexpensively produce gases with carbon monoxide and hydrogen. However, gases produced this way can be used economically only on site, either for electric power generation or by industrial plants. On the other hand, high-Btu gasification can produce gases consisting mainly of methane, which can be distributed economically to consumers via the same pipelines used to deliver natural gas. They are considered as a substitute for natural gas (SNG) accordingly. Furthermore, the high-Btu gasification process has potential, with further processing of its by-products, for providing industrial feedstocks for the manufacture of other synthetics.

Several approaches have been proposed for high-Btu gas production. The most updated technologies, which employ the concept of "hydrogasification" and the process of "shift conversion" and "methanation", can efficiently produce high-Btu gases with minimal gas and heat loss [32,64]. These processes can be summarized in the following major steps (Fig. 1.1).

(1) Gasification process:

(a) Hydrogasification: The coal is initially reacted with a hydrogen-rich gas to form substantial amounts of methane directly:

$$2CH_{0.8} + 1.2\ H_2 \rightarrow CH_4 + C$$

$$C + 2H_2 \rightarrow CH_4$$

(b) Oxygen-gasification: Some of the coal is burned to supply the required heat for the reaction process:

$$C + O_2 \rightarrow CO_2$$

(c) Steam-gasification: The reaction takes place at a relatively high temperature (above 2000°F) to produce hydrogen and carbon oxides:

$$C + H_2O \rightarrow CO + H_2$$

(2) Shift conversion process: The amount of methane in crude gas produced from the gasification process is low and further conversion of the crude gas is necessary to increase the methane content (methanation). To provide the required

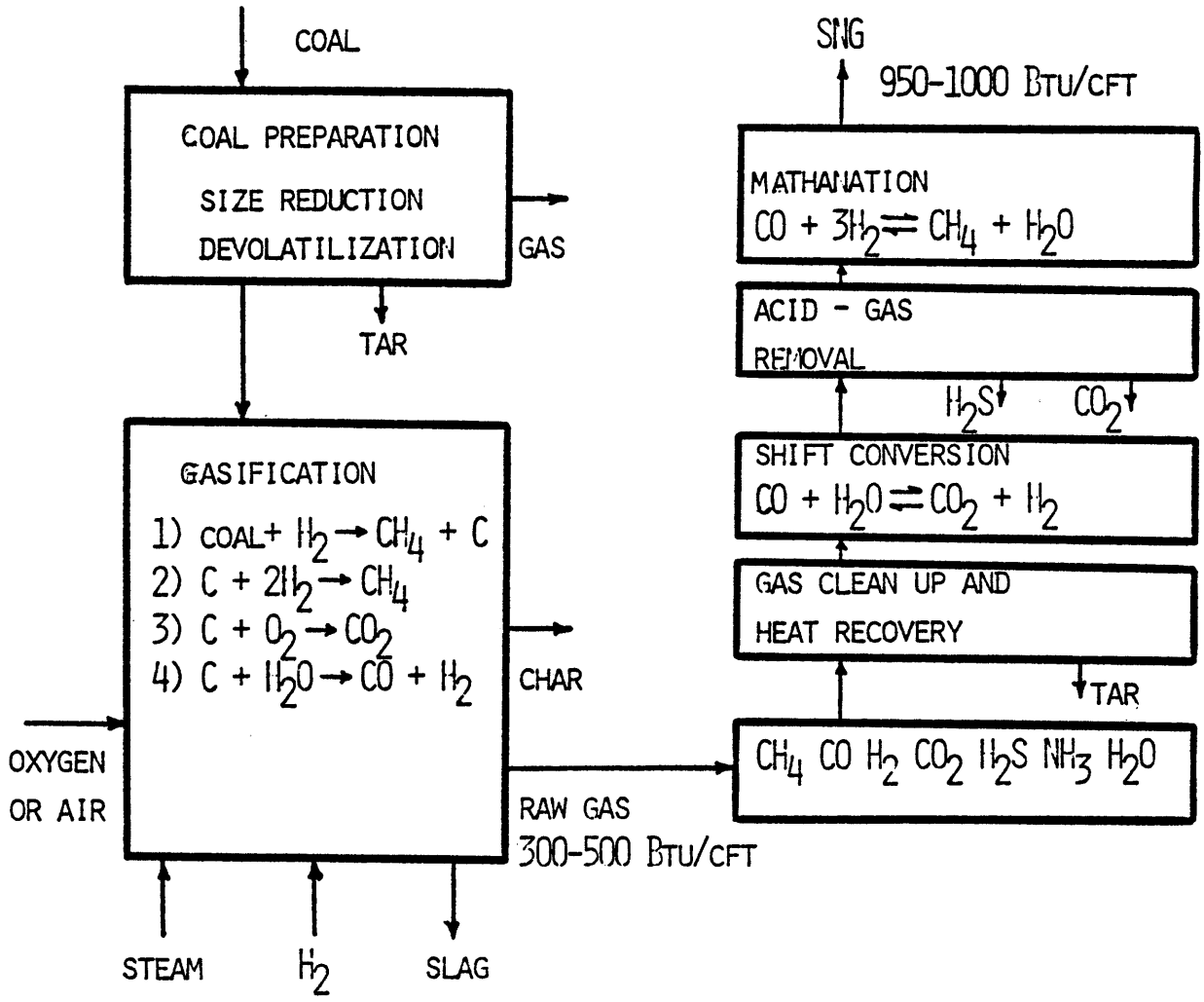

Figure 1.1 Coal Gasification Process [32]

hydrogen in the methanation process, the process termed shift conversion is performed by interacting crude gas with steam:

$$CO + H_2O \rightarrow CO_2 + H_2$$

(3) Methanation process: The crude gas is further reacted with hydrogen to produce more methane:

$$CO + 3H_2 \rightarrow CH_4 + H_2O$$

During the above mentioned processes, some intermediate steps such as gas/tar clean up and gas purification, are required to achieve the necessary steps. The above mentioned processes of coal gasification are outlined in Fig. 1.1 [32]. For more details the reader may refer to Refs. 32 and 64.

In addition to the above outlined chemical processes, the coal gasification processes also involve various mechanical systems [32,69]. These mechanical systems can be classified in several ways: by the method of supplying heat for the gasification reaction (internal heating or external heating); by the method of achieving contact between the reactants (fixed bed, fluidized bed, entrained bed, or molten bath bed); by the flow of reactants (current or counter current); and by the method of residue removal (slagging or non-slagging). Briefly, in a fixed bed system a grate supports lumps of coal through which the steam or hydrogen is passed; in a fluidized bed system gas flows through the coal, producing a lifting and boiling effect; in an entrained bed system the coal particles are transported in the gas prior to introduction into the reactor; and in a molten bath bed system the coal particles and gas are dispersed in a liquid.

Non-slagging (dry-ash) gasifiers have been used for a long time. The non-slagging gasifier usually operates at a relatively low temperature (less than 2000°F); in these gasifiers, the non-volatile constituents in the coal (i.e., ashes) are present as dry solid particles. These dry ashes need to be removed from the gasifier periodically. On the other hand, a slagging gasifier usually maintains a portion of the gasifier volume at temperatures above the melting point of the coal ashes (typically above 2500°F). The coal ashes in the slagging gasifier are present in a liquid form (molten slags) which can be removed easily and continuously, resulting in sterile, inert ash products for disposal. This type of gasifier offers several primary advantages over non-slagging (dry-ash) gasifiers, such as greater gas production capacity for a unit of given size, lower steam consumption, absence of tars and oils in the product steam, and relatively easy removal of ashes during operation. Examples of such slagging gasifiers [7] are: (1) for the fixed-bed system: British Gas-Lurgi gasifiers, and GFERC pilot plane; (2) for the entrained-bed system: Koppers-Totzek, Texaco, Shell and C-E gasifiers.

The present work deals with the thermomechanical behavior and corrosion effects associated with these slagging gasifiers. In the next section specific problems in this respect will be summarized.

§1.2 RESEARCH PROBLEMS ASSOCIATED WITH THE LININGS OF SLAGGING GASIFIERS

In slagging gasifiers, operating temperatures of the order of 2500 to 3300°F are maintained, and the ash is present as molten slag. This slag generally runs down the walls of the gasifiers, and goes through a

slag tap to a quench tank from which it can be removed as a granular material. The molten slag is corrosive to the vessel shell. To maintain a high operating temperature and to protect the vessel shells from corrosion attack, refractory-brick lining systems (Fig. 1.2) are usually used. Such lining systems are generally in the form of composite cylinders primarily composed of layers of bricks in vertical (axial) and radial directions. The bricks are usually connected to adjacent bricks with jointing materials, such as mortars, for improving the system integrity and stability. Cooling systems are frequently adopted to fulfill certain requirements of temperature control during operation.

During the lifetime of a refractory-brick lining in a slagging gasifier, two general categories of failure may be observed [34]: (1) cracking, spalling, and joint failure due to thermal attack and (2) material degradation and mass loss due to corrosion attack by the slags and gases.

The refractory lining is subjected to heat flux at the interior face (hot face) of the vessel and generally is cooled from the exterior face (Fig. 1.2). The adoption of a cooling system may reduce the hot-face temperature, enabling a stable layer of slag to form on the inside hot face [36]. This layer may protect the refractory lining from exposure to the corrosive gases and molten slags. Moreover, the cooling system can reduce the shell temperature to a level that the corrosive agents on the shell are not active [30]. On the other hand, if the temperature differences across the lining thicknesses are large, a critical stress combination of tensile, compressive, and shear

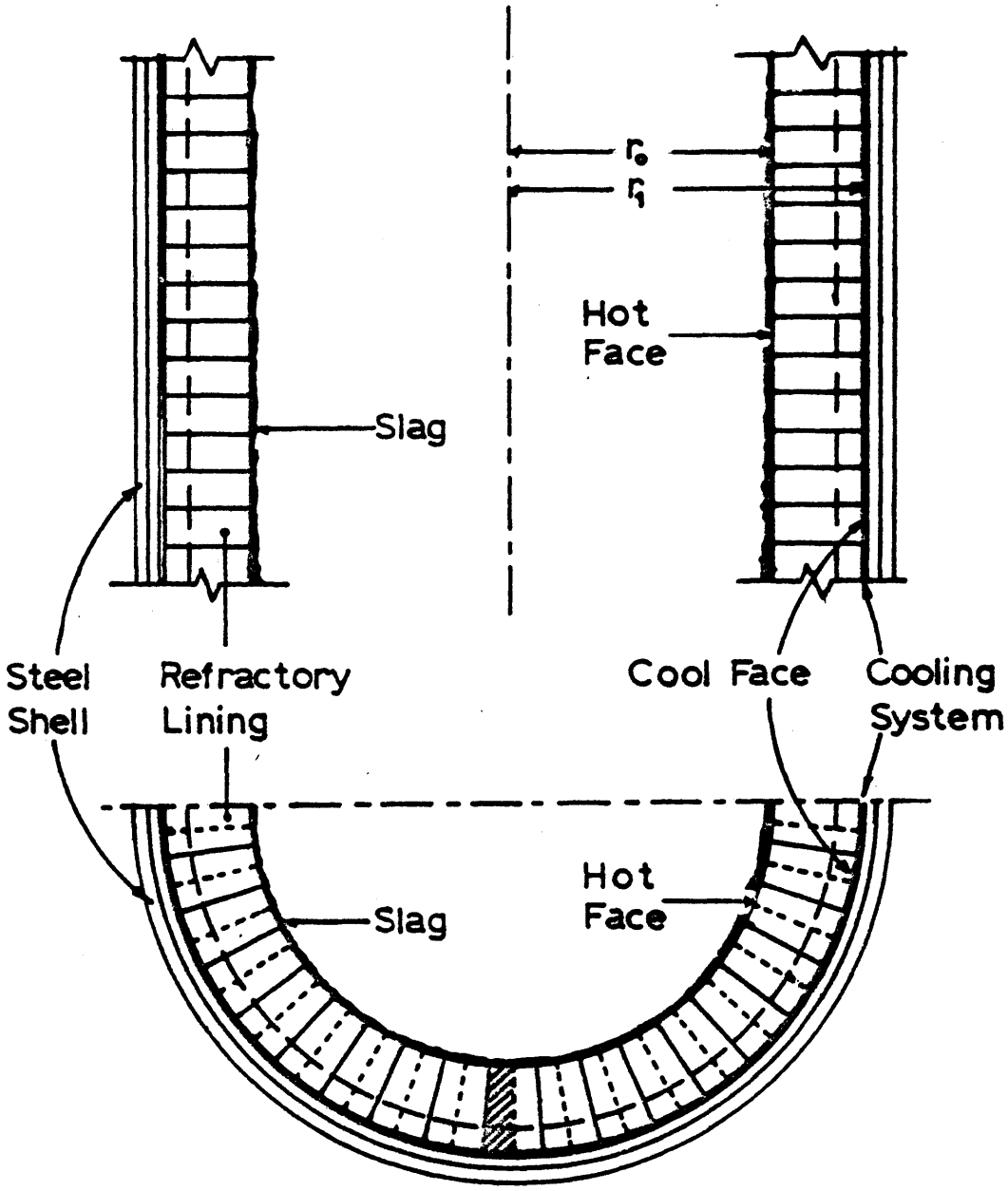

Figure 1.2 Schematic of Refractory Brick Lining System

stresses may arise in the lining. Such critical stress states may cause cracking, and spalling problems in the bricks, and failures of the joints between the bricks. Furthermore, heat accumulation due to the reduction in thermal conductivity at locations across the cracks together with the possible degradation of the brick material due to hot slag penetration may accelerate the deterioration of the lining, leading to eventual damage to the vessel shell.

In both acidic and basic coal slags, high-alumina and high-chromia dense refractories are usually used to reduce corrosion attack. Water cooling at the exterior face of the lining also gives a beneficial effect. Substantial slag corrosion of the linings is still observed, however, due to its exposure to high-temperature gasification environments during the life time of the system [30]. The corrosion process involves three mechanisms: dissolution, penetration, and erosion. The chemical process of dissolution and penetration has been extensively studied for certain candidate refractories for slagging gasifiers [45,49,50,51,90]. Dissolution in a slag-refractory system is the chemical reaction between the slag and the refractory, by which the refractory is gradually dissolved in the slag composite. The slag penetration can result in the changes of chemical and mechanical properties of the refractory. A common mechanical effect is the formation of numerous microcracks in the refractory and the resulting strength degradation. Erosion itself is not a problem for high-alumina and high-chromia bricks in slags. However, when it is accompanied by slag penetration and thermal stresses, it can result in significant spalling problems [65]. Such a spalling mechanism is not well

understood. More studies toward a better understanding of this type of deterioration process are needed.

An optimum design and operational control will reduce the corrosion and thermal-attack problems in the lining system. In order to achieve a safe design and determine the optimum operational schemes, a thorough understanding of the behavior of lining systems in slagging gasification environments is required. Such a behavioral understanding will involve both thermomechanical material and system behavior, and corrosion behavior, as well as their interaction in the gasification environment. The present work is an attempt to accomplish these objectives, with the aim to provide an analysis and design methodology for achieving reliable and durable lining systems. It is hoped that the results of this study will benefit the coal-gasification industry.

§1.3 REVIEW OF THE PREVIOUS MIT WORK

Over the past several years, comprehensive analytical and experimental studies have been undertaken at MIT dealing with the thermomechanical behavior of monolithic refractory concrete linings [19,20,70,88].

Constitutive models have been developed for both dense and insulating monolithic refractory concretes applicable to coal gasification vessel linings. In the development, experiments were performed on refractory concrete plate specimens subjected to biaxial compression at various temperatures. Based on the test results, a

general hypoelastic model was developed for the thermomechanical constitutive behavior of refractory concretes. The essential features of the model include a temperature dependent failure surface, elastic modulus and stress-strain curve. Within certain limitations the model can be used to model behavior under cyclic thermal loadings. A temperature dependent creep model based on the concept of thermo-rehologically simple material was also developed. The creep model incorporates a transient delayed elastic strain component and a nonlinear irreversible flow component. These models were incorporated in a three dimensional thermo-mechanical finite element program for predicting the behavior of dual-component, monolithic refractory concrete lined coal gasification vessels. A finite difference solution was used for the analysis of transient heat transfer analysis through cracked, layered media, and incorporated in the three-dimensional nonlinear finite element computer program for the stress analysis.

The experience from this previous experimental and analytical work at MIT has been applied to the current research. However, special materials, systems, environmental conditions and related problems encountered in the current work required substantial new developments in modeling and analytical/numerical procedures. New material models for the refractory bricks, structural models, a preliminary model for corrosion prediction, and analysis capability have been developed. With these new tools, the general behavior of a refractory lining system in a slagging environment can be extensively studied.

§1.4 CURRENT RESEARCH OBJECTIVES AND APPROACH

The general objectives of the present study are (1) to develop predictive material models and an analysis capability to study the system behavior of refractory-brick linings in high-temperature, high-corrosion environments, and (2) through analytical/numerical simulations to reach specific guidelines for the design and operation of the lining systems.

The specific objectives of the study are:

(1) based on the available test data, to develop general time-dependent, temperature-dependent material models. These models, when implemented in finite element program, will predict the thermomechanical behavior of linings in a transient heating process;

(2) to develop a general methodology and analysis capability (finite element program) for studying the reliability of lining systems in gasification environments;

(3) through simulation and parameter studies, to assess the governing effects of different design factors and operational schemes on the lining behavior;

(4) to develop an analytical model for studying the long-term corrosion behavior of the linings, and through simulation, to understand the corrosion behavior of the linings with different lining materials, and in various operating conditions in the slagging gasifiers;

(5) based on the analysis results, to provide specific guidelines for the design and operational control of the lining systems in slagging gasifiers.

In the determination of a proper configuration and operational scheme for a lining system, the designer usually faces many trade-offs before a final optimal solution is reached. Examples of these trade-offs exist in materials selection (corrosion resistance, strength at elevated temperatures, and thermal conductivity); in operational procedures (levels of pressure, temperature, gas velocity, etc.); in the lining geometry (number of layers, thicknesses, etc.); in the heating scheme, and in the use of a cooling system. Such trade-offs can be assessed through accurate prediction of the overall lining performance in a gasification environment. The final optimal solution can be determined on an economic basis, comparing the total cost of lining materials, labor, construction, replacement (material, labor, and down-time loss) due to possible damage in the lining systems, to projected benefits. Such an optimization process requires a broad knowledge covering materials science, mechanical engineering, structural engineering, chemical engineering, the manufacture of refractories and gasifiers, and many other fields. Hence, an important aspect of this work is the integration of results with results obtained from other sources to provide a complete characterization of the lining system.

The approach used to conduct this research may be summarized in the following steps:

(1) Collect and evaluate material data for hot refractory bricks and mortar. For different temperature levels the data includes compressive strength, stress-strain curves, modulus of elasticity, strength under multiaxial loading conditions,

creep curves, thermal conductivity, thermal expansion behavior, and corrosion rate.

(2) Based on the available data and a general knowledge of refractories, develop constitutive models for refractory materials. Compare and verify predictions from the models with experimental data.

(3) Study the long-term corrosion behavior of refractories in slag. Develop analytical methods to predict residual lining thickness and to evaluate long-term reliability of a lining system.

(4) Study the effect of corrosion on the thermomechanical properties of refractories. Modifications in thermomechanical properties of refractories due to slag corrosion will be included in the thermomechanical analysis of the lining systems.

(5) Develop a conductivity model for cracked media. Perform transient heat transfer analyses and examine the local effects of heat accumulation and stress concentration.

(6) Implement the developed material models into a finite element program. Develop special elements for mortar and brick. Simplify the structural model and define appropriate boundary conditions.

(7) Perform thermomechanical analyses of linings using the developed models. Predict stress-strain distributions within the brick-mortar linings. Detect crack formation, spalling, and joint failure by analysis.

(8) Perform parameter studies to assess the effects of different designs of the linings and different heating schedules on the thermomechanical behavior and reliability of the lining systems. Optimize operational procedures and lining designs.

(9) Complete evaluation of analytical/numerical results. Make design and operational recommendations.

(10) Based on the analytical/numerical results, recommend future needs for experimental and analytical research.

§1.5 ORGANIZATION

A review of the lining systems and candidate materials used in a slagging gasifier is given in Chapter 2. The chapter includes the description of the gasification environment, the typical factors destructive to a refractory lining, the conceptual design of a lining system and the selection of candidate lining materials for slagging gasifiers. In Chapter 3 the material behavior, including thermophysical and thermomechanical behavior, of the candidate materials is summarized. Associated temperature-dependent material models are proposed for implementation in the finite element program. These include the conductivity model, the time-independent constitutive model, and the creep model.

In Chapter 4, the slag corrosion behavior of refractory linings is studied. The typical corrosion mechanisms in a slag-refractory system are reviewed first. Analytical models for predicting residual lining

thicknesses are proposed. Based on these models, the deterioration behavior of the linings in corrosive environment is studied.

In Chapter 5 the finite element formulations for the heat-transfer analysis and for the stress analysis are summarized. The finite element implementation of the interaction between heat transfer and stress resultants is presented. The modeling of the mortar-refractory joint behavior is included, and the implementations of the effects of slag-penetration and spalling are also described. In Chapter 6 extensive parameter studies are performed. Different combinations of refractory materials, number of layers, layer thicknesses, and heating schedules are studied. The results of these parameter studies constitute the basis for the determination of an optimal design and operational scheme.

Recommendations on conceptual design and operation of a refractory lining system for slagging gasifiers are given in Chapter 7. Finally, in Chapter 8 a summary of the study, conclusions, and future research directions are presented.

CHAPTER 2

LINING SYSTEM AND LINING MATERIALS

§2.1 GASIFICATION ENVIRONMENT

The slagging gasifier is conceptually a leading candidate for coal gasification. It offers several primary advantages over other types of gasifiers. These include greater gas production capacity for a given size unit, lower steam consumption, absence of tars, oils, and condensable hydrocarbons in the product steam, and relatively easy removal of ash during operation. However, this highly efficient conversion process is generally accompanied by high operating temperatures and pressures, complex gaseous composites, and molten slag. This results in an extraordinarily severe environment for the structural components of the slagging gasification system.

Increasing temperature and pressure in the gasifier can usually increase operational efficiency and reduce the size of gasifier [64]. The adopted temperatures and pressures in a slagging gasifier generally depend on the specific gasification process, the reactivity of the coal, and the fluidity of the slag. The operating temperatures are usually in the range of 2500°F - 3300°F, and gas pressures are generally in the range from one atmosphere to 600 psi, but can be above 1000

psi. The high temperatures are not permissible for the vessel shell of the gasifier, and thus the shell is generally protected by a refractory lining system.

Gases typical to a slagging gasifier primarily consist of H_2O (steam), H_2, CO and CO_2. Small amounts of CH_4, N_2, NH_3, and H_2S may also exist. These processing gases can attack the refractory lining and vessel shell in various ways, and the level of damage by gas attack is generally temperature and pressure dependent. The steam can oxidize the iron-containing metal shell and cause cracking and spalling problems in the shells during heating cycles [2]. Such problems become very severe at high temperature levels. At elevated temperatures steam can affect refractory materials by causing the extraction of soluble oxides or hydroxides, resulting in the reduction of refractory strength and erosion resistance [40]. Hydrogen attack to the steel shell can be significant at temperature levels above 600°F, leading to loss in material ductility and toughness [63]. At high temperature levels (>1700°F), hydrogen can remove silica and solid SiO_2 from refractories and result in weight loss from the refractories [31]. CO disintegration of refractories, which causes the spalling of iron-containing materials and the corrosion of silicate refractories, is also an important factor in the lining design. In the consideration of the abovementioned gas attacks, the design of a gasifier usually adopts (1) a controlled low shell temperature (<650°F) with a protection layer (usually, made of chromium oxide) for the shell surface, and (2) dense, low silica-containing refractory materials for the lining.

The high temperature in the slagging coal gasifiers melts the coal ashes into fluid slags. Slags run down the wall, flow over the bed of

the gasifier, go through a slag tap to a quench tank and are removed as a granular material. This scheme conceptually provides an easy method for waste disposal and creates minimal environmental problems. However, the molten slag is corrosive to the vessel shell of the gasifier. Hence, a lining system is designed not only as thermal barrier, but also as a protective system for the containment shell. Linings made of refractory bricks, with proper mortar joints and cooling systems, are usually adopted for these purposes.

The interaction between slag and the refractory is complex. It depends on the chemical compositions of the slag and the refractory, the slag temperature, and the slag viscosity. Usually the coal ash slags are very corrosive to most refractories. They are basically mixtures of various oxides, such as SiO_2, $A\ell_2O_3$, FeO, CaO, MgO, Fe_2O_3, MnO, Na_2O_3, k_2O, TiO_3, TiO_2 and P_2O_5. In general, one can conveniently categorize both the refractories and the slags into three classes, acid, neutral, and basic, through the definition of a "Bases-to-Acids Ratio"(B/A Ratio):

$$\text{Bases-to-Acids Ratio} = (CaO + MgO + FeO + Fe_2O_3 + MnO + Na_2O + K_2O)/(SiO_2 + A\ell_2O_3 + TiO_3 + TiO_2 + P_2O_5)$$

This ratio can be evaluated either on a molar or a weight basis. Ratios greater than 1 are considered basic, less than 1 acidic, and neutral if equal to 1. An acidic refractory will resist an acidic slag but will be attacked by (or dissolved in) a basic slag, and conversely. For each individual type of coal slag, theoretically, there is an optimum refractory with a minimum corrosion (dissolution) rate at certain temperatures. For corrosion resistance, high melting point and high

softening temperature (refractoriness) are required in addition to high strength. It has been shown by extensive laboratory tests [6,17,42,43,45,50,51,90] that those refractories consisting mainly of Cr_2O3 , $A\ell_2O_3$, and MgO are sufficiently resistant to attack by most US coal slags.

The penetration of slags into refractories depends on the porosity and the temperature of the refractories. The penetrated slags cause differential volumetric change between the refractory matrix and the slag, which may introduce local cracking, crushing, and the degradation in strength of the slag-penetrated refractory. Combined with thermal loadings and slag errosion, slag penetration finally creates serious spalling problems and weight loss of the refractory [65]. For this reason dense fusion cast refractory bricks are generally superior to high-porosity refractories, such as porous sintered refractories.

A slag layer may form on the face of the refractory lining due to the adhesion of molten ash at temperatures lower than the critical value marking the transition between viscous and plastic behavior of slag. Part of this layer will eventually flow down the lining surface under its own weight. The steady state thickness of this layer depends on the density and absolute viscosity of the slag, the amount of slag flowing per unit width, the hydraulic gradient, and the slag temperature [7,30,43]. This slag layer is desirable in the sense that it forms a protective layer for the refractories from hot slag penetration, and gas corrosion [14]. Such a protective layer can be obtained by reducing the slag temperature on the hot face of the refractory lining to a level below the critical temperature mentioned

previously. When the operational temperature in the gasifier is fixed, one may reduce slag temperature on the hot face of the refractory lining using high conductivity refractories and cooling systems, or reducing the heat transfer coefficient on the hot face by reducing operating pressure or gas velocity.

§2.2 FACTORS DESTRUCTIVE TO THE REFRACTORY LINING SYSTEMS

In a severe gasification environment the refractory lining system can deteriorate in a variety of ways [30,34,43], followed by a loss in required performance. In the present work the major factors considered to be destructive to the refractory lining systems include:

(1) Degradation in the strength of refractorites at elevated temperatures;

(2) Thermal-stress induced cracking, crushing and spalling of refractories, and failure of mortar joints;

(3) Slag dissolution;

(4) Slag penetration and errosion.

The mechanical properties of refractories, including compressive strength, tensile strength, initial Young's modulus, creep rate, and stress-strain relationship, are primarily temperature and load history dependent. The typical trends of strength (tensile or compressive) in monotonic loading at elevated temperatures [26,39] are shown in Fig. 2.1. As the critical temperature is reached, refractories lose their strength. This critical temperature depends on the melting point and refractoriness of the materials. The strength loss results in excessive deformation and the loss of load-carrying capability with the

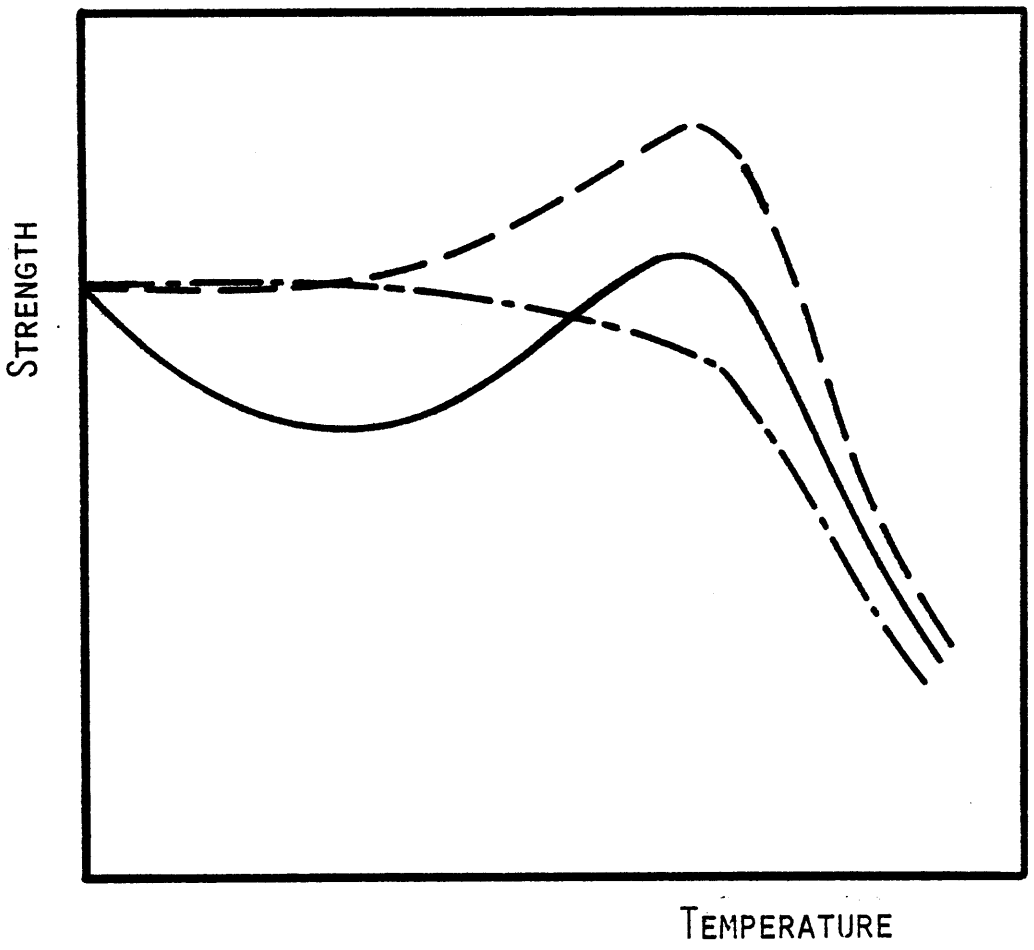

Figure 2.1 Typical Uniaxial Strength - Temperature Curves

consequent loss in integrity of the lining system. This problem is especially severe on the hot face of the lining during the heat-up process (e.g., spalling), and on the roof section (e.g., sagging). Hence, high strength refractories with high melting point are desirable for the lining material used in the slagging coal gasifiers. Other changes in the mechanical properties cause less damage, and some of them, such as creep, such as creep, may be helpful to the integrity of the lining system.

The variations of temperature in a refractory lining may cause cracking and joint failure due to differential thermal expansion and boundary confinment. Joint failure is usually found near the cold face (outer face) of linings and cracking near the hot face (interior face) during heating cycles. Furthermore, excessive compression combining with slag erosion may cause spalling problem on the hot face. One example from Ref. 16 is shown in Fig. 2.2, in which severe spalling from the face of a lining was found at an advanced stage during operation. In the present work temperature induced failure mechanisms are extensively studied, and more detailed discussions will be presented in later chapters.

Slag corrosion, in addition to gas corrosion, is of primary concern in choosing a suitable refractory for a slagging-gasifier lining. With respect to corrosion, the damage caused by the slag to the refractories can be classified in two major ways:

(1) Refractories exposed to slag might be dissolved in slag. This causes continuous loss in mass and thickness of the refractory linings. Fig. 2.3 shows the general trend of the thickness loss in the lining during its lifetime [11,38].

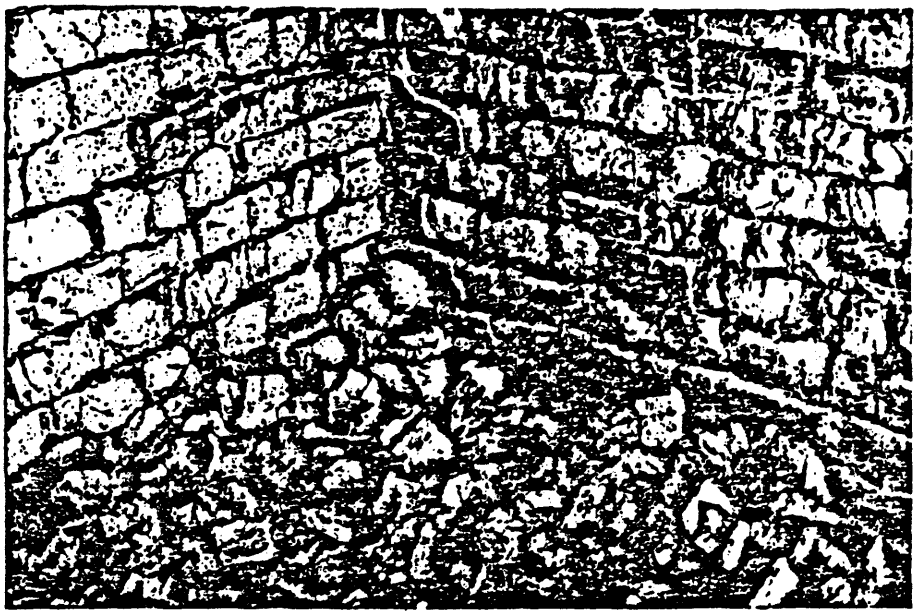

Figure 2.2 Cracking and Spalling of Refractory Lining at Advanced Stage [16]

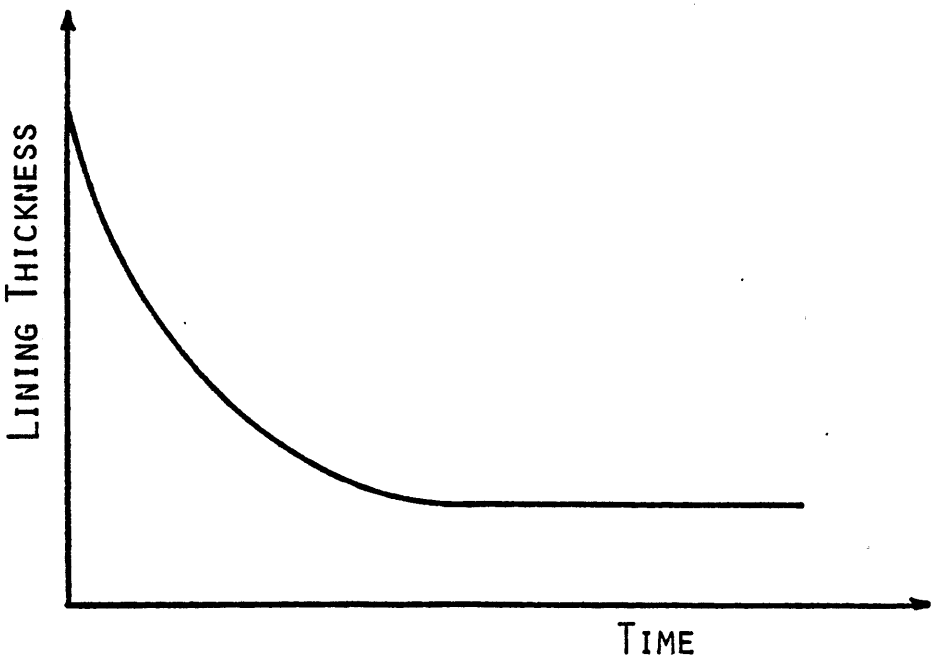

Figure 2.3 Refractory Lining Life Curve

(2) Slag may penetrate into refractories, especially along the grain boundaries. This creates local microcracking, reduces material stiffness, and causes cracking and spalling problems in the refractories.

Extensive corrosion experiments have been carried out at Argonne National Laboratory. Ref. 50 presents the mole percentage chemical composition of some refractories exposed to high iron oxide acidic coal slag at a temperature 2870°F (Figs. 2.4 to 2.7). Large amounts of FeO-substitution can be found which form spinal layers near the face of refractories exposed to coal slag. In Fig. 2.8 the dissolution rate of various water-cooled refractories exposed to high iron oxide acidic coal slag for 500 hours at 2870°F is shown. Most of the refractories experience severe loss in thickness. Although these results cannot be directly extrapolated to the linings in an actual gasifier, they point out the important role of slag corrosion on the evaluation of the long-term reliability of lining systems.

Slag erosion itself is usually not a governing destructive factor in most gasifier linings. However, when it is accompanied with the change in physical and chemical properties of refractories subjected to slag penetration and thermal attacks, the erosion problem becomes more significant.

The abovementioned factors destructive to refractory linings in high temperature, high corrosion gasification environments will be studied further in later chapters. The corrosion behavior of linings adopting particular candidate refractory materials is studied in Chapter 4, and in Chapter 6 the effects of thermal attack on linings with different designs and operational controls are assessed.

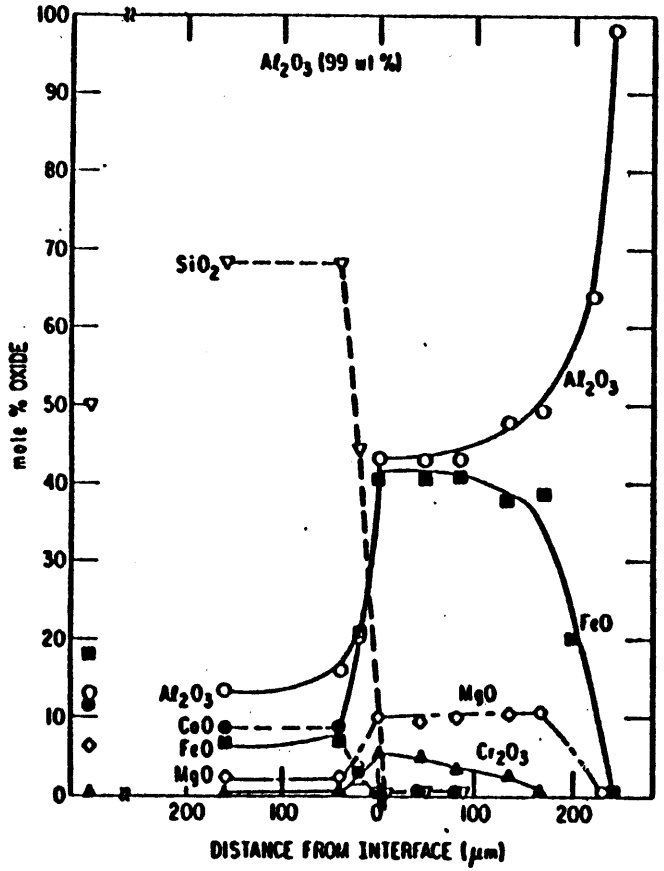

Figure 2.4 Mole Percentage of Chemical Composition in Slag-Refractory System (99% Al_2O_3 Refractory Exposed to High Iron Oxide Coal Slag) [50]

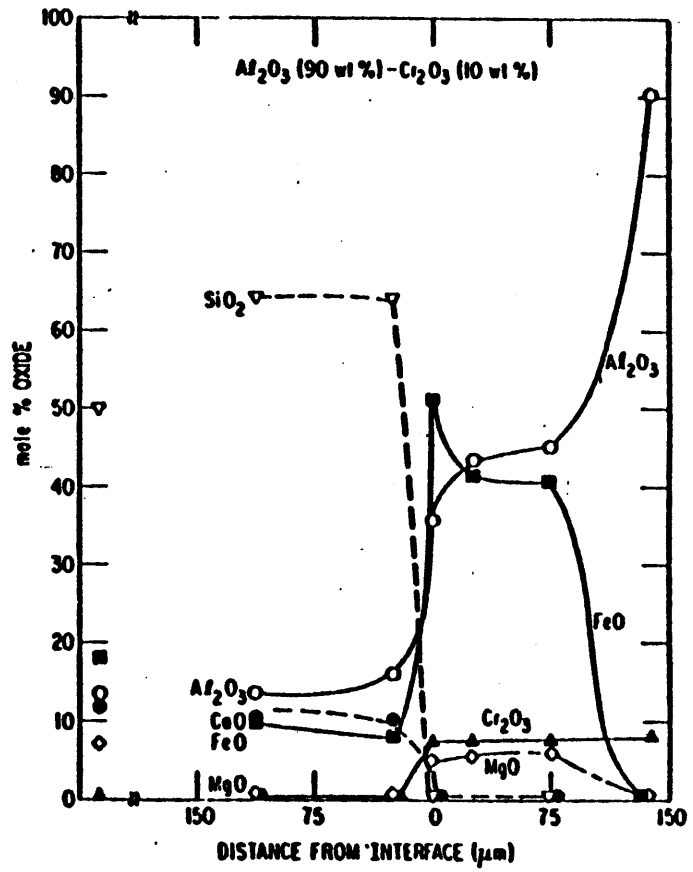

Figure 2.5 Mole Percentage of Chemical Composition in Slag-Refractory System (90% Al_2O_3 Refractory Exposed to High Iron Oxide Coal Slag [50]

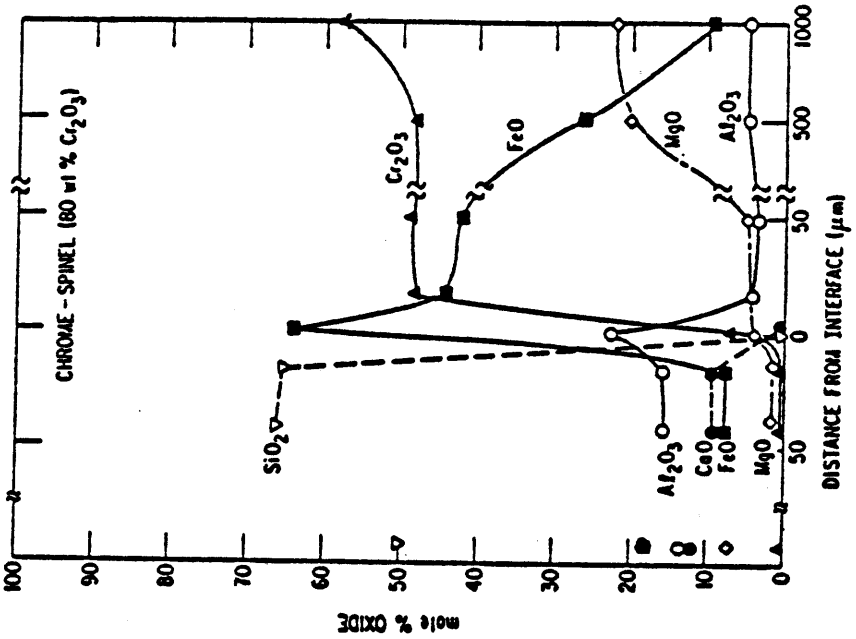

Figure 2.7 Mole Percentage of Chemical Composition in Slag-Refractory System (80% Cr_2O_3 Refractory Exposed to High Iron Oxide Coal Slag) [50]

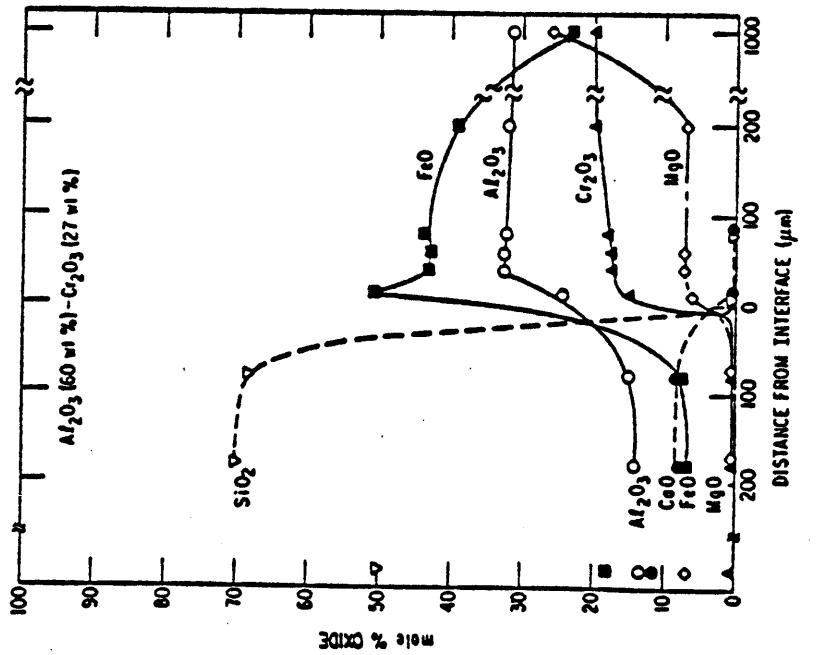

Figure 2.6 Mole Percentage of Chemical Composition in Slag-Refractory System (60% Al_2O_3 Refractory Exposed to High Iron Oxide Coal Slag) [50]

HIGH IRON OXIDE (20% FeO) ACIDIC COAL SLAG (B/A = 0.55)
500 h at 1575°C WITH WATER COOLING

NUMBER/TYPE	POROSITY (%)	COMPOSITION (wt %)
2-FC	1	Al_2O_3 (99)
190-S	17	Al_2O_3 (92), Cr_2O_3 (7.5), P_2O_5 (0.5)
16-S	16	Al_2O_3 (90), Cr_2O_3 (10)
86-C	21	Al_2O_3 (85), Cr_2O_3 (10), P_2O_5 (4.5)
109-C	23	Al_2O_3 (67), Cr_2O_3 (32), P_2O_5 (1)
260-S	25	Al_2O_3 (67), Cr_2O_3 (32)
400-S	13	MgO (42), Cr_2O_3 (27), Fe_2O_3 (16)
38-FC	5	Al_2O_3 (60), Cr_2O_3 (27), MgO (6)
280-FC	7	Al_2O_3 (65), Cr_2O_3 (32)
22-FC	6	Cr_2O_3 (80), MgO (8), Fe_2O_3 (6)

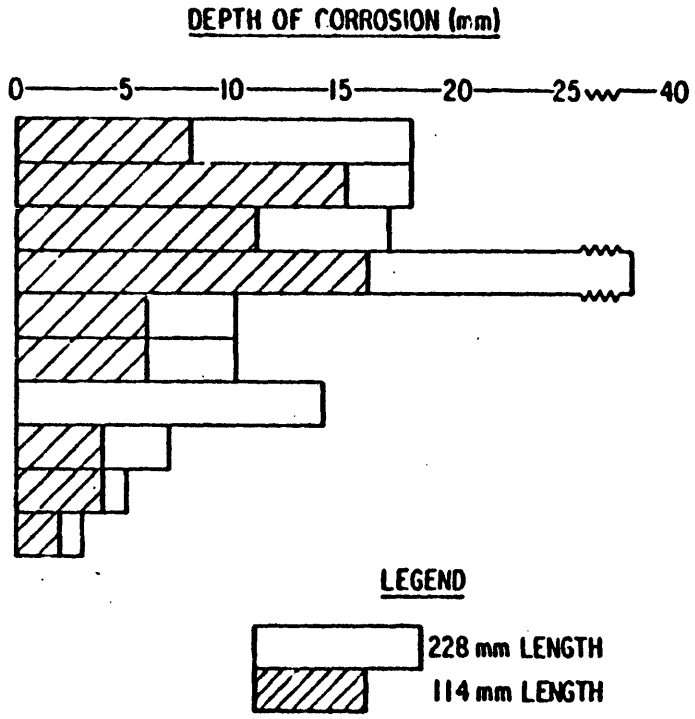

Figure 2.8 Corrosion of Refractories (FC = fused-cast, S = sintered, and C = chemically bonded) [50]

§2.3 CONCEPTUAL DESIGN OF A LINING SYSTEM

A rational design for lining systems of coal gasification vessels should optimize the material resistance to corrosion attack by gases and slags, and to thermal attack. It should also consider heat losses through the linings, difficulties in installation and replacement, and long term reliability of the entire system. The final choice of an optimum lining system should be based on an economic analysis which reflects the total cost of a lining system over the life time of the containment vessel. A preliminary estimation of the cost of the refractory lining reveals the importance of such an economic analysis, since the lining system may represent more than fifty percent of the total cost of the entire gasification reactor [43]. This cost evaluation includes the initial cost, the cost of all subsequent relines during the life time of the containment, and the indirect cost of down time.

In general, there are two major types of refractory lining design:

(1) Thick wall, or hot wall design;

(2) Thin wall, or cold wall design.

The major function of the thick wall design is to insulate the vessel shell from the high operating temperatures. The lining designed in this way is commonly composed of either a single layer of one type of high corrosion-resistance refractory brick, or two layers of refractories, including one layer of high corrosion-resistance refractory brick and one layer of back-up material with low thermal

conductivity, such as porous brick or refractory concrete (see Fig. 2.9). Such lining systems may be several feet in thickness and the effects of cooling systems are minimal.

Slag and gaseous corrosion are usually the major factors in determining refractory lining life for the thick wall design, because of its high hot-face temperature. As a consequence, refractories which are not soluble in slag, containing large grains to reduce the area of grain boundaries, and having low porosity to minimize free surface and slag penetration, are required for eliminating slag/gaseous attack. Candidate materials for this purpose are rare, since most refractories are prone to dissolution in slag at high temperatures. More importantly, linings designed in this way induce relatively high thermal stresses in the lining, which tends to spall and crack when subjected to sudden changes in temperature.

The idea of a thin wall design is to lower the hot face temperature so that the corrosion rate can be reduced and an equilibrium layer of (viscous-solid) slag may form along the hot face of the lining. Accordingly, the resistance of the refractory lining against corrosion attack is increased. The expected life of such a thin wall lining is 1 to 2 years. A thin wall design usually adopts refractories with relatively high thermal conductivity and uses an effective cooling system. One layer of refractory with high corrosion resistance and high thermal conductivity can be used. Multiple layers of refractory including one inner (primary, interface, or working) layer of refractory with high corrosion resistance and outer (secondary or permanent) layers of refractory with high conductivity, usually,

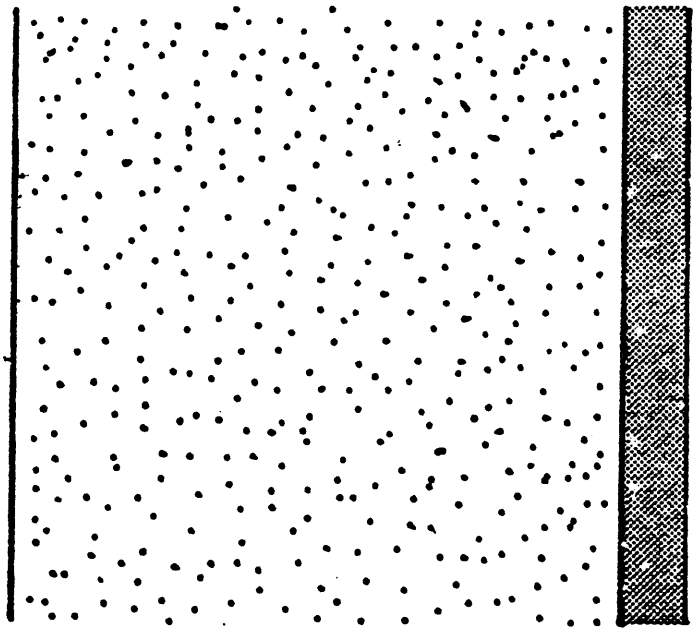

(a) Single-layered

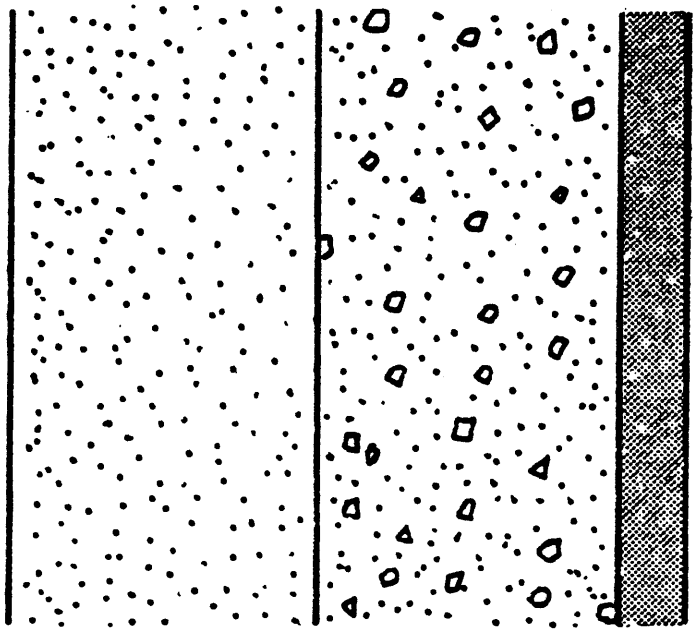

(b) Double-layered

Figure 2.9 Refractory Linings for Thick-Wall Design

Primary Lining

Insulating Castable

Shell

with high strength can be another alternative (See Fig. 2.10). The interface between the lining and shell can either be in contact, left as a gap, or filled up with additional back-up layers of refractory concrete, mortar, or compressible material. The back-up layers release excessive confining pressure from the vessel shell caused by the expansion of the lining.

Thin wall design offers certain advantages over thick wall design, such as a smaller size of gasifier vessel, lower initial cost, and longer lining life. Brick and castables have been chosen as candidate materials for thin wall linings. Brick is probably the more economical material to use over the long run, due to its high corrosion resistance and strength at elevated temperatures. Compatible mortars and cooling systems (see Fig. 2.11) are generally available for thin-wall-design lining systems.

Good control of the construction process, proper design of support systems and minimization or reuse of heat lost through the lining system should also be considered in the design of a thin-wall lining system.

In the present study only thin-wall linings composed of bricks, mortars, compressible materials, and cooling systems are considered.

§2.4 SELECTION OF REFRACTORY LINING MATERIALS

As mentioned in previous sections, the lining systems of coal gasifiers experience very severe environmental conditions during operation. This makes the selection of an optimum material very demanding. In general, the main consideration is the corrosion

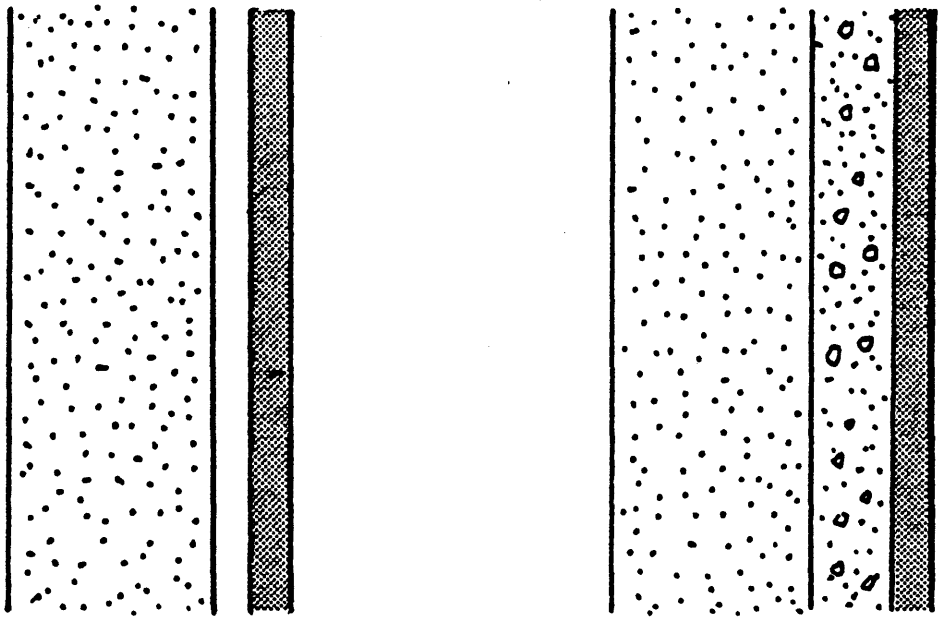

(a) Single-layered

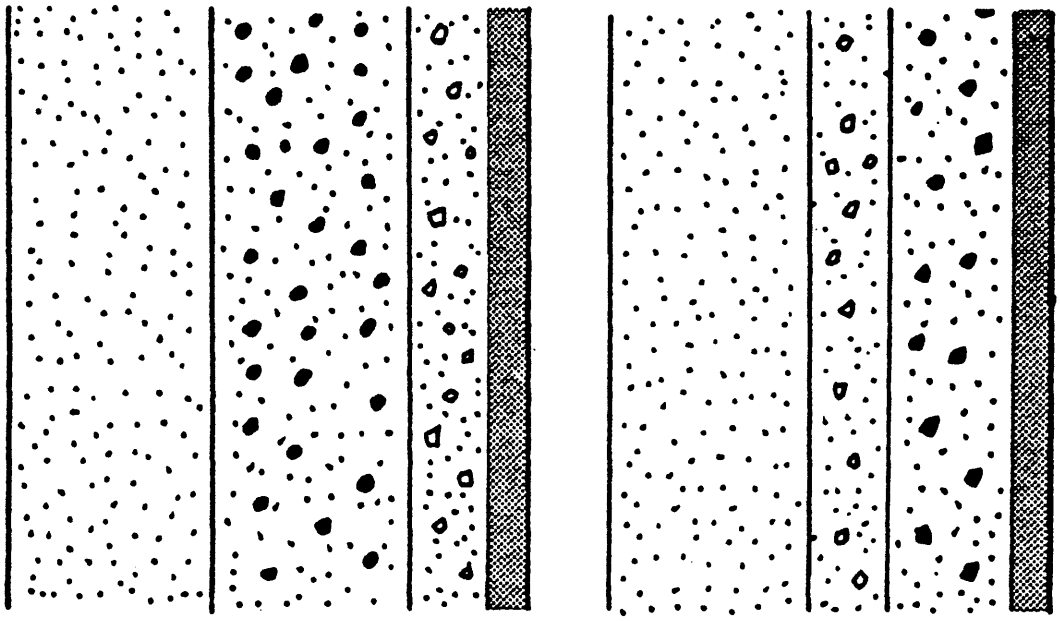

(b) Multiple-layered

Figure 2.10 Refractory Linings for Thin-Wall Design

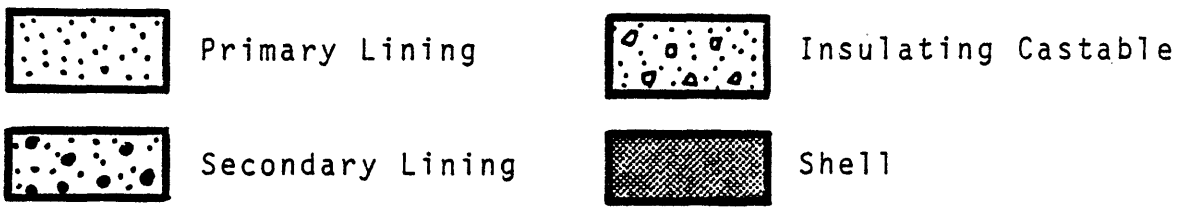

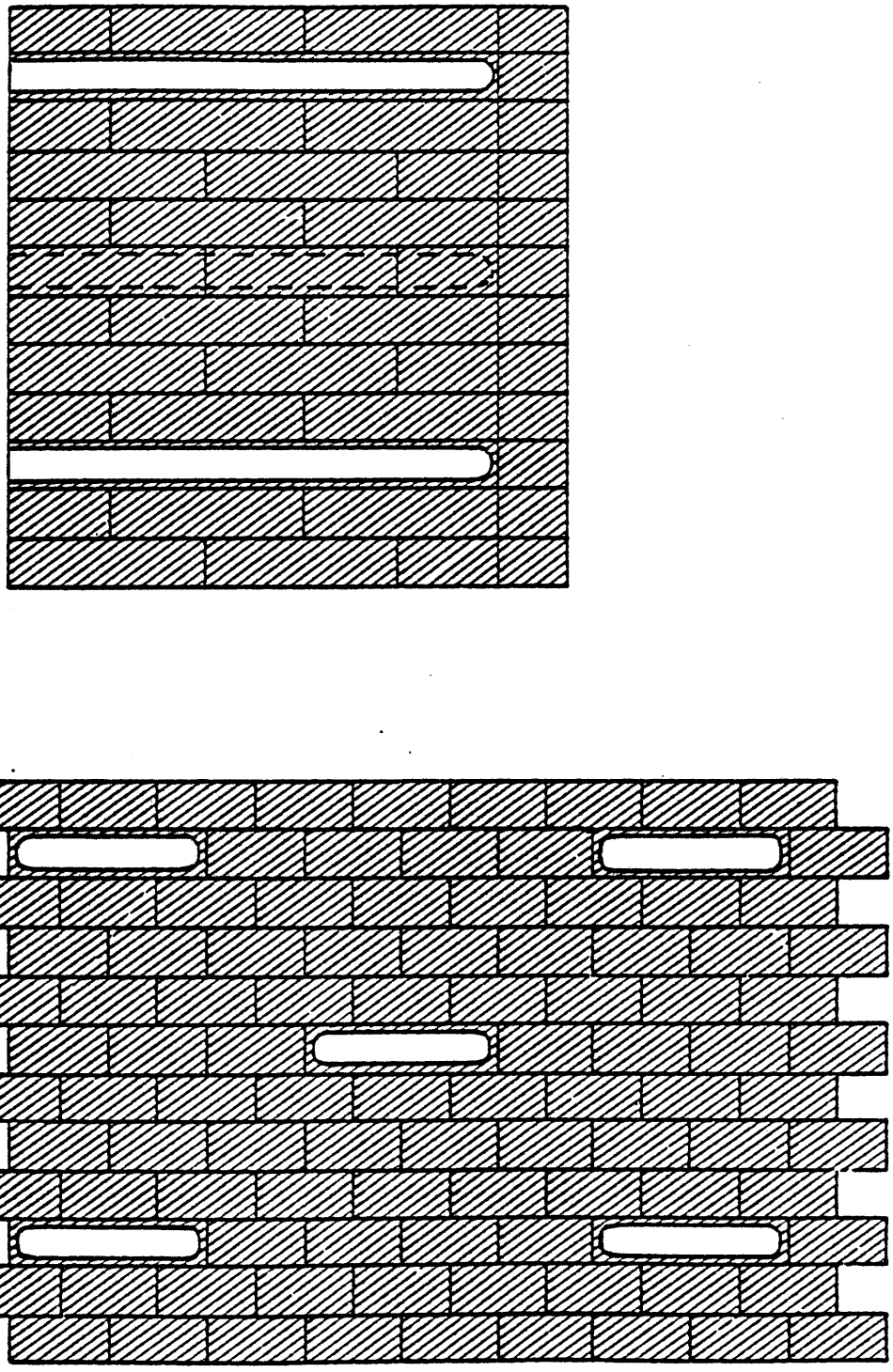

Figure 2.11 (a) Cooper Plate Cooled Wall in Slagging Coal Gasifier [43]

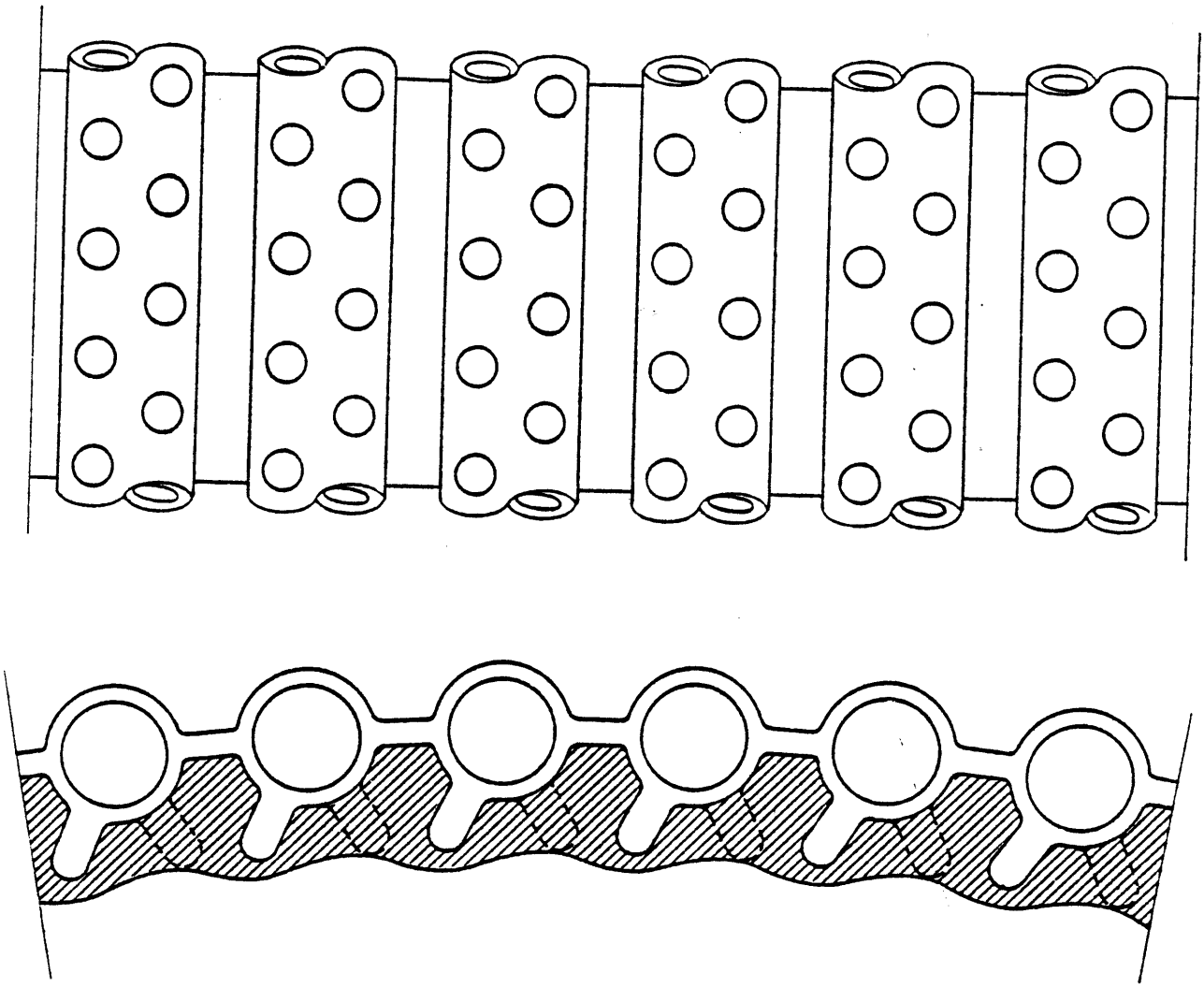

(b) Studded Membrane Wall in Slagging Coal Gasifier [43]

resistance to the slags and gases in the gasifier [30]. Extensive studies on the chemical reactions between slags/gases and refractories, in addition to numerous tests which can closely simulate refractory behavior under corrosion attack during the gasification process, are necessary.

Past efforts in this area generally focused on those refractories consisting mainly of Al_2O_3, Cr_2O_3, and MgO due to their good corrosion resistance. For slagging gasifiers the following two types of refractory bricks have been considered:

(1) High-Al_2O_3 Refractory Brick

(2) High-Cr_2O_3 Refractory Brick

90% Al_2O_3 and 80% Cr_2O_3 refractories have been developed by the Norton Company, Worcester, Massachusetts. Corrosion tests, termed as rotating sample slag tests (Fig. 2.12) have been conducted at the Norton Company [90]. This type of test can accelerate the rate of corrosion without running the risk of possibly different chemistry and corrosion mechanisms resulting from higher than normal temperature [59]. Two types of slag have been used: Black Mesa and Kentucky #9 (see Table 2.1) [62]. The speed of rotation of the samples is 60 RPM with temperatures controlled in the 1500-1600°C (2732 -2912°F) range. Each test takes 70 hours. The corrosion rates for the tested materials are shown in Table 2.2, where AX565 is a 90% Al_2O_3 + 10% Cr_2O_3 brick, and Radex and TX591 are 80% Cr_2O_3 + 20% MgO bricks.

The results indicate that 90% Al_2O_3 brick has relatively poor corrosion resistance and may not be suitable for long term applications at high temperature in a slagging gasifier. 80% Cr_2O_3 offers much

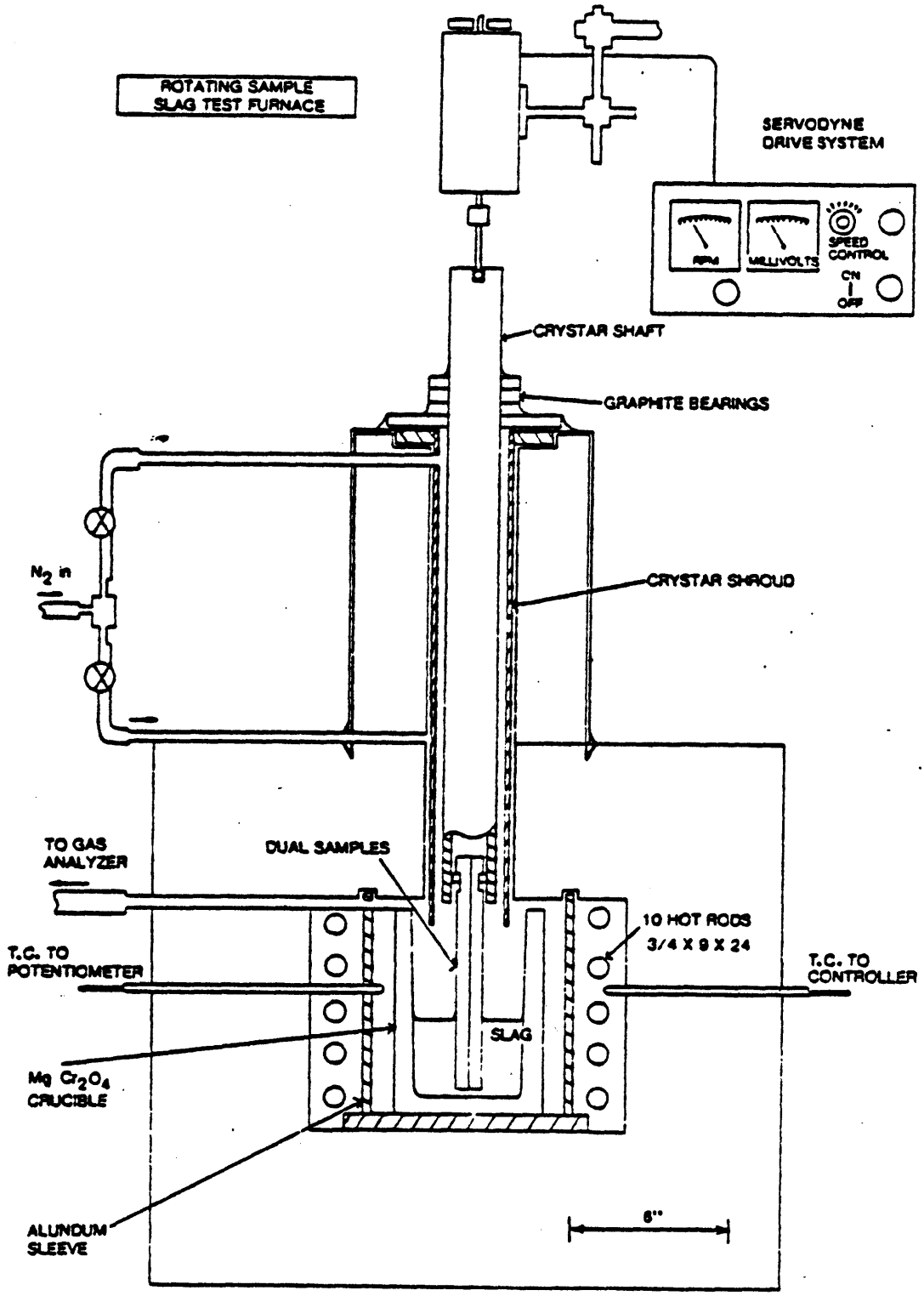

Figure 2.12 Test Furnace for Rotating Corrosion Test in Molten Slag [90]

Composition	Black Mesa	Kentucky #9
SiO_2	52.4	45.9
Al_2O_3	22.5	17.9
Fe_2O_3	6.0	22.5
TiO_2	1.1	.8
CaO	10.6	6.3
MgO	1.8	1.0
Na_2O	1.9	.7
K_2O	.5	2.5
Mn_3O_4	.03	.1
P_2O_5	.2	.2
SrO	.3	---
BaO	.3	.1
SO_3	---	2.1
C	2.0	2.0
$\frac{\text{Bases}}{\text{Acids}}$ =	$\frac{21.4}{76.2}$ = .28	$\frac{33.1}{66.9}$ = .49

Table 2.1 Slag Composition for Rotating Tests

Material / Maximum Corrosion Rate (mm/hr) / Slag	AX 565	TX 591	Radex	Zirchrome 60
RSST #13 (Kty #9, Simplified)	-0.042	-0.006	------	------
RSST #14 (Kty #9, Whole)	------	-0.007	------	------
RSST #15 (Black Mesa, Whole)	------	-0.008	------	-0.019
RSST #16 (Black Mesa, Whole)	------	-0.008	-0.015	------

Table 2.2 Summary of the Results from Corrosion Tests

better corrosion resistance. High-Al_2O_3 brick, however, has better thermal shock resistance than high-Cr_2O_3 brick [34]. In the present study both of them will be considered as candidate materials for the primary lining, but the final selection of the lining materials for a gasifier should be based on the minimum total cost over the lifetime of the gasifier.

For secondary linings and back-up materials used in the lining design, silicon carbide (SiC) bricks which provide high conductivity and high strength [66], and refractory concrete which has good insulating capability, are considered as candidate materials for different design needs. Compressible materials are also used for the compressible layers, if adopted.

In the present work, the afore-mentioned refractory bricks (i.e., 90% Al_2O_3 + 10% Cr_2O_3, 90% Cr_2O_3 + 20% MgO, SiC bricks), and refractory concrete are chosen as candidate materials for the lining in slagging gasifiers. In the next chapter, their thermophysical and thermomechanical properties are presented, and the associated material models are developed based on available test data for the candidate refractories. These material models can be implemented in a finite element program and used in the thermomechanical analysis discussed in Chapter 6.

CHAPTER 3

MATERIAL BEHAVIOR AND MATERIAL MODELING

§3.1 INTRODUCTION

The selection of proper lining materials and the design of lining configurations for high-temperature, high-corrosion gasification environments require a thorough understanding of material and lining system behavior. In this chapter, the thermophysical and thermomechanical behavior of selected candidate lining materials is studied. Corrosion and lining system behavior are discussed in Chapters 4 and 6 respectively.

The thermophysical behavior of lining materials is generally temperature dependent. For the study of lining behavior in a heating process, the following properties associated with the temperature-dependent thermophysical behavior of the materials are needed:

(1) Thermal conductivity;

(2) Density and specific heat; and

(3) Coefficient of thermal expansion.

The thermomechanical behavior of lining materials is complex. It may be temperature, load history and time dependent. The characterization of such behavior through rational modeling is essential for

accurate prediction of the lining behavior in a gasification environment. With regard to time effects, such mechanical behavior can be conveniently decoupled into

(1) Time-independent or instantaneous constitutive behavior; and

(2) Time-dependent creep behavior.

At this time, the available data is not sufficient to fully characterize these material behavior, especially stress-strain relationships of materials in generalized states of stress at elevated temperatures. In the development of material models, some extrapolations based on knowledge of similar materials are adopted whenever the data for candidate materials is found inadequate.

In the remaining sections of this chapter the general material behavior is first prescribed for each material property. The associated models are then presented, followed by regression results of model parameters for each material concerned. At the end of this chapter, properties of steel are also listed for use in later chapters.

§3.2 THERMOPHYSICAL PROPERTIES

The thermophysical properties of concern for the lining materials discussed in this section include thermal conductivity, material density, specific heat, and coefficient of thermal expansion.

§3.2.1 Thermal Conductivity

The thermal conductivity of refractory materials is temperature dependent. At elevated temperatures, void changes, the reconstruction

of structural components in the material matrix, such as aggregates and bonding agents, and potential chemical reactions may significantly modify the thermal conductivity of the refractories. Under uniform temperature conditions and before the application of external loads, the refractory materials can be assumed to be isotropic. The thermal conductivity of this isotropic solid is represented by "K_s" herein. For refractories under load, the possible separation between the aggregates and the bonding agents, with the resulting potential crack formation may modify the local thermal conductivity within the materials. Modeling of this phenomenon is presented in Chapter 5.

The functional dependence of K_s of the candidate materials on temperature (T) is well represented by a polynomial expansion. The parameters of the polynomial may be obtained by fitting the test data using the least squares method. For the materials under consideration, the following cubic polynomial functions are adopted for $K_s(T)$.

(1) 90% Al_2O_3 + 10% Cr_2O_3 refractory:

The data developed by the Applied Technology Laboratories (ATL) [62] on Norton AX565 refractory bricks is used for the regression. The data values for K_s are in the temperature range 200 to 1400°C. The results of the regression are shown in Fig. 3.1. The best fit polynomial functions are:

$$K_s \text{ (Watt/m-°C)} = 6.7779 + 9.5840\times10^{-4}T - 6.9043\times10^{-6}T^2 + 3.4805\times10^{-9}T^3 \quad , \quad T \text{ in °C}$$

$$\text{or } K_s\text{(Btu/hr-in-°F)} = 0.3245 + 3.2292\times10^{-5}T - 1.0536\times10^{-7}T^2 + 2.8736\times10^{-11}T^3 \quad , \quad T \text{ in °F} \qquad (3.1)$$

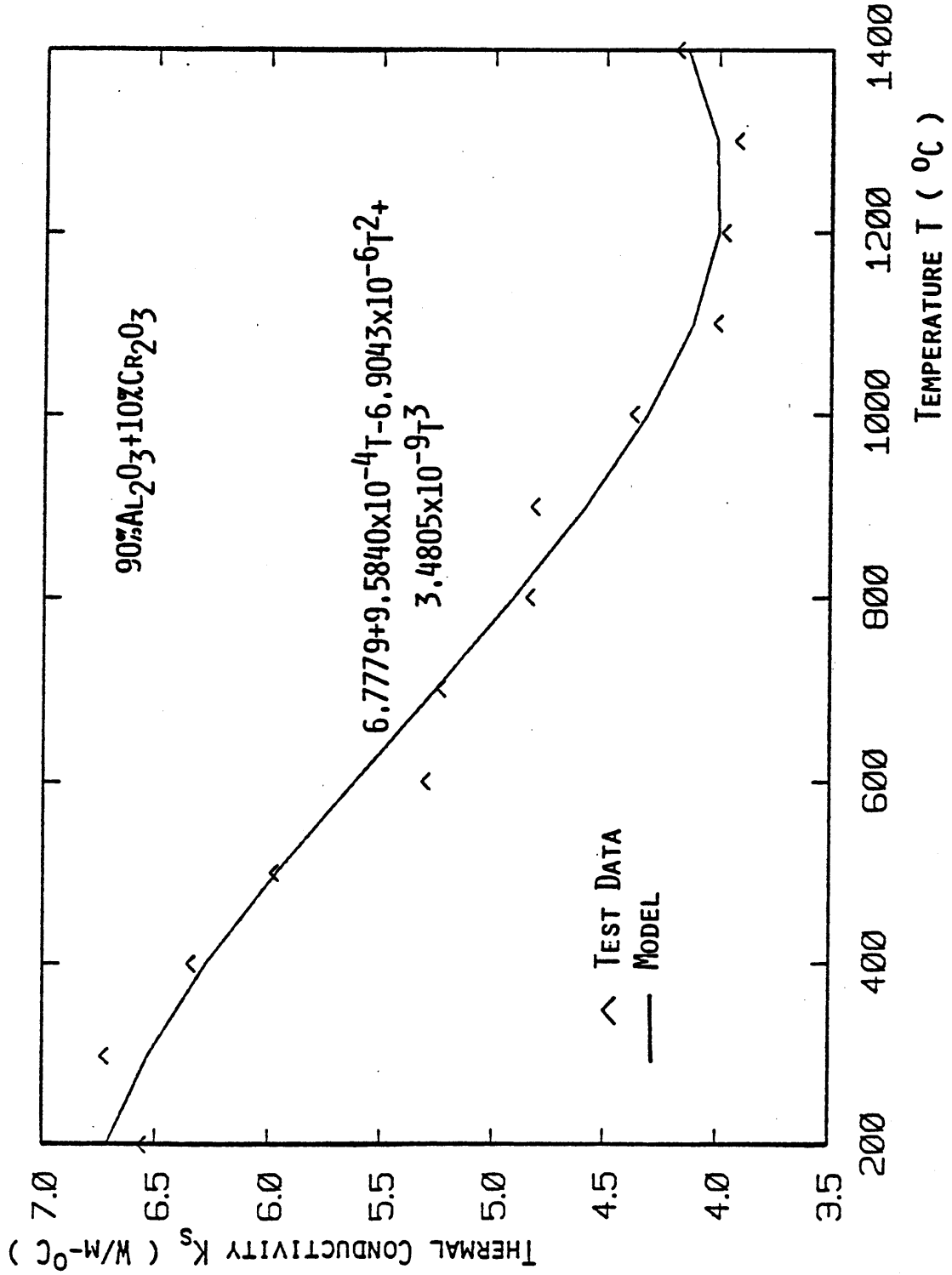

Figure 3.1 Thermal Conductivity (K_S) vs. Temperature (T) Relationship for 90% Al_2O_3 + 10% Cr_2O_3 Refractory

(2) 80% Cr_2O_3 + 20% MgO refractory:

The data for Norton TX591 refractory bricks tested by ATL [62] is used. The temperature range in the testing is 200 to 1400°C. The data points and the results of the regression are shown in Fig. 3.2. The best fit polynomial functions are:

$$K_s \text{ (Watt/m-°C)} = 5.6541 - 1.1981\times10^{-3}T + 3.6673\times10^{-7}T^2 - 2.2522\times10^{-10}T^3 \text{ , T in °C}$$

$$\text{or } K_s\text{(Btu/hr-in-°F)} = 0.2732 - 3.2404\times10^{-5}T + 5.6285\times10^{-9}T^2 - 1.4471\times10^{-13}T^3 \text{ , T in °F} \qquad (3.2)$$

(3) SiC refractory:

SiC bricks are commonly used as secondary lining materials in the lining systems. In the present study, sintered SiC bricks are selected for their high service temperature (up to 1700°C) and high thermal conductivity, which are needed for linings in slagging gasifiers. A regression fit of the data from Refs. 74, 85 and 89, (see Fig. 3.3) gives the following polynomial functions:

$$K_s\text{(Btu/hr-in-°F)} = 1.8491 - 1.1036\times10^{-3}T + 3.6650\times10^{-7}T^2 - 5.4264\times10^{-11}T^3 \text{ , T in °F} \qquad (3.3)$$

(4) Hydrogen (H_2)

Hydrogen is an active gas in the gasifier at high temperatures, and has the highest thermal conductivity among all gases in the gasifiers. The penetration of H_2 into the cracks of refractories affects the local thermal conductivity

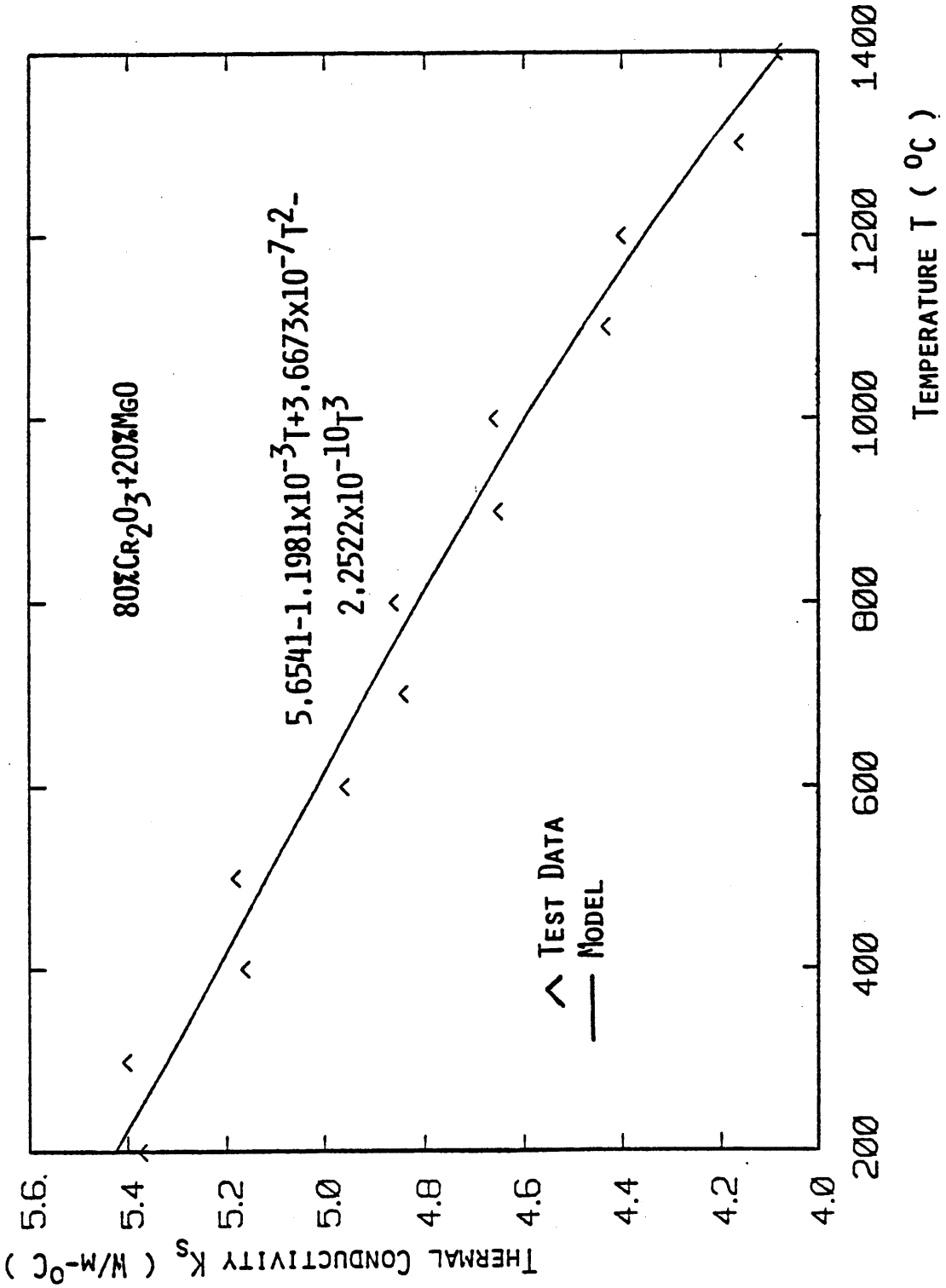

Figure 3.2 Thermal Conductivity (K_S) vs. Temperature (T) Relationship for 80% Cr_2O_3 + 20% MgO Refractory

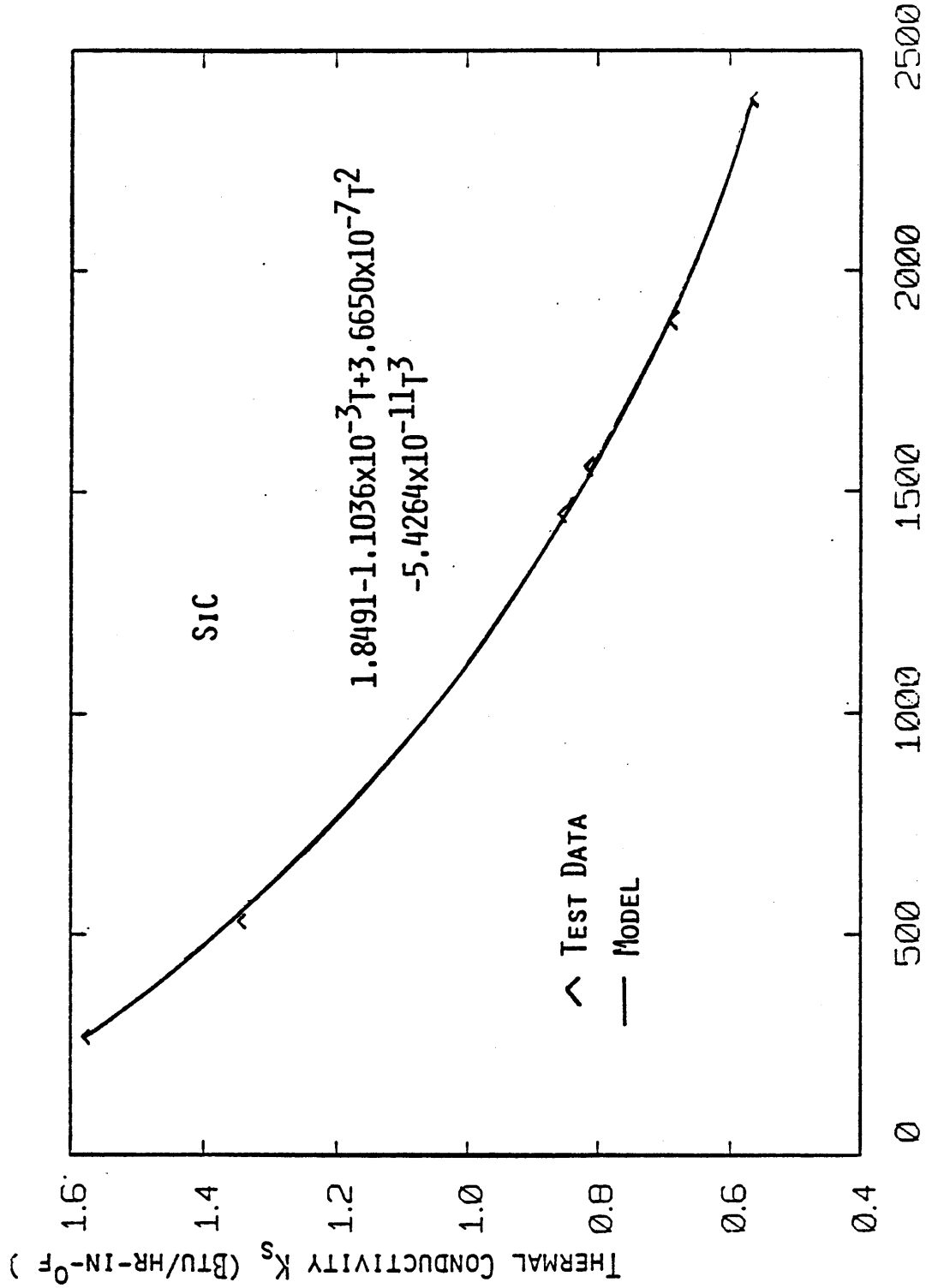

Figure 3.3 Thermal Conductivity (K_s) vs. Temperature (T) Relationship for SiC Refractory

of the materials, and this modification should be considered in the heat transfer analysis. The use of the data from Ref. 86 leads to the following regression function for the thermal conductivity of Hydrogen (see Fig. 3.4):

$$K_g(\text{Btu/hr-in-°F}) = 7.7498\times10^{-3} + 1.0843\times10^{-5}T - 1.4166\times10^{-9}T^2 + 3.3296\times10^{-13}T^3 \quad , T \text{ in °F} \qquad (3.4)$$

in which K_g represents the thermal conductivity of the gas considered (Hydrogen).

§3.2.2 Density and Specific Heat

Density (ρ) and specific heat (C_p) are assumed to be dependent on temperature only. Cubic polynomial functions of T are adopted for the product of ρ and C_p (ρC_p) .

(1) 90% Al_2O_3 + 10% Cr_2O_3 refractory:

The data used is that for Norton AX565 refractory bricks tested by ATL [65] (see Fig. 3.5). The results of the regression are:

$$\rho C_p\ (\text{Cal/cm}^3\text{-°C}) = 0.7179 + 5.9840\times10^{-4}T - 4.1825\times10^{-7}T^2 + 1.5371\times10^{-10}T^3 \quad , T \text{ in °C}$$

or

$$\rho C_p\ (\text{Btu/in}^3\text{-°F}) = 2.5515\times10^{-2} + 1.2340\times10^{-5}T - 5.4506\times10^{-9}T^2 + 9.5094\times10^{-13}T^3 \quad , T \text{ in °F} \qquad (3.5)$$

(2) 80% Cr_2O_3 + 20% MgO refractory:

The data used is that for Norton TX591 refractory bricks tested by ATL [62] (see Fig. 3.6). The regression results are:

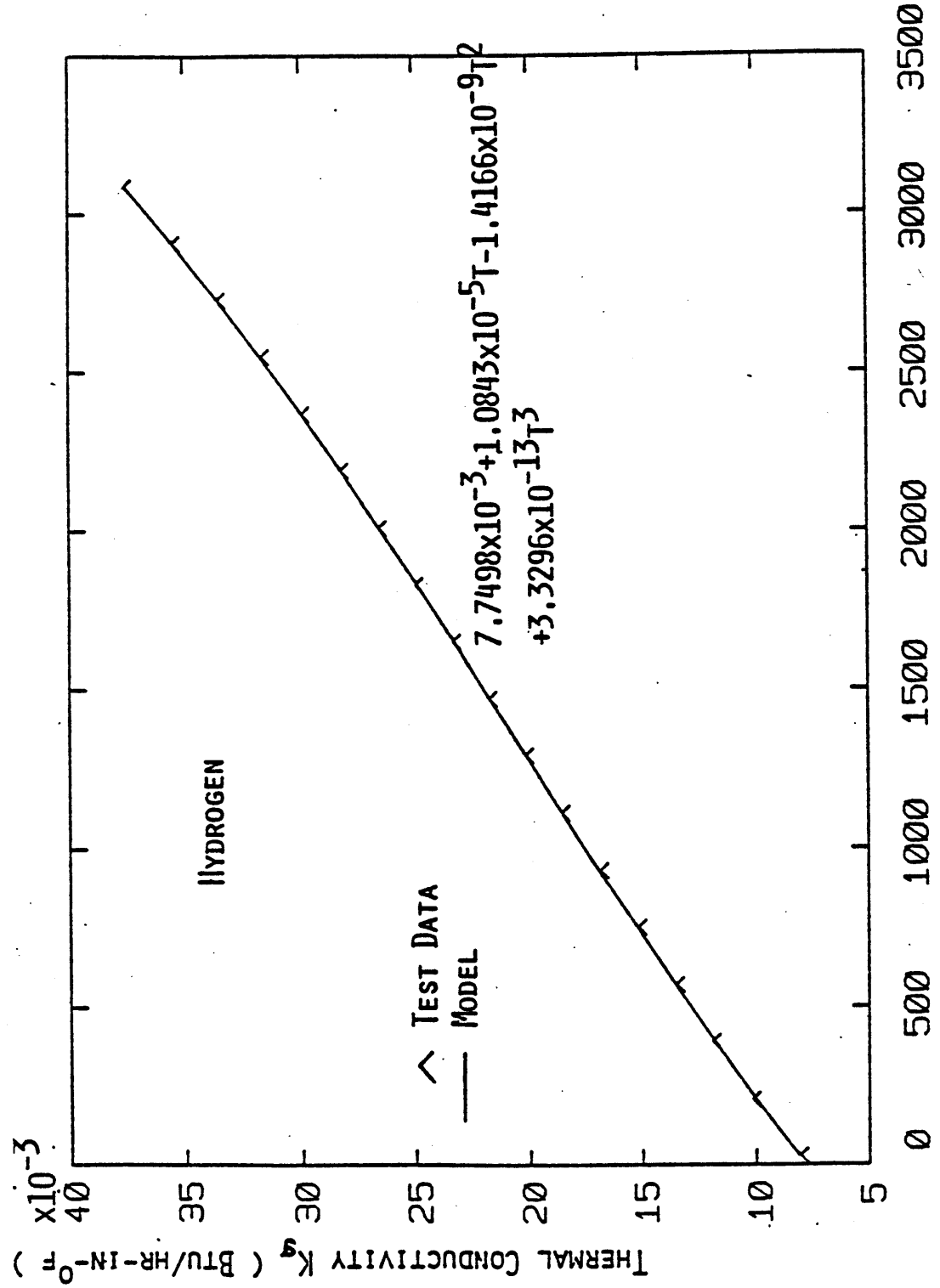

Figure 3.4 Thermal Conductivity (K_g) vs. Temperature (T) Relationship for H_2 (Hydrogen) Gas

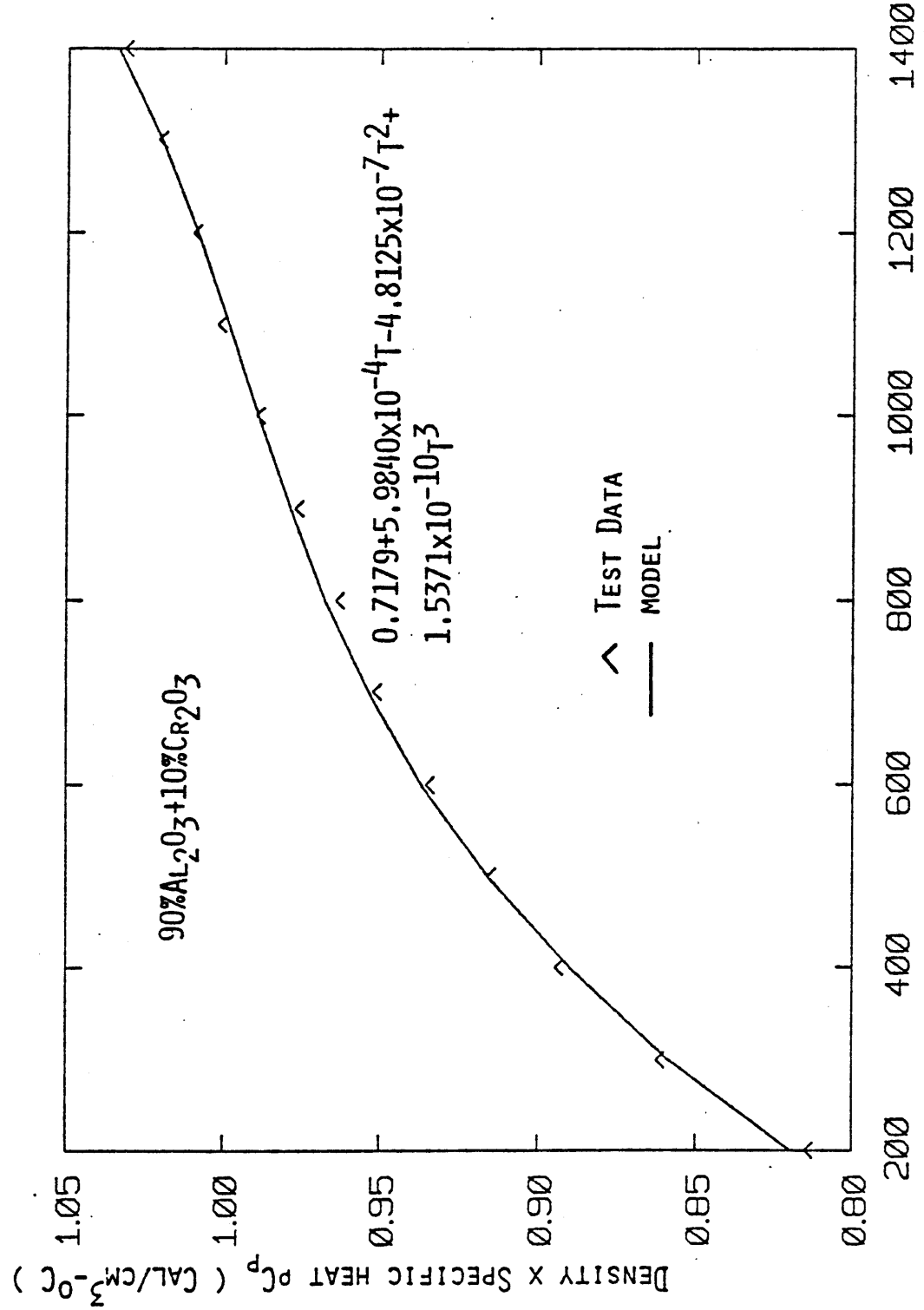

Figure 3.5 Product of Density (ρ) and Specific Heat (C_p) vs. Temperature (T) Relationship for 90% $A\ell_2O_3$ + 10% Cr_2O_3 Refractory

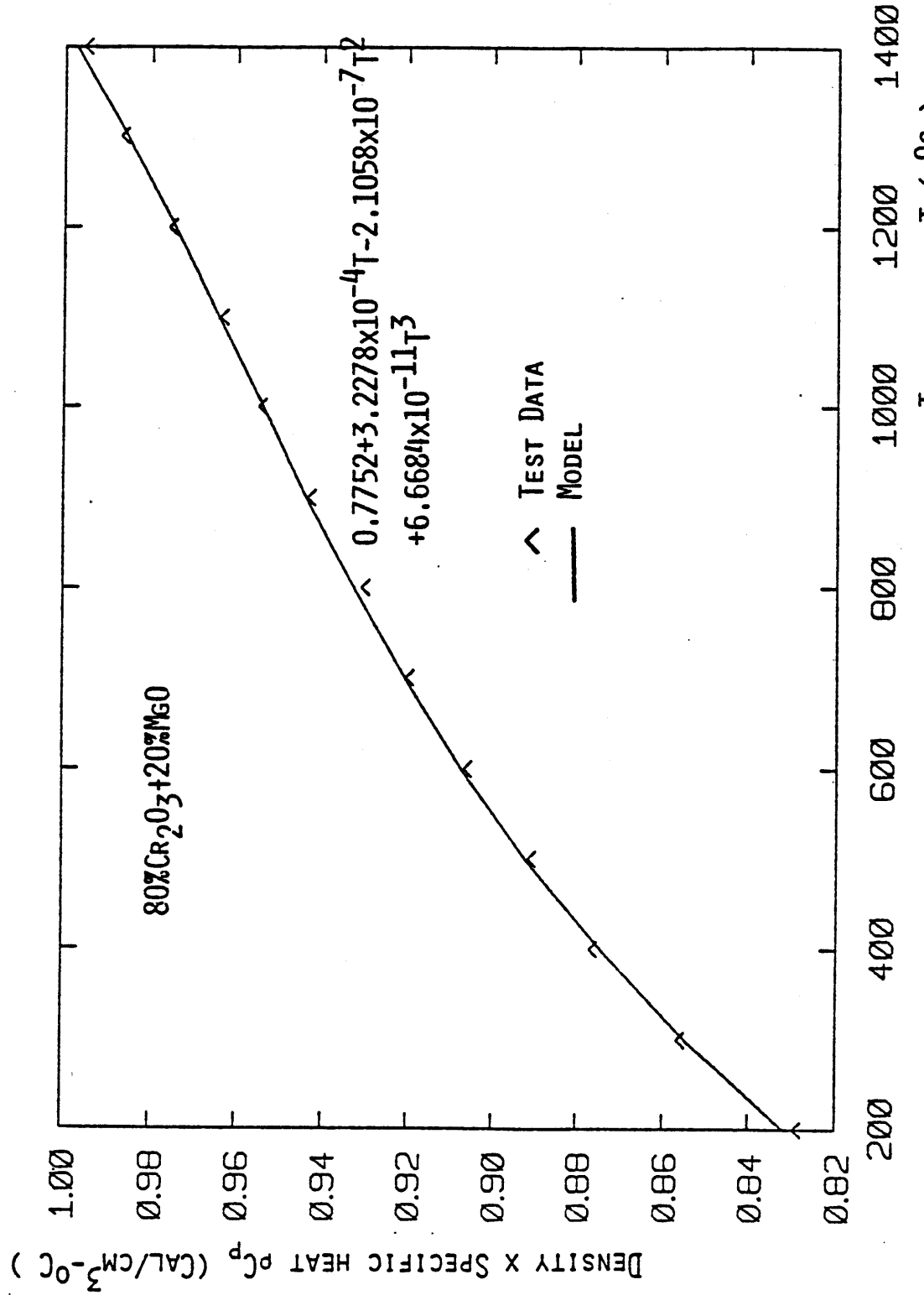

Figure 3.6 Product of Density (ρ) and Specific Heat (C_p) vs. Temperature (T) Relationship for 80% Cr_2O_3 + 20% MgO Refractory

$$\rho C_p \text{ (Cal/cm}^3\text{-°C)} = 0.7752 + 3.2278\times10^{-4}T - 2.1058\times10^{-7}T^2 + 6.6684\times10^{-11}T^3 \quad , T \text{ in °C}$$

or

$$\rho C_p \text{ (Btu/in}^3\text{-°F)} = 7.8174\times10^{-2} + 6.6212\times10^{-6}T - 2.3557\times10^{-9}T^2 + 4.1255\times10^{-13}T^3 \quad , T \text{ in °F} \qquad (3.6)$$

(3) SiC refractory brick:

The data from Ref. 86 is used for regression (see Fig. 3.7), and the following function is obtained:

$$\rho C_p \text{ (Btu/in}^3\text{-°F)} = 0.01188 + 1.6052\times10^{-5}T - 8.0077\times10^{-9}T^2 + 1.4985\times10^{-12}T^3 \quad , T \text{ in °F} \qquad (3.7)$$

§3.2.3 Coefficient of Thermal Expansion

Data for coefficient of thermal expansion (α) of 90% Al_2O_3 + 10%Cr_2O_3 , 80% Cr_2O_3 + 20% MgO, and SiC bricks are drawn from the afore-mentioned sources for K_s and ρC_p and Ref. 24. A quadratic polynomial function in T is adopted to fit the data for linear expansion and the derivative of that with respect to T is used to represent α . The data is shown in Figs. 3.8 to 3.10 for three candidate materials. The regression results are:

(1) 90% Al_2O_3 + 10% Cr_2O_3 refractory:

$$\alpha \text{ (°F}^{-1}) = 5.0070\times10^{-6} \qquad (3.8)$$

(2) 80% Cr_2O_3 + 20% MgO refractory:

$$\alpha \text{ (°F}^{-1}) = 6.435\times10^{-6} + 2.310\times10^{-9}T \quad , T \text{ in °F} \qquad (3.9)$$

(3) SiC refractory brick:

$$\alpha \text{ (°F}^{-1}) = 2.1661\times10^{-6} + 5.3986\times10^{-10}T \quad , T \text{ in °F} \qquad (3.10)$$

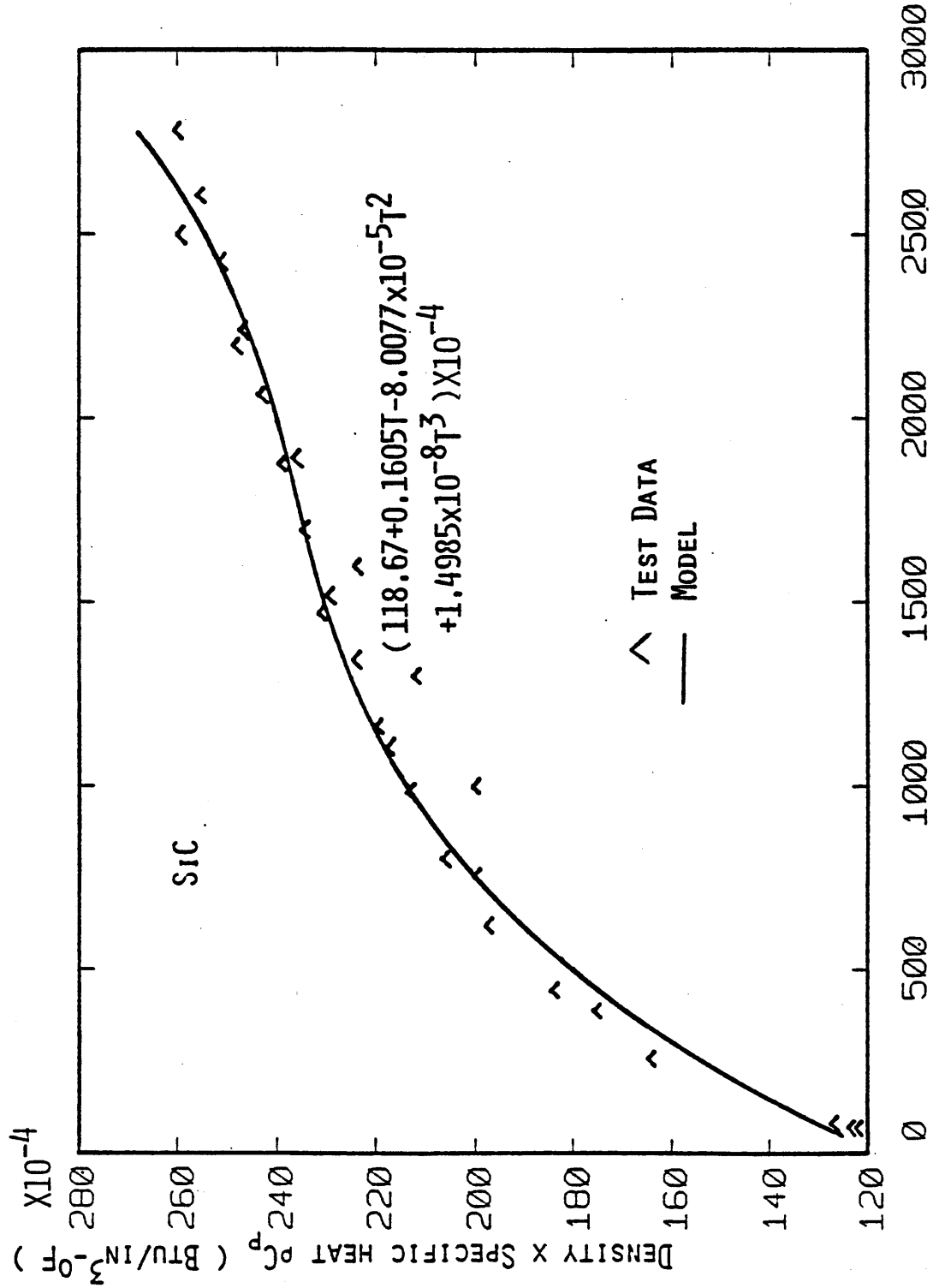

Figure 3.7 Product of Density (ρ) and Specific Heat (C_p) vs. Temperature (T) Relationship for SiC Refractory

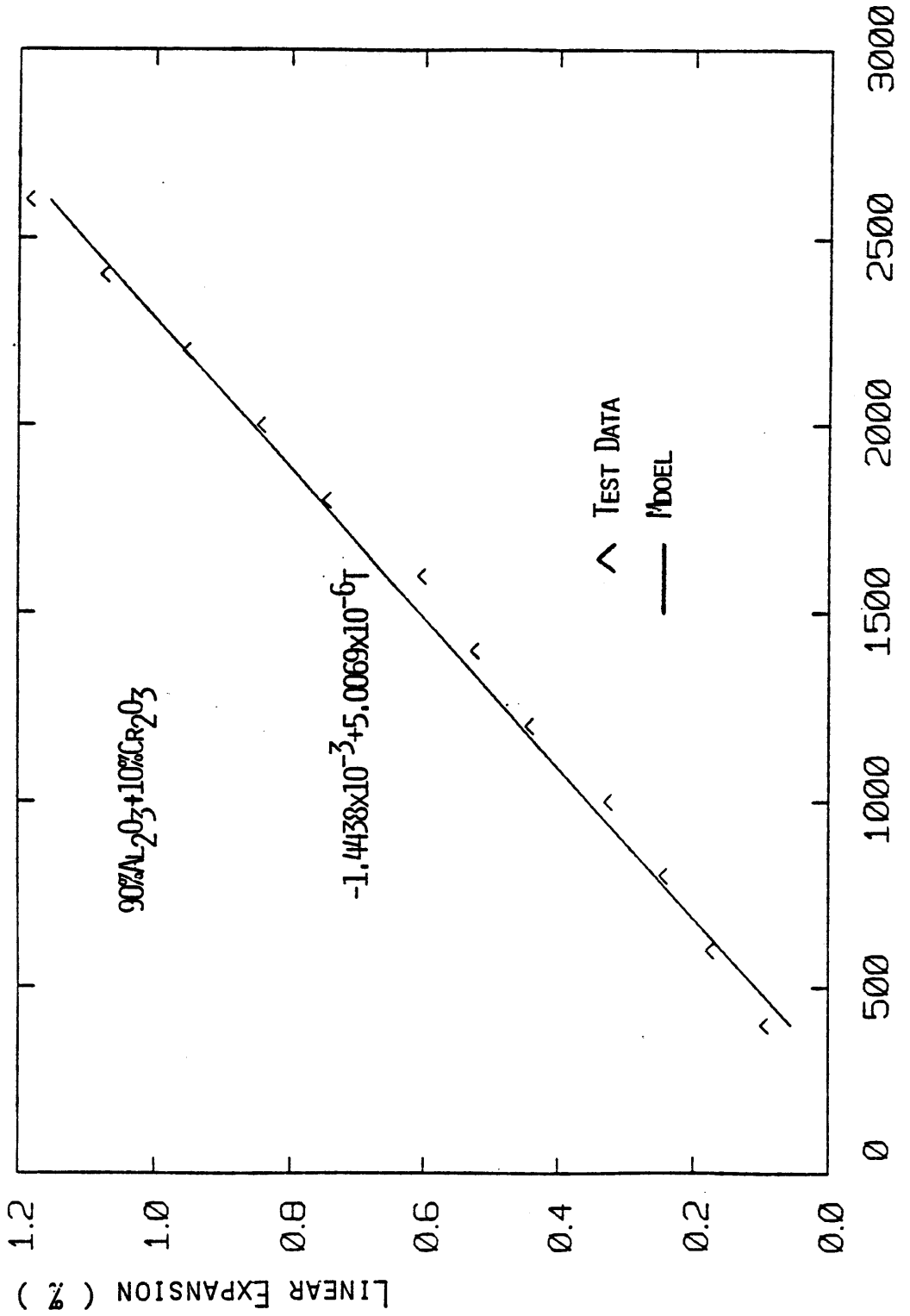

Figure 3.8 Linear Expansion vs. Temperature Relationship for 90% Al_2O_3 + 10% Cr_2O_3 Refractory

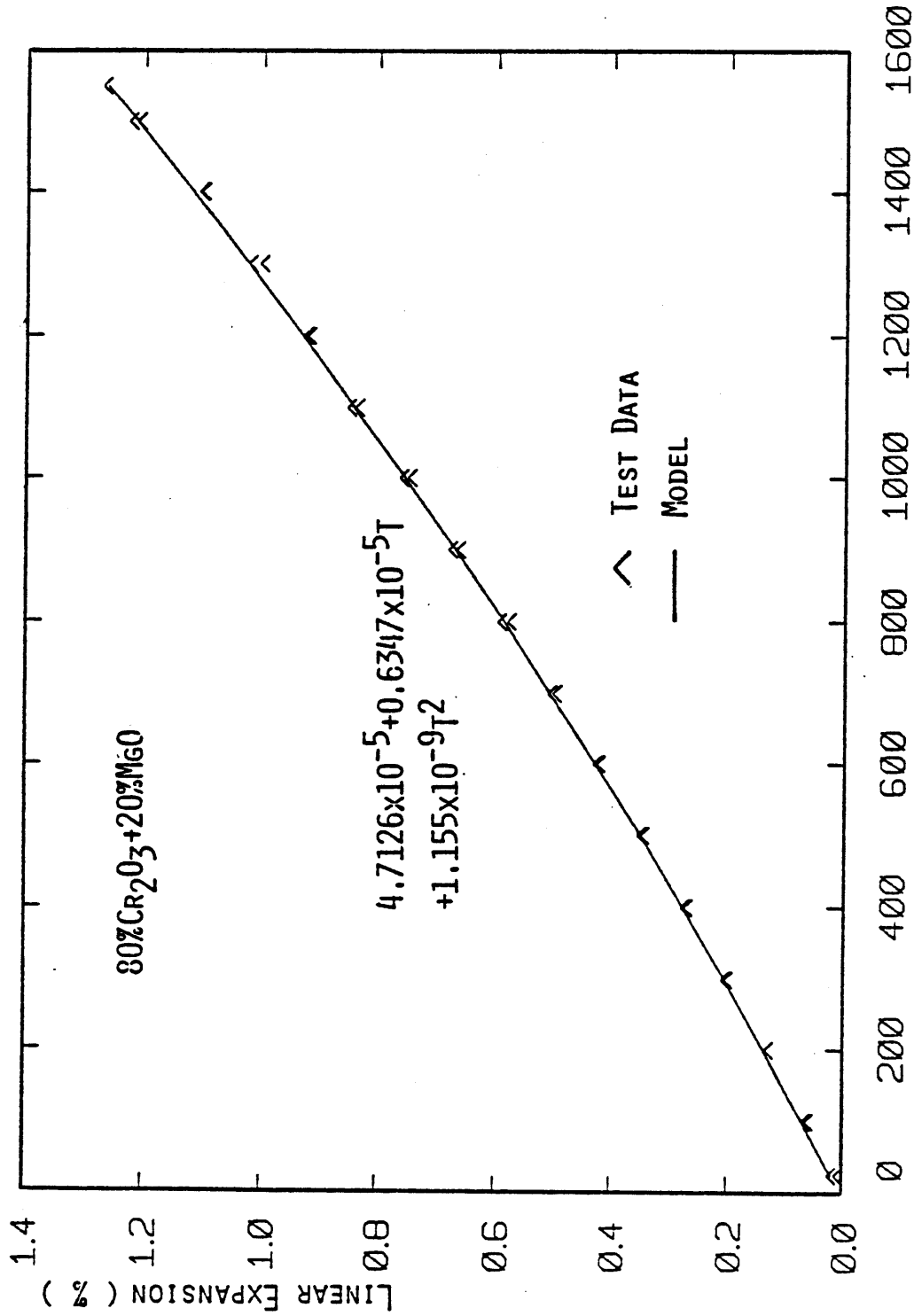

Figure 3.9 Linear Expansion vs. Temperature Relationship for 80% Cr_2O_3 + 20% MgO Refractory

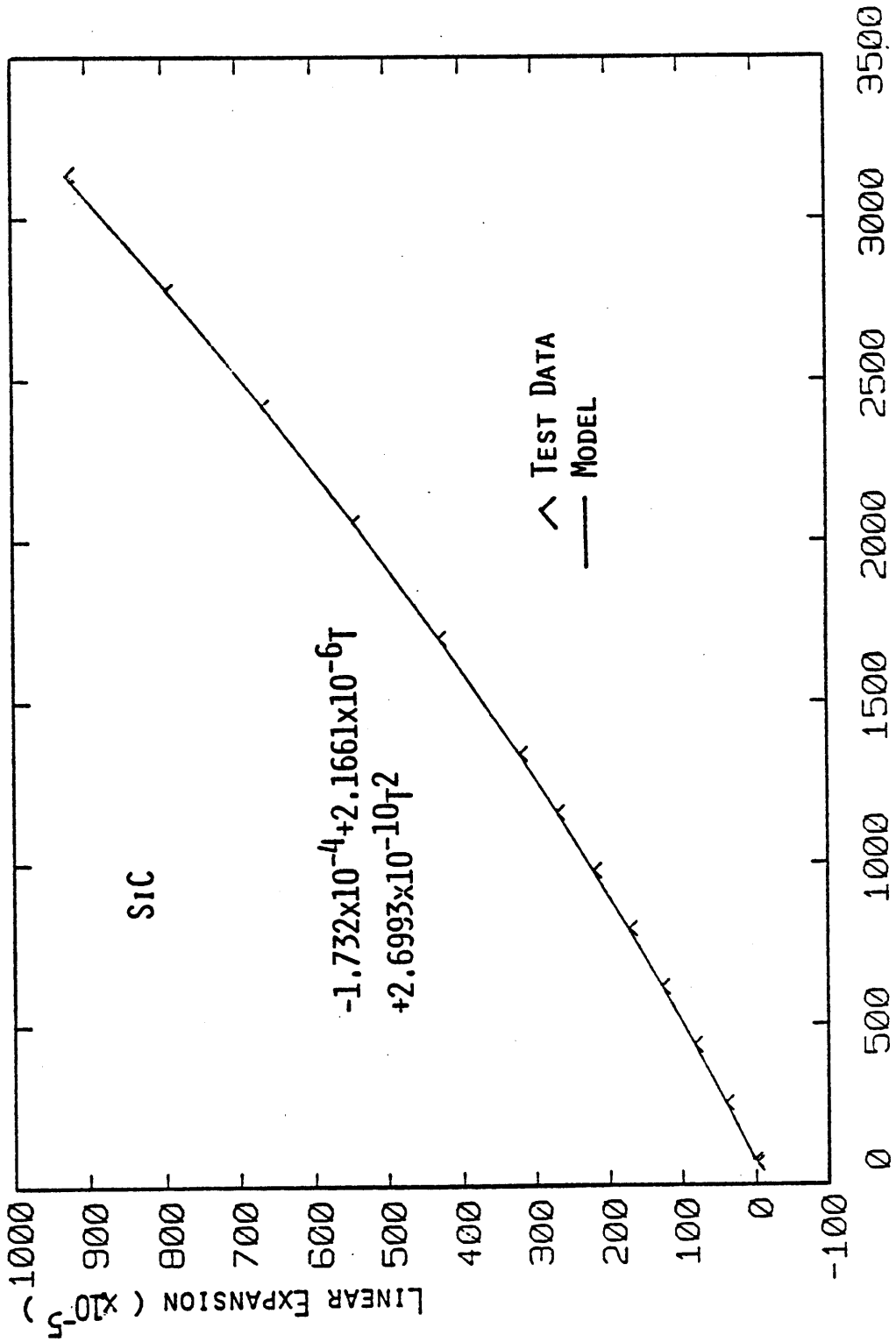

Figure 3.10 Linear Expansion vs. Temperature Relationship for SiC Refractory

§3.3 MODELING OF TIME-INDEPENDENT THERMOMECHANICAL BEHAVIOR

During the heating process, the materials in a lining system can experience various loads, resulting in a possible multiaxial and cyclic stress history. The time-independent material response to such loads is generally nonlinear plastic deformation. The associated constitutive behavior is typically load-history and temperature dependent. In this section, the important features of such complex behavior are reviewed, and associated constitutive models for the selected lining materials are proposed.

§3.3.1 90% Alumina Refractory, 80% Chromia Refractory, and Concretes

(1) Room Temperature

Refractory materials and concrete have similar characteristics in their structural composition. Both types of material are composed of grains (or aggregates) and bonding agents. Hence, they share the same type of time-independent constitutive behavior, and similar brittle failure mechanisms under loads. In general, both materials contain numerous microcracks even before the application of any external loads. This is attributed to the void volume changes between various material constituents such as grains and bonding agents. The void volume changes are primarily caused by the change of water content during manufacturing of the refractory bricks, and during the maturing period of the concrete. The void volume change in the refractory bricks may take place during the manufacturing process due to nonuniform temperature distributions over the brick volumes, and uneven thermal expansion between the structural constituents.

The short-term stress-strain curves show that refactories and structural concrete undergo nonlinear plastic deformations under loads [18,22,23,41,48,56,68]. This is attributed primarily to the progression of microcracks in the materials caused by the application of external loads. Under loads, extension and widening of the microcracks [27,81] results in the separation of the structural components in the material matrix, and relative boundary slippage between these components occurs [21,46]. Morover, frictional interlocking over the crack interfaces and local crushing may occur, resulting in further behavioral complexities, such as dilatancy and compaction during load cycles. These phenomena caused by the existance of microcracks and their propagation under loads are termed here as "damage" to the materials.

Acoustic emission measurements [81] show that such a damage process in concrete under uniaxial compressive loading is continuous, and starts at very low levels of applied strain. The magnitude of damage increases as strain increases. During subsequent unloading and reloading, the damage is observed only when the maximum axial strain previously experienced is exceeded. This suggests the use of a strain concept to evaluate the damage in the gross material. It is feasible that in multiaxial stress states a measure of damage might be based on a first or higher order strain vector [47,55].

The damage process which starts at very low stress/strain levels is often insignificant, and the overall stress-strain response may be assumed to be linear. With increased loads and the resulting microcracking, nonlinearity in the material behavior becomes more evident. Further increase of the load eventually results in unstable

fracture, after which the material cannot sustain further loading. This stage is usually defined as failure of the material, and the associated peak stress is referred to as ultimate strength. The stress combinations corresponding to the ultimate strength of materials under different monotonic loadings are usually represented by a so called "failure surface" (Fig. 3.11) in stress space. Various functional forms have been proposed for the failure surface for concrete (see e.g. Ref. 25) and refractories [1,5,80]. After this initial failure, the failure surface shrinks in size consistent with the falling branch of the stress-strain curves (Fig. 3.12), depending on the maximum damage (or maximum strain) experienced by the material. Tests on concrete materials [19,48,81] suggest that for a given damage level, failure stresses for monotonically and cyclically loaded specimens approximately coincide (Fig. 3.12). This suggests the existence of a unique innermost envelope in stress space, corresponding to a specific damage level, which encloses all the possible stress points and shrinks in size as damage accumulates. This envelope called "bounding surface" in the following plays an important role in characterizing material properties.

A realistic representation of stress-strain behavior may be achieved by decomposing the stress and strain into deviatoric and hydrostatic components [41,53,54]. The constitutive behavior is then formulated on the deviatoric plane and along the hydroaxis, i.e., a three dimensional representation is possible in using octahedral shear, and volumetric stresses and strains, respectively. Test results [23,77] show that (a) purely increased volumetric stress (strain) does not

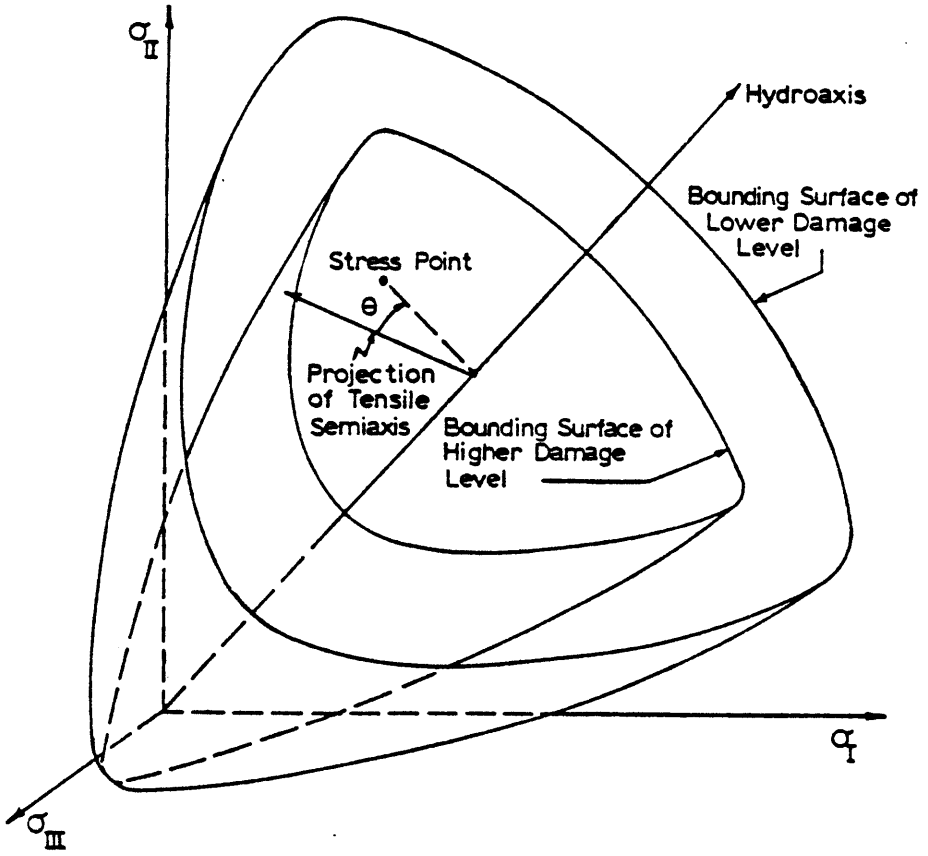

Figure 3.11 The Damage-Dependent Bounding Surface

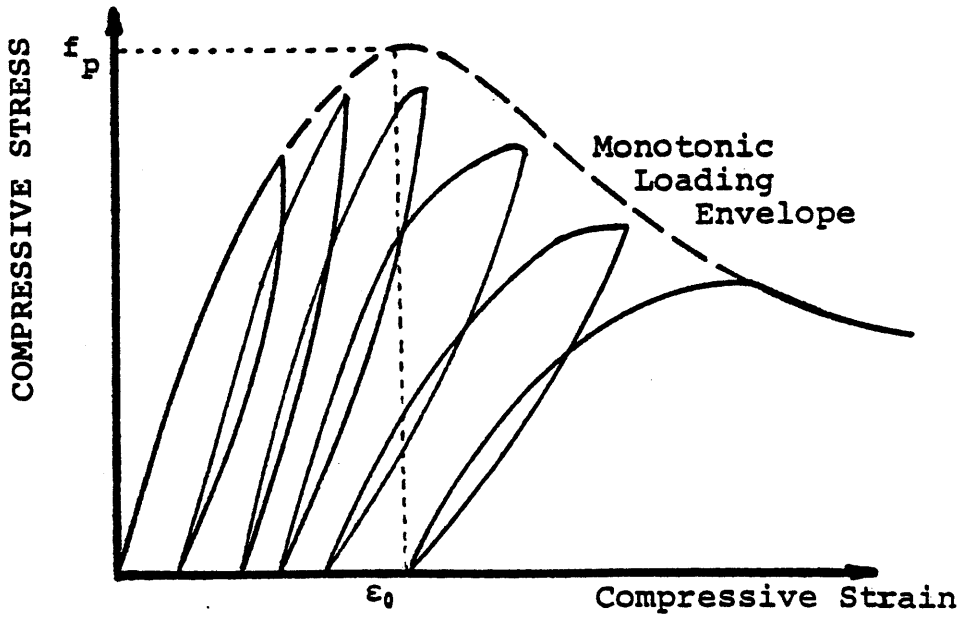

Figure 3.12 Stress-Strain Relationship for Ceramic Materials in Uniaxial Compression

cause any change in the octahedral shear strain components except at very high volumetric and octahedral stress states, and (b) the volumetric strain is influenced not only by the change in volumetric stress but also by the change in octahedral shear stress and strain. This coupling phenomenon between volumetric and octahedral shear components is generally interpreted as shear compaction and dilatancy. For a fixed volumetric stress it is shown in Ref. 77 that proportional loading and unloading on the deviatoric plane changes the volumetric strain. Deviatoric loading causes both dilatancy and compaction, while unlaoding and reloading up to the previous maximum deviatoric stress results only in dilatancy.

(A) Definitions

In the development that follows in this section (§3.3.1) the stresses σ_{ij} (i,j=1,2,3) and strains ε_{ij} are normalized with respect to the peak stress (f_p), and the associated strain (ε_p) from the uniaxial compressive loading curve respectively. A positive sign is assigned to compressive stress and to strain if it represents contraction.

Some definitions related to stresses and strains are summarized as follows (the usual summation convention for repeated indices is adopted):

I_1 = first stress invariant, $I_1 = \sigma_{kk}$ (k=1,2,3)

S_{ij} = deviatoric stress, $S_{ij} = \sigma_{ij} - \frac{1}{3}\delta_{ij} I_1$ where δ_{ij} is the Kronecker delta

J_2 = second deviatoric stress invariant, $J_2 = \frac{1}{2} S_{ij}S_{ij}$ (i,j=1,2,3)

J = third deviatoric stress invariant, $J_3 = \frac{1}{3} S_{ij}S_{jk}S_{ki}$ (i,j,k=1,2,3)

τ_o = octahedral shear stress, $\tau_o = \sqrt{\frac{1}{3} S_{ij}S_{ij}}$ (i,j=1,2,3)

θ = angle in radians between the projection of the position vector for principal stress and that of any tensile semiaxis on the deviatoric plane (see Fig. 3.13)

$$\theta = \frac{1}{3} \cos^{-1} \left(\frac{-3\sqrt{3}\, J_3}{2 J_2^{3/2}} \right)$$

ε_v = volumetric strain, $\varepsilon_v = \varepsilon_{kk}$ (k=1,2,3)

ε_v^p = volumetric strain due to plastic response

e_{ij} = devatoric strain, $e_{ij} = \varepsilon_{ij} - \frac{1}{3} \delta_{ij} \varepsilon_v$

e_{ij}^e = deviatoric strain due to elastic response

e_{ij}^p = deviatoric strain due to plastic deformation

γ_o^p = plastic octahedral shear strain

$$\gamma_o^p = \sqrt{\frac{1}{3} e_{ij}^p e_{ij}^p} \qquad (i,j = 1,2,3)$$

(B) Damage Parameter and Bounding Surface

As discussed previously, concrete and refractories are subjected to continuous damage during the loading process due to microcracking, fracturing, crushing and other interactions between the constitutents. Ultrasonic measurements on uniaxial cyclically loaded specimens [81] suggest the use of the strain vector to evaluate accumulated damage. An overall assessment of the damage, would be based on the plastic volumetric strain, ε_v^p, and plastic octahedral shear strain γ_o^p. The coupling of these two effects is achieved through a shear compaction-dilatancy factor.

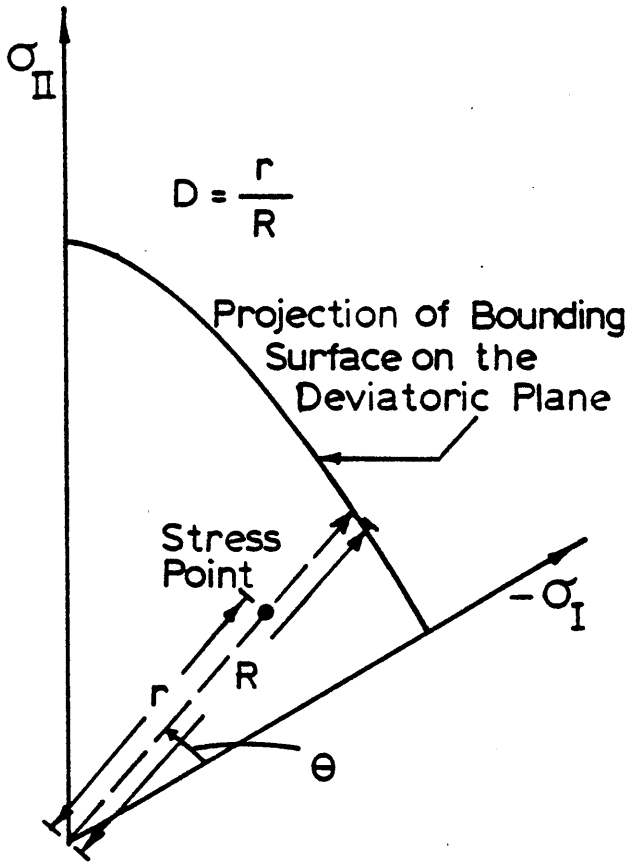

Figure 3.13 The Measure of Normalized Distance D

Representation of the damage along the hydroaxis is relatively trival since in this case, the damage can be measured primarily by a scalar quantity, and can be taken as a function of either ε_v or I_1. This can be implicitly included in the pure volumetric stress-strain formulation (no volumetric-deviatoric coupling) and explicitly shown in the degradation of tangent bulk modulus during loading. On the deviatoric plane, it is proposed that damage accumulation to be evaluated by the use of a "damage parameter", "K" , which is related to γ_o^p. This damage accumulation, defined on the deviatoric plane, is sensitive to the hydrostatic pressure and is stress path dependent. Under higher confining stress states, the same increase in γ_o^p is expected to produce less damage on the deviatoric plane than under lower confining stress. Hence, it seems that a realistic modeling of this damage accumulation under complex stress paths can be achieved by defining K in an incremental form as

$$dK = \frac{d\gamma_o^p}{F_1(I_1, \theta)} \tag{3.11}$$

and

$$K = \int_{\substack{\text{loading} \\ \text{history}}} dK \tag{3.12}$$

The function $F_1(I_1,\theta)$ is chosen to be proportional to the plastic octahedral shear strain at failure under monotonic loadings at different I_1 , and θ . The proportionality factor is determined in such a way that K reaches a certain value, say 1 , at failure under

monotonic loading. Using the test data from Refs. 48,52,53 and 56, the following regression forms are proposed:

For deviatoric loading

$$F_1 = \begin{cases} 0.23\ (I_1 + 0.3)^2/F_2 & \text{for } I_1 \leq 3.18 \\ 1.60\ (I_1 - 1.44)/F_2 & \text{for } I_1 > 3.18 \end{cases} \tag{3.13}$$

and

For deviatoric unloading

$$F_1 = 1.4\ [0.85 - (I_1 + 0.3)/(I_{2,max} + 0.3)]\ .\ F_{1,max}/F_2 \tag{3.14}$$

where

F_2 = $(12 + 11 \cos 3\theta)^{1/6}$

$I_{1,max}$ = maximum I_1 before recent unloading

$F_{1,max}$ = maximum F_1 before recent unloading

Definitions of loading and unloading are found at the end of this section.

The bounding surface is defined as the innermost focus of stress points which always encloses the current stress point, and is a function of stress invariants and the damage parameter (see Fig. 3.11). This surface is postulated to be unique and shared by both monotonic and cyclic loadings. In the present study, the bounding surface (F) is proposed to be a function of σ_{ij} (or stress invariants) and K_{max} , the maximum value of K ever experienced by the material:

$$F(\sigma_{ij}, K_{max}) = 0 \tag{3.15}$$

The following function, which is obtained by modifying the failure surface, proposed in Ref. 35 for monotonic loading, to include K_{max}, is chosen for F:

$$F(\sigma_{ij}, K_{max}) = \frac{1.85(\sqrt{J_2} + 0.378\ J_2)(12 + 11\cos 3\theta)^{1/6}}{I_1 + 0.3} - \frac{40}{K_{max}^2 + 39} \tag{3.16}$$

As previously mentioned, the function F evaluated with $K_{max} = 1$ represents the usual monotonic failure surface. This arrangement allows adoptation of the formulation to different materials with different failure criteria, if desired.

The bounding surface defined above will permit (i) a characterization of the strength of the material at varying stress/strain states, and (ii) the evaluation of material moduli by measuring the distance from the present stress point to the bounding surface along a certain direction. In the present formulation, the distance between the stress point and the bounding surface is measured along the S_{ij} direction (Fig. 3.13). By this definition, octahedral stress-strain behavior can be characterized. Moreover, since the bounding surface on the deviatoric plane is I_1 dependent, a normalized distance measure "D" is introduced.

$$D = \frac{r}{R} \tag{3.17}$$

where r is the distance from the projection of the current stress point to the devioratic plane to the hydroaxis, and R is the distance to bounding surface from the hydroaxis along the S_{ij} direction (see Fig.

3.13). Thus, when D = 1 , the material is assumed to have failed. This definition of D allows one to characterize material moduli through a bounding surface.

The functional formulations of the proposed damage parameter and bounding surface are primarily based on data and observations for concrete materials. It is postulated that refractories share the same set of functions in a normalized stress-strain space. However, in the unnormalized stress-strain space, the associated formulas for each refractory material can be obtained by scaling the proposed functions with the appropriate fp and ε_p.

Loading and unloading along the hydroaxis and on the deviatoric plane are defined separately:

(i) Hydroaxis loading is defined as a process with $dI_1 \geq 0$, and unloading with $dI_1 < 0$.

(ii) Deviatoric loading is defined as a process with $dD \geq 0$, and unloading with $dD < 0$.

Thus, any general stress path can be represented by the combination of these loading and unloading conditions.

(C) Constitutive Model

It is convient to decompose the strain increment $d\varepsilon_{ij}$ into its deviatoric and volumetric components:

$$d\varepsilon_{ij} = de_{ij} + \delta_{ij} \frac{d\varepsilon_{kk}}{3} \qquad (k=1,2,3) \qquad (3.18)$$

The deviatoric strain increment can be further decomposed into elastic and plastic components, de^e_{ij} and de^p_{ij}

$$de_{ij} = de^e_{ij} + de^p_{ij} \qquad (3.19)$$

The elastic deviatoric strain increment de^e_{ij} is related to the stress increment by Hooke's Law.

$$de^e_{ij} = \frac{1}{H^e} dS_{ij} \tag{3.20}$$

where H^e is the generalized elastic shear modulus and dS_{ij} is the deviatoric stress increment.

The plastic deviatoric strain increment de^p_{ij} is assumed to be independent of any volumetric change, and the projection of de^p_{ij} on the deviatoric plane $I_1 = 0$ is assumed to be directed along the projection of the position vector of the stress point. In other words, de^p_{ij} is proportional to S_{ij}. This propotionality yields

$$\frac{de^p_{ij}}{S_{ij}} = \frac{d\gamma^p_o}{\tau_o} \tag{3.21}$$

and, assuming incremental linearity, one can write

$$d\gamma^p_o = \frac{d\tau_o}{H^p} \tag{3.22}$$

where the generalized shear modulus H^p, depends on the history of stress and strain.

The effects of the incremental volumetric stress dI_1 and the incremental deviatoric stress $d\tau_o$ on the volumetric strain increment $d\varepsilon_{kk}$ are assumed to be decoupled, in which case the portion of $d\varepsilon_{kk}$ caused by dI_1, $d\varepsilon^o_{kk}$, is calculated as

$$d\varepsilon^o_{kk} = \frac{dI_1}{3K_t} \tag{3.23}$$

where tangent modulus K_t is assumed to be a function of I_1. The

remaining portion of $d\varepsilon_{kk}$, $d\varepsilon^{d}_{kk_p}$, is directly associated with deviatoric strain increment, $d\gamma_o$ by the linear relationship

$$d\varepsilon^{d}_{kk} = \beta d\gamma^{p}_{o} \tag{3.24}$$

where the shear compaction-dilatancy factor β is function of stress and strain.

$$d\varepsilon_{kk} = d\varepsilon^{o}_{kk} + d\varepsilon^{d}_{kk} \tag{3.25}$$

Combining Eqs. (3.18) to (3.24) and by expressing $d\tau_o = \partial\tau_o/\partial\sigma_m \, d\sigma_{km} = S_{km} \, d\sigma_{km}/3\tau_o$ (k,m = 1,2,3) , one can obtain the following relationship between $d\varepsilon_{ij}$ and $d\sigma_{ij}$:

$$d\varepsilon_{ij} = \frac{d\sigma_{ij}}{H^e} + \frac{1}{3H^p\tau_o}\left(\frac{S_{ij}}{\tau_o} + \delta_{ij}\frac{\beta}{3}\right) S_{km} \, d\sigma_{km} + \delta_{ij}\left(\frac{1}{9K_t} - \frac{1}{3H^e}\right) d\sigma_{kk} \qquad (k,m = 1,2,3) \tag{3.26}$$

(D) Determination of the Model Paramters

The parameters of the proposed model, H^e , H^p , K_t , and β are determined by fitting experimental data. Results given below, which are based on data drawn from Refs. 19,44,48,52,53,56 and 77, are representative of the average behavior of concrete material. The data includes uniaxial, biaxial (monotonic and cyclic), and triaxial (monotonic) loading tests. For candidate refractory materials, a complete set of stress-strain curves including monotonic, cyclic, and multiaxial loads, is not available. Hence, it is postulated that the functional representation of the stress-strain relationship proposed here be based on the test data of concrete materials, which will approximate the general stress-strain behavior of refractories in a normalized stress-strain space. The candidate refractory materials

may have a larger linear range in the normalized stress space and have more linear behavior during unloading and reloading cycles, especially at lower temperature levels.

To obtain the stress-strain relationship in unnormalized stress-strain space, the associated f_p and ε_p for each concrete or refractory material should be adopted.

The results of parameter estimations are summarized as follows:

(i) Generalized elastic shear modulus H^e: This is simply taken as the initial shear modulus at the beginning of the loading process and is determined to be

$$H^e = 2.0 \tag{3.27}$$

This value is used for both deviatoric loading and unloading processes.

(ii) Generalized plastic shear modulus H^P : Usually a unique relationship between $d\tau_o$ and $d\gamma_o^p$ is proposed in constitutive models [23,52,53,54]. However, when the material is close to failure, this uniqueness does not hold for different stress paths involving large deformations (see e.g., Ref. 23). To account for this observation, of a relationship between dD and dK is hereby proposed

$$dK = \frac{dD}{H^*}$$

and (3.28)

$$H^P = \frac{R}{F_1} H^*$$

For deviatoric loading and unloading H^* is determined as follows:

For loading:

$$H^* = \frac{2.4\ (1-D)^{0.65D^2}}{(1 + 0.7\ K_{max}^2)A_L} \tag{3.29}$$

where

$$A_L = \begin{cases} 1.02-0.81\,\dfrac{K_R}{K_{max}} & \text{if } K < K_{max} \\ 1 & \text{if } K = K_{max} \end{cases}$$

and K_R is the associated value of "K" at the beginning of recent loading process.

For unloading:

$$H^* = \frac{2.4}{(1 + 0.7\,K_{max}^2)\,A_u} \tag{3.30}$$

where

$$A_u = \begin{cases} 0 & \text{if } K < 0.2\,K_{max} \\ \dfrac{K_u - 0.2\,K_{max}}{0.8\,K_{max}} & \text{if } K \geq 0.2\,K_{max} \end{cases}$$

and K_u is the associated value of "K" at the beginning of recent unloading process.

Note that H^P is negative during the initial stage of the unloading process (see Eq. (3.30)) which implies interlocking behavior during this stage.

For the softening branch, H^P can be calculated based on the assumption that after initial failure, the stress point moves on the failure surface, by which $dF = \frac{\partial F}{\partial \sigma_{ij}}\, d\sigma_{ij} + \frac{\partial F}{\partial K_{max}}\, dK_{max} = 0$.

A general formulation for H^P derived in this way is complex. For the present purpose, an approximation from the simple uniaxial case will be adopted. The following form for H^P on the softening branch is found to be satisfactory in representing the overall postfailure behavior of concrete in combined loads:

$$H_p = -0.15\, e^{-0.025(K_{max}-1)^2} \tag{3.31}$$

(iii) Bulk tangent modulus K_t: the volumetric stress-strain relationship of concrete is nonlinear [44,77]. Under compressive hydrostatic loading, it is characterized by a decrease in K_t with increasing I_1, followed by an increase. For practical purposes the following model, which fits the softening range, is found to be generally acceptable.

$$K_t = \begin{cases} \dfrac{1.2}{1 + 0.358\, I_1^{1.5}} & \text{, for hydroaxis loading} \\ 1.2 & \text{, for hydroaxis unloading} \end{cases} \tag{3.32}$$

(iv) Shear compaction-dilatancy factor β : The effect of deviatoric deformation upon volumetric strain has been observed [e.g., 77]. The combined effects of shear compaction and dilatancy on volumetric strain can be conveniently separated as:

(a) Compaction: This is primarily the result of shear crushing and void reduction by which the material is compacted during the shearing process. Experimental results [77] indicate that shear compaction occurs continuously during monotonic deviatoric loading and not during successive unloading and reloading until further damage appears. This suggests that shear compaction occurs only when $K = K_{max}$.

(b) Dilatancy: Shear dilatancy phenomena can be clearly observed during loading, unloading and reloading [56,77]. Data drawn from an unloading and reloading process is used first to fit a dilatancy factor, β_2 , by which $d\varepsilon_{kk}^{d2} = \beta_2 d\gamma_o^p$.

Combining this result with monotonic deviatoric loading curve, one can determine a compaction factor β_1, by which

$$d\varepsilon_{kk}^{d1} = \beta_1 d\gamma_o^p \quad , \quad \text{and}$$

$$d\varepsilon_{kk}^{d} = d\varepsilon_{kk}^{d1} + d\varepsilon_{kk}^{d2} = (\beta_1 + \beta_2)\, d\gamma_o^p = \beta\, d\gamma_o^p \qquad (3.33)$$

Consequently, the following functions for β_1 and β_2 are obtained:

$$\beta_1 = \begin{cases} 1.1e^{-30(K_{max}-0.6)^2} & , \text{ for } K = K_{max} \\ 0 & , \text{ for } K < K_{max} \end{cases} \qquad (3.34)$$

and

$$\beta_2 = 1.97 \cdot \lambda_1 \cdot e^{-2\lambda_1^2}$$

where

$$\lambda_1 = D - 0.2\, K_{max}^2 \qquad (3.35)$$

(E) Application and Comparison

The predicted stress-strain responses from the proposed model are verified for different loading conditions by comparing the predictions with associated experimental results. In cases where the peak stress f_p and associated strain ε_p in uniaxial loading are unknown, they are estimated from available data in such a way that the initial monotonic stress-strain curves from the test results fit those from the model prediction.

(i) Concrete Material:

Conventional monotonic loading of concrete is first considered:

(a) The biaxial test results performed by Kupfer, et al [56] with $\Delta\sigma_1 = \Delta\sigma$, $\Delta\sigma_2 = \alpha\Delta\sigma$, and $\Delta\sigma_3 = 0$, for the stress ratio $\alpha = 0$,

0.52, and 1 are compared with the prediction in Fig. 3.14. Good aggrement between the test results and the model prediciton has been found. (b) The triaxial test results obtained by Kotsovos and Newman [52] (see Fig. 3.15) in which the specimens are first loaded along the hydroaxis with $\Delta\sigma_1 = \Delta\sigma_2 = \Delta\sigma_3 = \Delta\sigma_0$, followed by a uniaxial loading $\Delta\sigma_1 = \Delta\sigma$, with $\Delta\sigma_2 = \Delta\sigma_3 = 0$. The model prediction is satisfactory. (c) the triaxial results obtained by Schickert and Winkler [78] (Fig. 3.16), in which the specimens are first loaded along the hydroaxis with $\Delta\sigma_1 = \Delta\sigma_2 = \Delta\sigma_3 = \Delta\sigma_0$, and then followed by a pure deviatoric loading including: Path 1: $\Delta\sigma_1 = \Delta\sigma$, with $\Delta\sigma_2 = \Delta\sigma_3 = -1/2\Delta\sigma$, Path 2: $\Delta\sigma_1 = \Delta\sigma$, $\Delta\sigma_2 = 0$, and $\Delta\sigma_3 = -\Delta\sigma$; and Path 3: $\Delta\sigma_1 = \Delta\sigma_2 = \Delta\sigma$, with $\Delta\sigma_3 = -2\Delta\sigma$. (all $\Delta\sigma > 0$). Generally good agreement between the test results and the prediction is found for monotonic stress-strain behavior.

For cyclic behavior the model predictions are compared with (a) a uniaxial test by Karsan and Jirsa [48] (Fig. 3.17), and (b) a generalized plain strain biaxial test performed by Buyukozturk and Tseng [19] (Fig. 3.18) in which a predetermined value of ε_2 was applied, followed by the application of $\Delta\sigma_1 = \Delta\sigma$ with $\Delta\varepsilon_2 = 0$. As seen from Figs. 3.17 and 3.18, the overall performance of the proposed model in predicting the behavior of concrete in cyclic loading is satisfactory.

(ii) Refractories bricks:

For high-$A\ell_2O_3$ refractories, the uniaxial stress-strain curve obtained at room temperature is compared with the prediction from the proposed model. Test results from Babcock & Wilcox [4] and

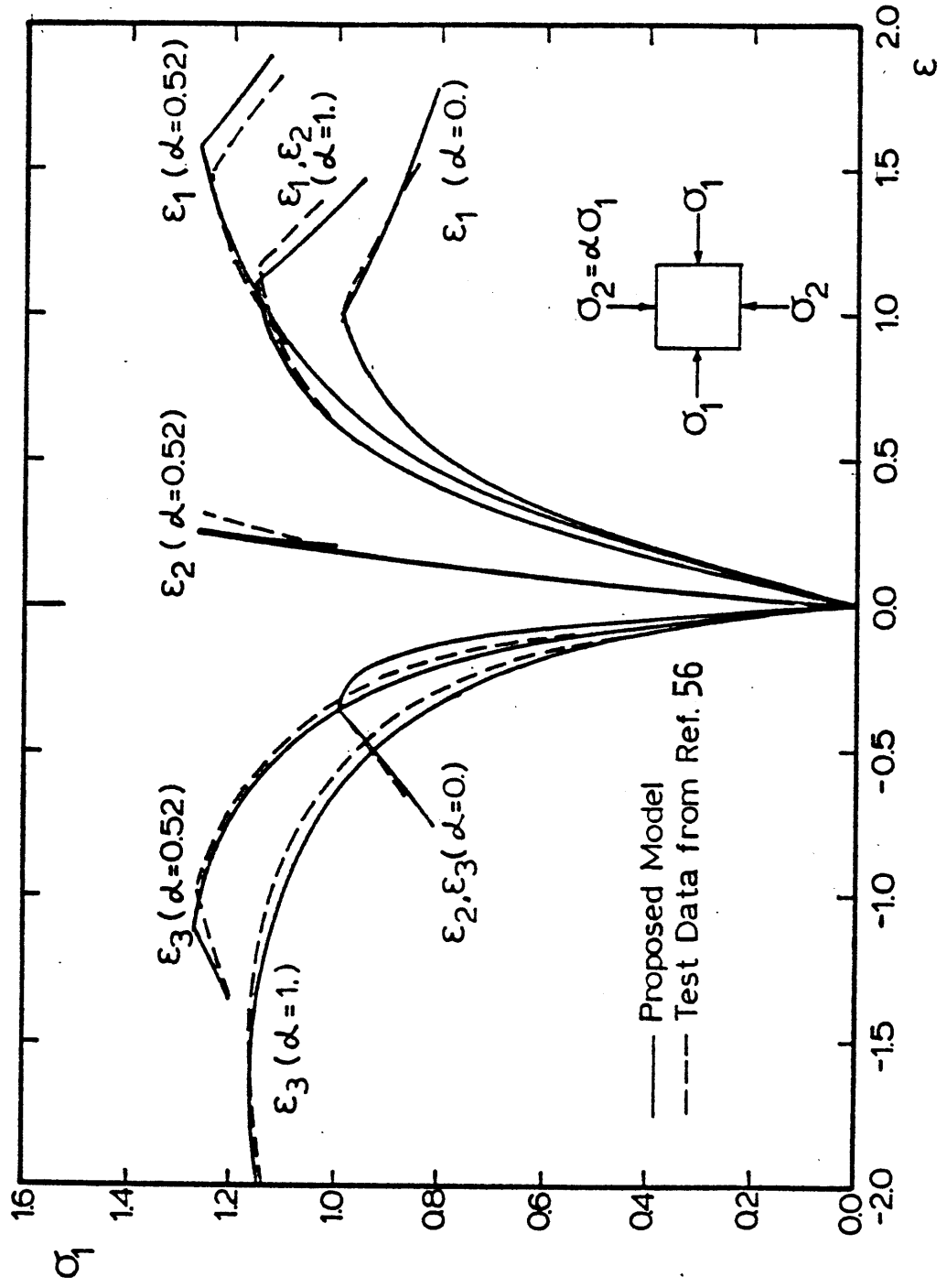

Figure 3.14 Comparison of Model Prediction with Monotonic Biaxial Compression Test Data of Concrete

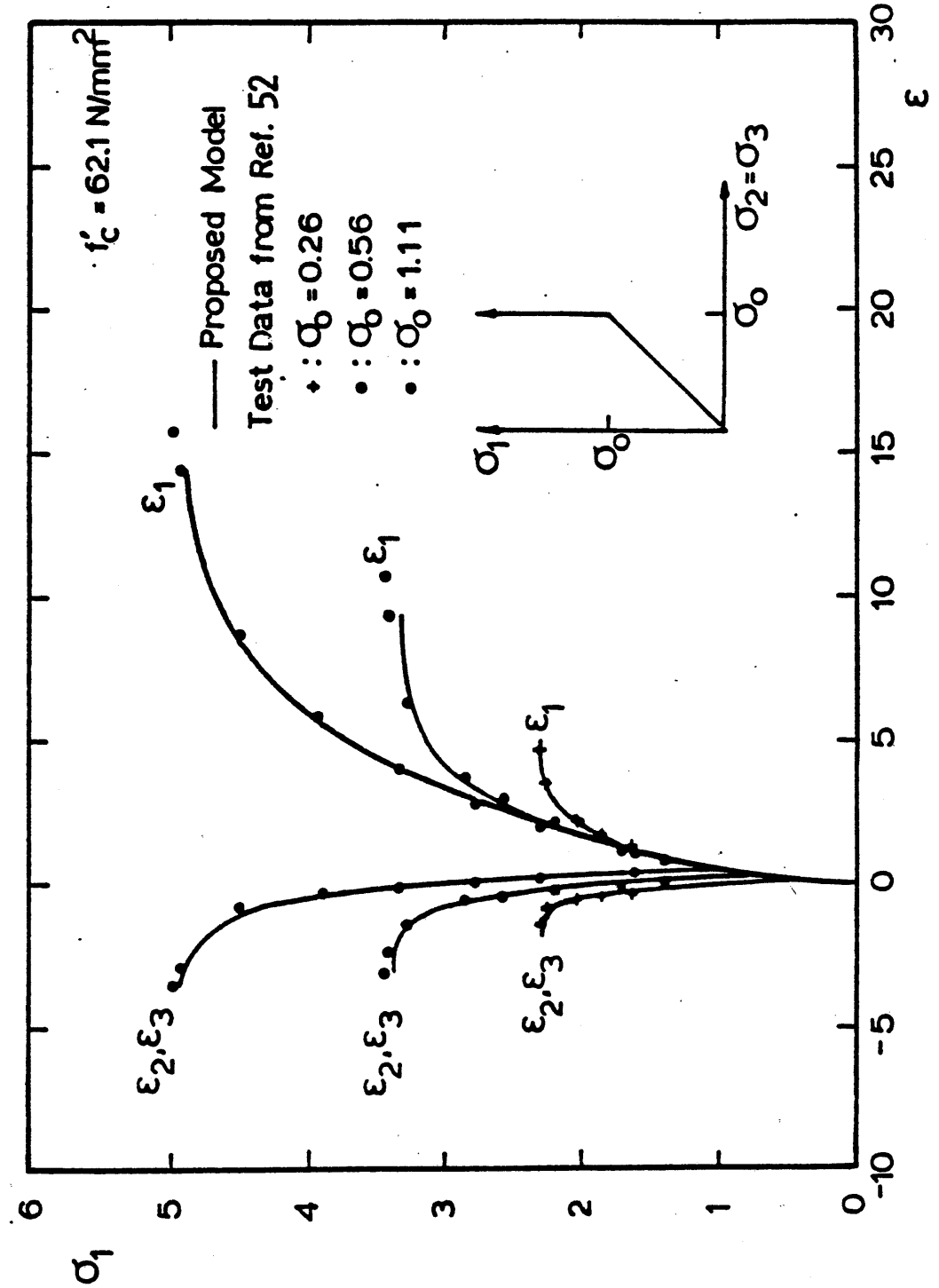

Figure 3.15 Comparison of Model Prediction with Monotonic Triaxial Compression Test Data ($\theta = 60^o$) of Concrete

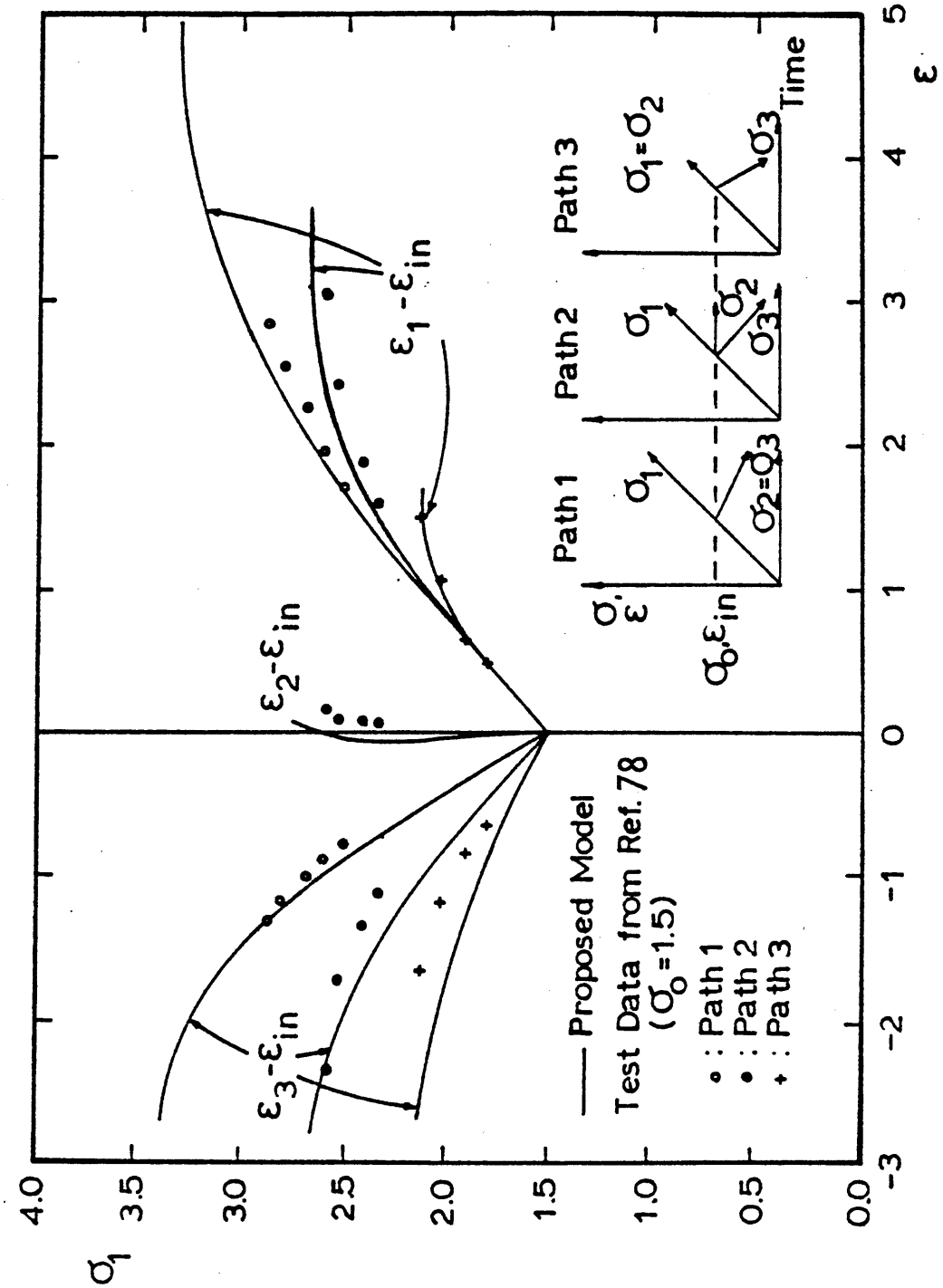

Figure 3.16 Comparison of Model Prediction with Monotonic Triaxial Compression Test Data (I_1 = constant) of Concrete

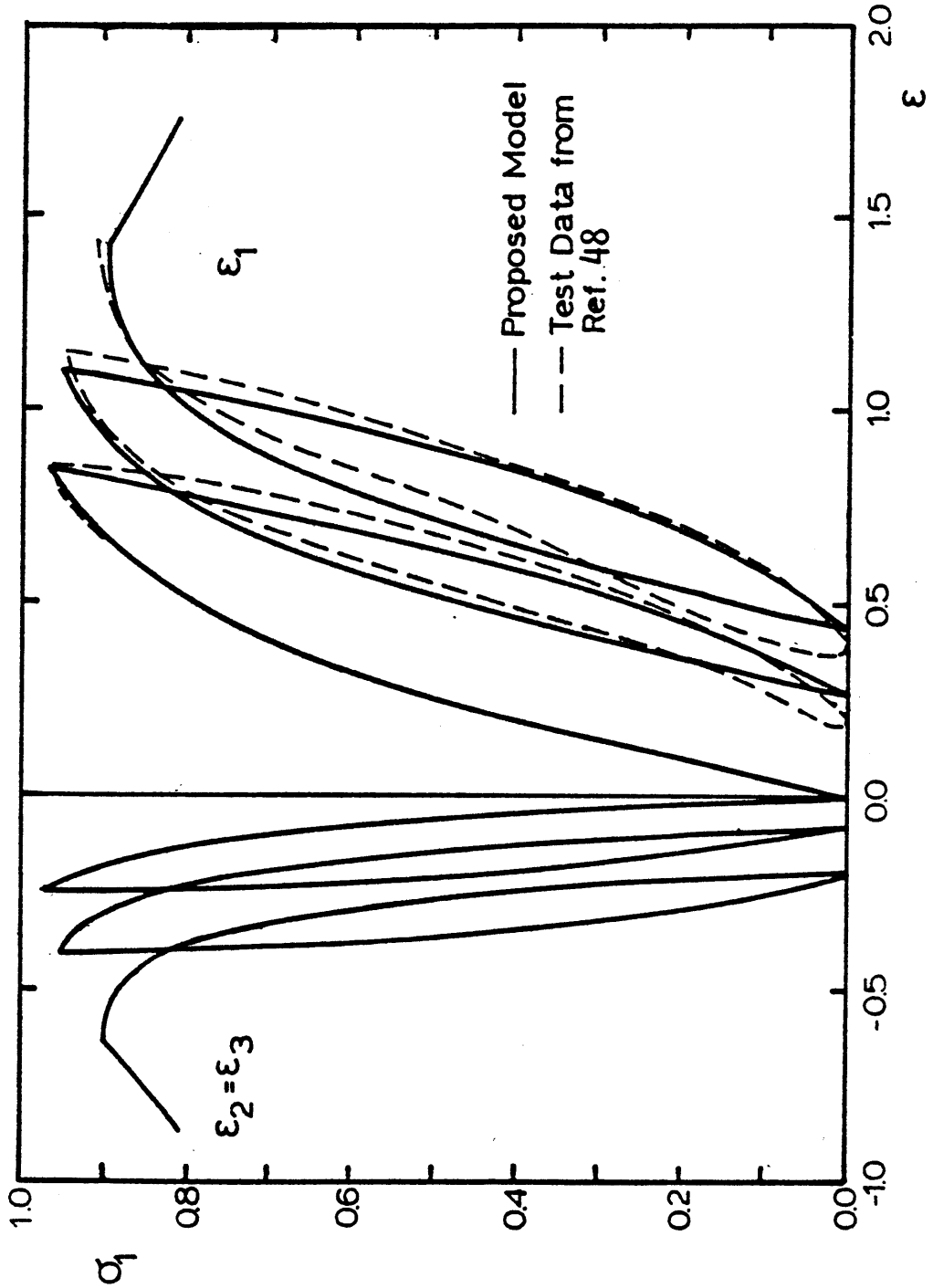

Figure 3.17 Comparison of Model Prediction with Cyclic Uniaxial Compression Test Data of Concrete

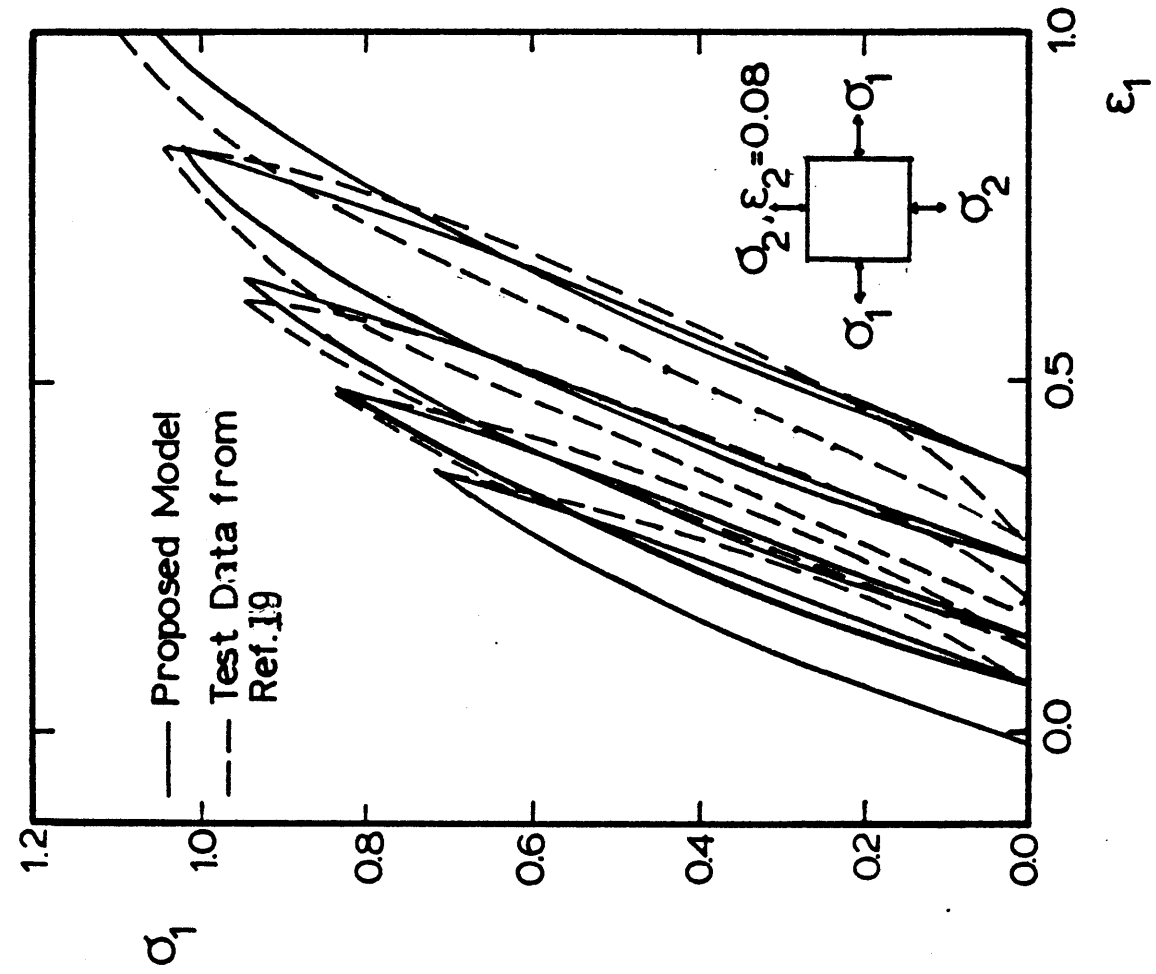

Figure 3.18 Comparison of Model Prediction with Cyclic Biaxial Compression Test Data (Generalized Plain Strain) of Concrete

the model prediction are shown in Fig. 3.19. In general, the stress-strain curves from tests at high σ_1/f_p levels manifest slightly more linear behavior than those from the prediction; nevertheless, the overall correlation is good.

(2) Elevated temperatures

The damage-type bounding surface model proposed for modeling the constitutive behavior of the candidate refractory materials at room temperature can be generalized to elevated temperatures. However, experiments on stress-strain behavior for general load conditions in the desired wide range of service temperatures are scarce. Available test results are for uniaxial compressive tests at selected temperatures. In view of this limitation, the previously proposed normalized stress-strain space model is assumed also valid for modeling high temperature constitutive behavior of the candidate materials. However, the actual peak stress $f_p(T)$ and associated axial strain ε_p from the stress-strain curve at different temperature levels of each material under uniaxial compressive stress are used to scale the stress-strain curves into unnormalized stress-strain space.

In general, fp and ε_p for the candidate materials are sensitive to temperature. Figs. 3.20 and 3.21 give the temperature dependent f_p of 90% Al_2O_3 + 10%Cr_2O_3 refractory and 50% Al_2O_3 insulating castable (concrete). ε_p's of candidate materials at high temperature can not be measured reliable due to the involvement of high-temperature creep in the measurement of ε_p. In the present study, at given temperature level, ε_p is estimated so that the initial Young's modulus in uniaxial stress-strain curve fits that from the model prediction. The

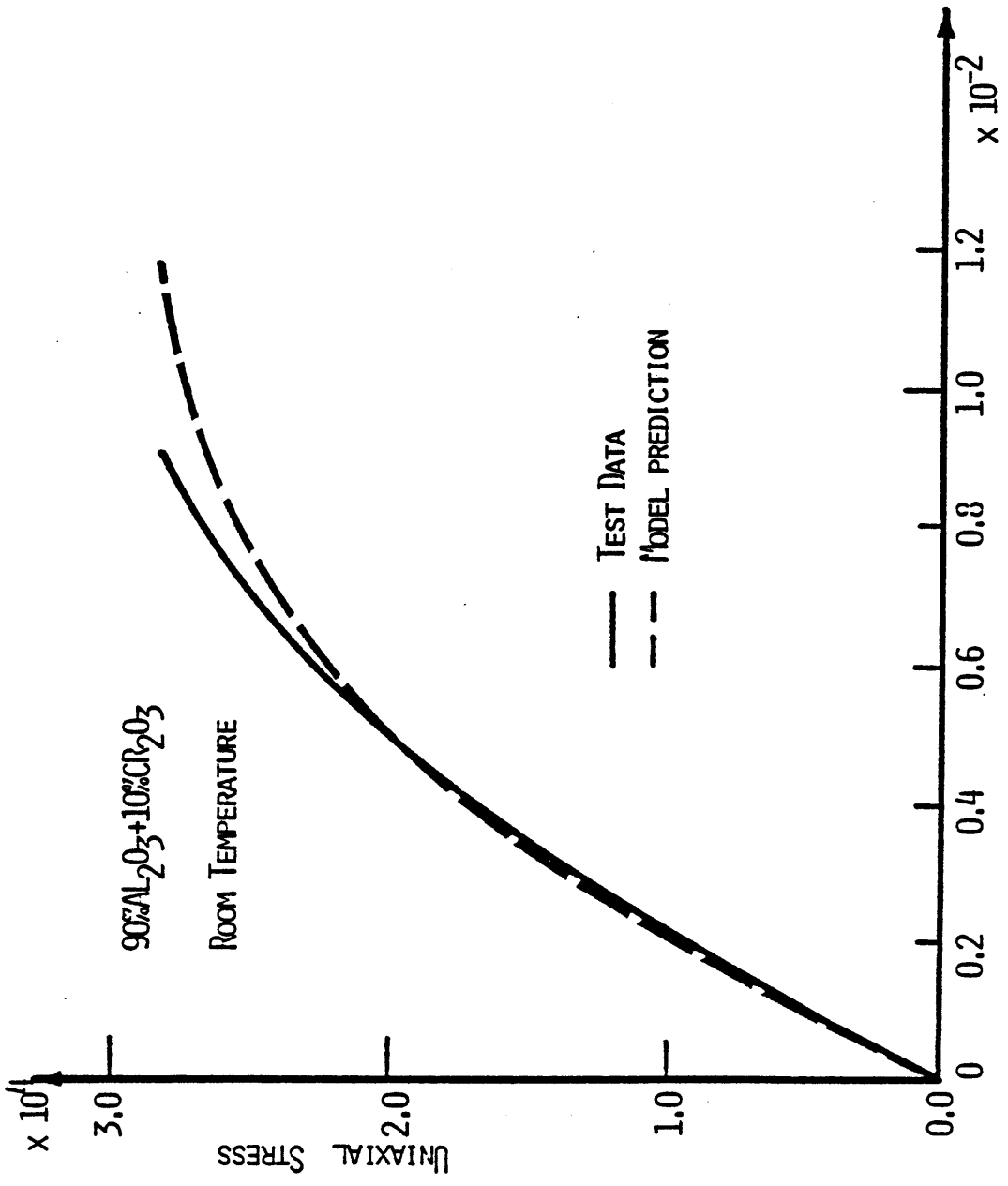

Figure 3.19 Comparison of Model Prediction with Monotonic Uniaxial Compression Test Data of 90% $A\ell_2O_3$ + 10% Cr_2O_3 Refractory at Room Temperature

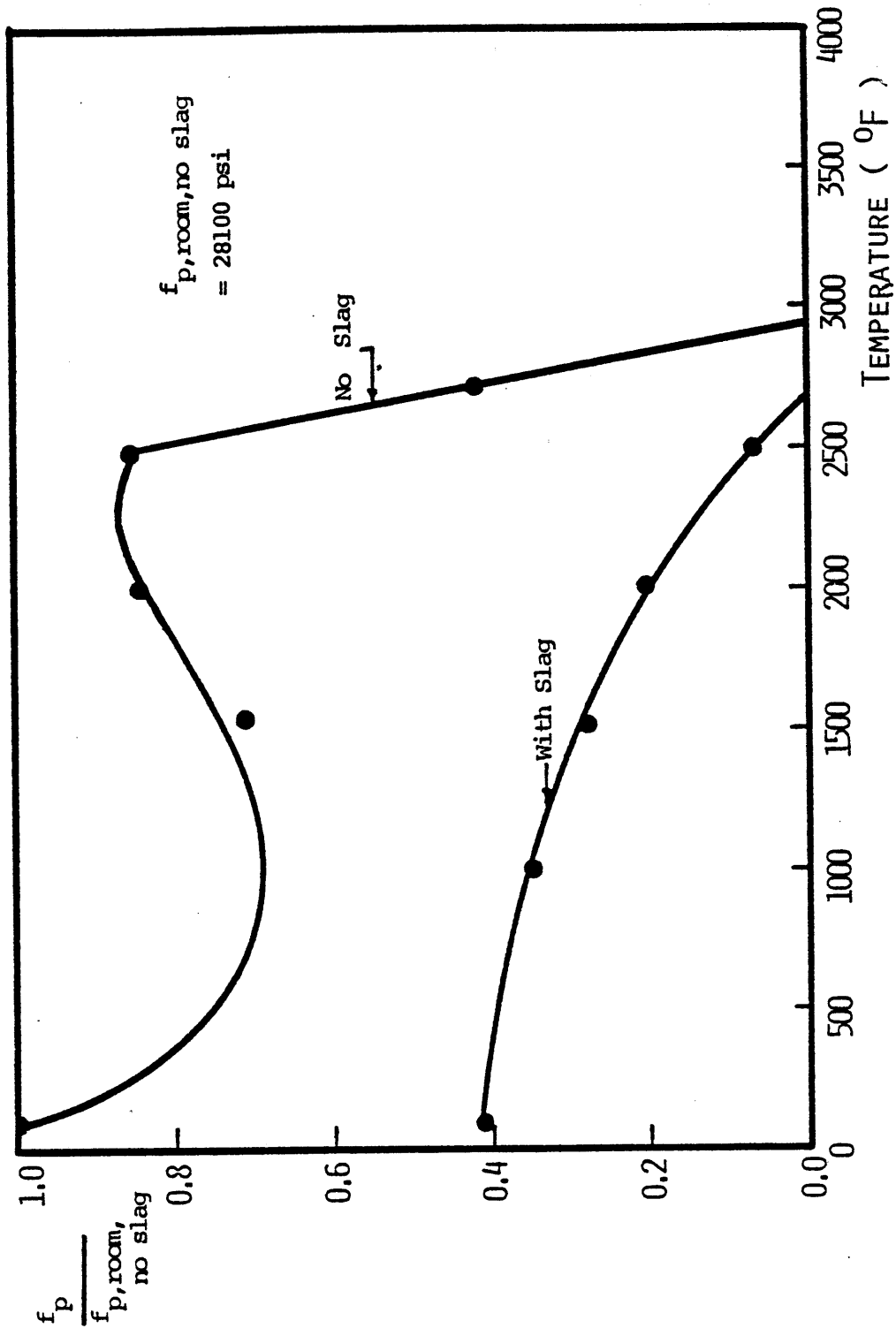

Figure 3.20 Uniaxial Compressive Strength vs. Temperature for 90% $A\ell_2O_3$ + 10% Cr_2O_3 Refractory (without and with slag saturation) [4]

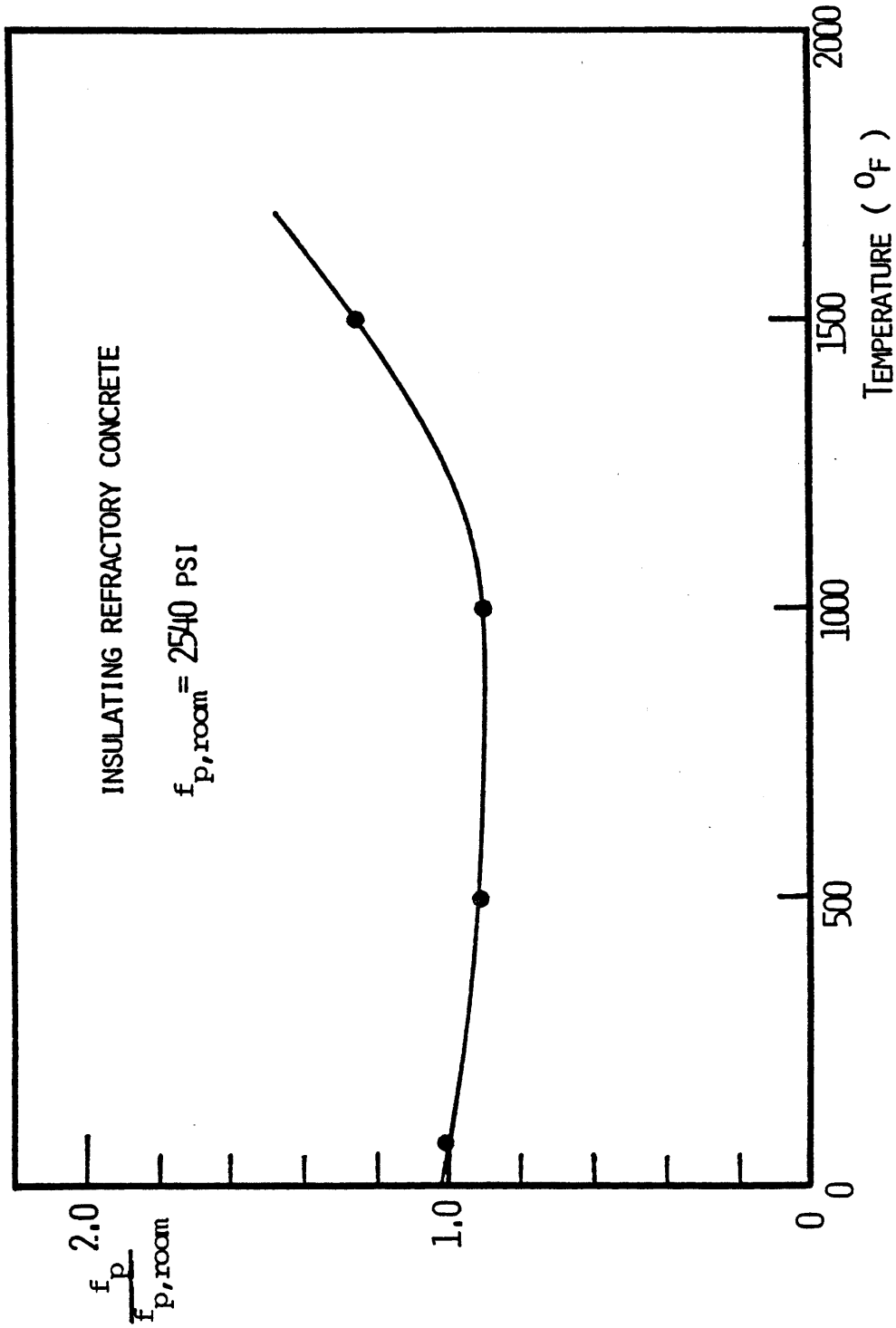

Figure 3.21 Uniaxial Compressive Strength vs. Temperature for 50% Al_2O_3 Insulating Refractory Concrete [88]

polynomial representations of f_p and ε_p for the candidate material are given as follows:

(i) 90% Al_2O_3 + 10% Cr_2O_3 refractory:

Based on the test data from Ref. 4, the following polynomial is obtained by regression:

$$f_p(\text{psi}) = 30067 - 27.22T + 2.05\times10^{-2}T - 4.23\times10^{-6}T^3 \quad \text{for } T < 2500°F$$

$$= 24048\times(2950-T)/450 \quad \text{for } 2500°F \leq T < 2950°F$$

$$= 0 \quad \text{for } T \geq 2950°F$$

$$\varepsilon_p = 0.0127 - 5.24\text{x}10^{-6}T + 6.12\text{x}10^{-9}T^2$$

(T in °F) (3.36)

(ii) 80% Cr_2O_3 + 20% MgO refractory:

At present, data on the stress-strain curve and uniaxial compressive strength of 80% Cr_2O_3 refractory is not available.

(iii) 50% Al_2O_3 insulating castable:

Data drawn from Refs. 66 and 88 yields the following expression for fp and ε_p as a function of temperature T

$$f_p(\text{psi}) = 2565 - 0.356T - 7.366\text{x}10^{-4}T^2 + 8.138\text{x}10^{-7}T^3$$

$$\varepsilon_p = 0.0027 + 3.25\text{x}10^{-6}T \quad (3.37)$$

(T in °F)

Comparisons of the model predictions with test results [4] on 90% Al_2O_3 refractory at T=2000°F and 2500°F are shown in Figs. 3.22 and 3.23. Overall agreement is found satisfactory.

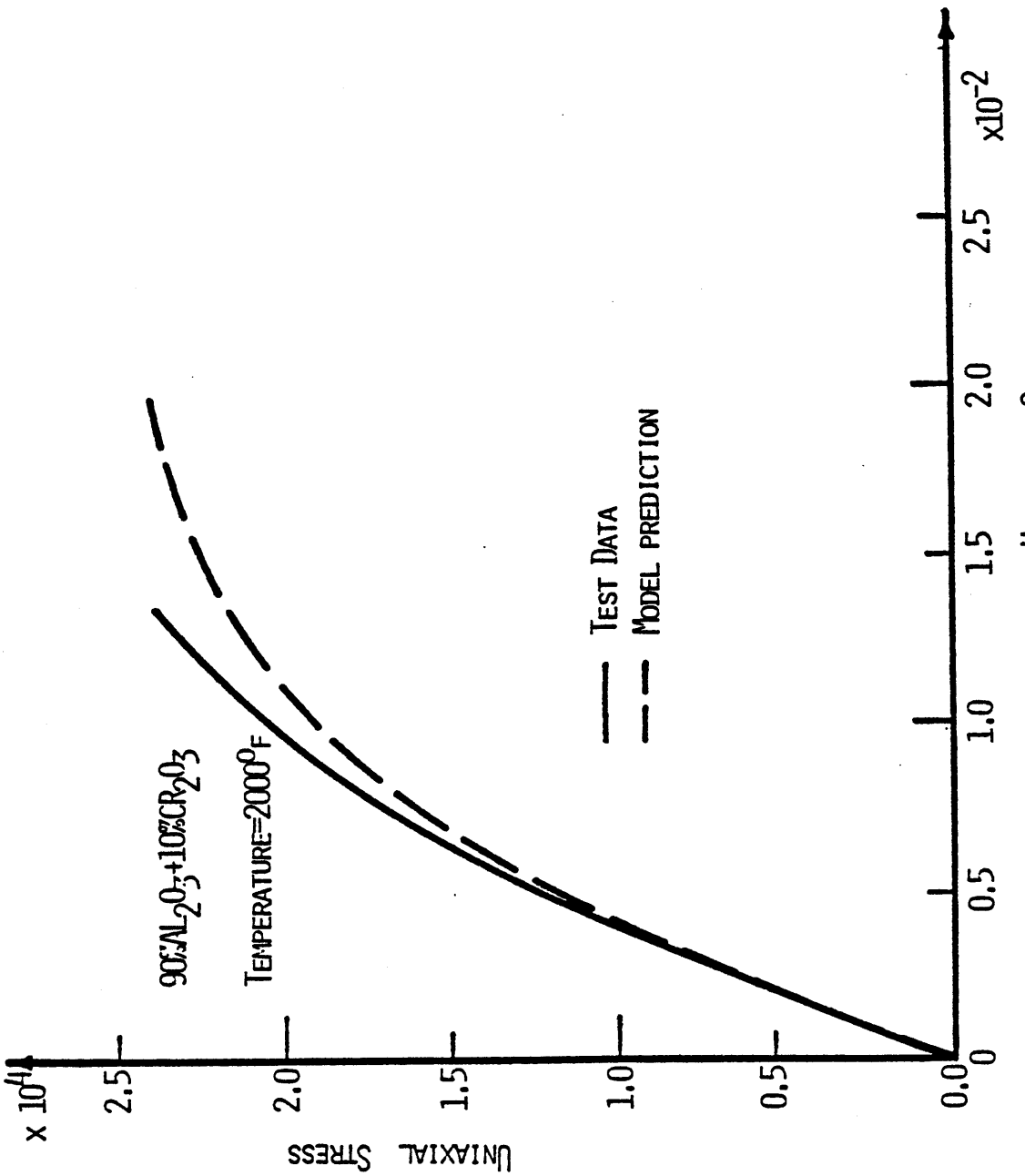

Figure 3.22 Comparision of Model Prediction with Monotonic Uniaxial Compression Tests Data of 90% $A\ell_2O_3$ + 10% Cr_2O_3 Refractory at 2000°F

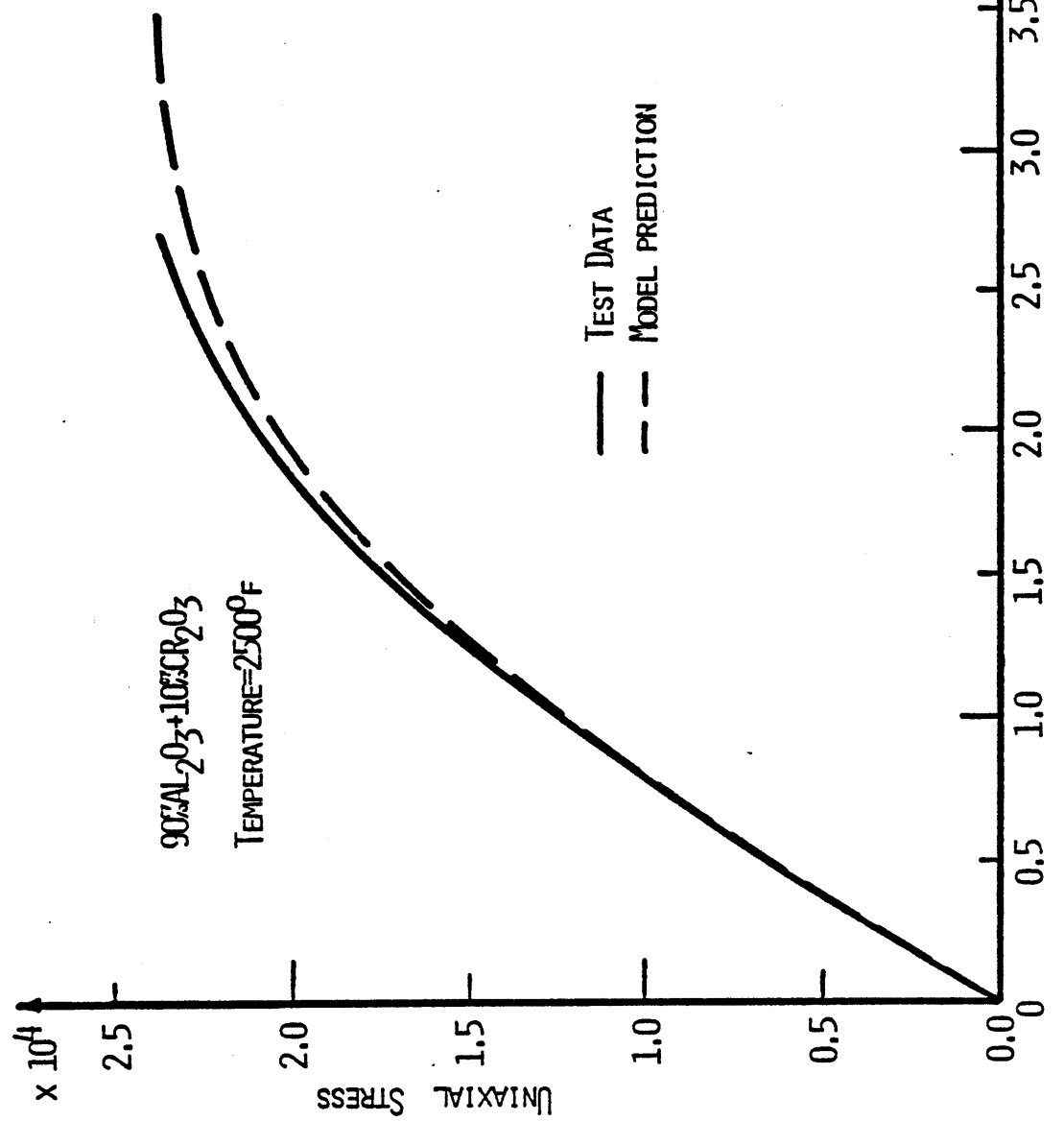

Figure 3.23 Comparison of Model Prediction with Monotonic Uniaxial Compression Tests Data of 90% Al_2O_3 + 10% Cr_2O_3 Refractory at 2500°F

§3.3.2 SiC Refractory and Steel

A linear elastic isotropic model is adopted for the SiC bricks and the steel. The SiC bricks are high strength materials. Their stress-strain behavior is primarily linear elastic in the service stress range. Steel also performs in a linear elastic fashion up to the yield stress level. Since the maximum design stress in steel is generally required to be substantially lower than the yield stress, a linear elastic model should be sufficient for modeling constitutive behavior for the steel.

For a linear elastic material, with the assumption of isotropy, the material constitutive law can be written as

$$\sigma_{ij} = 2\mu\, \varepsilon_{ij} + \lambda\, \delta_{ij}\, \varepsilon_{kk} \quad (k = 1,2,3) \tag{3.38}$$

where μ and λ are Lame's constants, and

$$\mu = \frac{E}{2(1+\nu)} \quad \text{and} \quad \lambda = \frac{E\nu}{(1+\nu)(1-2\nu)}$$

E is Young's modulus and ν is Poisson's ratio.

The temperature of the steel shell in the lining system is generally controlled to be lower than a specified temperature, usually of the order of 600°F . In this temperature range the material properties E and ν can be assumed to be essentially constant. The constant values for E and ν for steel are taken to be:

$$E = 2.9 \times 10^7 \text{ psi}$$
$$\nu = 0.33 \tag{3.39}$$

Young's modulus E of SiC refractory is temperature dependent. Test results from Refs. 28 and 85 show that E of SiC is generally decrease linearly with increasing temperature T up to 2200°F. The following linear function for E of SiC is proposed:

$$E(psi) = 2.85\times10^{7} - 8.92\times10^{2}\ T \qquad (T \text{ in } °F) \qquad (3.40)$$

Poisson's ratio for SiC refractory is approximately constant in the service stress and temperature range, and an average value $\nu = 0.165$ is adopted from Ref. 28.

§3.4 Creep

The term "creep" refers to the time-dependent deformation exhibited by the materials under sustained loads (Fig. 3.24). The creep behavior of the candidate refractory materials used in slagging coal gasification vessel linings is temperature dependent. At high temperature levels the creep of the materials is very significant. This may modify the stress distribution in the lining system in a variety of ways. In short, creep can release local stresses and may be beneficial to local material stability. However, stress redistribution might damage other areas, depending on the lining geometry, previous stress history, boundary conditions, and the heating/cooling process. Assessment of behavioral trends so that a proper control of material creep characteristics in the design and operation of the lining system would be possible to reduce the damage is one objective of the present study.

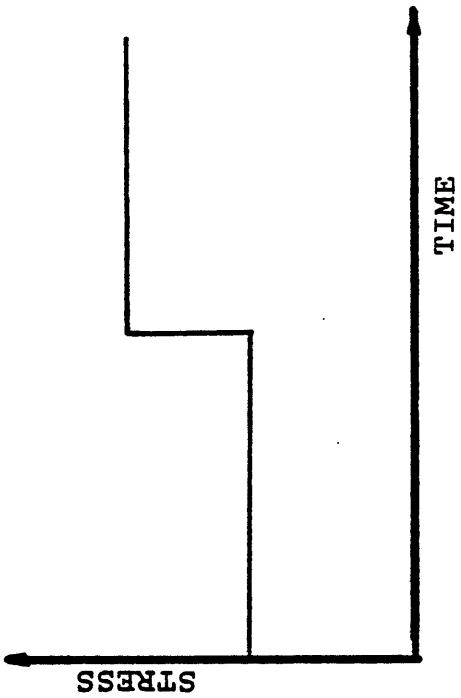

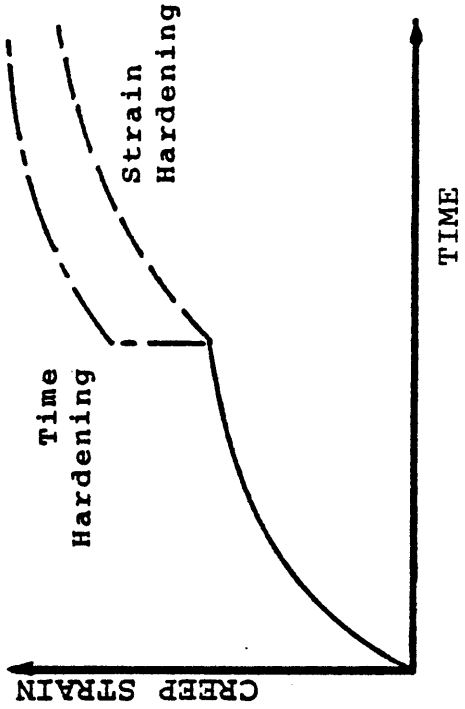

Figure 3.25 Strain Hardening Model and Time Hardening Model

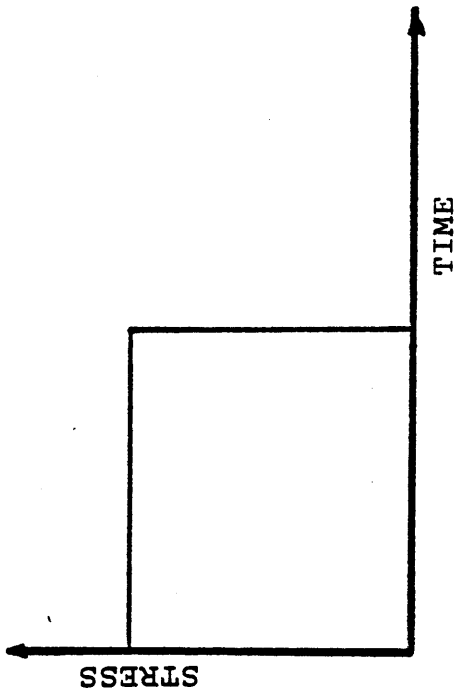

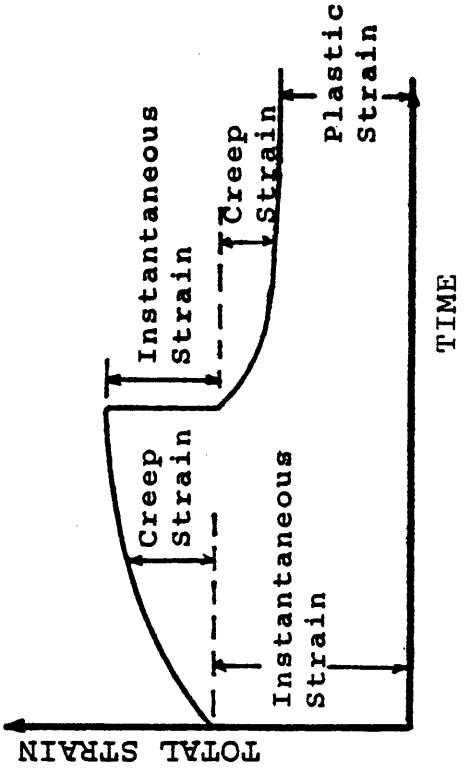

Figure 3.24 Typical Creep Curve

Creep behavior of refractory materials in general states of stress is complex. Creep may result in the change of both volumetric and deviatoric strain components. It may introduce partially irrecoverable deformations upon the stress removal. It is also stress path dependent in multiaxial states of stress. A creep model for the present objective should accommodate all these important features, at least at high temperature states. However, the refractory materials considered here are recently developed materials and creep tests are extremely limited. Most of the available test data are for uniaxially compressed specimens at either constant temperature or non-isothermal conditions [60], with only axial strain measured. In view of this limitation, some reasonable assessment needs to be made as to the sensitivity of the analytical results to creep.

For convenience the creep strain ε^c_{ij} $(i,j = 1,2,3)$ can be decomposed into its deviatoric, e^c_{ij} and the volumertic ε^c_v, components:

$$\varepsilon^c_{ij} = e^c_{ij} + \delta_{ij} \frac{\varepsilon^c_v}{3} \tag{3.41}$$

For each component a simple constitutive equation is used. This type of equation is generally suitable for predicting the creep behavior of thermo-rheologically simple materials [12,37]. Under constant temperatures, the constitutive equations for creep can be written as:

$$e^c_{ij}(t) = \int_0^t J^D(t,s)\, dS_{ij}(s) \tag{3.42}$$

and

$$e^c_v(t) = \int_0^t J^V(t,s)\, d\sigma_m(s) \tag{3.43}$$

where $\sigma_m = \frac{I_1}{3}$. The deviatoric creep function $J^D(t,s)$ gives the deviatoric creep strain response at time t due to a unit deviatoric stress at time s, while the volumetric creep function $J^V(t,s)$ gives the volumetric creep strain at time t due to unit octahedral stress at time s. Since S_{ij} and σ_m are time dependent, Eqs. (3.42) and (3.43) can be equivalently written as

$$e^c_{ij}(t) = \int_0^t J^D(t,s) \frac{ds_{ij}(s)}{ds} ds \tag{3.44}$$

and

$$\varepsilon^v_c(t) = \int_0^t J^V(t,s) \frac{d\sigma_m(s)}{ds} ds \tag{3.45}$$

In the uniaxial case with constant stress and constant temperature, one may simplify Eqs. (3.44) and (3.45) to yield

$$\begin{aligned} \varepsilon^c_{11} &= e^c_{11} + \frac{1}{3}\varepsilon^c_v \\ &= (\frac{2}{3}J^D + \frac{1}{9}J^V)\sigma_{11} \\ &= J^D S_{11} + \frac{1}{3}J^V\sigma_m \end{aligned} \tag{3.46}$$

and

$$\begin{aligned} \varepsilon^c_{22} &= e^c_{22} + \frac{1}{3}\varepsilon^c_v \\ &= (-\frac{1}{3}J^D + \frac{1}{9}J^V)\sigma_{11} \end{aligned} \tag{3.47}$$

and define a Possion's ratio for creep, ν_c, as $\nu_c = -\varepsilon^c_{22}/\varepsilon^c_{11}$

or $$\nu_c = -\frac{\varepsilon^c_{22}}{\varepsilon^c_{11}} = \frac{\frac{1}{3}J^D - \frac{1}{9}J^V}{\frac{2}{3}J^D + \frac{1}{9}J^V} \tag{3.48}$$

Thus, $$J^V = \frac{3(1-2\nu_c)}{1+\nu_c} J^D \tag{3.49}$$

At high temperatures, most of the creep strains are irrecoverable. A commonly used power law for creep functions is adopted here. In uniaxial cases this model is assumed in the form:

$$\varepsilon_{11} = A \frac{\sigma_{11}}{H^e} t^n \tag{3.50}$$

where A and n are material constants. Further expansion of this equation, with the assumption of constant Poisson's ratio for creep, gives:

$$\varepsilon_{11} = a \frac{\sigma_{11}}{H^e} t^n + \frac{1}{3} b \frac{\sigma_{11}}{H^e} t^n \tag{3.51}$$

$$= \left(\frac{3}{2} \frac{a}{H^e} t^n\right) S_{11} + \frac{1}{3} \left(3 \frac{b}{H^e} t^n\right) \sigma_m$$

Combining Eqs. (3.46) to (3.51) results in

$$J^D = \frac{3}{2} \frac{a}{H^e} t^n \tag{3.52}$$

$$J^V = \frac{3b}{H^e} t^n \tag{3.53}$$

$$a + \frac{1}{3} b = A \tag{3.54}$$

$$\frac{a}{A} = \frac{1+\nu_c}{1.5} \tag{3.55}$$

If only uniaxial creep test results are available, one may use these results to fit parameters A and n . With a reasonable choice of ν_c , the parameters a and b , or the creep functions J^D and J^V can be found using Eqs. (3.52) to (3.55).

Suppose that stress is not constant but variable. Direct use of Eqs. (3.44) and (3.45) leads to discontinuity in creep strain history whenever stress is discontinuous (Fig. 3.25). This result does not occur in reality, and can be removed by using a strain rate formulation. For example, in uniaxial cases

$$e_{11}^c = a \frac{\sigma_{11}}{H^e} t^n \tag{3.56a}$$

$$\dot{e}_{11}^c = n\, a \frac{\sigma_{11}}{H^e} t^{n-1} \tag{3.56b}$$

$$= n \left(a \frac{\sigma_{11}}{H^e}\right)^{\frac{1}{n}} (e_{11}^c)^{1-\frac{1}{n}}$$

and

$$\varepsilon_v^c = \frac{3b}{H^e} t^n \sigma_m \tag{3.57a}$$

$$\dot{\varepsilon}_v^c = n \frac{3b}{H^e} \sigma_m t^{n-1}$$

$$= n \left(\frac{3b\, \sigma_m}{H^e}\right)^{\frac{1}{n}} (\varepsilon_v^c)^{1-\frac{1}{n}} \tag{3.57b}$$

The choice of a rate form can mathematically model the creep process of decreasing creep strain rate. This process is often called "hardening". The relations (3.56a) and (3.57a) are usually called "time hardening" since the hardening phase is modelled using the time parameter. Meanwhile, the relations (3.56b) and (3.57b) are called a

"strain hardening" model since strain, instead of time, is adopted for creep. These two models give the same result for constant stress. However, their predictions of creep behavior under varying stress conditions are different (Fig. 3.26). The strain hardening model gives a better prediction, in general.

These results can be easily generalized to the multiaxial cases under constant temperature. If the strain hardening model is adopted, the creep rate can be expressed as:

$$\dot{e}^c_{ij} = \frac{3}{2}\left(\frac{a}{H^e}\right)^{\frac{1}{n}} \left(\frac{\bar{e}^c}{\bar{\sigma}}\right)^{1-\frac{1}{n}} S_{ij} \tag{3.58}$$

and

$$\dot{\varepsilon}^c_v = n\left(\frac{3b\,\sigma_m}{H^e}\right)^{\frac{1}{n}} (\varepsilon^c_v)^{1-\frac{1}{n}} \tag{3.59}$$

where $\bar{\sigma} = \sqrt{\frac{2}{3} s_{ij} s_{ij}}$ $\quad (i,j = 1,2,3)$

$$\bar{e}^c = \sqrt{\frac{2}{3} e^c_{ij}\, e^c_{ij}}$$

and

$$\Delta\varepsilon^c_{ij} = \left(\dot{e}^c_{ij} + \delta_{ij}\frac{\dot{\varepsilon}^c_v}{3}\right) \cdot \Delta t \tag{3.60}$$

where Δt is an infinitesimal time increment.

These creep models and solution schemes can be easily implemented into a finite element program, in which state variable $\bar{e}^c$ and ε^c_v are calculated and stored at each time step.

The influence of the temperature on creep is important. It is usually found that creep strain rate increases exponentially with temperature at a given stress. This exponential dependence is known

as Arrhenius's law [12,37], and has been widely applied to the creep modelling of many physical materials. This observation suggests the use of a so called temperature shift factor, a_T , which is an exponential function of temperature, to model temperature effects on the creep strain rate. Specifically, time t is replaced by a reduced time $\zeta = t/a_T$ in the previous creep equations.

Many forms for a_T have been proposed. One based on the concept of activation energy has been generally applicable to most materials; this form can be written as [12,37]

$$\frac{1}{a_T} = \exp\left[\frac{\Delta H}{R_g}\left(\frac{1}{T_0} - \frac{1}{T}\right)\right] \tag{3.61}$$

where

ΔH = thermal activation energy

R_g = universal gas constant (Boltzmann's constant)

T = absolute temperature

T_0 = reference temperature

For a specific material the model parameters, including A, n, ΔH, and T_0 , can be obtained by fitting creep data at various temperature and stress levels. In a lining system for a gasification vessel, significant creep exists in the area near the hot face due to the generally experienced high temperatures. Hence, the creep behavior in the primary (working) lining should be considered in the thermomechanical analysis of such a lining system. In Chapter 6 the 90% Al_2O_3 refractory brick is chosen for the primary linings. Creep tests on 90% Al_2O_3 refractory have been conducted by McGee [60]. Based

on the results (Figs. 3.26 to 3.28) from these tests, the following model parameters obtained for 90% Al_2O_3 refractory:

$$A = 7.85 \quad (\ ^{1}/_{(hr)^{0.61}}\ )$$

$$h = 0.61$$

$$\Delta H/R_g = 2.94 \times 10^4 \ (°k)$$

$$T_o = 1622 \ (°k)$$

In Figs. 3.26 to 3.28 the model predictions are also given to compare with those test results. Generally good agreement is found.

SiC refractories may be adopted for secondary linings. At the temperature levels commonly existing in the secondary linings, the creep of SiC materials can be neglected [79].

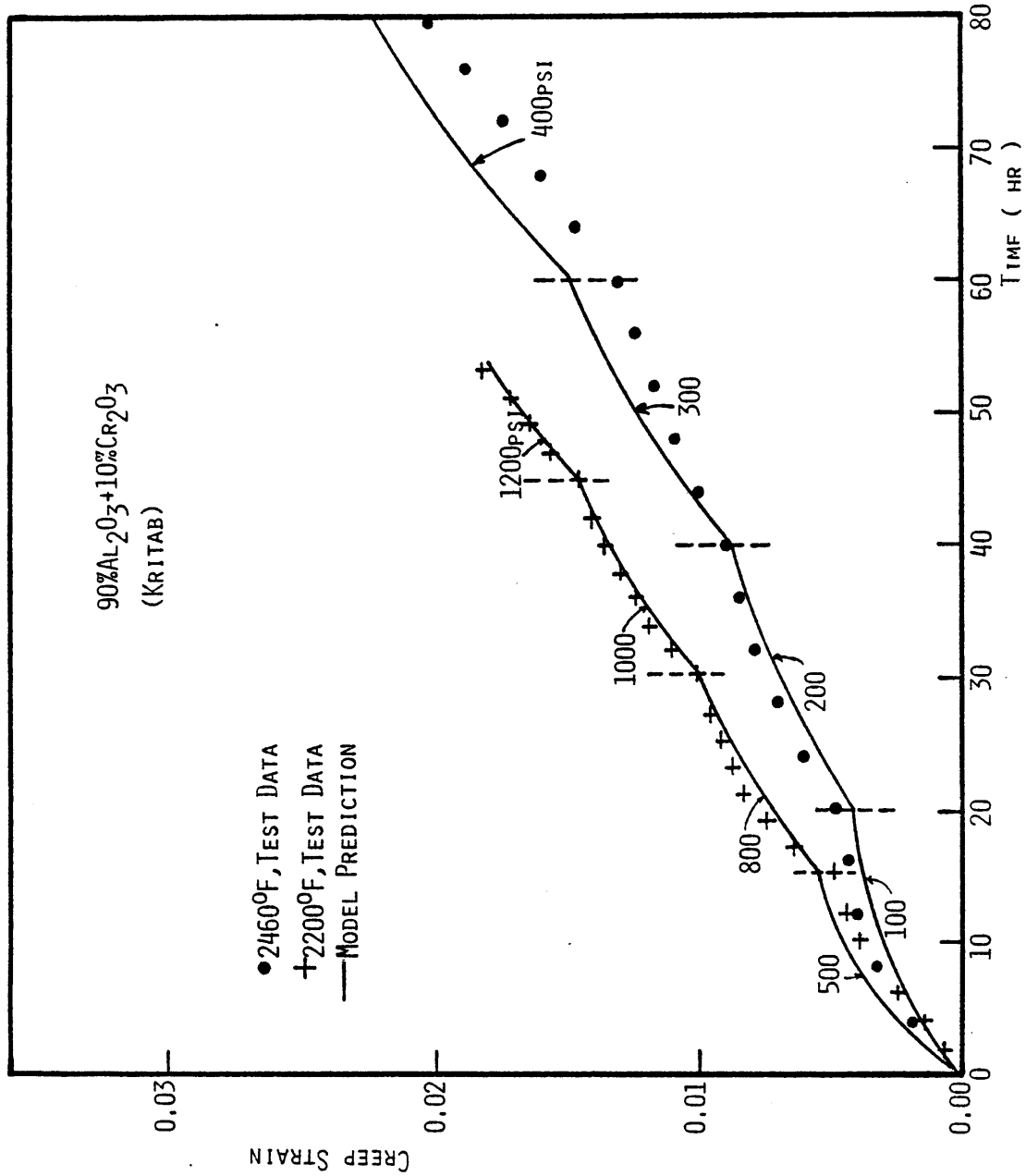

Figure 3.26 Comparison of Model Prediction with Creep Data at 2200°F and 2460°F

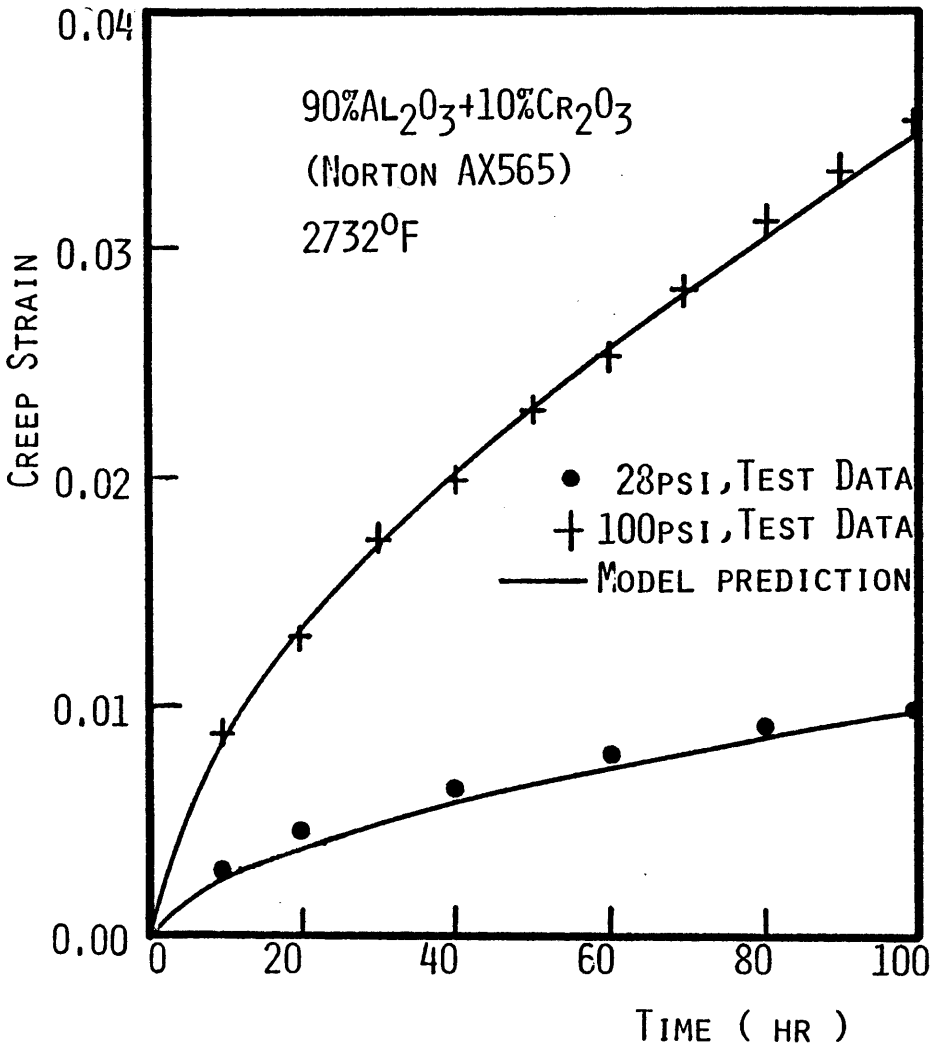

Figure 3.27 Comparison of Model Prediction with Creep Data at 2732°F

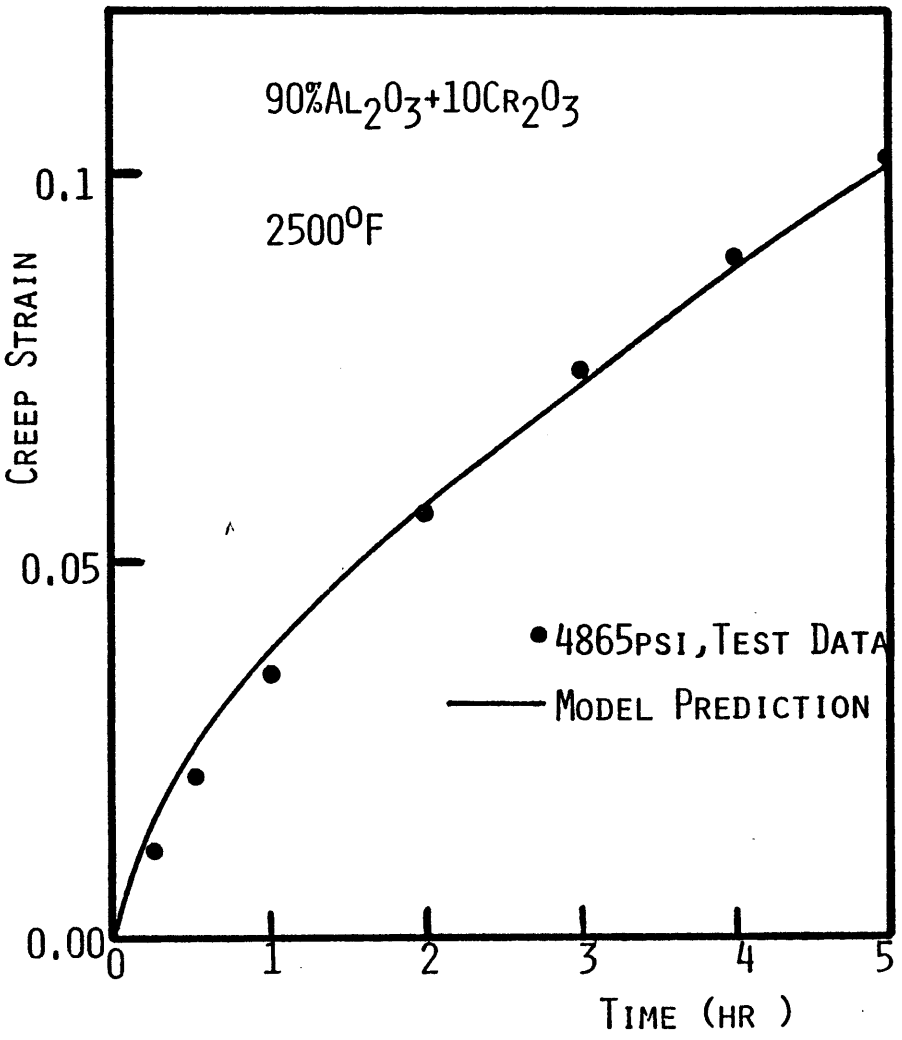

Figure 3.28 Comparison of Model Prediction with Creep Data at 2500°F

CHAPTER 4

SLAG CORROSION OF REFRACTORY LININGS

§ 4.1 INTRODUCTION

Corrosion resistance is usually considered as one of the most important issues in selecting a proper material for the lining of slagging gasifiers. In the quest for high operational efficiency, several new gasification processes have been developed in which the gasifiers are operated at temperatures in the range of 2500°F to 3300°F. At these temperatures, the mineral impurities associated with the coal melt and form a highly corrosive coal slag which flows down the vessel wall and is removed at the bottom of the gasifier. Therefore, a refractory material is needed that can resist the coal slag attack and minimize heat losses through the wall. For this purpose, extensive slag tests [45,50,89] have been conducted on various refractories under laboratory conditions and for short periods of time to study the corrosion process and lining life of the refractories. Information from these tests cannot be used directly to predict lining lifetimes in an actual gasifier, but it can be used to (1) provide a qualitative, relative ranking of the performance of the refractories under corrosion attack, (2) identify the important variables of the

slag corrosion process, and (3) evaluate the effects of slag corrosion on the thermal and mechanical behavior of refractories. It would be desirable to perform large-scale test in which the actual slagging environment can be simulated and the corrosion effects can be quantitatively evaluated.

In view of the limited experience on the long-term corrosion behavior of refractories and because of the urgent need for a predictive method to assess the lining behavior in a gasifier, in this chapter a simple corrosion model is proposed. This model incorporates the important corrosion mechanisms and, based on rational assumptions, can extrapolate the results from short-term corrosion tests to long-term corrosion behavior of refractory linings.

§4.2 CORROSION MECHANISMS

Generally speaking, the corrosion process is any type of interaction between a solid phase and a fluid phase that results in a deleterious effect to either of the phases [29]. The solid phase is that of primary concern in the present lining problem. In the slagging coal gasifier, the corrosion mechanisms between slags and refractories are complex and depend on many factors. The degradation process can be generally grouped into three major categories: (1) dissolution (or diffusion), which is a chemical process by which the refractory materials are continually dissolved, (2) penetration, by which the slag penetrates into the refractory and causes material deterioration through both chemical and mechanical effects, and (3) erosion, which is the abrasion process of refractory materials subjected to slag (and gas)

movements. The first two mechanisms can be simulated and understood to some extent through laboratory tests. Erosion alone is generally not a problem in lining design; however, when erosion is accompanied with dissolution and penetration, the resulting loss of lining materials can be very rapid.

Dissolution (diffusion) of the refractory in a liquid slag is usually measured in terms of dissolution rate. For a specific refractory-slag system at temperature T_o, the rate of dissolution $j^*_{T_o}$ is defined as the rate at which the thickness of the refractory is depleted. Generally, $j^*_{T_o}$ is controlled by diffusion through the slag boundary layer adjacent to the refractory, the thickness of which is determined by hydrodynamics. The transport rate of the material through the boundary layer depends on the effective diffusion coefficient. Based on these concepts, Cooper [29,76] proposed the relation

$$j^*_{T_o} = \frac{D^*}{\delta^*} \frac{(C_i - C_\infty)}{(1 - C_i V)} \tag{4.1}$$

where D^* = effective binary diffusion coefficient in the solution for exchange of solute and solvent

δ^* = thickness of boundary layer in the slag

C_i = volume concentration of refractory (volume refractory/volume refractory and bulk solution) at the interface

C_∞ = volume concentration of refractory in the bulk liquid

V = partial volume of the refractory oxide

The dissolution rate is also temperature dependent.

Temperature dependence of the corrosion process has often been represented by an exponential law [76] of the type

$$j_T^* = A \text{ Exp } [- B (\frac{1}{T} - \frac{1}{T_o})] \qquad (4.2)$$

where j_T^* = dissolution rate at temperature T , in °k .

A = dissolution rate at reference T_o , $j_{T_o}^*$.

B = model constant, in °k .

T_o = reference temperature, in °k .

Equations (4.1) and (4.2) suggest that a thicker slag layer, a lower temperature, and a slower renewal of slag result in a reduction of dissolution rate. Such a reduction can be achieved if the temperature of the hot face is kept low enough, which generally requires thin and high-conductive linings as well as heavy cooling facilities, if the operating temperature in the gasifier is fixed.

Slag penetration is another mechanism that causes refractory degradation. The penetration process of the candidate refractories by some or all the constituents of the slag can cause deterioration of the refractories by the following mechanisms:

(1) partially or completely encasing a volume of the refractories by slag,

(2) causing differential expansion or contraction between refractories and penetrating-slag with the associated development of stresses, and

(3) change in mechanical, optical, or chemical properties of the refractories.

For the purpose of thermomechanical analysis, the aspects of concern of the deterioration process are:

(1) the penetration depth into the lining; and

(2) the changes in thermophysical and mechanical properties of refractories after slag-penetration.

A general method to estimate the depth of fluid penetration is based on the moving boundary diffusion theory [29] at high temperatures. This method requires knowledge of a coefficient for the slag-refractory diffusive penetration process which is not yet available for the materials of interest here. A simple method by which such depth of penetration can be estimated with good approximation and implemented into the numerical analysis procedure of the next chapter should be developed.

Up to this point the general term "slag penetration" has not been clearly defined, because different components of the slag can penetrate into the refractory at different depths. None of the slag components, except iron oxide, causes significant change in the material properties of the refractory. However, the portion of refractory material that reacts with iron oxide can develop a spinel layer [51] with visible crackings (see e.g., Fig. 4.1) and strength degradation [4]. This phenomenon may be caused by the volumetric increase due to the chemical transition from Fe^{+2} to Fe^{+3} (iron bursting). Such a destructive effect should be considered in the analysis. Hereafter, the term "slag penetration" will be restricted to the penetration by iron oxide whereas "depth of slag penetration" will refer to the thickness of the spinel layer in the refractories.

Laboratory tests to measure the depth of slag penetration into different candidate refractories have been carried out at Argonne

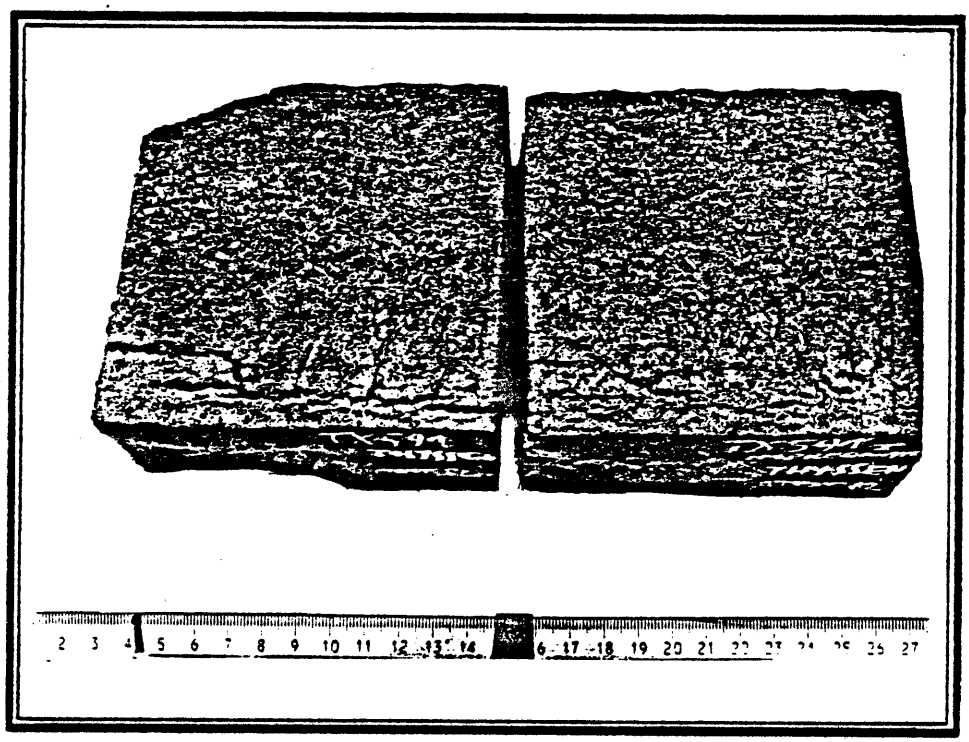

Figure 4.1 Cracking of Refractory Bricks in Slagging Gasifier
(Courtesy of Norton Company, Worcester, Massachusetts)

National Laboratory [49,50,51]. Fig. 4.2 [50,51] shows the depth of slag penetration into refractory bricks exposed to high iron oxide acidic coal slag at 1525°C (2867°F) on one side and water cooled on the other side at temperatures 80 to 90°C (176 to 194°F). The bricks are either 9" (228 mm) or 4.5" (114 mm) long. Based on these results, a criterion based on critical temperature T_c is proposed for each refractory-slag system to evaluate the depth of slag penetration: When a portion of the refractory from the hot face is at a temperature higher than or equal to the associated critical temperature, one may assume that this portion is penetrated by slag (Fig. 4.3) (Iron Oxide). To verify this criterion, the slag penetration problem on two 90% Al_2O_3 +10% Cr_2O_3 bricks of 9" and 4.5" long used in Refs. 50 and 51 is studied below.

Based on the hot-face and cold-face temperatures reported in Refs. 50 and 51, and on the thermal conductivity of 90% Al_2O_3 refractory material in Chapter 3, the steady-state temperature profile for each brick can be calculated (see Fig. 4.4). For an assumed critical temperature T_c = 2650°F, the estimated depths of slag penetration for 9" and 4.5" bricks are 0.122 and 0.431 in., which are very close to the measured values of 0.12 and 0.43 in., respectively (Fig. 4.4). Similar results are shown in Fig. 4.5 for the 80% Cr_2O_3 refractory with an assumed value for T_c of 2800°F. Such a high T_c value of 80% Cr_2O_3 refractory implies a good resistance of the material to slag penetration.

The previous method is easy to implement into a finite element code to estimate the depth of slag penetration, since temperature profile through the lining can be accurately calculated through thermal analysis.

NUMBER/TYPE	POROSITY (%)	COMPOSITION (wt %)
2-FC	1	Al_2O_3 (99)
190-S	17	Al_2O_3 (92), Cr_2O_3 (7.5), P_2O_5 (0.5)
16-S	16	Al_2O_3 (90), Cr_2O_3 (10)
86-C	21	Al_2O_3 (85), Cr_2O_3 (10), P_2O_5 (4.5)
109-C	23	Al_2O_3 (67), Cr_2O_3 (32), P_2O_5 (1)
260-S	25	Al_2O_3 (67), Cr_2O_3 (32)
400-S	13	MgO (42), Cr_2O_3 (27), Fe_2O_3 (16)
38-FC	5	Al_2O_3 (60), Cr_2O_3 (27), MgO (6)
280-FC	7	Al_2O_3 (65), Cr_2O_3 (32)
22-FC	5	Cr_2O_3 (80), MgO (8), Fe_2O_3 (6)

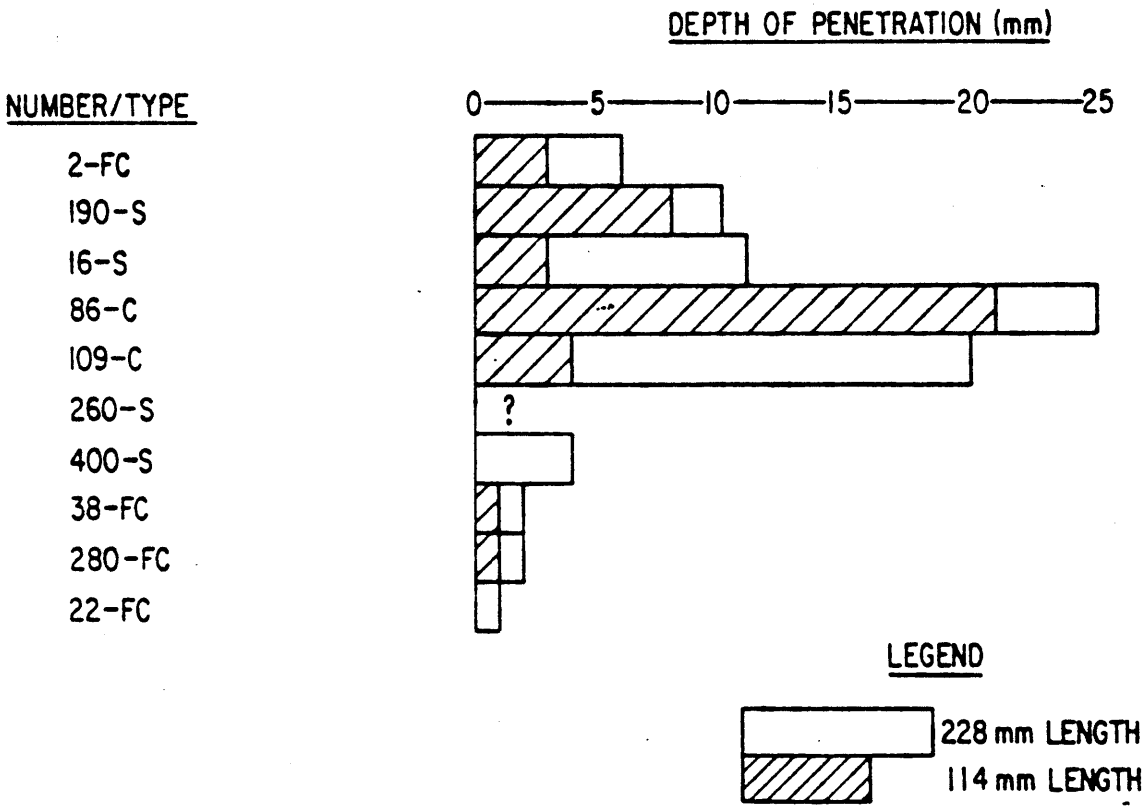

Figure 4.2 Approximate Depths (as measured from the final position of the slag-refractory interface) of Slag Penetration into Refractories [50]

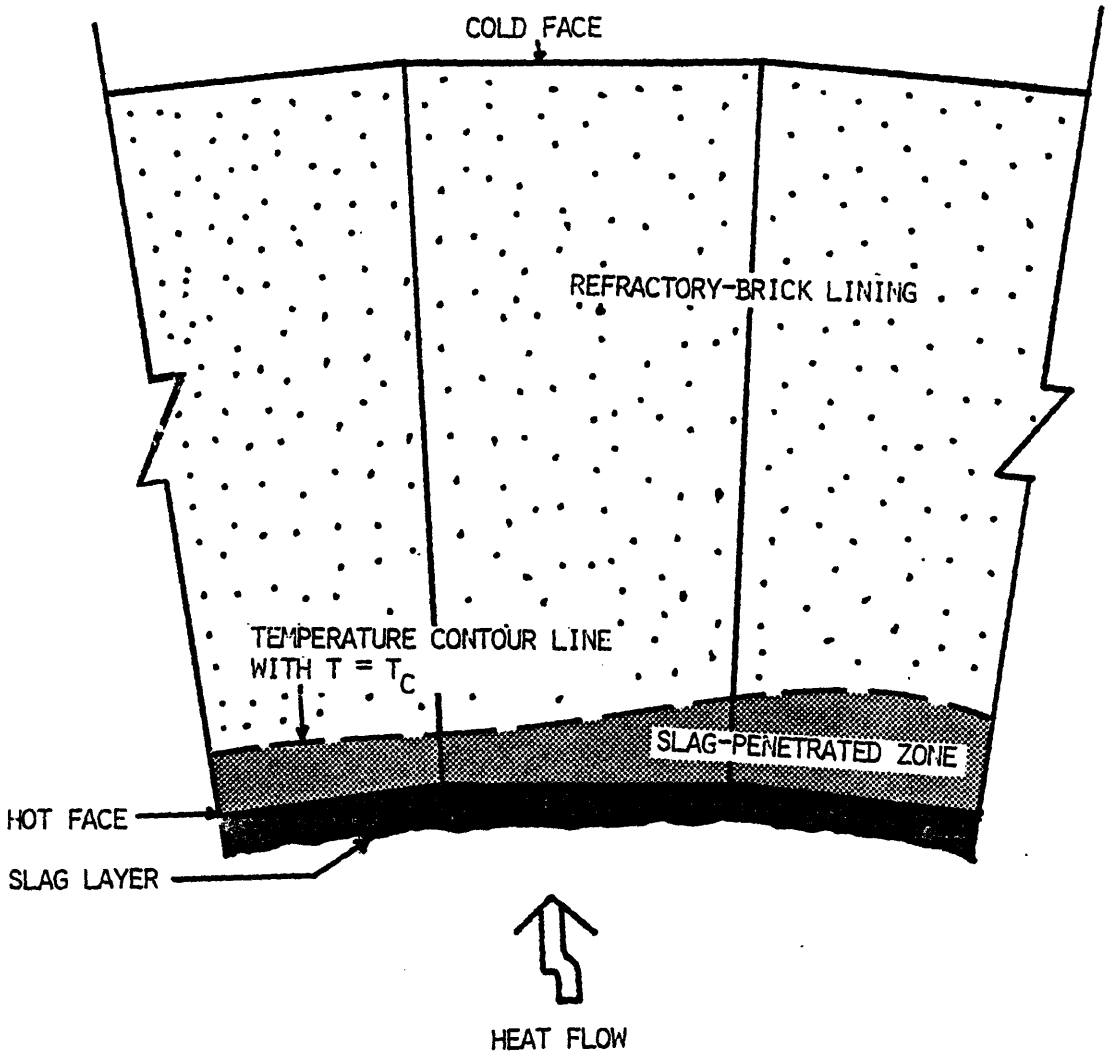

Figure 4.3 Estimation of Slag-Penetrated Zone in a Lining

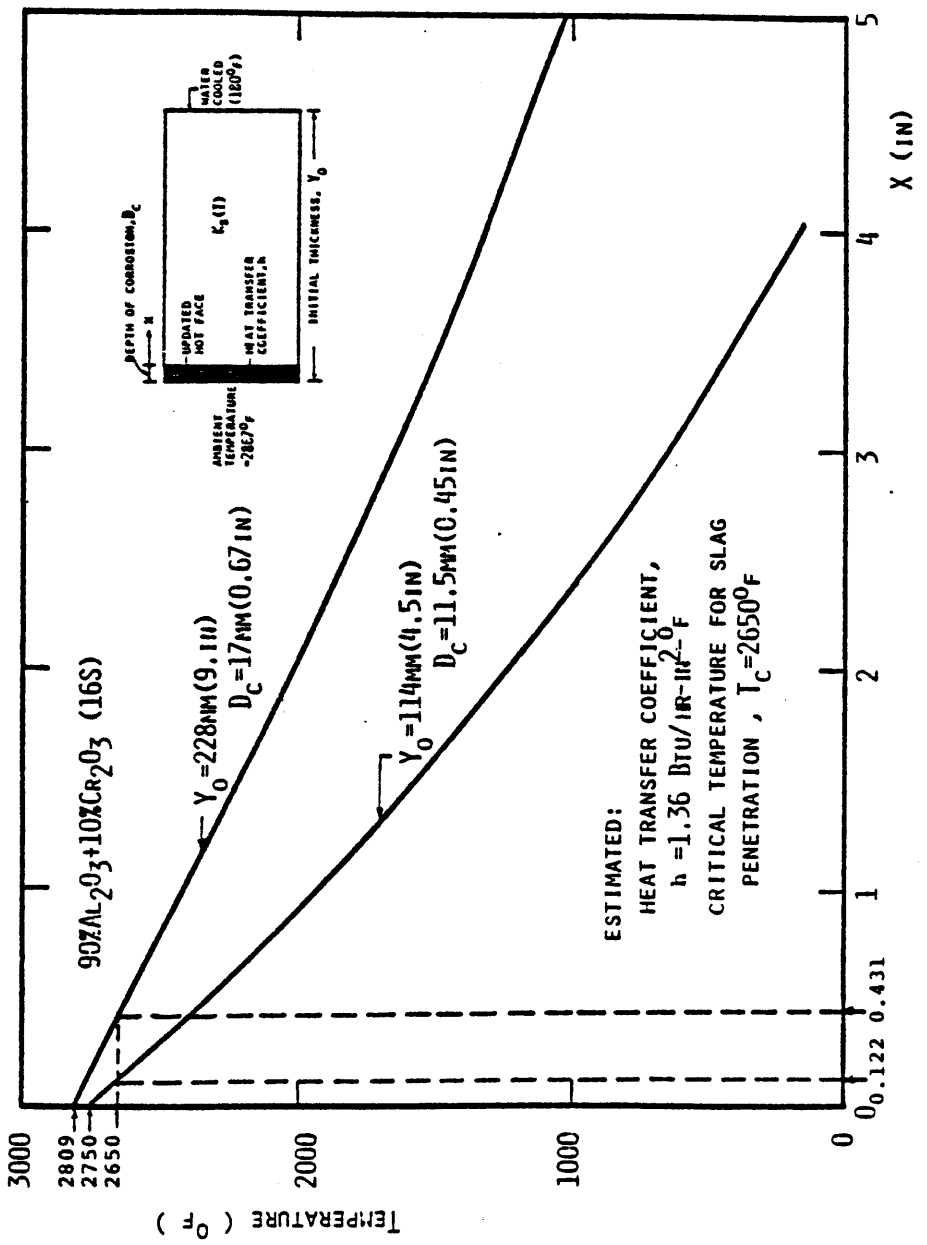

Figure 4.4 Estimation of Critical Temperature of Slag Penetration into 90% Al_2O_3 Refractory (U.S. Coal Slag System)

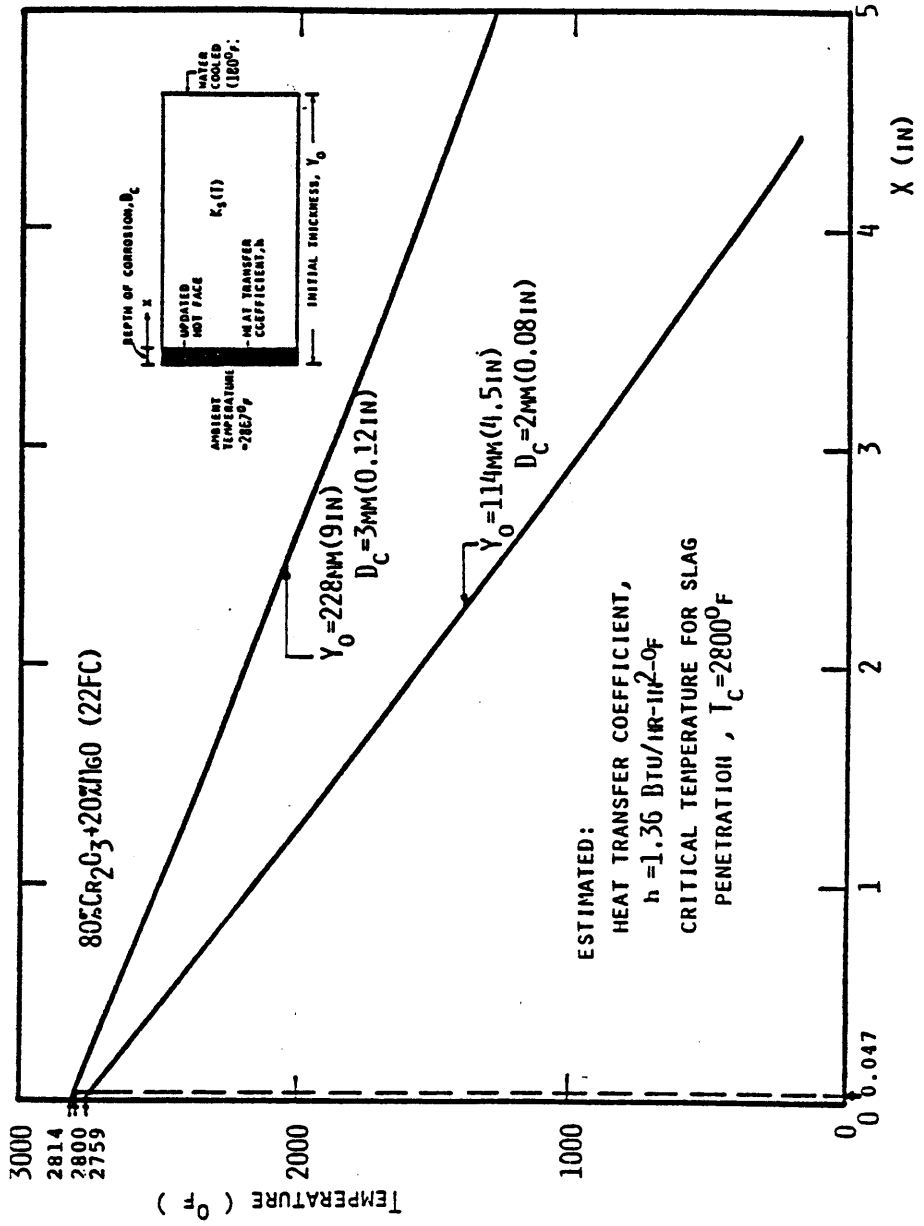

Figure 4.5 Estimation of Critical Temperature of Slag Penetration into 80% Cr_2O_3 Refractory (U.S. Coal Slag System)

The thermophysical and mechanical properties of refractory materials are considerably influenced by slag penetration. Figs. 3.20, 4.6, 4.7 and 4.8 show the uniaxial compressive strength, initial Young's modulus, creep behavior and thermal conductivity of 90% Al_2O_3 brick before and after slag penetration. The large reduction in strength and stiffness of the refractory material due to slag penetration, especially at high temperatures level, may contribute to hot face spalling and cracking problems. These changes in thermophysical and mechanical properties of the refractory materials due to slag penetration are included in the thermomechanical analyses reported in this study.

Erosion occurs primarily by the abrasion of high-velocity slag containing char and ash and high-velocity gases on the lining materials, which may lead to the spalling of the hot-face lining. Available short-term laboratory tests cannot simulate such an erosive environment due to experimental uncertainties. Therefore, precise evaluation of the long-term reliability of lining systems relies on full-scale, long operating-period tests in gasifers that represent actual coal conversion process; reliability predictions are meaningful only when the uncertain nature of the corrosion processes can be properly characterized.

The candidate materials considered in the present work for hot-face lining, such as high-Al_2O_3 and high-Cr_2O_3 refractory bricks, have good erosion resistance when they are manufactured. However, as mentioned before, the slag penetration can deteriorate the material strength on the hot face, which accelerates the erosion process.

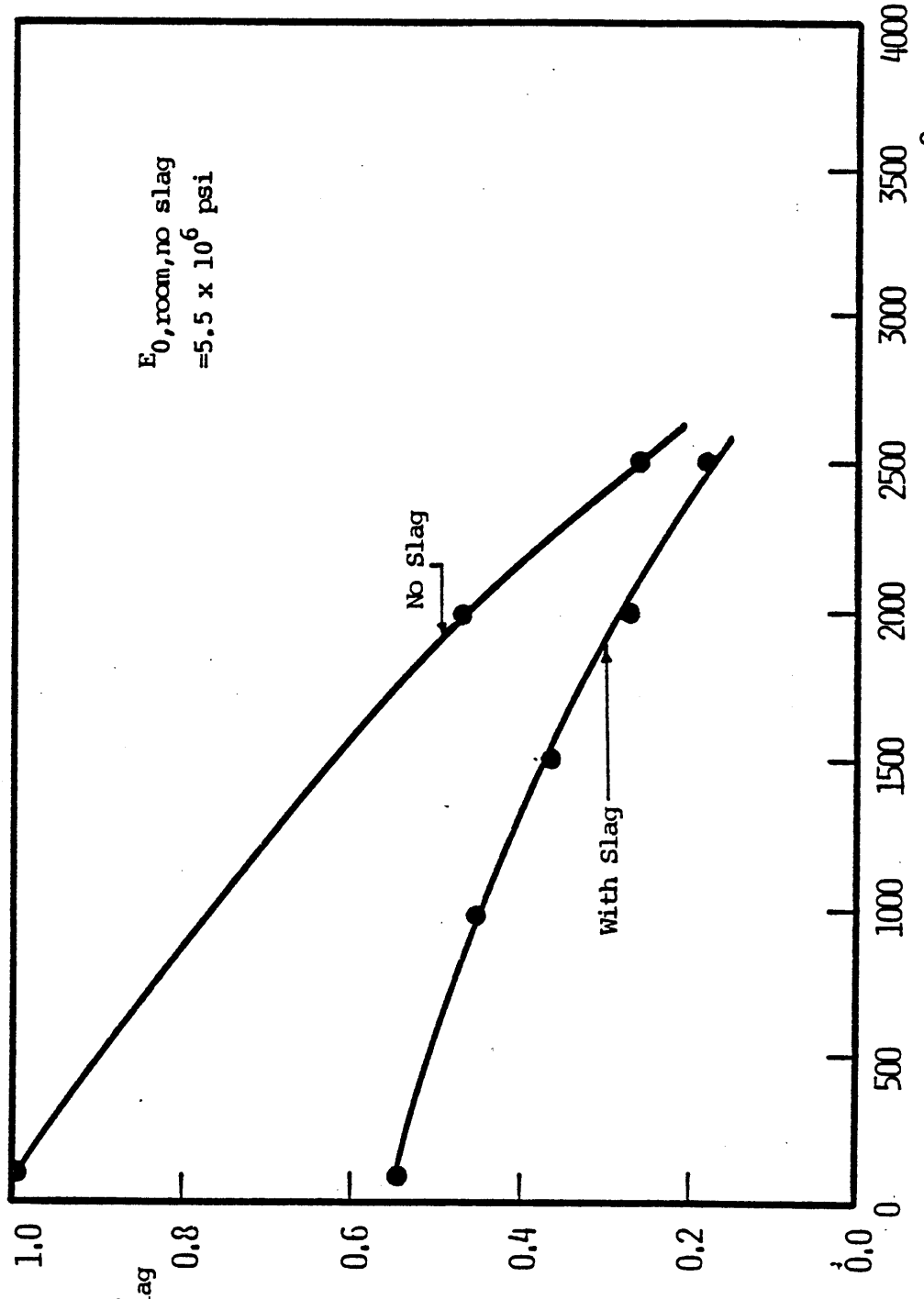

Figure 4.6 Effects of Slag Penetration on Initial Young's Modulus of 90% Al_2O_3 Refractory [4]

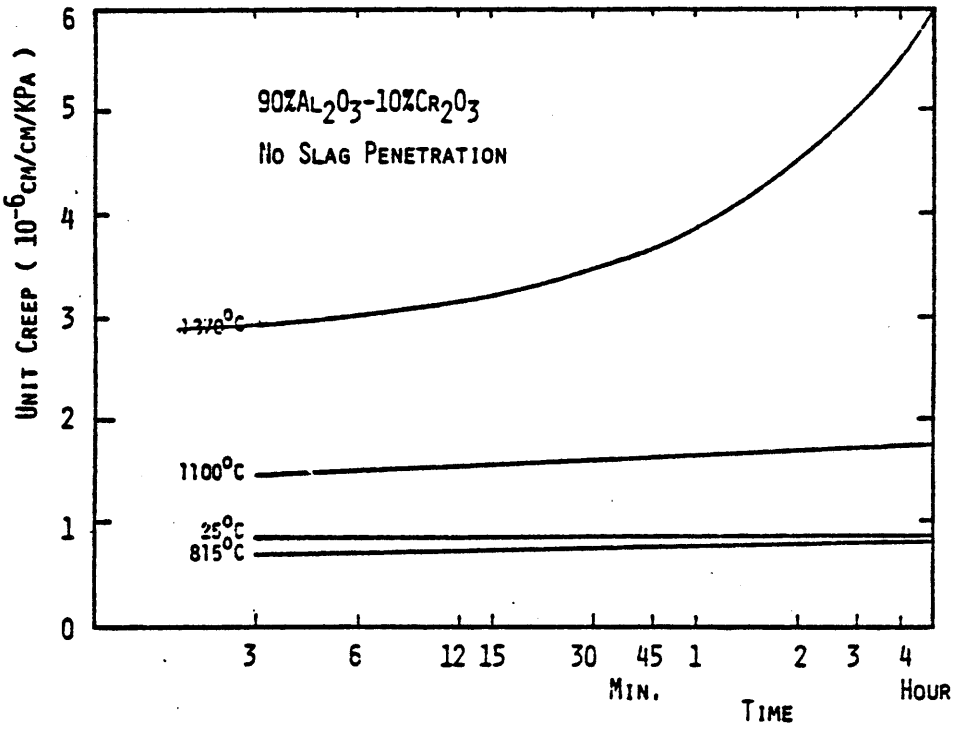

(a) Before Slag Penetration [4]

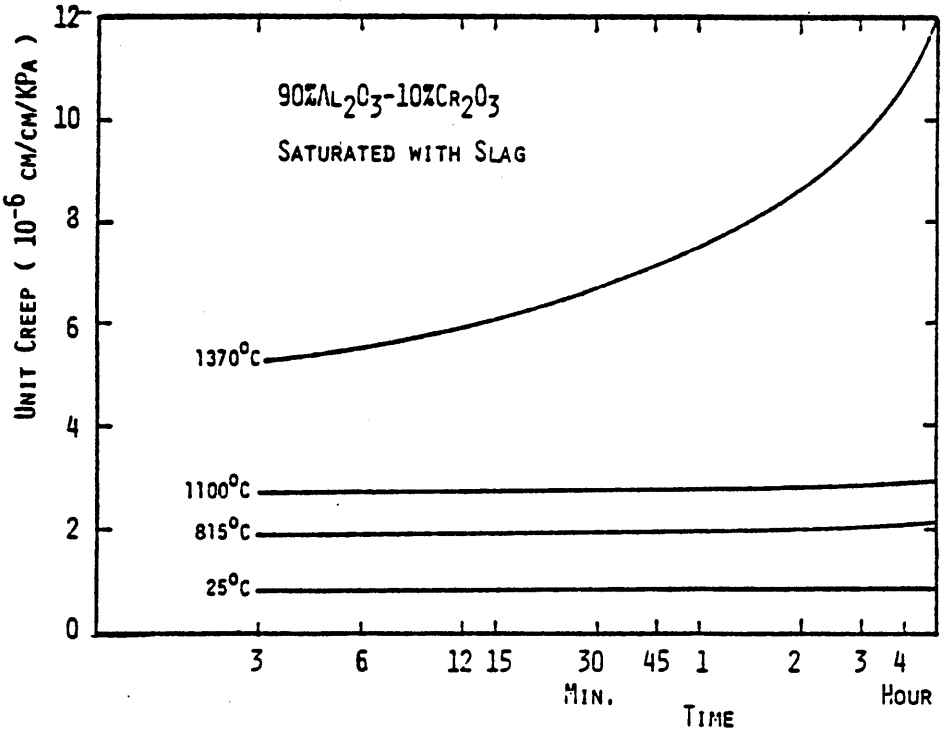

(b) After Slag Penetration [4]

Figure 4.7 Effects of Slag Penetration on Creep Behavior of 90% $A\ell_2O_3$ Refractory (uniaxial stress = 4865 psi)

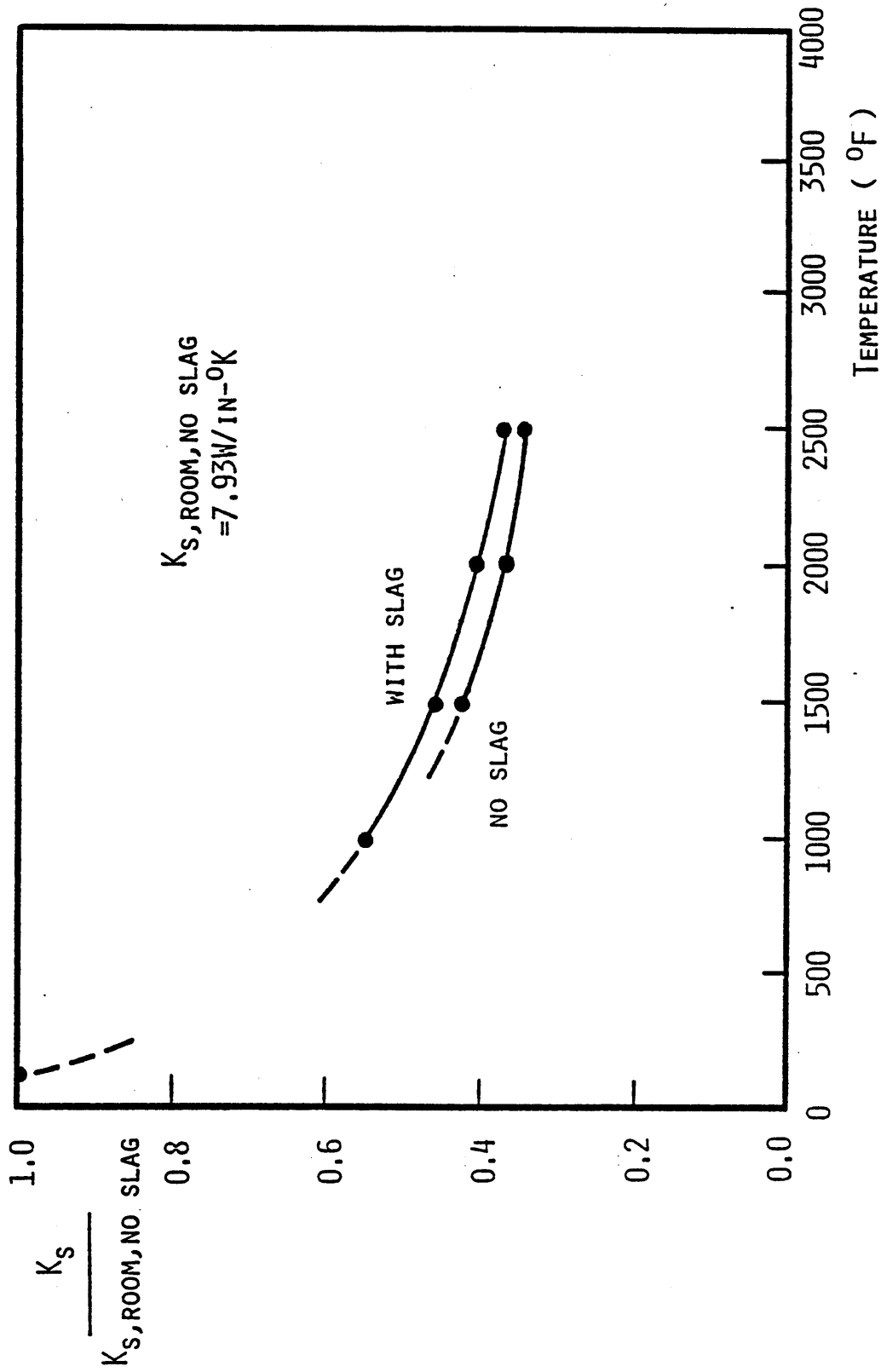

Figure 4.8 Effects of Slag Penetration on Thermal Conductivity of 90% $A\ell_2O_3$ Refractory [4]

In the next section, a simple corrosion model is proposed, which includes both dissolution and spalling mechanisms to predict the long-term corrosion behavior of the lining.

§4.3 CORROSION MODEL

After a lining system is exposed to a corrosive environment for days, months, or years, the lining thickness will be reduced due to the interaction of the lining materials with slags and gases. For structural integrity and operational efficiency, the lining should be replaced when a critical lining thickness is reached. Operation below this critical thickness is inefficient or unsafe. Thus, for a good design, knowledge is needed of the thickness reduction process and of the uncertainties that affect this process. This would result in a better selection among competitive system designs or candidate materials. It is the objective of this section to develop a corrosion model for linings such that (1) the average residual lining thickness during operation can be predicted through a small number of short-term corrosion tests, and (2) uncertainty in the corrosion process can be quantified.

A general method is presented, which interprets the reduction process of lining thickness as the result of corrosion and heat transfer. The method can be generally formulated as follows:

(1) Given (see Fig. 4.9)

(a) lining thickness, Y ,

(b) dimension of the gasifier, say, r_0 ,

(c) conductivity of the lining material, K_S , (in general, K_S is a function of temperature T),

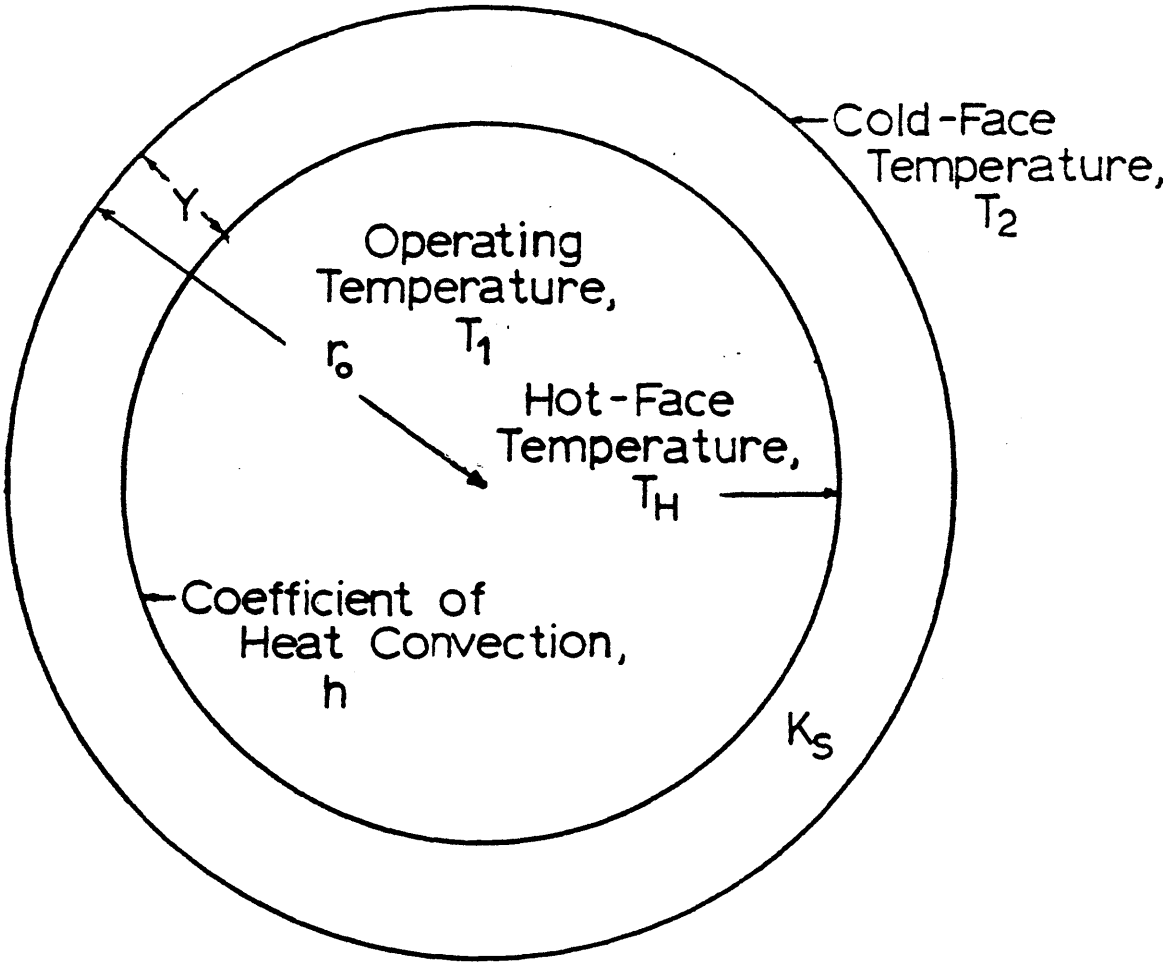

Figure 4.9 Schematic of Single-Layer Lining System and Boundary Conditions

(d) coefficient of heat transfer on the hot (inner) face of the lining, h (in general, $h = h(T)$) ,

(e) operating temperature, T_1 , and

(f) control temperature on the outer face of lining, T_2 ,

one can obtain a relationship between the hot face temperature of the lining, T_H , and Y at steady state, i.e.,

$$T_H = f(Y) \tag{4.3}$$

(2) Given the operation conditions, one can express the corrosion rate (the thickness reduction rate $-\dot{Y}$ as a function of the hot face temperature T_H and of time t , i.e.:

$$-\dot{Y} = g(T_H, t) \tag{4.4}$$

where $\dot{Y} = \frac{dY}{dt}$.

(3) Combining Eq. (4.3) and Eq. (4.4), one obtains

$$-\dot{Y} = g(f(Y), t) \tag{4.5}$$

(4) Solving Eq. (4.4) with the initial condition

$$Y(t = 0) = Y_0 \tag{4.6}$$

one obtains Y as a function of t

$$Y = Y(t) \tag{4.7}$$

Eq. (4.7) gives the desired relationship for residual lining thickness at any given time. The determination of $f(Y)$ and $g(T_H,t)$, the influence of the model parameters on the behavior of $Y(t)$ and the uncertain nature of $Y(t)$ need to be studied further. The following sections present these details.

§4.3.1 Relationship between Hot-Face Temperature and Lining Thickness

Consider a one-layer symmetrical lining, as shown in Fig. 4.9, subjected to convection boundary conditions on the inner (hot) face while outer face temperature has constant value T_2. The operating temperature in the gasifier, T_1, is assumed to be constant. The conductivity of the lining material, K_S, is generally temperature dependent and can be well approximated by a cubic polynomial in T (see Chapter 3):

$$K_S = a_0 + a_1T + a_2T^2 + a_3T^3 \qquad (4.8)$$

The following additional assumptions are made:

(1) the coefficient of heat transfer, h, on the inner face is assumed not to depend on temperature; and

(2) joint opening and cracking of the lining have little influence on the hot face temperature; therefore, only one dimensional (radial) heat transfer analysis is sufficient and hot face temperature T_H is primarily determined by the convection process.

The governing equation for heat-transfer in the above mentioned system is [67]:

$$\frac{d}{dr}\left(k_s r \frac{dT}{dr}\right) = 0 \qquad (4.9)$$

with boundary conditions (b.c.'s)

$$K_s \frac{dT}{dr} = h(T_H - T_1) \qquad \text{at} \quad r = r_0 - Y \qquad (4.10a)$$

$$T = T_2 \qquad \text{at} \quad r = r_0 \qquad (4.10b)$$

$$T = T_H \qquad \text{at} \quad r = r_0 - Y \qquad (4.10c)$$

Integrating Eq. (4.9) and combining the result with Eq. (4.8) gives

$$a_0 T + \frac{1}{2} a_1 T^2 + \frac{1}{3} a_2 T^3 + \frac{1}{4} a_3 T^4 = c_1 \ln r + c_2 \qquad (4.11)$$

where c_1 and c_2 are constants to be determined from the b.c.'s (Eq. (4.10)). Imposing Eqs. (4.10) one finds

$$T_H = T_1 + \frac{c_1}{h}\left(\frac{1}{r_0} - Y\right) \quad , \qquad (4.12a)$$

$$a_0 T_2 + \frac{1}{2} a_1 T_2^2 + \frac{1}{3} a_2 T_2^3 + \frac{1}{4} a_3 T_2^4 = c_1 \ln r_0 + c_2 \qquad (4.12b)$$

and

$$a_0 T_H + \frac{1}{2} a_1 T_H^2 + \frac{1}{3} a_2 T_H^3 + \frac{1}{4} a_3 T_H^4 = c_1 \ln (r_0 - Y) + c_2 \qquad (4.12c)$$

By solving the simultaneous equations (4.12a), (4.12b) and (4.12c) one can get c_1 , c_2 , and T_H in terms of the coefficients a_i, r_0, h , and Y. For a certain lining material and lining geometry, a_i and r_0 are given. The coefficient h depends on the gasification process, mainly through the composition, velocity, pressure, density, and viscosity of the processing gases. For a given set of a_i, r_0 , and h , the relationship between T_H and Y can be obtained:

$$T_H = f(Y) \qquad (4.13)$$

Case studies have been performed by using 90% $A\ell_2O_3$ and 80% Cr_2O_3 refractories with the following material properties:

For the 90% $A\ell_2O_3$ refractory:

$$K_s = 0.325 + 0.323 \times 10^{-4}T - 0.105 \times 10^{-6}T^2 + 0.287 \times 10^{-10}T^3$$

Btu/hr-in-°F , T in °F (4.14a)

For the 80% Cr_2O_3 refractory:

$$K_s = 0.273 - 0.324 \times 10^{-4}T + 0.563 \times 10^{-8}T^2 - 0.145 \times 10^{-12}T^3$$

Btu/hr-in-°F , T in °F (4.14b)

The operating temperature T_1 is assumed to be 3000°F and the cold face temperature T_2 is fixed at 150°F . For sensitivity analysis, several combinations of the r_0 and h have been used:

r_0 = 60", 108", and 180"

h = 0.01 , 0.1, 1.0 , 10.0 Btu/hr-in^2-°F

Figs. 4.10 , 4.11 and 4.12 give the relationship $T_H = f(Y)$ for a few cases with different combinations of r_0 and h . It can be seen that the function f is not sensitive to the change of the dimension of the gasifiers (r_0) in the range of practical values (60" -180") . However, f is highly dependent on h , i.e., on the gasification process. Based on these results, in following analyses r_0 is fixed to a conceptual value r_0 = 108" , while h is still considered as a free parameter. Fig. 4.13 shows the relationship $T_H = f(Y)$ for 80% Cr_2O_3 linings with different h, while r_0 is taken to be 108".

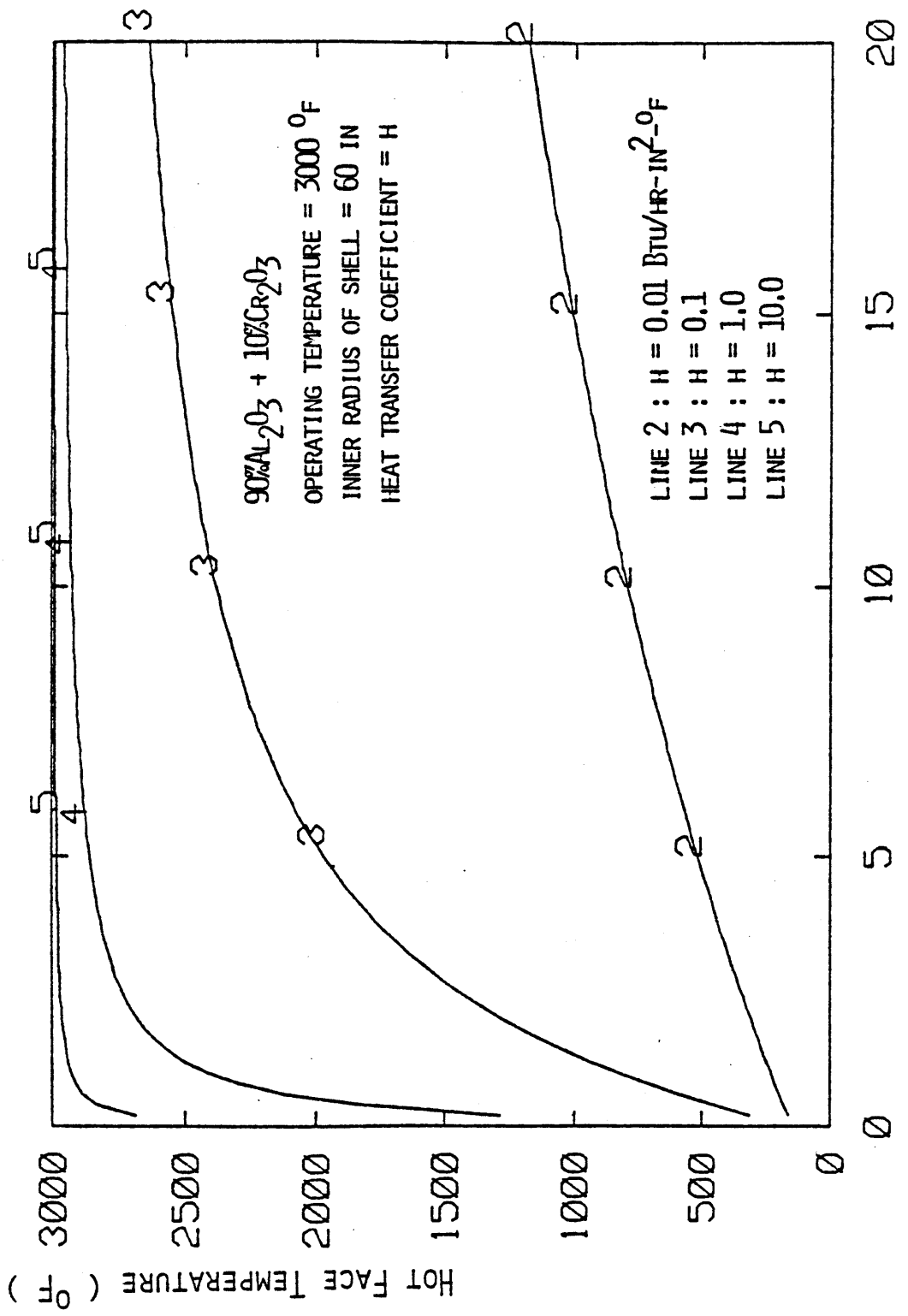

Figure 4.10 Hot-Face Temperature vs. Lining Thickness Relationship (r_0 = 60") for 90% Al_2O_3 Refractory Lining

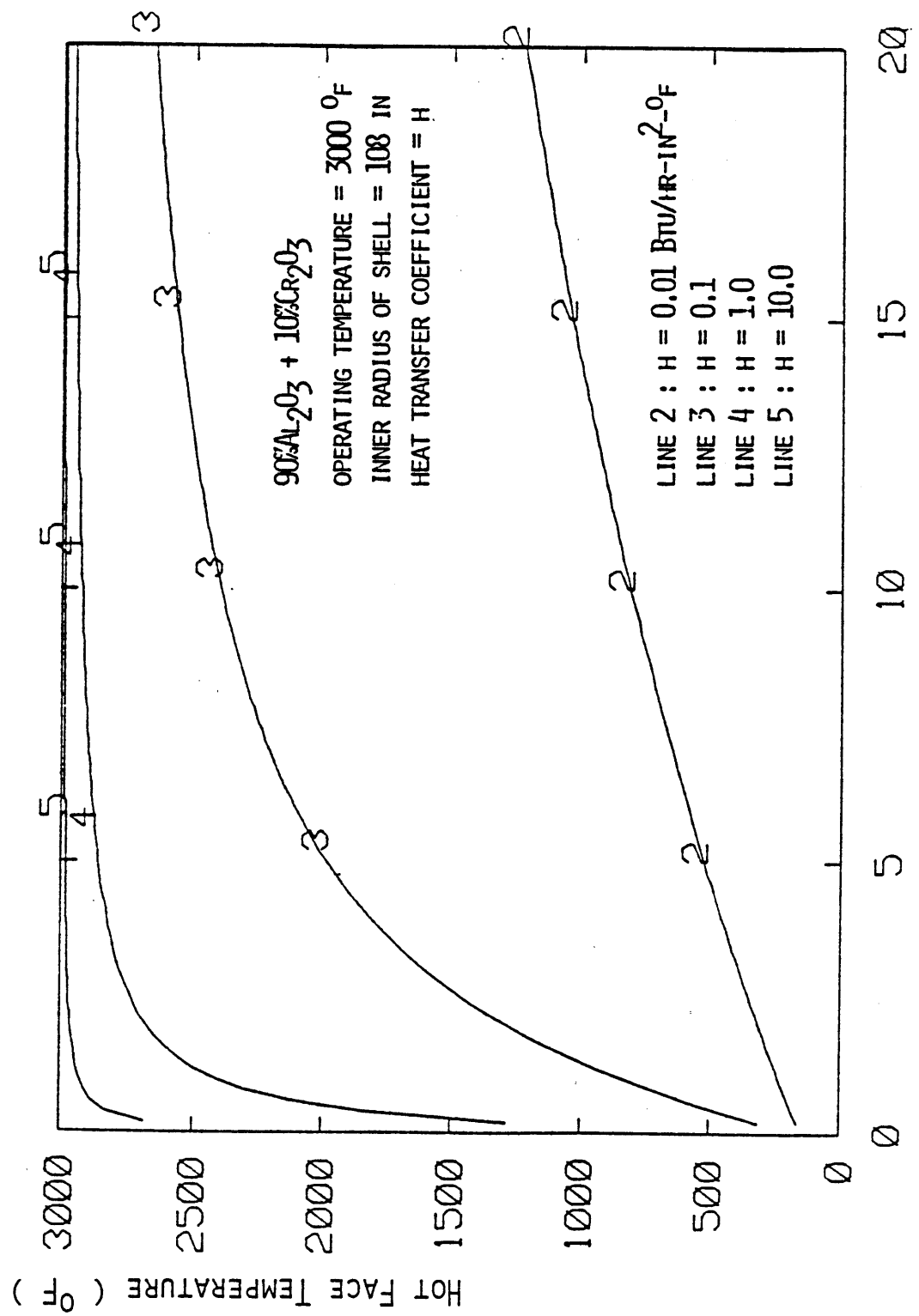

Figure 4.11 Hot-Face Temperature vs. Lining Thickness Relationship (r_0 = 108") for 90% $A\ell_2O_3$ Refractory Lining

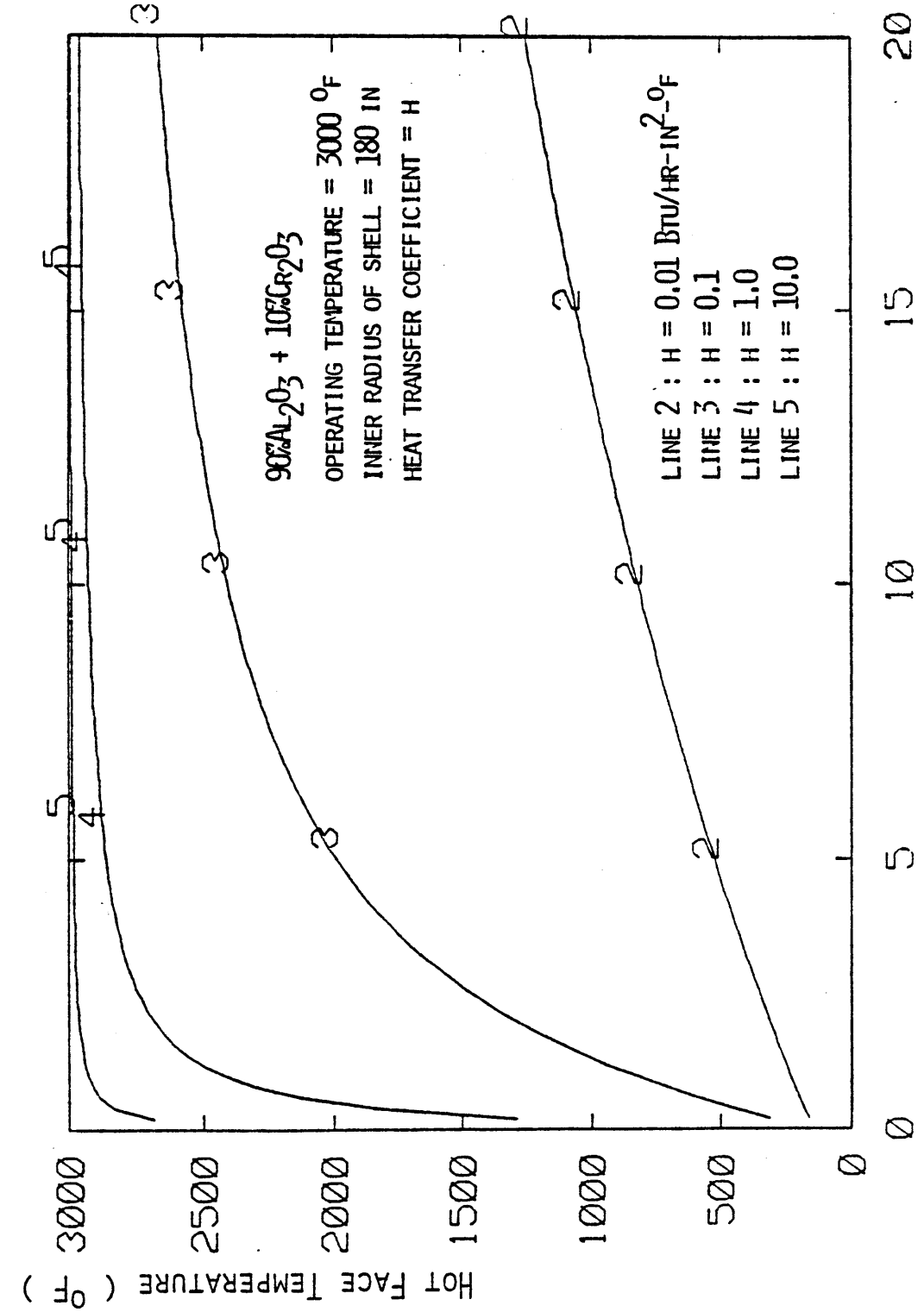

Figure 4.12 Hot-Face Temperature vs. Lining Thickness Relationship (r_0 = 180") for 90% Al_2O_3 Refractory Lining

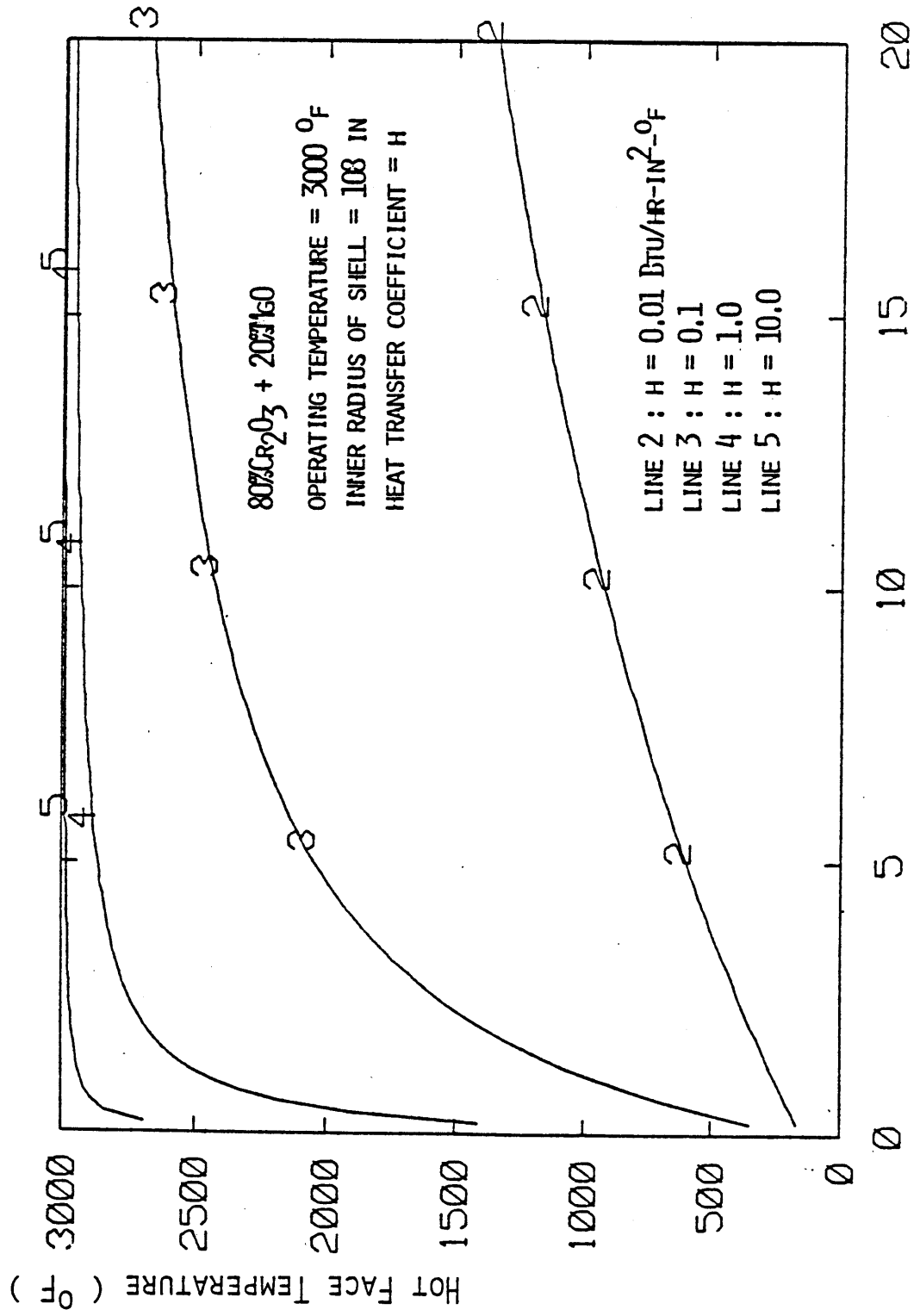

Figure 4.13 Hot-Face Temperature vs. Lining Thickness Relationship (r_0 = 108") for 80% Cr_2O_3 Refractory Lining

For a more general multiple-layer lining system, the same approach can be applied to each layer. Continuity in temperature should be imposed at the interface of any two layers. Accordingly, the resulting function f(Y) depends on the thermal properties of all the layers.

§4.3.2 Proposed Corrosion Model

As mentioned earlier in this chapter, there are three major types of corrosion mechanisms: dissolution, penetration, and erosion. A proper corrosion function g should account for all the mechanisms.

Dissolution rate can be generally represented by Eq. (4.1) and its temperature-shifting effect can be represented by Eq. (4.2). Penetration itself usually does not cause any reduction of thickness; however, slag-penetration reduces the strength and stiffness of the refractory material (see Figs. 3.20 and 4.6) and creates weak zones next to the hot face. In these zones where compressive hoop stresses exist cracks form parallel to the hot face (see Fig. 4.1). This weak zone can spall along the crack interfaces when subjected to erosive slag/gases movement [65]. A conservative estimate of the thickness of each spalling piece is the penetration depth. That is, the corrosion rate can be conservatively calculated as:

$$-\dot{Y} = g(T_H,t) = A \text{ Exp } (-B(\frac{1}{T_H} - \frac{1}{T_o})) + D_p[t_{i-1},t_i]\ \delta(t_i) \qquad (4.15)$$

The first term on the right hand side refers to the dissolution process. The second term represents the spalling process under the combining effects of slag-penetration and erosion, where $D_p[t_{i-1},t_i]$ is the maximum penetration depth from the location of the hot face at $t = t_i^-$ during the $(i-1)^{th}$ and $(i)^{th}$ occurrence of spalling. t_i is the occurrence time of $(i)^{th}$ spalling and δ is the Dirac delta function:

$$\delta(t_i) = \begin{cases} 0 , & \text{if } t \neq t_i \\ \infty , & \text{if } t = t_i \end{cases} \qquad (4.16)$$

To complete the model, one needs to know the parameters A , B , and t_i for the refractory-slag system. The first two quantities can be estimated from laboratory tests (e.g., test mentioned in §2.4), whereas the last quanlity requires field observations. It is worthy of mention that these three quantities are uncertain due to the high variability of the gasification environment for which dispersion of A, B , and t are of concern.

§4.3.3 Residual Lining Thickness

By combining Eqs. (4.13) and (4.15) and eliminating T_H from the two equations, one can obtain Y as function of t ; however, the explicit analytical solution is not known and must resort to numerical analysis in discrete-time approach.

A computer program for the Simulation of Residual Lining Thickness (SRLT) has been written to calculate (1) the hot face temperature as a function of residual lining thickness, (2) the depth of slag penetration as a function of the residual lining thickness, and (3) the lining thickness as a function of time. The listing of the program and an example are given in Appendix I.

To understand the typical form of Y(t) in a single-layer lining system, the following parameter values are used from test results in Refs. 50, 51 and 89. Reader should keep in mind that these numbers are adopted here only to represent average behavior and can not be used directly for a specific design without further justification.

Y_0 = 9 in.

r_0 = 108 in.

K_s : same as in equation 4.14 (referred to 90% Al_2O_3 brick and 80% Cr_2O_3 bricks)

T_1 = 3000°F

T_2 = 150°F

A = 1.339×10^{-3} in/hr for 90% Al_2O_3 brick and

= 2.362×10^{-4} in/hr for 80% Cr_2O_3 brick

B = 46900°k for 90% Al_2O_3 brick ,

= 43700°k for 80% Cr_2O_3 brick

T_o = 1813°K for both bricks

Δt = $t_i - t_{i-1}$ ($i = 1,2,\ldots$), interarrival time of spalling events

= 100 hr, 1000 hr, 10000 hr, and ∞ .

T_c = critical temperature to evaluate the depth of slag penetration

= 2650°F for 90% Al_2O_3 brick, and

= 2800°F for 80% Cr_2O_3 brick

h is still taken as a variable parameter with values

h = 0.1, 1.0, 10.0 Btu/hr-in^2-°F

Figs 4.14 to 4.19 show the functions Y(t) for 90% Al_2O_3 and 80% Cr_2O_3 linings with different combinations of h and Δt . It is interesting that, in all cases, the corrosion rate decreases in time and the residual thickness tends to stablize. These phenomena are caused by the decrease of hot face temperature due to the decrease of lining thickness and depend on the heat transfer characteristics on the the hot face and the cold-face temperature. It is also found that spalling

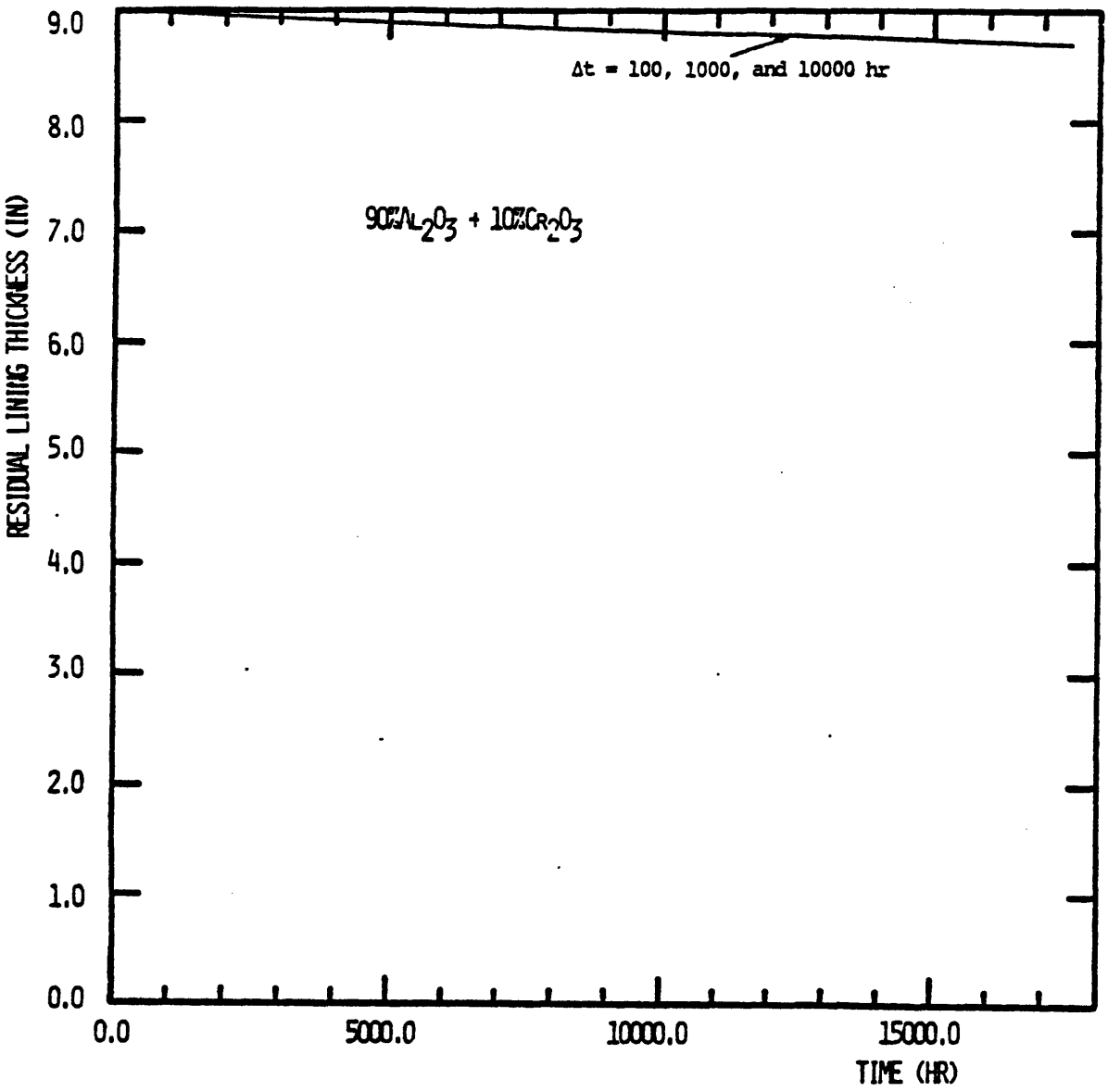

Figure 4.14 Residual Lining Thickness vs. Time for 90% $A\ell_2O_3$ Refractory Lining (h = 0.1 Btu/hr-in^2-^{o}F, T_1 = 3000^{o}F)

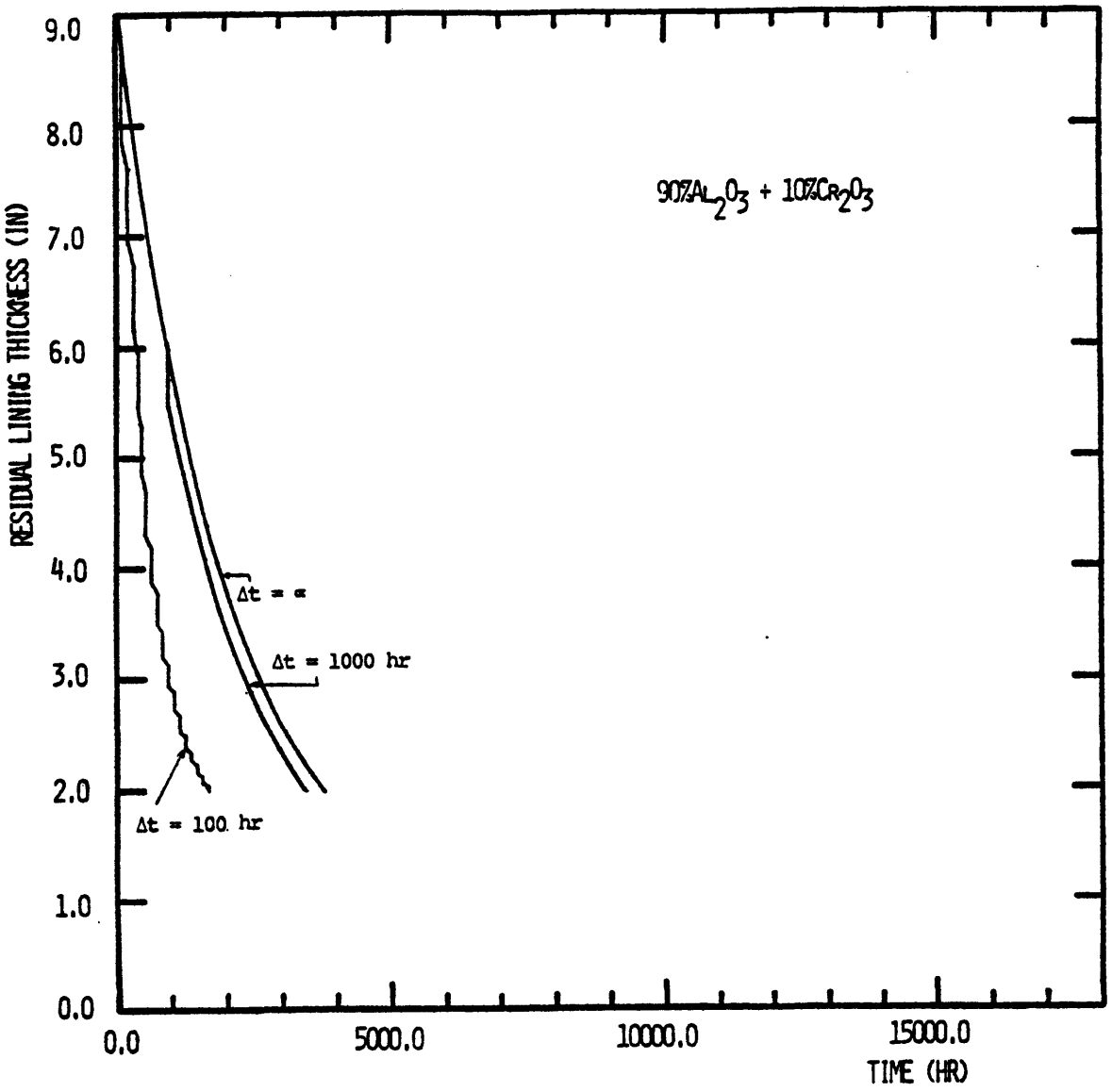

Figure 4.15 Residual Lining Thickness vs. Time for 90% Al_2O_3 Refractory Lining ($h = 1.0$ Btu/hr-in^2-^oF, $T_1 = 3000^oF$)

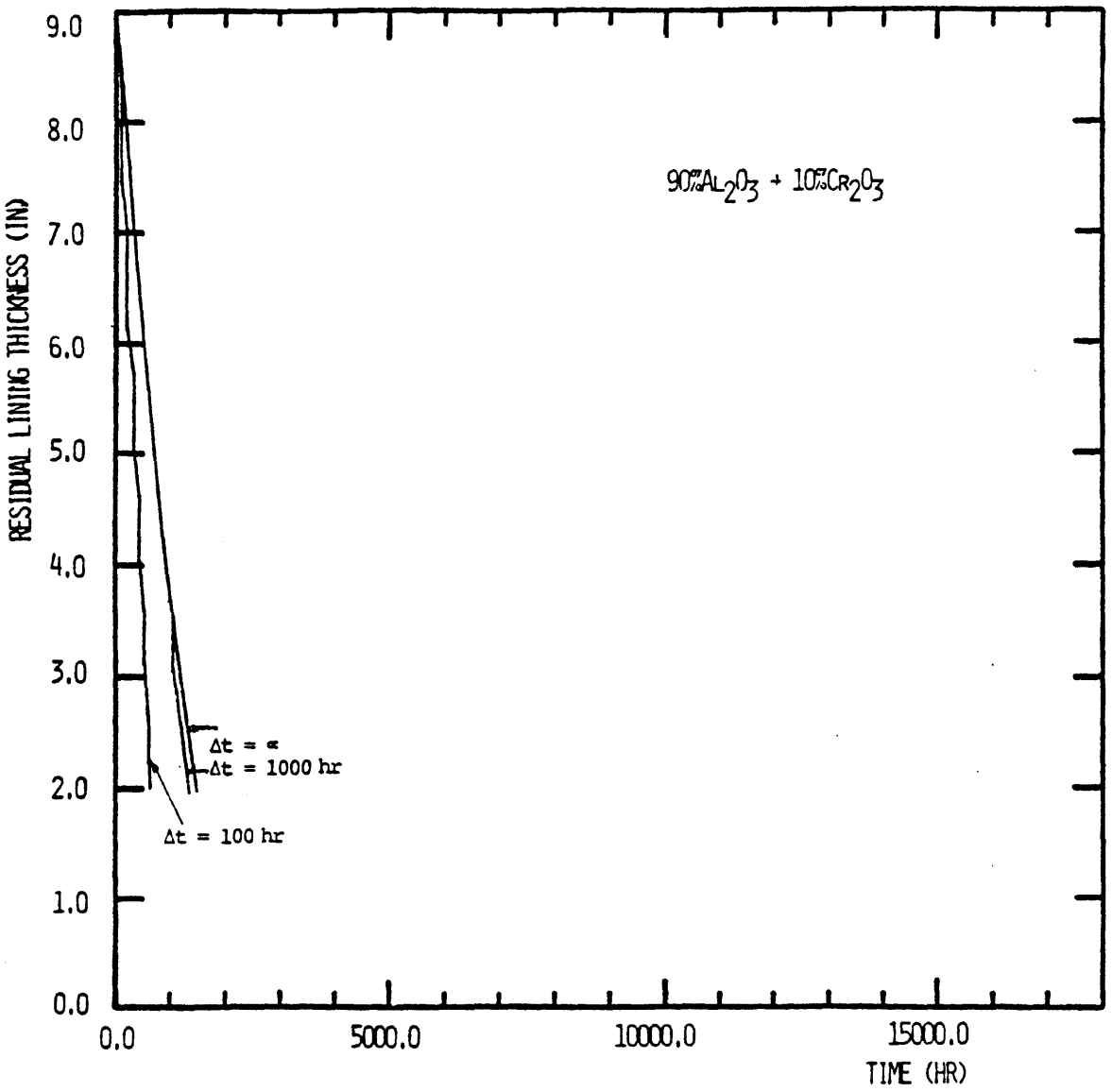

Figure 4.16 Residual Lining Thickness vs. Time for 90% $A\ell_2O_3$ Refractory Lining (h = 10.0 Btu/hr-in^2-^{o}F, T_1 = 3000^{o}F)

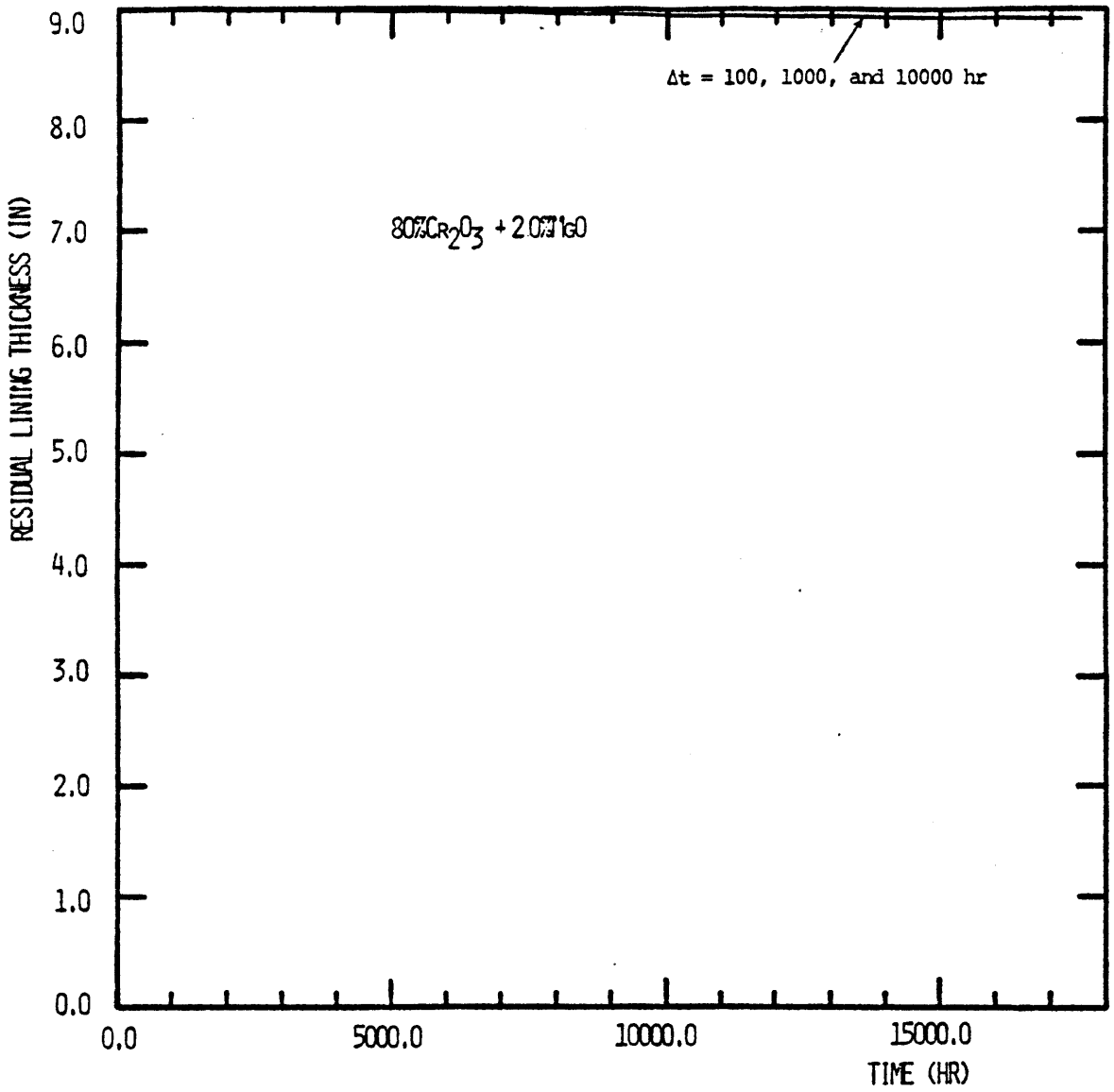

Figure 4.17 Residual Lining Thickness vs. Time for 80% Cr_2O_3 Refractory Lining (h = 0.1 Btu/hr-in^2-^{o}F, T_1 = 3000^{o}F)

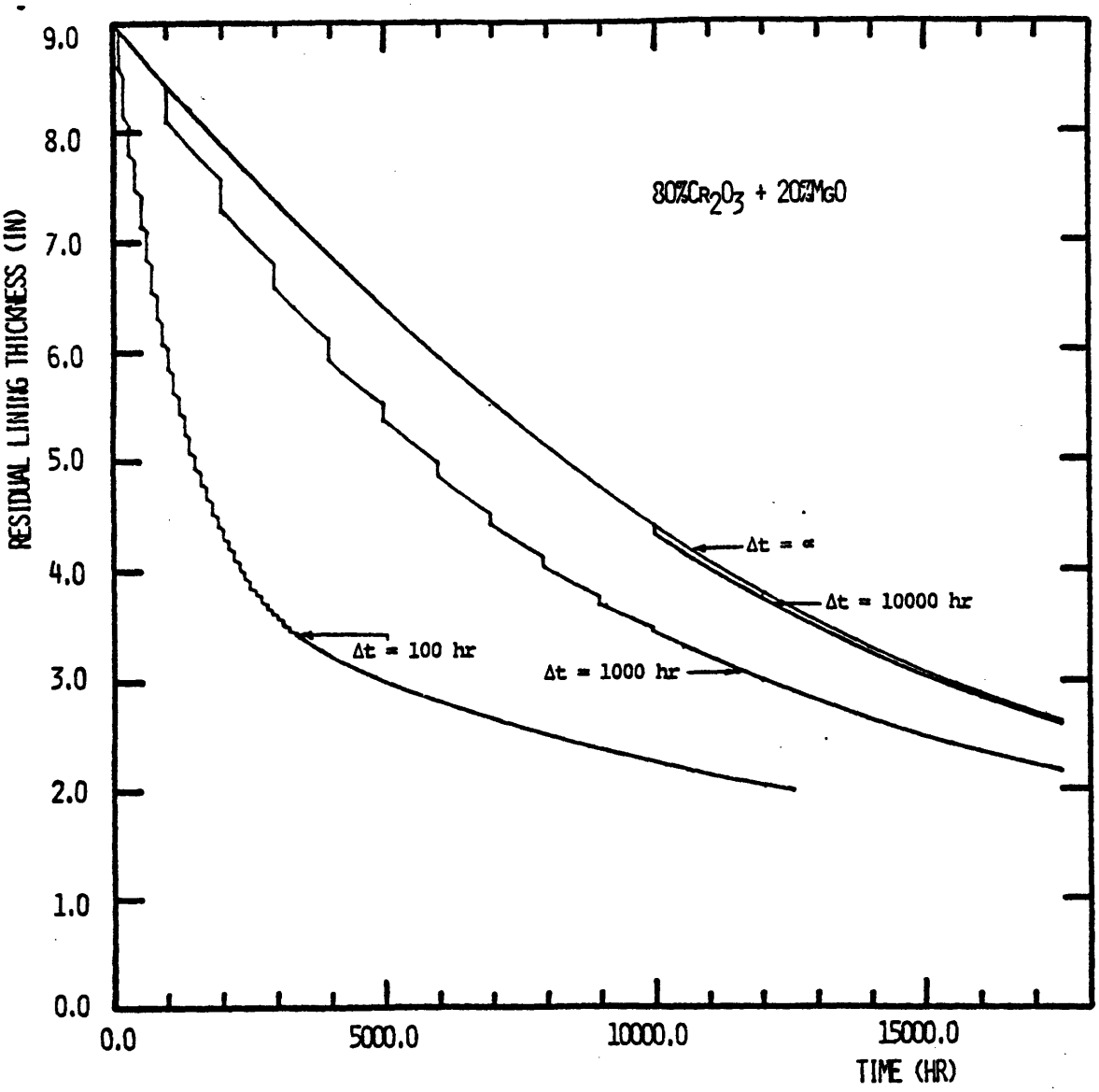

Figure 4.18 Residual Lining Thickness vs. Time for 80% Cr_2O_3 Refractory Lining (h = 1.0 Btu/hr-in^2-^{o}F, T_1 = 3000^{o}F)

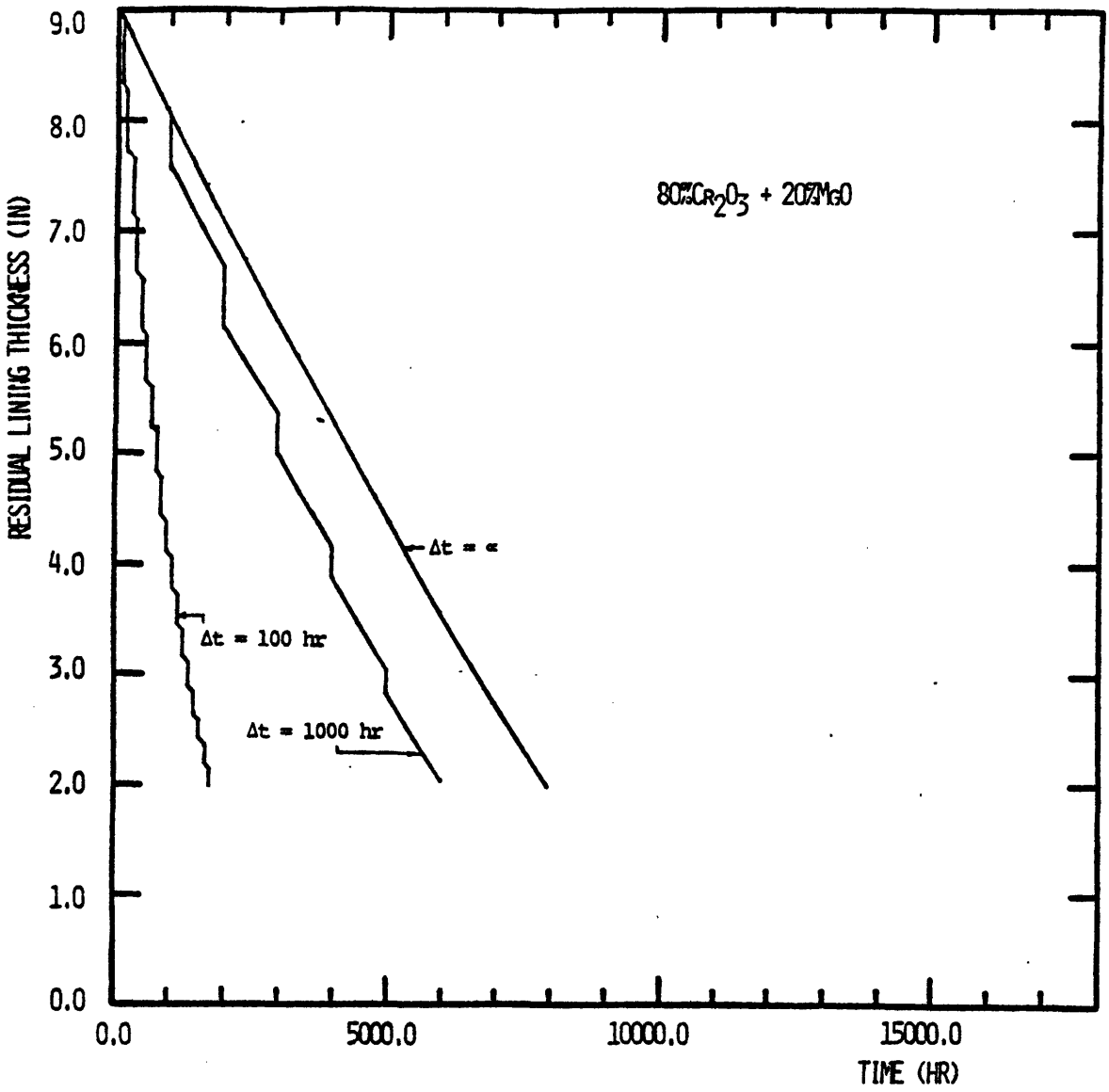

Figure 4.19 Residual Lining Thickness vs. Time for 80% Cr_2O_3 Refractory Lining (h = 10.0 Btu/hr-in^2-^{o}F, T_1 = 3000^{o}F)

of hot face material can significantly increase the corrosion rate, if it is not well controlled. For the considerations of long-term reliability and total cost, the previous numerical results suggest that:

(1) By decreasing the hot face temperature, which can be done by decreasing the value of h, one can slow down the corrosion rate. Furthermore, lowering hot-face temperature can result in a layer of viscous-solid slag on the hot face of the lining [14] (not included in present analyses), which protects the lining from further corrosion. This layer is desirable in the design of lining systems for long-term operation. However, use of small h values (e.g., through the reduction of operating pressure, gas speed, etc.) may lead to an inefficient gasification process. Hence, the optimal value of h should be determined on the basis of this trade-off.

(2) Material upgrading for reduction of the dissolution rate and depth of slag penetration can effectively control the corrosion rate. As shown by the previous results, the 80% Cr_2O_3 refractory gives generally longer life time than 90% Al_2O_3 refractory under the same operating conditions. This is due to the relatively high resistance of the 80% Cr_2O_3 refractory against slag dissolution and penetration. On the other hand, 80% Cr_2O_3 bricks are relatively expensive. Further studies should be made to explore the possible modifications of operating conditions such that more inexpensive materials (e.g., high Al_2O_3 refractories) can be used with minimum sacrifice of operational efficiency.

(3) Spalling plays an important role in the overall corrosion process. A better control of the spalling process can produce a longer service life. Hence, improvements of the spalling control, e.g., by a proper operational scheme or design to reduce hot face stress, or by adopting certain treatments to the lining materials to increase their resistance to slag penetration, should be areas of future research.

Regarding the second possibility, further analyses have been made of the effects of operating temperature on corrosion. The lining material is 90% Al_2O_3 refractory with properties and boundary conditions as before, except that the operating temperatue T_1 is reduced from 3000°F to 2800°F. The coefficient h is taken to be 1 Btu/hr-in-°F. The residual lining curves in such systems are shown in Fig. 4.20 for different values of Δt. Comparing Fig. 4.20 with Fig. 4.15, it can be seen that a significant improvement of the lining life can result from modification of the operating temperature, however with possible reduction of operational efficiency. Again, the final determination of the lining material and operating conditions should be made on the basis of a total cost/benefit analysis during the expected life of the gasifier.

§4.4 Y(t) AS A RANDOM PROCESS

In a refractory-slag system the governing factors such as dissolution rate and spalling time of the corrosion process are not exactly known. Uncertainties inherent in the system result in uncertaint residual lining thickness as a function of time, i.e., Y(t) is a random process.

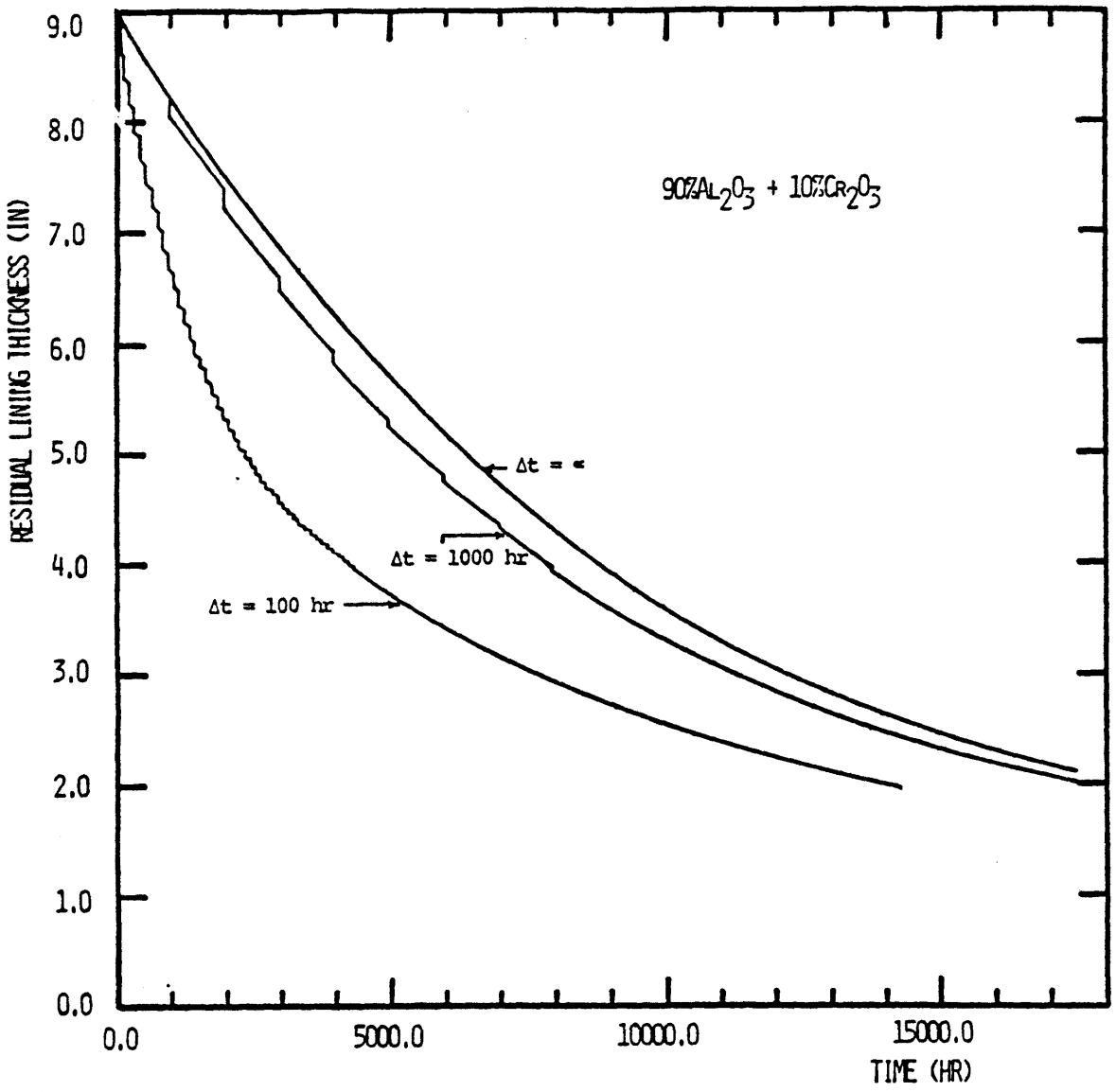

Figure 4.20 Residual Lining Thickness vs. Time for 90% $A\ell_2O_3$ Refractory Lining (h = 1.0 Btu/hr-in^2-^{o}F, T_1 = 2800^{o}F)

The 90% Al_2O_3 and 80% Cr_2O_3 linings with the same lining geometry and material properties are used here to study the uncertainty of Y(t). The following assumptions and parameter values are further used to model uncertainty in the corrosion process:

(1) The reference dissolution rate A is assumed to be a random variable with cumulative distribution function $F_A(a)$ where:

$F_A(a)$ = Probability that A is smaller than or equal to a

In the following study, A is assumed to be a random variable (r.v.) with a truncated normal distribution, i.e.:

$$F_A(a) = \begin{cases} \dfrac{\Phi(a) - \Phi(0)}{1 - \Phi(0)} & \text{if } a \geq 0 \\ 0 & \text{if } a < 0 \end{cases} \qquad (4.17)$$

where Φ is the normal distribution function defined by [10]:

$$\Phi(a) = \int_{-\infty}^{a} \frac{1}{\sqrt{2\pi}\,\sigma_A} e^{-\frac{1}{2}\left(\frac{X-m_A}{\sigma_A}\right)^2} \qquad (4.18)$$

and the parameters m_A and σ_A are the mean and standard deviation of r.v. A , respectively. For the present study the following values are chosen

$m_A = 1.339 \times 10^{-3}$ in/hr for 90% Al_2O_3 brick, and

$= 2.362 \times 10^{-4}$ in/hr for 80% Cr_2O_3 brick.

V_A = coefficient of variation of r.v. A

$= \sigma_A/m_A$

$= 0.01$ and 0.1

(2) Δt is taken to be a r.v. with exponential cumulative distribution function [10]:

$$F_{\Delta t}(x) = \begin{cases} 1 - e^{-\alpha x} & , \quad x \geq 0 \\ 0 & , \quad x < 0 \end{cases} \tag{4.19}$$

where α is the mean occurence rate. This is based on the assumption that events follow a Poisson process [10] with rate α .

According to the Poisson process, the physical mechanism that generates the spalling events should satisfy the following conditions [10]:

(1) The probability of an event in a short interval of time from t to $t + h$ is approximately αh , for any t .

(2) The probability of two or more events in a short interval of time is negligible compared to αh .

(3) The number of events in any interval of time is independent of the number of events in any other adjacent interval. For the present study $1/\alpha$ is set equal to 100 and 1000 hours.

The analytical solution for the probability distribution of Y(t) is not known. The Monte Carlo simulation technique [57,73] is used instead. For a specific lining system, this procedure can be summarized as follows:

(1) By using a random number generator, one obtains a value of A from the distribution F_A and a sequence of random spalling times t_i.

(2) By using the simulated values of A and t_i , one can find the function Y(t) in the same way as in the deterministic approach (Eq. 4.15).

(3) By repeating steps (1) and (2) in terms, one generates n realizations of the process Y(t). Probabilistic

characteristics, such as the mean, standard deviation, and marginal distribution of Y at any given time t can be estimated from these n realizations.

The previous method has been incorporated into the computer program SRLT (see Appendix I), which simulates the functions Y(t). The estimation of mean, standard deviation and distribution of Y at selected times is performed by a program for the Probabilistic Analysis of Residual Lining Thickness (PARL) (see Appendix II).

Figs. 4.21 and 4.22 show the mean and standard deviation of Y as functions of t , for 90% $A\ell_2O_3$ and 80% Cr_2O_3 linings respectively, and for different combinations of σ_A and α. The operating temperature used in these cases is 3000°F. The heat transfer coefficient h is fixed at 1.0 Btu/hr-in^2-°F . Fig. 4.23 shows the mean and standard deviation of Y as a function of time for the lining with 90% $A\ell_2O_3$ refractory, while the operating temperature is taken to be 2800°F. The h value is still 1.0 Btu/hr-in^2-°F. The important findings from these results are:

(1) The uncertainty in the spalling process contributes significantly to the overall uncertainty on the residual lining thickness, especially during the initial stage of the lining life. A better control of the spalling process resulting in a reduced spalling rate would give a more reliable lining, in the sense that the probability of getting higher loss of lining thickness is smaller due to the smaller dispersion of Y . This better control may be obtained by various means: for example, by controlling the gas velocity and the size of the particles in gases and slags, or by special treatments to the refractory (consisting of modifiying the chemical composition of the

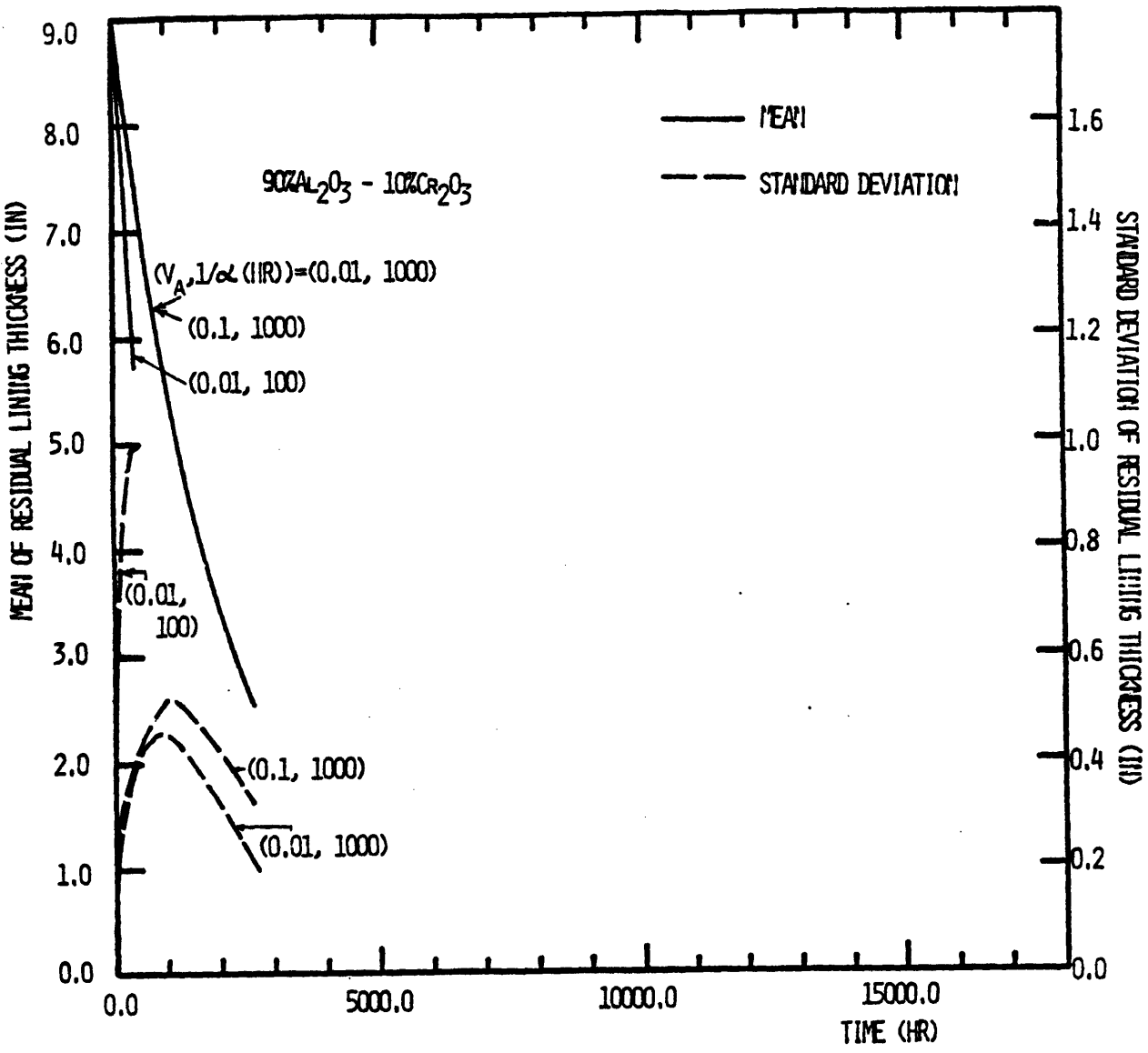

Figure 4.21 Mean and Standard Deviation of Lining Thickness vs. Time for 90% $A\ell_2O_3$ Refractory Lining (h = 1.0 Btu/ hr-in^2-^{o}F, T_1 = 3000^{o}F)

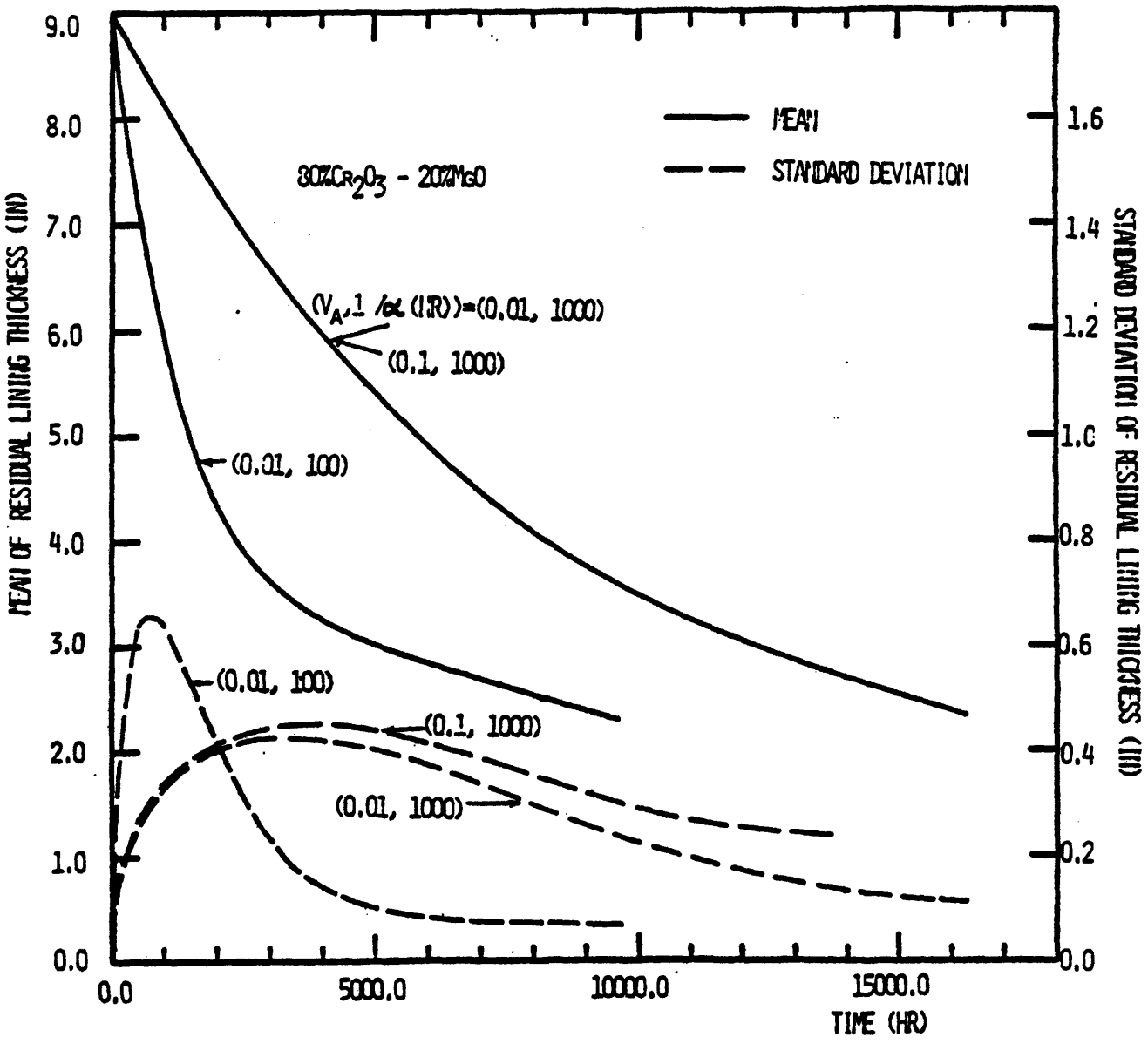

Figure 4.22 Mean and Standard Deviation of Lining Thickness vs. Time for 80% Cr_2O_3 Refractory Lining ($h \doteq 1.0$ Btu/hr-in^2-$^\circ$F, $T_1 = 3000^\circ$F)

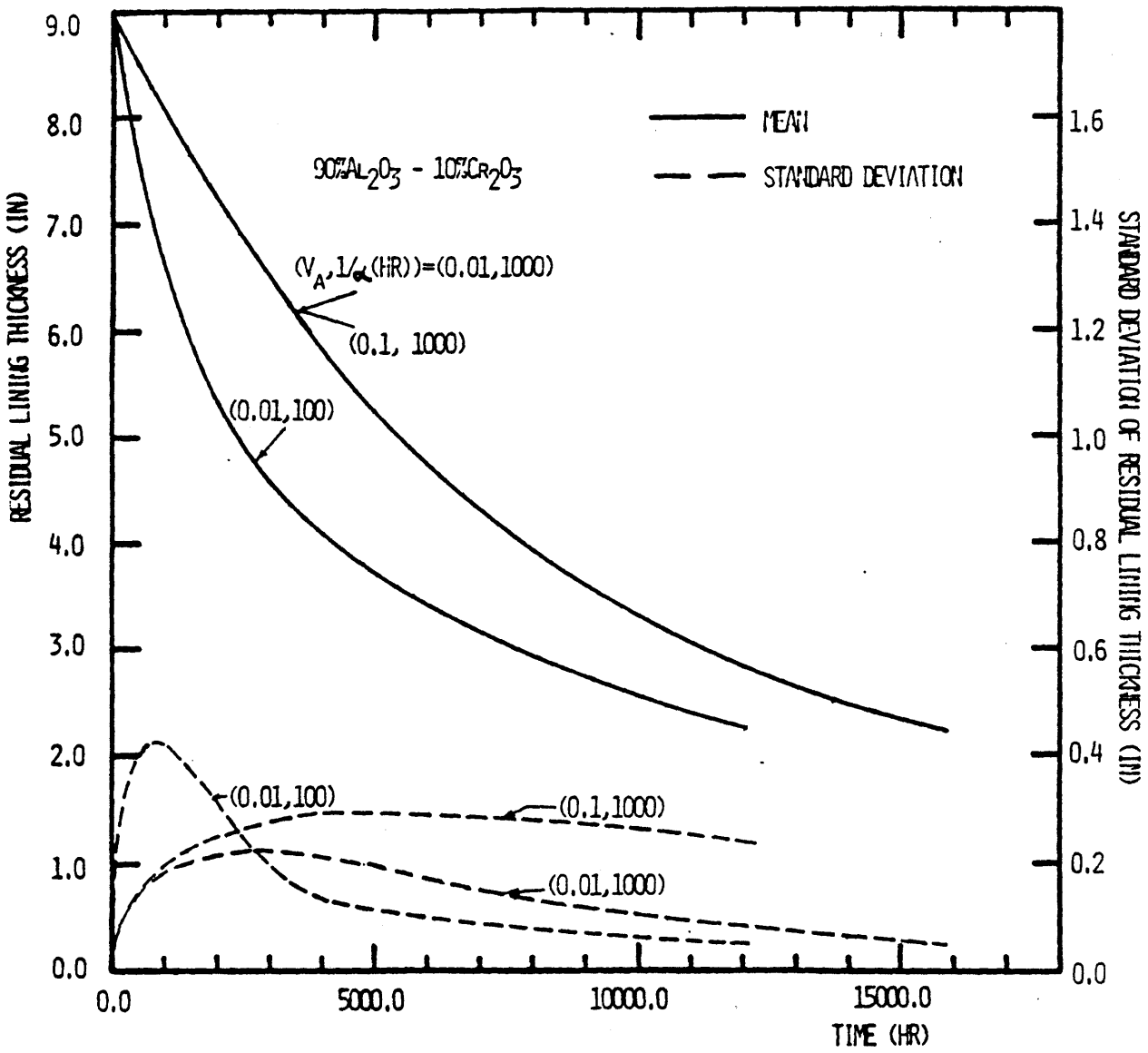

Figure 4.23 Mean and Standard Deviation of Lining Thickness vs. Time for 90% $A\ell_2O_3$ Refractory Lining (h = 1.0 Btu/ hr-in^2-^{o}F, T_1 = 2800^{o}F)

refractory to reduce the depth of slag penetration and to minimize the material deterioration if penetrated by slag, or structurally reinforcing (in the radial direction of) the refractory -at least, in the near field of hot face).

(2) The uncertainty of residual lining thickness during the final stage of lining life (say, when the lining is less than 3" thick) is primarily contributed by uncertainty on the dissolution rate, or in A .

(3) During the final stage of the lining life the uncertainty of the lining thickness tends to be smaller than during intermediate stage. This is the result of lower hot face temperature in this stage, which in turn reduces the corrosion rate and its dispersion.

§4.5 APPROXIMATE MODEL

The model in Eq. (4.15) is in the form of a nonlinear differential equation and requires numerical methods to be solved. A simplified approximate method based on Taylor series expansion can be formulated which results in a differential equation with analytical solution. This method includes

(1) approximating the first term on the right hand side of Eq. (4.15) by Taylor series expansion about the initial lining thickness Y_0 , i.e.,

$$A\ \mathrm{Exp}\left(-B\left(\frac{1}{T_H(Y)} - \frac{1}{Y_0}\right)\right) \cong \sum_{k=0}^{n} a_k (Y-Y_0)^k + \text{higher order terms} \quad (4.20)$$

(2) replacing the spalling process with a continuous process; i.e., replacing $D_p\,[t_{i-1},t_i] \rightarrow D_p(t) = D_p(Y(t))$, and

$$\delta[t_i] \rightarrow \frac{1}{\Delta t} \quad , \text{ where} \tag{4.21}$$

Δt is the interval between consecutive spalling events. If spalling is assumed to occur uniformly then Δt is independent of time.

(3) approxmating $D_p(Y)$ by a Taylor series expansion about the initial lining thickness Y_0 , i.e.,

$$D_p(Y) \cong \sum_{k=0}^{m} b_k(Y-Y_0)^k + \text{higher order terms} \tag{4.22}$$

Using Eqs. (4.20), (4.21) and (4.22) and under the assumption of constant spalling rate, Eq. (4.15) becomes

$$-\dot{Y} = \sum_{k=0}^{n} a_k(Y-Y_0)^k + \frac{1}{\Delta t} \sum_{k=0}^{m} b_k(Y-Y_0)^k \tag{4.23}$$

Eq. (4.23) can be easily solved, especially when the order of the approximation is low, i.e., the integers n and m are small.

Examples are given, which use the approximate model in Eq. (4.23) for the cases shown in Fig. 4.15. Linear (first order) approximation ($n = m = 1$) and quadratic second order approximation ($n = m = 2$) are used. The approximated evolution of lining thickness in time for the cases of Fig. 4.15 are shown in Fig. 4.24. It is found that for a broad range of parameter, the second order approximation is sufficiently accurate.

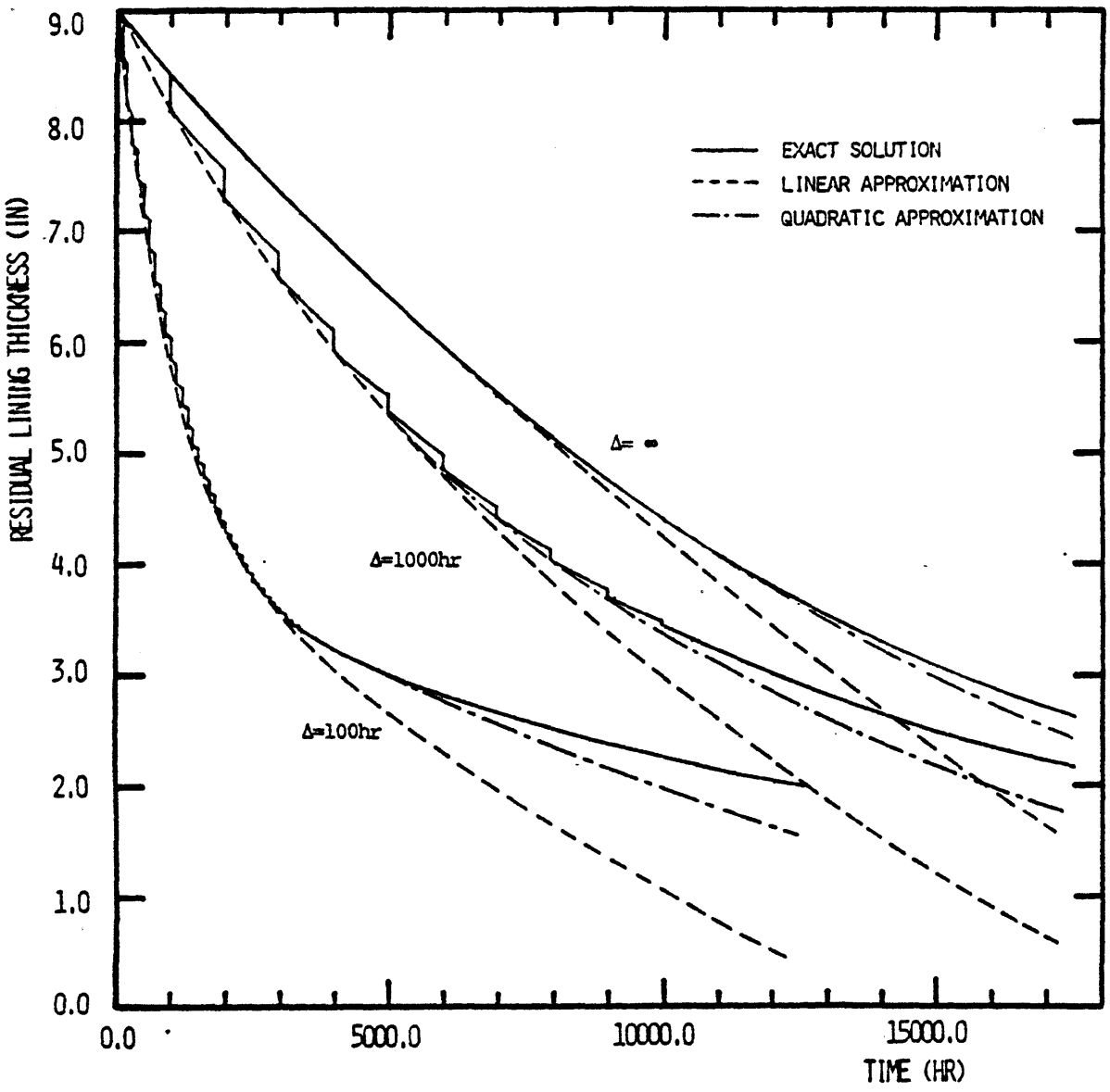

Figure 4.24 Comparison of Lining Thickness Predictions from Approximate Model and Exact Model

CHAPTER 5

THERMOMECHANICAL ANALYSIS OF LINING SYSTEMS BY THE FINITE ELEMENT METHOD

§5.1 INTRODUCTION

The Finite Element Method has been recognized as a powerful numerical technique for solving continuum problems. In the finite element method, the actual body is represented as an assemblage of subdivisions called finite elements. These elements are interconnected at specific points which are called nodes or nodal points. The nodes usually lie on the element boundaries. The variation of the field variables (such as displacement, stress, or temperature) inside a finite element can be approximated by a simple function. These approximating functions (called interpolating functions) are defined in terms of the values of the field variables at the nodes. When the field equations are written for the discretized finite-element model, the unknowns are the nodal values of the field variables. By solving the discretized field equations, which are generally in the form of matrix equations, the nodal values of the field variables are obtained. Once these quantities are known, the approximating functions define the field variables through the entire body.

Different approaches have been proposed to construct the discrete field equations, such as the direct approach, the weighted residual

approach, and variational methods. [8,71,93]. In the last method, the finite element analysis is interpreted as an approximate means for solving a variational problems if the physical or engineering problem can be stated in variational forms.

The general procedure of the variational finite element method is composed of the following steps:

(1) For a specific problem, a function π is defined in terms of the unknown vector $\underset{\sim}{u}$ which includes all unknown field variables, i.e.,

$$\pi = \int_{\Omega} F(\underset{\sim}{u})\, d\Omega + \int_{\Gamma} G(\underset{\sim}{u})\, d\Gamma \tag{5.1}$$

where F and G are specified operators associated with the domain Ω and the boundary Γ, respectively.

(2) The unknown vector $\underset{\sim}{u}$ is such that π is stationary, i.e.,

$$\delta\pi\Big|_{\underset{\sim}{u}} = 0 \tag{5.2}$$

(3) The domain is discretized into a number of finite elements (in the sense that each element has a finite size), as shown in Fig. 5.1, and each element has a certain number of nodes.

(4) For each element i, a set of interpolating functions $\underset{\sim}{N}^i$ is introduced, which produces an approximate to the unknown vector $\underset{\sim}{u}^i$ by its value at the element nodes, $\underset{\sim}{u}^i{}_n$,

$$\underset{\sim}{u}^i = \underset{\sim}{N}^i(\underset{\sim}{x})\ \underset{\sim}{u}^i{}_n \tag{5.3}$$

where $\underset{\sim}{x}$ is the general coordinate of the system, superscript i is associated with the i^{th} element, and subscript n means nodal quantity.

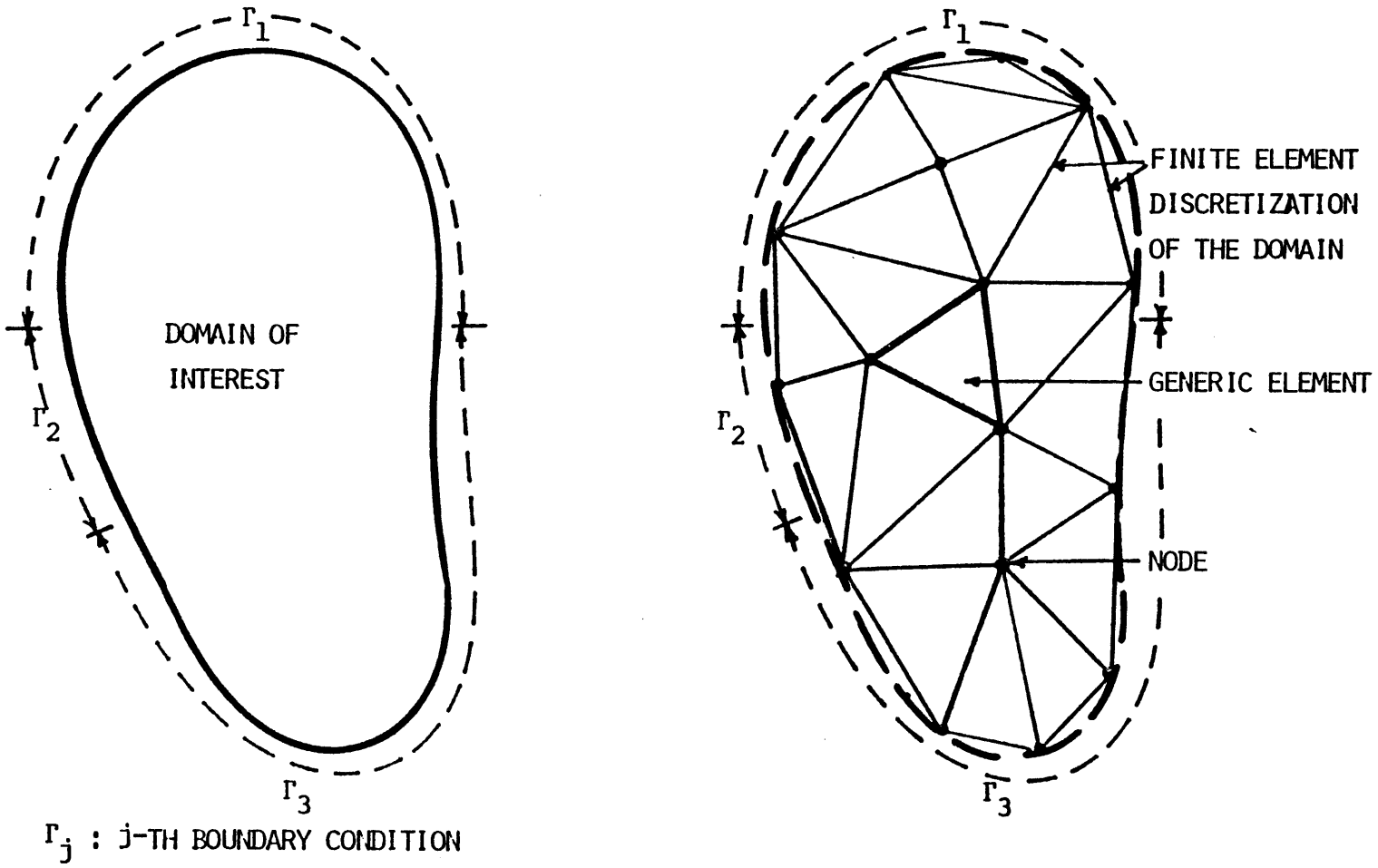

Figure 5.1 Finite Element Representation of Domain of Interest in A Field Problem

For all elements in the domain,

$$\underset{\sim}{u} = \sum_{i} \underset{\sim}{N}^{i} \underset{\sim}{u}_{n}^{i} = \underset{\sim}{N} \underset{\sim}{u}_{n} \tag{5.4}$$

where $\underset{\sim}{u}_n$ is the unknown vector at all the nodes.

(5) Using Eqs. (5.1), (5.2) and (5.4), one can write

$$\delta\pi = \frac{\partial \pi}{\partial \underset{\sim}{u}_{n}} \delta \underset{\sim}{u}_{n} = 0 \tag{5.5}$$

which is valid for any variation $\delta \underset{\sim}{u}_n$ only when

$$\frac{\partial \pi}{\partial \underset{\sim}{u}_{n}} = 0 \tag{5.6}$$

Typically, this condition can be written explicitly as

$$\frac{\partial \pi}{\partial \underset{\sim}{u}_{n}} = \underline{\underline{K}} \underset{\sim}{u}_{n} + \underset{\sim}{f} = 0 \tag{5.7}$$

(6) The vector $\underset{\sim}{u}_n$ is found by solving Eq. (5.7). Therefore, the field vector $\underset{\sim}{u}$ at any point in the domain can be approximated through Eq. (5.4).

For the present study of the thermomechanical behavior of refractory lining, the field problems encountered include the heat transfer problem and the stress analysis problem. The following features should be also included:

(1) The interaction between heat transfer and resulting stress; specifically, the temperature distribution can cause thermal stresses, and conversely the stress distribution changes the thermophysical properties of the material and the thermal boundary conditions;

(2) The behavior of the mortar-refractory joint interface, including joint failure, stress redistribution, and joint closing;

(3) The modification of material behavior and structural geometry due to corrosion effects, such as slag penetration, material degradation, and spalling process; and

(4) Nonlinear, time and temperature dependent material properties.

In what follows, the general finite element formulations for heat transfer and stress analysis (including creep analysis) are presented. Then, the incorporation of the interaction between heat transfer and stress is discussed. Verification tests of the developed methodology and of the computer program are performed when necessary. In the last two sections, the model of joint behavior and the effects of slag corrosion on material behavior and structural geometry, i.e., slag penetration and spalling, are presented.

§5.2 TRANSIENT HEAT TRANSFER ANALYSIS

In a three-dimensional coordinate system (x,y,z) , the governing equation for the heat conduction in an infinitesimal body dx dy dz , based on the energy balance (without heat generation), can be written as [67]:

$$\frac{\partial}{\partial x}\left[k_x \frac{\partial T}{\partial x}\right] + \frac{\partial}{\partial x}\left[k_y \frac{\partial T}{\partial x}\right] + \frac{\partial}{\partial x}\left[k_y \frac{\partial T}{\partial z}\right] = \rho C_p \frac{\partial T}{\partial z} \qquad (5.8)$$

where k_x, k_y, k_z = thermal conductivity in the x,y,z, directions

T = temperature of the body

ρ = density of the material

C_p = specific heat of the material

t = time

Since this differential equation is of second order in x,y,z and first order in time, two boundary conditions and one initial condition need to be specified. Possible boundary conditions are:

(1) prescribed temperature on boundary Γ_1

$$T(x,y,z,t) = \bar{T}(x,y,z) \quad \text{for} \quad t > 0 \quad \text{on} \quad \Gamma_1 \tag{5.9}$$

(2) convection condition on boundary Γ_2

$$k_n \frac{\partial T}{\partial n} + h(T-T_\infty) = 0 \quad \text{on} \quad \Gamma_2 \tag{5.10}$$

where $\bar{T}$ = prescribed temperature,

k_n = thermal conductivity in the direction normal to the boundary Γ_2 ,

h = heat transfer coefficient of convection,

T_∞ = ambient temperature

Γ_1 = boundary on which temperature is specified,

Γ_2 = boundary on which the convective heat loss is specified.

The typical initial condition is

$$T(x,y,z,t = 0) = \bar{T}_0(x,y,z) \quad \text{in} \quad \Omega \tag{5.11}$$

where Ω = domain of the solid body.

This heat conduction problem can be stated in an equivalent variational form as

$$\pi = \iiint_{\Omega} \left[k_x\left(\frac{\partial T}{\partial x}\right)^2 + k_y\left(\frac{\partial T}{\partial y}\right)^2 + k_z\left(\frac{\partial T}{\partial z}\right)^2 + 2\rho C_p \frac{\partial T}{\partial t} T\right] d\Omega + \iint_{\Gamma_2} h(T-T_\infty)^2 \, d\Gamma \tag{5.12}$$

and the variational approach in solving the heat conduction problem is to find the value of T that satisfies

$$\left.\frac{d\pi}{dT}\right|_T = 0 \tag{5.13}$$

In the finite element analysis, the domain Ω is divided into E finite elements with M nodes each and an interpolating function is assumed for each element i, which relates the temperature T^i in the element to its values at the nodes $\underset{\sim}{T}^i_n$,

$$T^i(x,y,z) = \underset{\sim}{N}(x,y,z)\ \underset{\sim}{T}^i_n(t) \tag{5.14}$$

where $$\underset{\sim}{T}^i_n = \begin{bmatrix} T_1(t) \\ T_2(t) \\ \vdots \\ T_M(t) \end{bmatrix}$$

and $$\underset{\sim}{N}(x,y,z) = [N_1(x,y,z),\ N_2(x,y,z),\ldots N_M(x,y,z)]$$

Incorporating Eq. (5.14) into Eqs. (5.12) and (5.13), one finds the field equation for the system in the form [71]

$$\underline{C}\,\dot{\underset{\sim}{T}}_n + \underline{k}_s\,\underset{\sim}{T}_n = \underset{\sim}{P} \tag{5.15}$$

where $\underline{C}$ = heat capacity matrix

$$= \sum_{i=1}^{E} [\underline{C}^i]$$

$\underline{k}_s$ = heat conductivity matrix

$$= ([\underline{K_s}^i]_1 + [K_s^i]_2)$$

$\underset{\sim}{P}$ = heat supply vector

$$= \sum_{i=1}^{E} \underset{\sim}{p}^i$$

$$[\underline{c}^i] = [c^i_{m\ell}]$$

$$= \left[\iiint_{\Omega_i} C_p\, N_m N_\ell \, d\Omega\right] \qquad (m,\ell = 1,2,3)$$

$$[\underline{k_s}^i]_1 = [k^i_{m\ell}]_1 \qquad (m,\ell = 1,2,3)$$

$$= \left[\iiint_{\Omega^i} k_x \frac{\partial N_m}{\partial x}\frac{\partial N_\ell}{\partial x} + k_y \frac{\partial N_m}{\partial y}\frac{\partial N_\ell}{\partial y} + k_z \frac{\partial N_m}{\partial z}\frac{\partial N_\ell}{\partial z} d\Omega\right]_1$$

$$[\underline{k}^i_s]_2 = [k^i_{m\ell}]_2$$

$$= \left[\iint_{\Gamma_{2i}} h\, N_m N_\ell \, d\Gamma\right] \qquad (m,\ell=1,2,3)$$

$$\underset{\sim}{p}^i = [P^i_m]$$

$$= \left[\iint_{\Gamma_{2i}} h\, T_\infty\, N_m \, d\Gamma\right] \qquad (m = 1,2,3)$$

$\underset{\sim}{T}_n$ = vector of the nodal temperature unknowns of the system.

Integration of the function in Eq. (5.15) can be accomplished by numerical techniques which approximate integral with weighted summation at discrete points (see e.g., Fig. 5.2).

Eq. (5.15) is time dependent and can be solved by means of a finite difference scheme. This scheme discretizes the time axis into a number of time steps with time interval Δt , and then approximates the first derivative of $\underset{\sim}{T}_n$ as

$$\dot{\underset{\sim}{T}}_{n,j} = \frac{d\underset{\sim}{T}}{dt}\bigg|_{t_j} = \frac{\underset{\sim}{T}_{n,j} - \underset{\sim}{T}_{n,j-1}}{\Delta t} \tag{5.16}$$

where $\underset{\sim}{T}_{n,j}$ = temperature vector at time step j.

Thus, Eq. (5.15) can be written as

$$\underline{C}\,\frac{\underset{\sim}{T}_{n,j} - \underset{\sim}{T}_{n,j-1}}{\Delta t} + \underline{k}_s \underset{\sim}{T}_{n,j} = \underset{\sim}{P}_j \tag{5.17}$$

or

$$\underline{C}\,\underset{\sim}{T}_{n,j} + \Delta t\,\underline{k}_s\,\underset{\sim}{T}_{n,j} = \Delta t\,\underset{\sim}{P}_j + \underline{C}\,\underset{\sim}{T}_{n,j-1} \tag{5.18}$$

which satisfies the initial condition $\underset{\sim}{T}_{n,0} = \underset{\sim}{\bar{T}}_n(t = 0)$.

Eq. (5.18) can be written in a standard form

$$\underline{k}\,\underset{\sim}{T}_{n,j} = \underset{\sim}{f}_j \tag{5.19}$$

where $\underline{k} = (\underline{C} + \Delta t\,\underline{k}_s)$ and

$$\underset{\sim}{f}_j = (\Delta t\,\underset{\sim}{P}_j + \underline{C}\,\underset{\sim}{T}_{n,j-1})$$

Notice that $\underline{C}$ and $\underline{k}_s$ are temperature (state) dependent in general, since the conductivity and heat capacity of a material may be temperature dependent. By using an incremental finite-difference

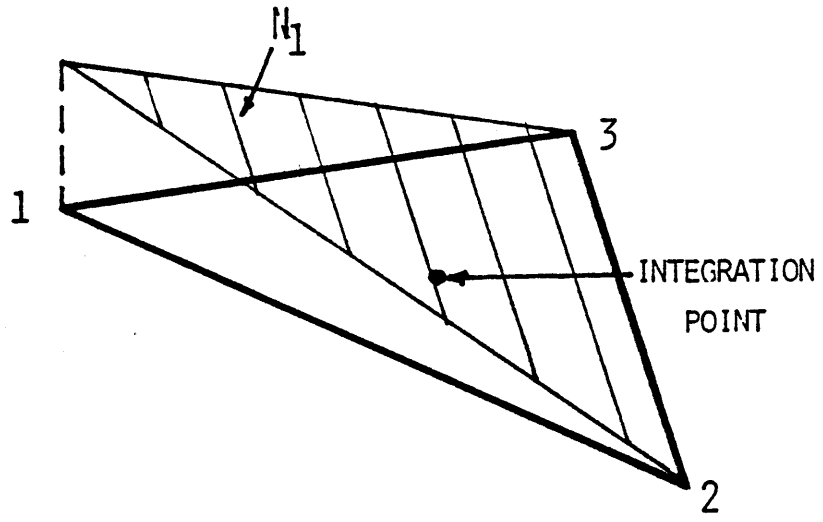

Figure 5.2 Triangular Element with Linear Interpolating Function

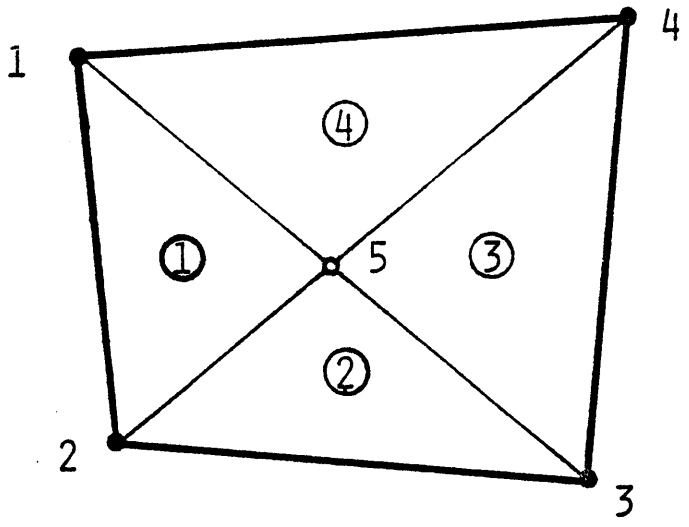

Figure 5.3 Four-Triangle Quadrilaterial Element (1 ~ 5: nodal number; ①~④: element number)

scheme, one may assume $\underline{C}$ and $\underline{k}_s$ in Eq. (5.18) to be constant in each step. As a result, $\underline{k}$ in Eq. 5.19 is also constant in each step. Updating of $\underline{C}$ and $\underline{k}_s$ is necessary when a new state is calculated. For highly nonlinear dependence of $\underline{C}$ and $\underline{k}_s$ on temperature, small time steps should be chosen, or alternatively, for large time steps, one should use iteration schemes [8,71].

By solving Eq. (5.19) with the boundary conditions over Γ_1, one can obtain the temperatures at all nodes in the system, and through the interpolation functions, the temperature at any point in Ω.

For the lining system of the present analysis, the variation of the temperature in the vertical direction, say the z direction, is negligible. Hence, only a two-dimensional thermal analysis is needed. If one uses triangular elements with three nodes each, as shown in Fig. 5.2, Eqs. (5.12) to (5.15) can be explicitly expressed in terms of the element geometry [71]. Results are summzarized in Appendix III.

The two-dimensional heat transfer analysis has been implemented into a finite element program for Thermomechanical Analysis of Refractory Linings (TARL), in which the four-triangle quadrilateral element (Fig. 5.3) is used. The four-triangle quadrilateral element is composed of four triangular elements of the type mentioned above. The center node is condensed before system assemblage [33], so that the number of simultaneous equations involved in Eq. (5.15) is reduced, and the problem of skewness generally encountered when using triangular elements is avoided. A brief description about program TARL is given in Appendix IV.

The heat transfer program has been used in the following examples:

(1) The first example is the one-dimensional transient heat-transfer problem shown in Fig. 5.4, with given geometry, boundary conditions and material properties. Fig. 5.6 shows the variation of temperature with time at x = 0, 1 and 4 (see definitions of X in Fig. 5.4) from the analytical solution (solid line) [72] and from the finite element program (dashed line) using the mesh shown in Figure 5.5. Good agreement between two predictions is found.

(2) The second example is a two-dimensional transient heat-transfer problem shown in Fig. 5.7 with analytical solution from Ref. 67. The associated finite element model and discretized mesh are shown in Fig. 5.8. In Fig. 5.9 the temperature variations at points A, B and C in Fig. 5.7 are shown for both the analytical and the finite element solution. Again, the numerical results are satisfactory.

§5.3 STRESS ANALYSIS (DISPLACEMENT METHOD)

The finite element displacement method is based on the principle of minimum potential energy by which a displacement state satisfying compatibility and boundary conditions, and the associated stress satisfying equilibrium make the total potential energy minimum. The functional which is minimized is

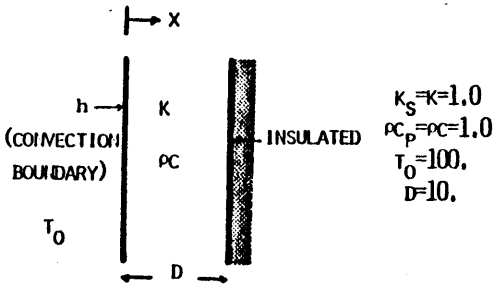

Figure 5.4 One-Dimensional Heat Transfer Problem Through a Wall

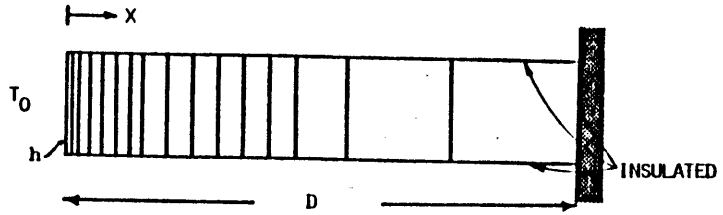

Figure 5.5 Finite Element Representation of the Wall

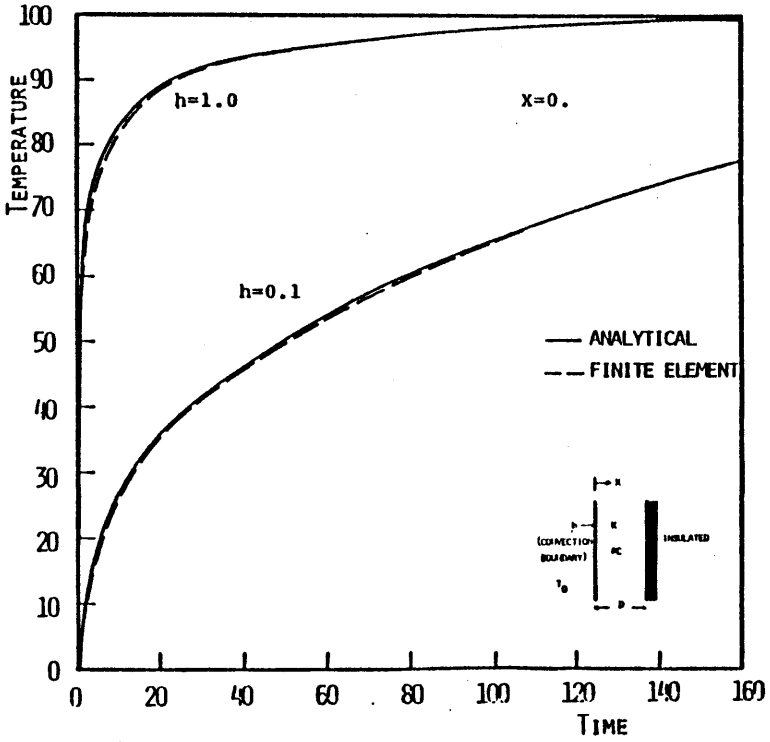

Figure 5.6 (a) Comparison of Predictions for the Temperature History (x = 0.0)

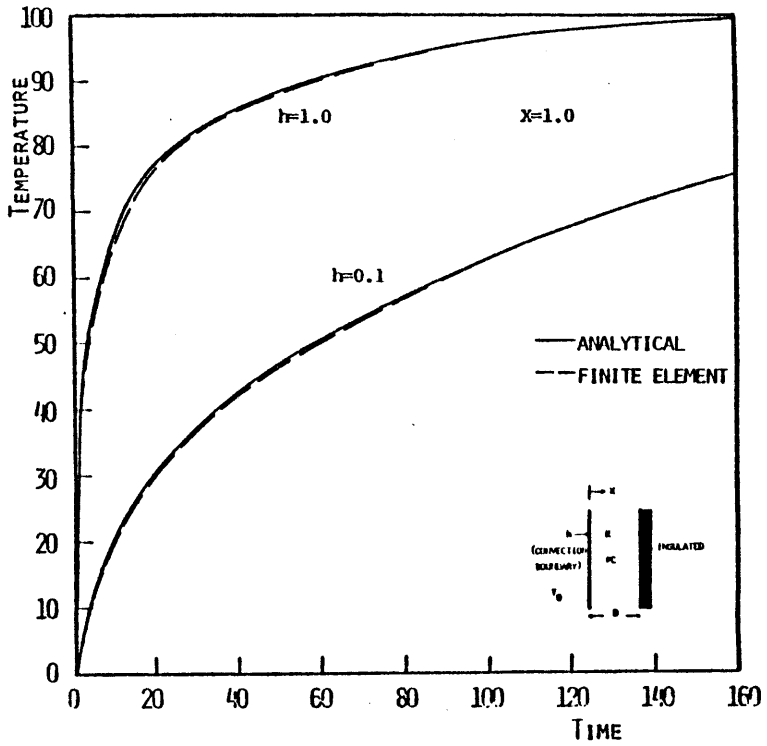

Figure 5.6 (b) Comparison of Predictions for the Temperature History (x = 1.0)

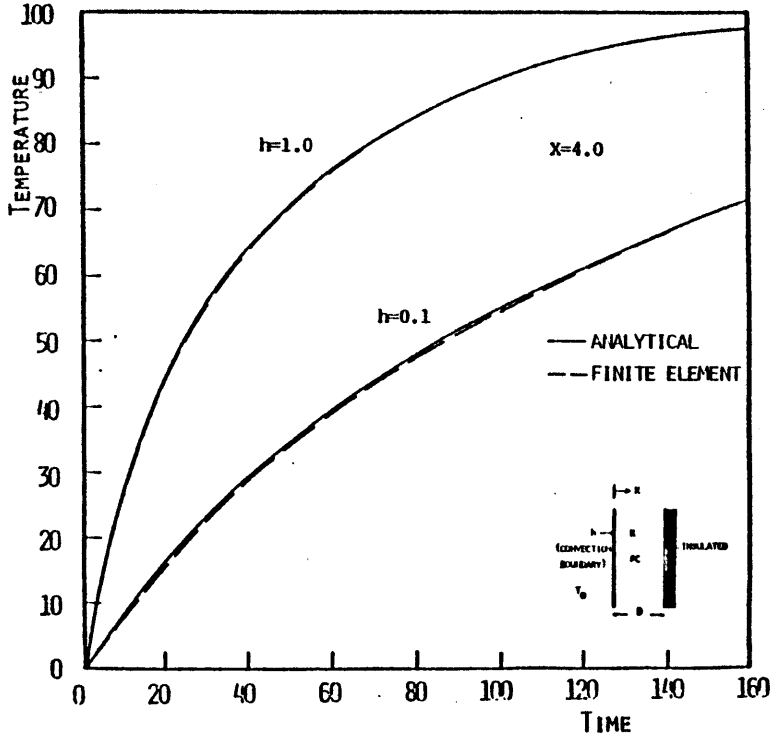

Figure 5.6 (c) Comparison of Predictions for the Temperature History (x = 4.0)

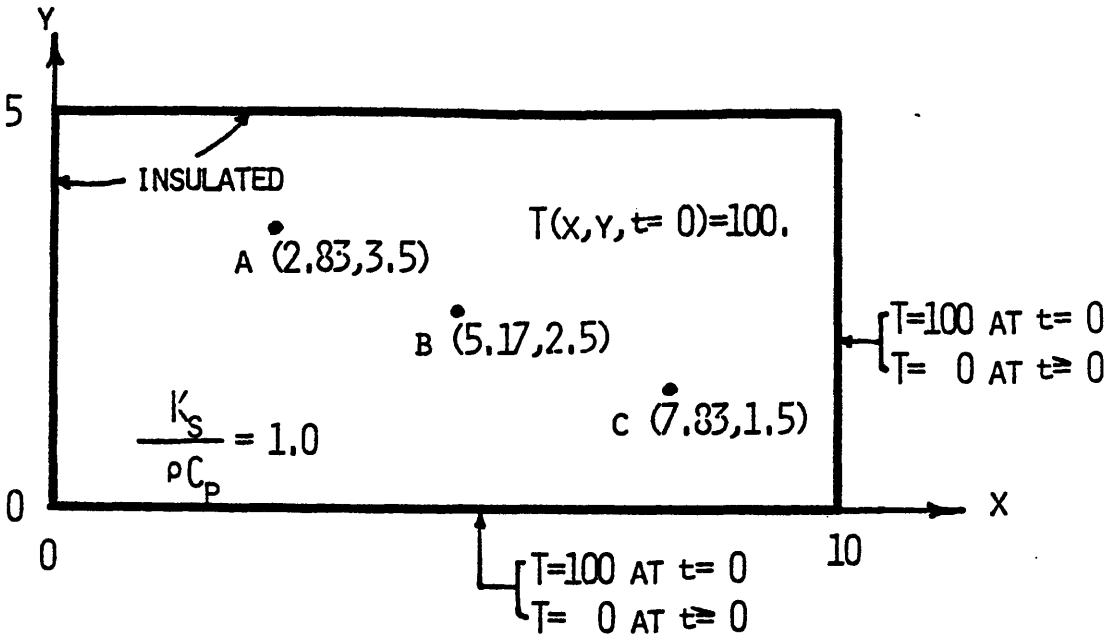

Figure 5.7 Two-Dimensional Heat Transfer Problem Through a Plate

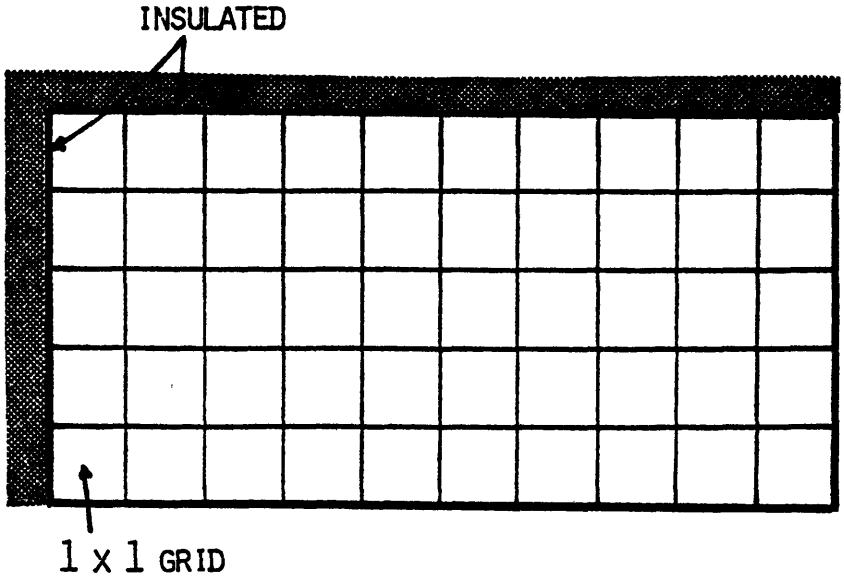

Figure 5.8 Finite Element Representation of the Plate

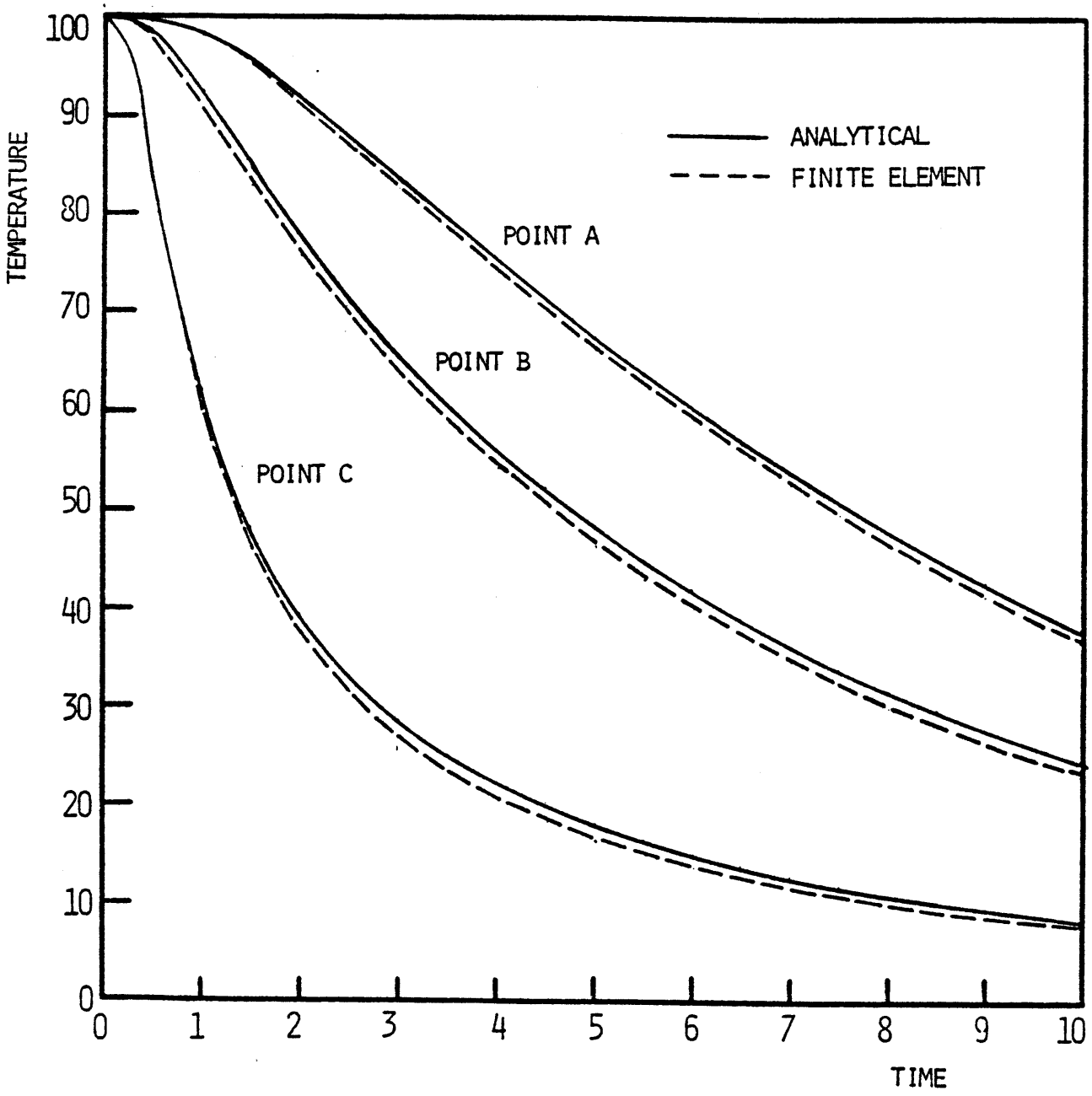

Figure 5.9 Comparison of Predictions for the Temperature History

$$\pi = \iiint_{\Omega} \left(\frac{1}{2} (\underset{\sim}{\varepsilon}-\underset{\sim}{\varepsilon}_0)' \ \underline{D} \ (\underset{\sim}{\varepsilon}-\underset{\sim}{\varepsilon}_0) - \underset{\sim}{u}' \underset{\sim}{b}\right) d\Omega$$

$$- \iint_{\Gamma_2} \underset{\sim}{u}' \underset{\sim}{f}_T \, d\Gamma - \sum_{\ell} F_{\ell} u_{\ell} \qquad (5.20)$$

where $\underset{\sim}{\varepsilon}$ = strain vector

$= \{\varepsilon_{xx} \ \varepsilon_{yy} \ \varepsilon_{zz} \ \gamma_{xy} \ \gamma_{yz} \ \gamma_{zx}\}'$,

$\underset{\sim}{\varepsilon}_0$ = initial strain vector associated with $\underset{\sim}{\varepsilon}$,

$\underline{D}$ = material rigidity matrix, $\underset{\sim}{\sigma} = \underline{D}(\underset{\sim}{\varepsilon}-\underset{\sim}{\varepsilon}_0)$,

$\underset{\sim}{\sigma}$ = stress vector

$= \{\sigma_{xx} \ \sigma_{yy} \ \sigma_{zz} \ \tau_{xy} \ \tau_{yz} \ \tau_{zx}\}'$,

$\underset{\sim}{u}$ = displacement vector

$= \{u_x \ u_y \ u_z\}'$,

$\underset{\sim}{b}$ = body force vector

$= \{b_x \ b_y \ b_z\}'$,

$\underset{\sim}{f}_T$ = boundary traction vector

$= \{f_{Tx} \ f_{Ty} \ f_{T2}\}'$

F_{ℓ} = concentrated load at point ℓ ,

Γ_2 = boundary on which the traction is specified,

The prime symbol denotes transformation.

In the finite element displacement method, the continuous domain Ω is divided into a number of elements, each element having M nodes. An interpolating function $\underline{N}^i$ is then assumed for each element i, which relates the displacements $\underset{\sim}{u}^i$ in the i^{th} element to the displacement of the nodes $\underset{\sim}{u}^i{}_n$:

$$\underset{\sim}{u}^i(x,y,z) = \underline{N}^i(x,y,z)\underset{\sim}{u}^i_n \tag{5.21}$$

where $\underset{\sim}{u}^i_n = [\{\underset{\sim}{u}\}_1 \ \{\underset{\sim}{u}\}_2 \ . \ . \ . \ \{\underset{\sim}{u}\}_M]'$

$$\{\underset{\sim}{u}\}_j = \{u_x \ u_y \ u_z\}_j \qquad (j = 1 \sim M)$$

and $\underline{N}^i$ = interpolating function of element i

$$= [\{\underset{\sim}{N}(x,y,z)\}_1 \ \{\underset{\sim}{N}(x,y,z)\}_2 . \ . \ . \ [\{\underset{\sim}{N}(x,y,z)\}_M]^i$$

$$\{\underset{\sim}{N}\}_j = [N_x(x,y,z) \ \ N_y(x,y,z) \ \ N_z(x,y,z)]'_j \qquad (j = 1 \sim M)$$

The strain in a generic element i, $\underset{\sim}{\varepsilon}^i$, can be related to the nodal displacement $\underset{\sim}{u}^i_n$ by the strain-displacement definition:

$$\underset{\sim}{\varepsilon}^i = \underline{B}^i \underset{\sim}{u}^i_n \tag{5.22}$$

$$\underline{B}^i = \begin{bmatrix} \frac{\partial}{\partial x} & 0 & 0 \\ 0 & \frac{\partial}{\partial y} & 0 \\ 0 & 0 & \frac{\partial}{\partial z} \\ \frac{\partial}{\partial y} & \frac{\partial}{\partial x} & 0 \\ 0 & \frac{\partial}{\partial z} & \frac{\partial}{\partial y} \\ \frac{\partial}{\partial z} & 0 & \frac{\partial}{\partial x} \end{bmatrix} \underline{N}^i$$

Incorporating Eqs. (5.21) and (5.22) into Eq. (5.20) and minimizing Eq. (5.20) with respect to the nodal displacements, one obtains:

$$\sum_{i=1}^{E} \left(\iiint_{\Omega_i} \underline{B}^{i\,\prime} \underline{D}^i \underline{B}^i \, d\Omega \ \underset{\sim}{u}^i - \left(\iiint_{\Omega_i} \underline{N}^{i\,\prime} (\underset{\sim}{b}^i + \underline{D}^i \underset{\sim}{\varepsilon}^i_o) d\Omega - \iint_{\Gamma_2} \underline{N}^{i\,\prime} \underset{\sim}{f}_T^{\,i} \, d\Gamma \right) \right)$$

$$- \underset{\sim}{F} = 0 \tag{5.23}$$

where $\underset{\sim}{F}$ = nodal force vector, including all concentrated load F_ℓ. The index i is associated with element i.

Eq. (5.23) can be written in the general form of Eq. (5.7) as

$$\underline{k}\,\underset{\sim}{u}_n = \underset{\sim}{f} \tag{5.24}$$

where $\underline{k}$ = system assemblage stiffness matrix

$$= \sum_{i=1}^{E} \left(\iiint_{\Omega_i} \underline{B}^{i\,\prime}\, \underline{D}^i\, \underline{B}^i \, d\Omega \right)$$

$\underset{\sim}{u}_n$ = system assemblage nodal displacement vector

$$\underset{\sim}{f} = \left(\sum_{i=1}^{E} \left(\iiint_{\Omega_i} \underline{N}^{i\,\prime} \left(\underset{\sim}{b}^i + \underline{D}^i \underset{\sim}{\varepsilon}_o^i \right) d\Omega + \iint_{\Gamma_2} \underline{N}^{i\,\prime}\, \underset{\sim}{f}_T^{\,i}\, d\Gamma \right) \right) + \underset{\sim}{F}$$

By solving Eq. (5.24) with the prescribed boundary displacement on Γ_1, one can get the displacement vector $\underset{\sim}{u}_n$. For each element i, the strain and stress at any point can be obtained from Eq. (5.22) and from

$$\begin{aligned} \underset{\sim}{\sigma}^i &= \underline{D}^i (\underset{\sim}{\varepsilon}^i - \underset{\sim}{\varepsilon}_o^{\,i}) \\ &= \underline{D}^i \underline{B}^i \underset{\sim}{u}_n^i - \underline{D}^i \underset{\sim}{\varepsilon}_o^{\,i} \end{aligned} \tag{5.25}$$

Creep and material nonlinearities involved in the present study can be incorporated into the finite element formulation as follows:

(1) Creep: Creep is a time-dependent material behavior. In the finite element analysis, the time-marching scheme is usually used for the creep analysis. The time axis is

discretized into a number of steps with interval Δt . During each time interval, the stress in the body is assumed constant, and the incremental creep strain caused by such stress is evaluated through Eq. (3.60). This incremental creep strain can then be incorporated into Eq. (5.23) by treating it as an initial strain. The incremental stress in each step caused by the incremental creep strain and other general loading, such as those from material nonlinearity and thermal loadings, is added to the stress obtained at the end of the previous step.

(2) Material nonlinearity: The three basic solution schemes of nonlinear finite element problems are incremental procedures, iterative methods, and mixed procedures [8]. The choice of a specific scheme depends on the type of problem. For the present analysis, the loading is primarily caused by thermal strains and nonrecoverable creep which are very significant at high temperatures. For these reasons small time intervals should be used. Since the adoption of small time intervals generally results in small load increments, an incremental procedure is used. The basis of this procedure is the subdivision of the total load into a number of small load increments. The load is applied in increments and during the application of each increment the system equations, Eq. (5.24), are assumed to be linear; a fixed value of $\underline{k}$ in Eq. (5.24) is assumed during each time step, but $\underline{k}$ is allowed to have different values during different steps. The solution for each step gives an increment of the state variables (displacements,

strain, and stress). These state increments are accumulated to obtain the state of the system at any given time. Thus, the nonlinearity is essentially treated as piecewise linear.

In the present study, the two-dimensional stress analysis is performed in parallel with the two-dimensional heat transfer analysis. These analyses simplify the three-dimensional body by making assumptions in certain direction, say the z direction, such as plain stress, plain strain, and generalized plain strain. In plain stress analysis, the stress in the z-direction, σ_z , is assumed to be zero; in plain strain analysis, the strain in the z-direction, ε_z , is assumed to be zero; and in the generalized plain strain analysis, ε_z is assumed to be constant. Description of the two-dimensional finite element formulation with triangular elements can be found in most finite element books [e.g. 8,33,71].

Two-dimensional stress analysis has been implemented into the finite element program TARL, in which the quadrilateral elements mentioned in the previous section are used. The validity and accuracy of the program in predicting stress and strain distributions will be demonstrated in the next section.

§5.4 HEAT TRANSFER - STRESS RESULTANT INTERACTION

In the refactory lining systems, the thermal and mechanical behaviors are coupled. This coupling phenomenon has been incorporated in the present study through consideration of the following effects:

(1) Thermal stresses: temperature changes in a body cause volumetric changes through thermal expansion or shrinkage. This results in stresses due to either non-uniform volumetric change through the body or to boundary constraints.

(2) Stress-induced changes in the thermophysical properties of the body: excessive stresses in ceramic materials cause cracking and consequent modification of local heat transfer characteristics. The relative significance of such modification depends on he width of crack opening and the gas filling the cracks.

The finite element model of this interactive behavior is summarized in the following section.

§5.4.1 Thermal Expansion

Thermal expansion of a body is usually characterized by a "Coefficient of Thermal Expansion", α , which relates the thermal strain vectors increment, $\Delta\varepsilon$, to the temperature increment, ΔT , at any point in the body by

$$\Delta\underset{\sim}{\varepsilon} = [1\ 1\ 1\ 0\ 0\ 0]' \cdot \Delta T \cdot \alpha \qquad (5.26)$$

In the finite element analysis the thermal strains are usually treated as part of the initial strains. Namely, in Eq. (5.23) the initial strain vector $\underset{\sim}{\varepsilon}_0^i$ for element i can be taken as the sum of the initial strain vector in the system $(\underset{\sim}{\varepsilon}_{00}^i)$, the creep strain $(\underset{\sim}{\varepsilon}_{0c}^i)$, and the thermal strain $(\underset{\sim}{\varepsilon}_{0T}^i)$:

$$\underset{\sim}{\varepsilon}_o^i = \underset{\sim}{\varepsilon}_{oo}^i + \underset{\sim}{\varepsilon}_{oc}^i + \underset{\sim}{\varepsilon}_{oT}^i \qquad (5.27)$$

This scheme has been implemented into program TARL. In this repect, two problems were solved to verify the validity of the procedure in TARL:

(1) The first example intends to verify the accuracy of TARL in predicting the thermal stress over a cyclindrical wall (2-D analysis). The geometry and boundary conditions are shown in Fig. 5.10. Figs. 5.11 and 5.12 show the temperature profiles and stress distributions over the lining thickness according to the exact analytical solution [84] and the finite element prediction. Accurrate prediction are obtained from TARL.

(2) The second example is to verify (A) the creep model developed for refractory materials (§3.4), (B) the polynomial representation of thermal expansion (§3.2.3), (C) the time-independent mechanical model (§3.3), and (D) the thermomechanical analysis method. A high alumina (85% $A\ell_2O_3$) refractory brick is uniformly heated from 1000°C (1832°F) to 1450°C (2642°F) at a constant heating rate of 150°C/hr (270°F/hr) with the imposed constraint $\Delta\varepsilon_x$ as shown in Fig. 5.13 (a) and (b). The experimental measurement of the history of σ_x as reported by Sweeney and Cross [82,83] is shown in Fig. 5.13 (c) (solid line). Also shown in Fig. 5.13 (c) is the finite element prediction (dashed line) using the material models for high $A\ell_2O_3$ refractory bricks as described in Chapter 3. The agreement between the predicted and measured responses is satisfactory.

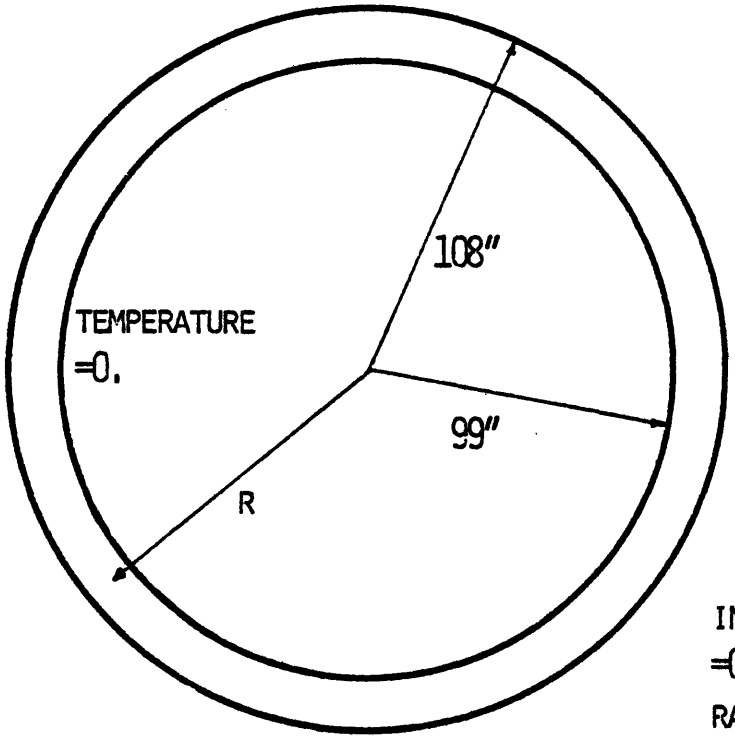

INITIAL TEMPERATURE
=0.
RATE OF TEMPERATURE
$=50^{o}F/HR$

GENERALIZED PLANE STRAIN WITH ZERO END FORCE

LINEAR ELASTIC CONSTITUTIVE MODEL

YOUNG'S MODULUS	$= 6.0 \times 10^{6}$ PSI
POISSON'S RATIO	$= 0.3$
COEFFICIENT OF THERMAL EXPANSION	$= 5.0 \times 10^{-6}\ {}^{o}F^{-1}$
THERMAL CONDUCTIVITY	$= 0.03$ BTU/HR-IN-^{o}F
DENSITY X SPECIFIC HEAT	$= 0.3$ BTU/IN^{3}-^{o}F

Figure 5.10 A Generalized Two-Dimensional Thermomechanical Problem through a Cyclindrical Wall

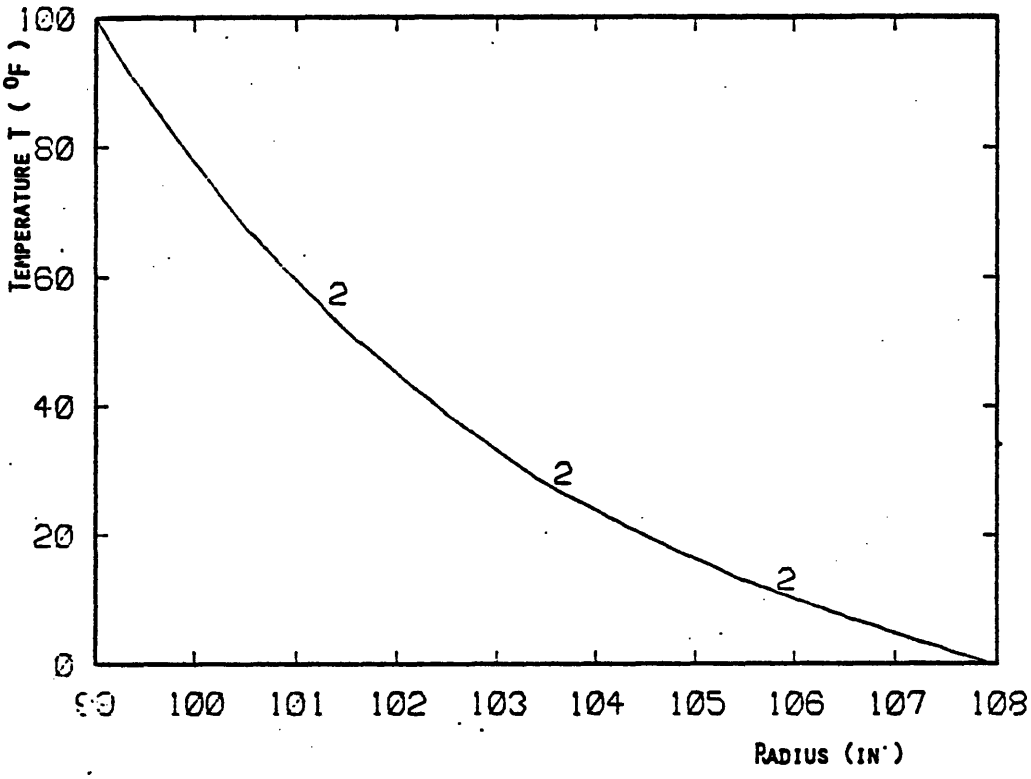

Figure 5.11 Temperature Distribution Though the Wall Thickness

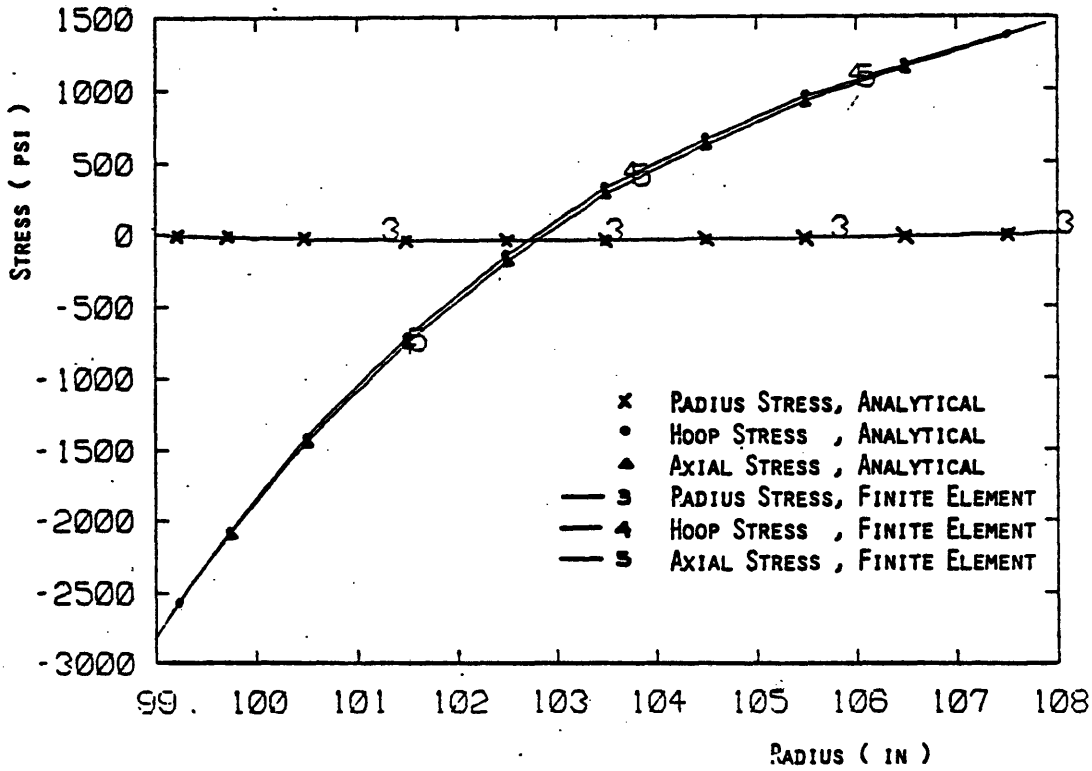

Figure 5.12 Comparison of Finite Element vs. Analytical Predictions for Stress Distribution

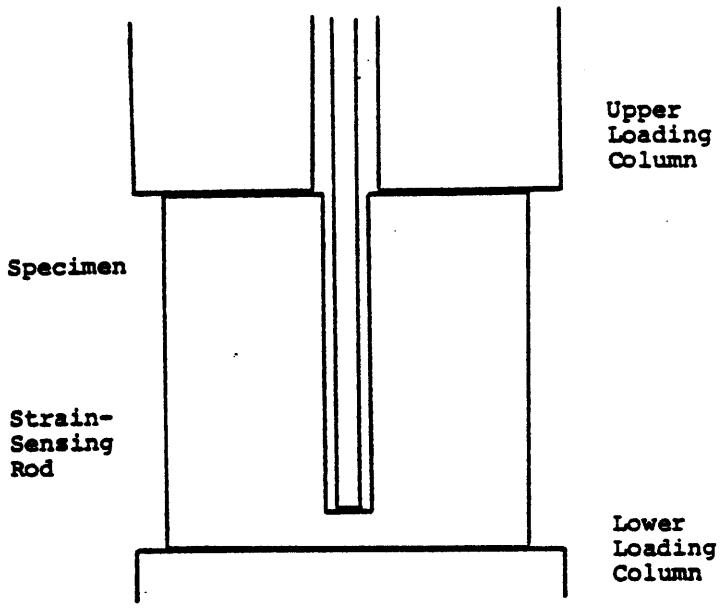

Figure 5.13 (a) Test Specimen and Test Conditions

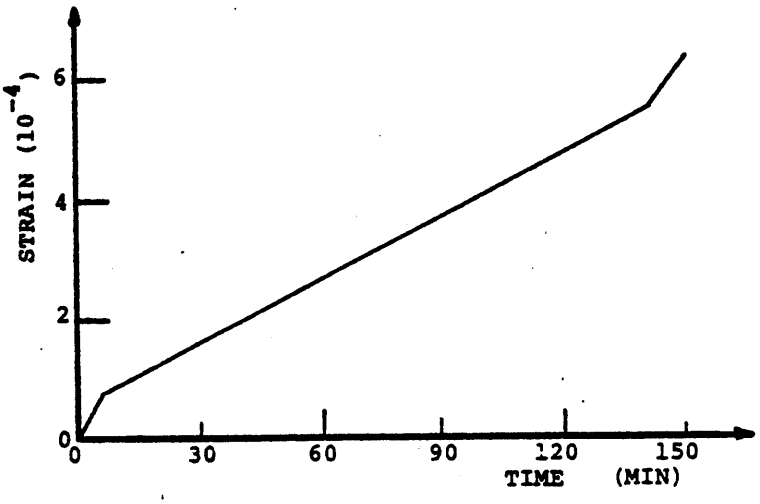

Figure 5.13 (b) History of Axial Strain

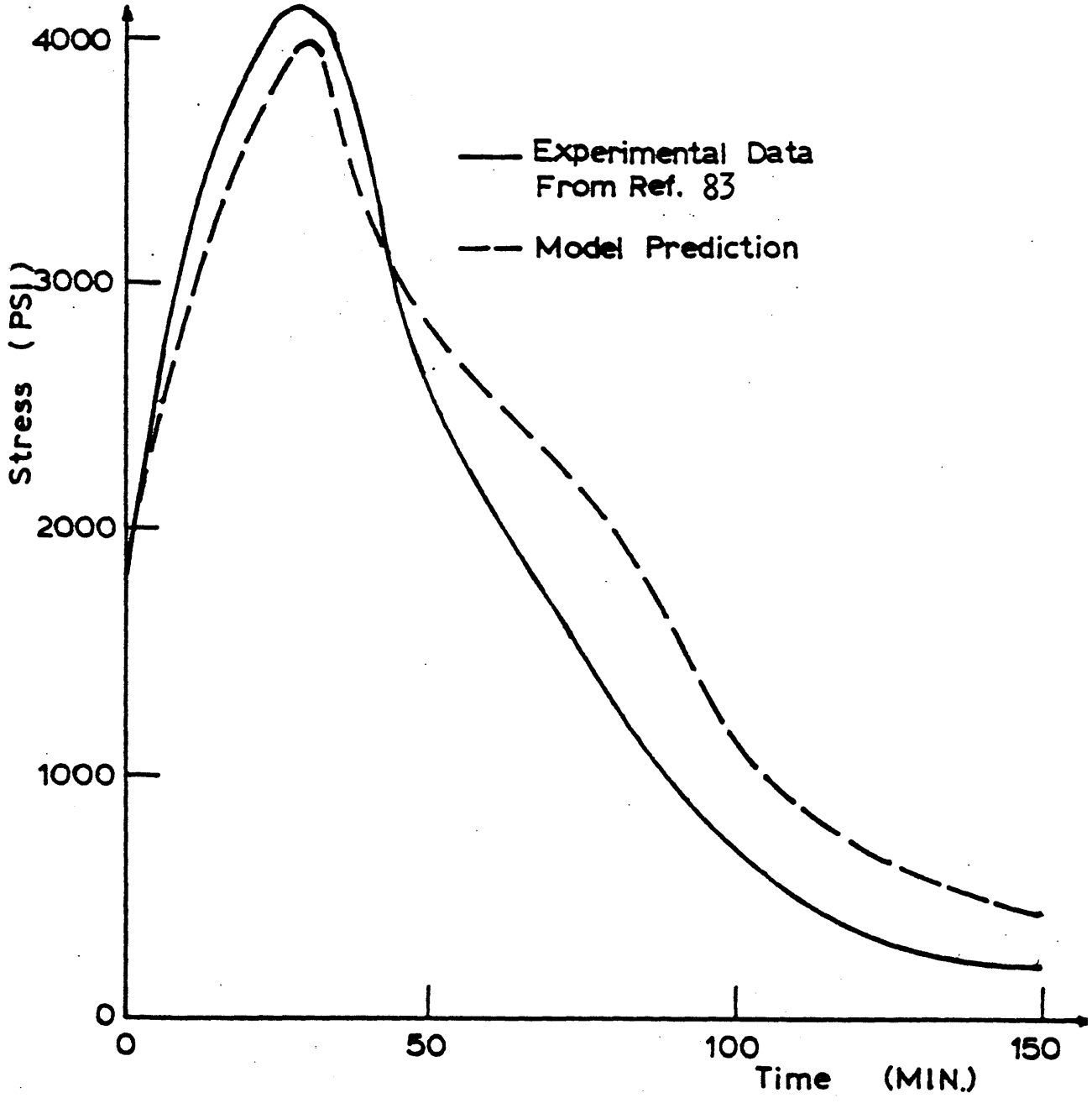

Figure 5.13 (c) Comparison of Model Prediction of Axial Stress History with Test Data

§5.4.2 Conductivity Model for Cracked Media

In the present heat transfer anlaysis, the uncracked two-dimensional medium is assumed to be isotropic, i.e., the thermal conductivity in the x-y Cartesian coordinate system is expressed by $k_x = k_y = k_s$, where k_s is the uncracked conductivity of the solid body. After the initiation of a crack, the local conductivity should be modified due to the formation of gaps by cracking, and the gas penetration.

In the two-dimensional finite element analysis, a material conductivity matrix is formed, which accounts for the conduction behavior of the area surrounding each integration point. When a crack is identified at any integration point, it is assumed that this crack is smeared through its associated area. Essentially, this cracked area can be represented as a porous medium with certain crack-density in terms of crack volume ratio, V_a , defined as the ratio of the volume introduced by the crack opening to the total volume in a medium with uniformly-distributed cracks. The value of V_a can be calculated as a function of the post-cracking strain ε_a (see Fig. 5.14):

$$V_a = \frac{\varepsilon_a}{1+\varepsilon_a} \tag{5.28}$$

Modification of the material conductivity matrix in a 2-D finite element analysis can be made by the following procedure:

(1) Based on the crack orientation, set up the local coordinate system x' - y' , as shown in Fig. 5.15.

(2) Construct the material conductivity matrix $\underline{D}_{UC}$ in Eq. (A.3.6) for an uncracked medium in the local coordinate system (x',y')

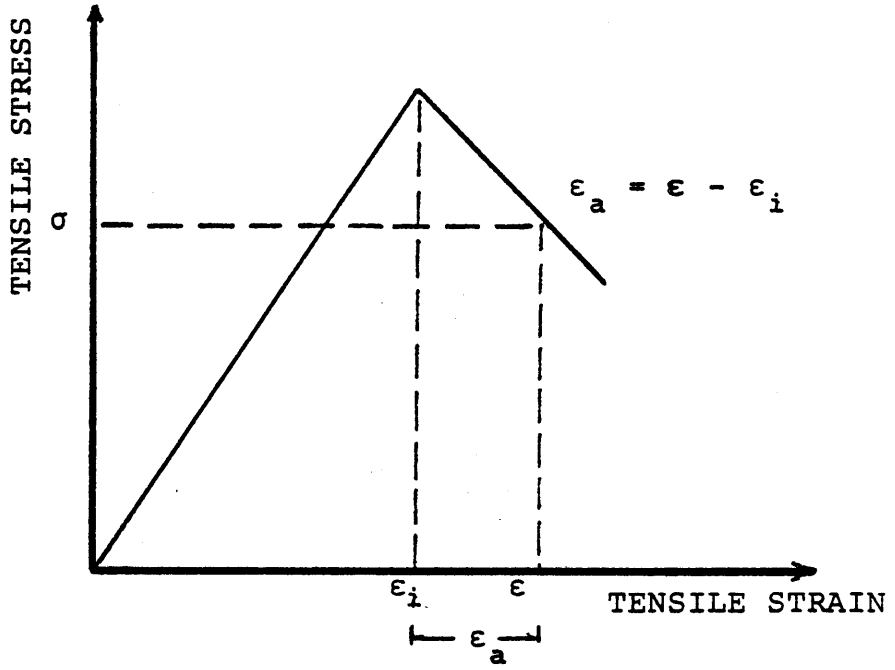

Figure 5.14 Post-Cracking Strain in Tensile Stress-Strain Curve

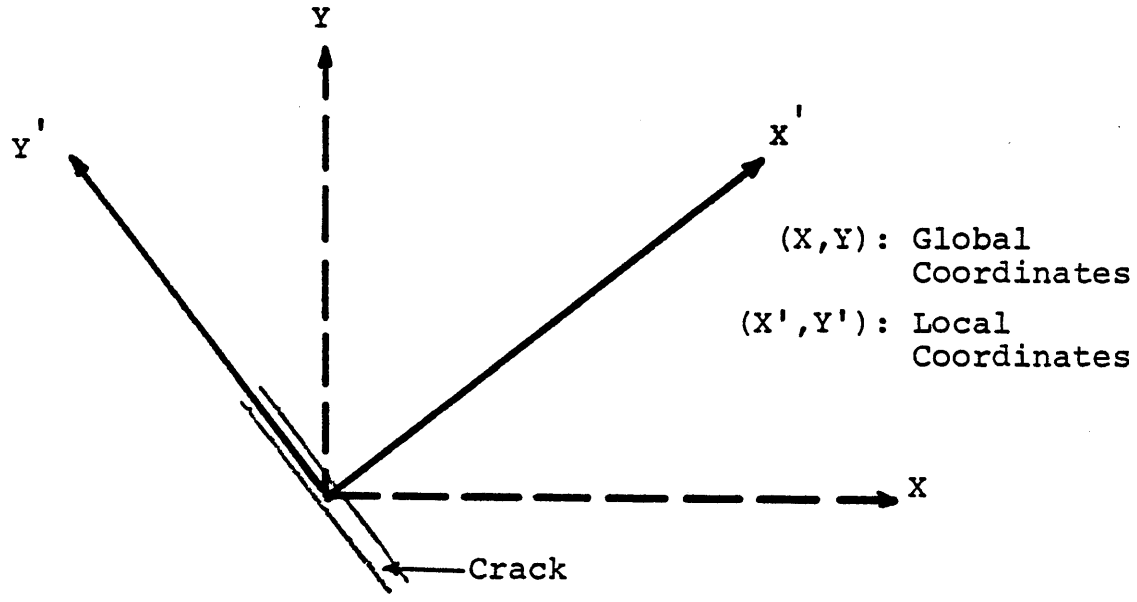

Figure 5.15 Coordinate System Associated with Crack Orientations

$$\underline{D}_{UC} = \begin{bmatrix} k_s & 0 \\ 0 & k_s \end{bmatrix} \tag{5.29}$$

(3) Modify $\underline{D}_{UC}$ to incorporate the crack effects by assuming that cracking affects the conductivity in the direction perpendicular to the crack orientation, but not in the parallel direction.

$$\underline{D}^* = \begin{bmatrix} k_{CR} & 0 \\ 0 & k_s \end{bmatrix} \tag{5.30}$$

(4) Transform $\underline{D}^*$ to the global coordinate system (x,y) to obtain the updated material conductivity matrix $\underline{D}_{CR}$

$$\underline{D}_{CR} = \underline{H}' \, \underline{D}^* \, \underline{H} \tag{5.31}$$

where $\underline{H}$ is the coordinate transformation matrix

$$\underline{H} = \begin{bmatrix} \cos\theta & \sin\theta \\ -\sin\theta & \cos\theta \end{bmatrix} \tag{5.32}$$

and θ is the angle between the x and the x' axes.

Many models have been proposed to evaluate k_{CR} for a porous material with distributed cracks. An overview is given by Tseng [88]. For the present study, in conjunction with the thermomechanical finite element analysis, Maxwell's model [58] based on potential theory is used:

$$k_{CR} = \frac{2k_s + k_g - 2V_a(k_s - k_g)}{2k_s + k_g - V_a(k_s - k_g)} \, k_s \qquad (5.33)$$

where k_{CR} = the local effective conductivity over the crack

k_g = the conductivity of the gas filling the crack

In the brick lining system it is frequently found that some cracks occur behind and parallel to the hot face of the lining. The existence of such cracks creates thermal barriers which modifiy the temperature distribution in different ways. To demonstrate the influence of such cracks on the temperature distribution in the lining, a 4" × 9" brick has been studied. The brick has a pair of symmetry edge cracks. By symmetry, only half of this brick with an edge crack needs to be analyed. This is shown in Fig. 5.16. The two sides of the half-brick perpendicular to the hot face are assumed to be perfectly insulated due to symmetry. The brick is initially at a constant reference temperature, say 0°F, and a step temperature at time t = 0 is prescribed on the hot face, equal to 1000°F, while the cold face temperature is kept at 0°F . In addition, the following parameters are used:

k_s = 0.1 Btu/hr-in-°F

ρc_p = 0.01 Btu/in^3-°F

k_g/k_s = 0.1

V_a = 0.5

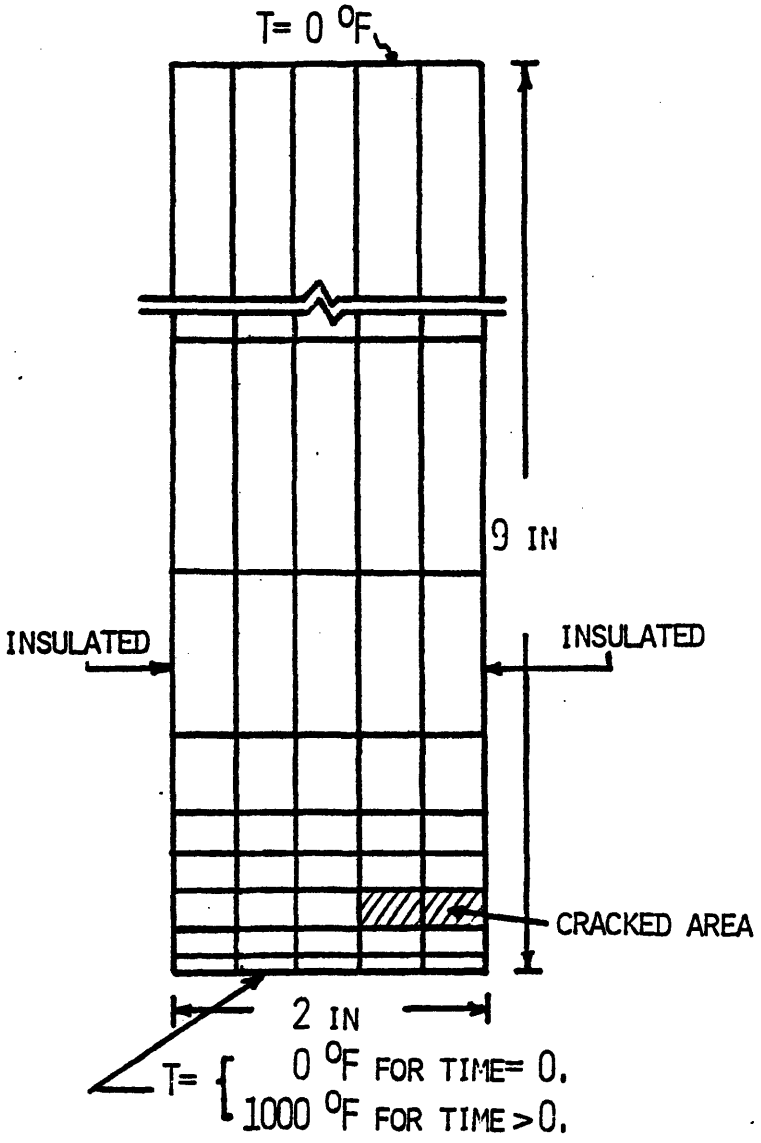

Figure 5.16 Rectangular Brick with Edge Cracked Zone

In Figs. 5.17(a) and (b), the temperature contour lines around the cracked area at time = 0.2 and 1.0 hours (dashed lines) are shown. Also shown in these figures are the temperature contour lines (solid lines) under same thermal boundary conditions, but without any cracked area. These results show that the crack considered here introduces a thermal barrier which increases the thermal gradient behind the crack, and accordingly, increases the stresses around the crack. This implies that cracking is a progressive process, in the sense that cracking introduces heat accumulation around the crack, which leads to increases of the thermal gradient and thus of the stresses around crack, resulting in further cracking.

§5.5 BRICK-MORTAR JOINT MODEL

In the brick-lined lining system, the bricks are bonded together by joint material, such as mortar. Under external loads these joints will fail when the stresses in the interface exceed the bonding strength of the joint. Joint failure directly affects the lining system behavior, because it modifies the boundary conditions for the bricks and results in a less stable lining system.

§5.5.1 Joint Strength

Joint strength is usually represented by a failure envelope as a function of the stress state over the joint interface. Fig. 5.18 shows a typical joint-strength envelope in terms of the normal stress (σ_n) and the shear stress (τ) in the joint interface. In general, this envelope is a nonlinear function of σ_n and τ. However, in the present analysis,

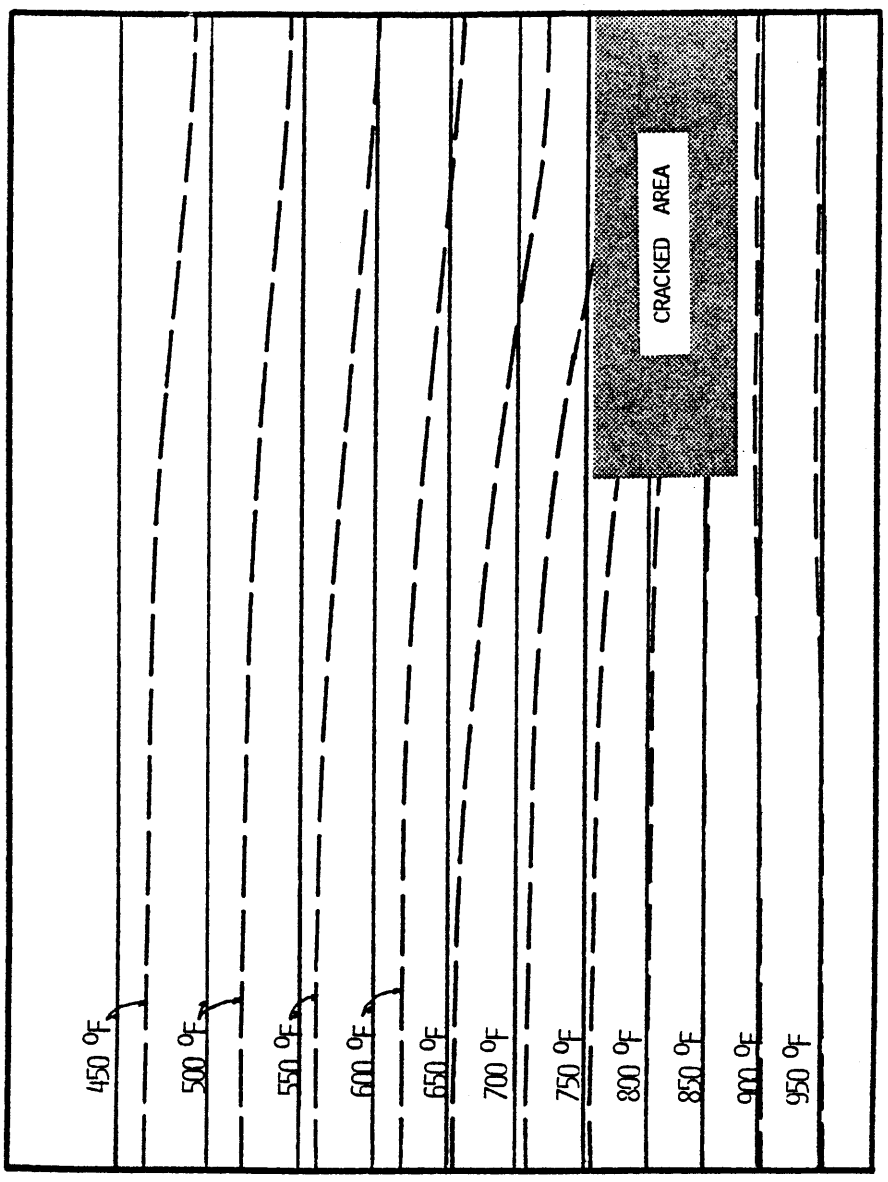

Figure 5.17 (a) Temperature Contours at 0.2 hour

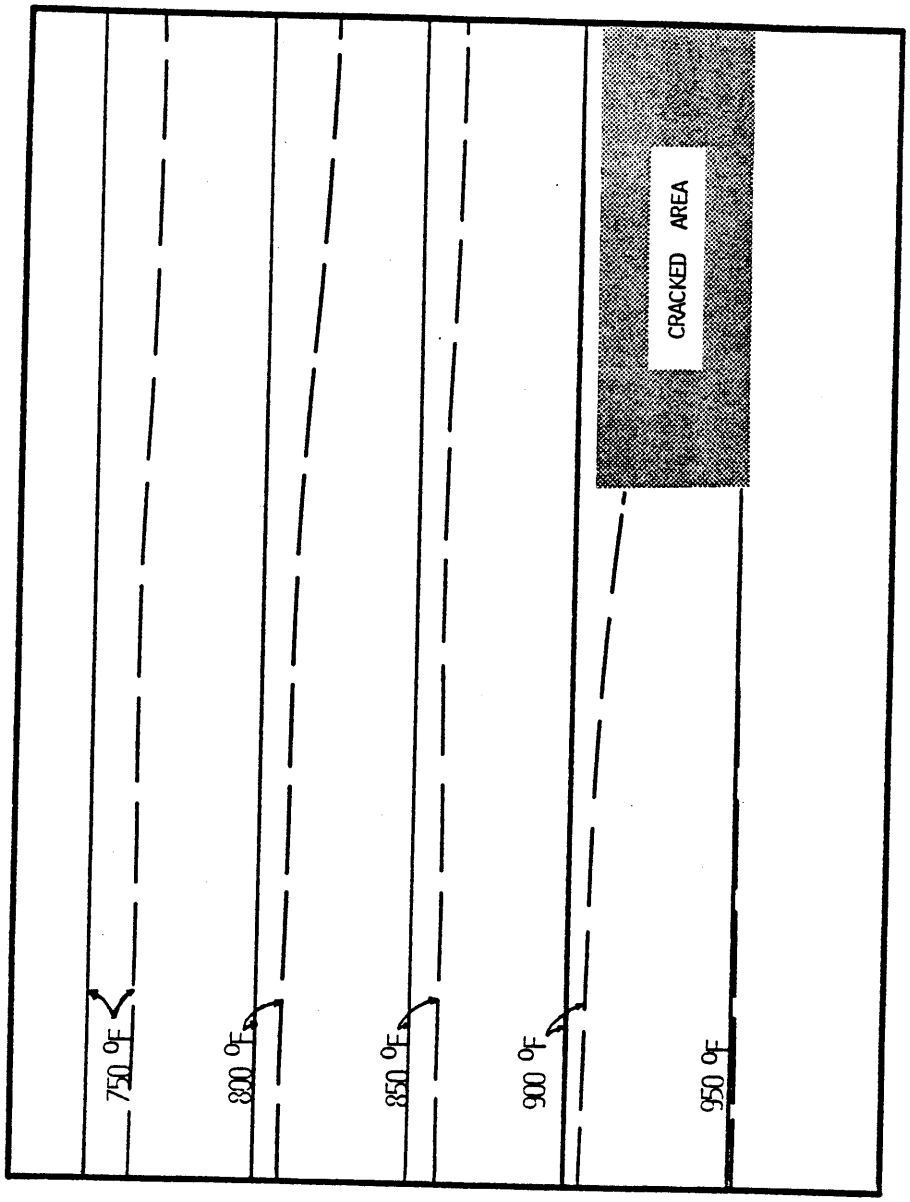

Figure 5.17 (b) Temperature Contours at 1.0 hour

a linear approximation is used due to insufficient test data. When the stress state on the joint interface exceeds the envelope, joint failure occurs, by which the cohesive and the tensile strength are reduced (in the limit, to zero) and the jont-strength envelope shrinks as shown in Fig. 5.18.

§5.5.2 Joint Elements

In the finite element representation, the joint is modeled as a physical element with a small thickness (joint element). The stresses in the joint element are checked against the joint-strength envelope during the loading process. Once the stress state in the joint element reaches or exceeds the joint-strength envelope, failure is assumed to occur. At this point

(1) the joint-strength envelope is modified to reflect the loss of adhesion after failure;

(2) the excessive stresses in the joint element relative to the modified joint-strength envelope are released to the surrounding elements; and

(3) the stiffness of the joint element is taken to be zero, if the joint occurs in the combination of tension and shear stress; otherwise, the stiffness is left unchanged.

During loading a previously opened joint may close again. This can be detected through the strain in the joint; that is, when the strain in a joint element becomes zero or negative, the joint is closed and the stiffness of the joint element is reassigned. However, the failure envelope at this stage is that one associated with the post-failure.

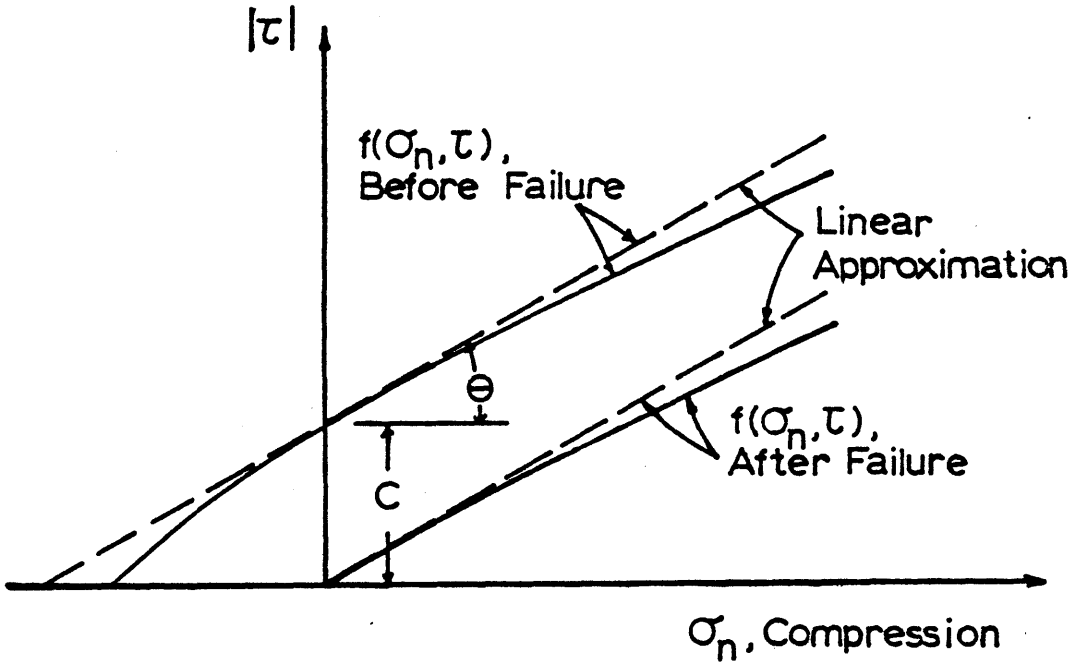

Figure 5.18 Failure Envelope for Joint Interface

§5.6 SLAG PENETRATION AND SPALLING

§5.6.1 Slag Penetration

At high temperatures the hot face of the refractory lining in slagging gasifier is subjected to slag penetration. It has been shown in Chapter 4 that slag penetration can cause significant changes in the strength and stiffness of the refractories. Such changes may be attributed to spalling and erosion, and, must be accounted for in the thermomechanical analysis. In the finite element approach this is done as follows:

(1) The critical temperature (T_c) of slag penetration is determined for each slag-refractory system (see details in Chapter 4).

(2) The temperature profile through the lining is found through heat transfer analysis.

(3) The results of (1) and (2) are combined to determine the depth of lining from the hot face the temperature of which exceeds T_c . This depth is taken to be the zone of slag penetration.

(4) The material properties of the finite elements associated with the zone of slag penetration are modified.

§5.6.2 Spalling

Spalling contributes to mass loss from the hot face of the lining. During the transient heating process, spalling is primarily caused by failure of the lining material. Failure may be of compressive type, tensile type, or a combination of the two. If any principal strain associated with this failure is large than zero (tension), a crack can be assumed to occur perpendicular to this strain direction. Spalling results if such failed material is not confined.

In the finite element analysis, material failure can be detected at integration points. If the finite elements associated with these points are well confined in any tensile principal strain direction (e.g., element groups 2 in Fig. 5.19), the constitutive behavior at these points is one of the softening type. However, if the elements are not confined in the direction of principal tensile strain, e.g. elements near the hot face with cracks parallel to that face (groups 1 in Fig. 5.19), the area associated with these points is assumed to be spalled. After spalling, the following modifications are made at the associated integration points: (1) thermal conductivity is set to infinity, and (2) the strength and stiffness is set to zero (Fig. 5.19).

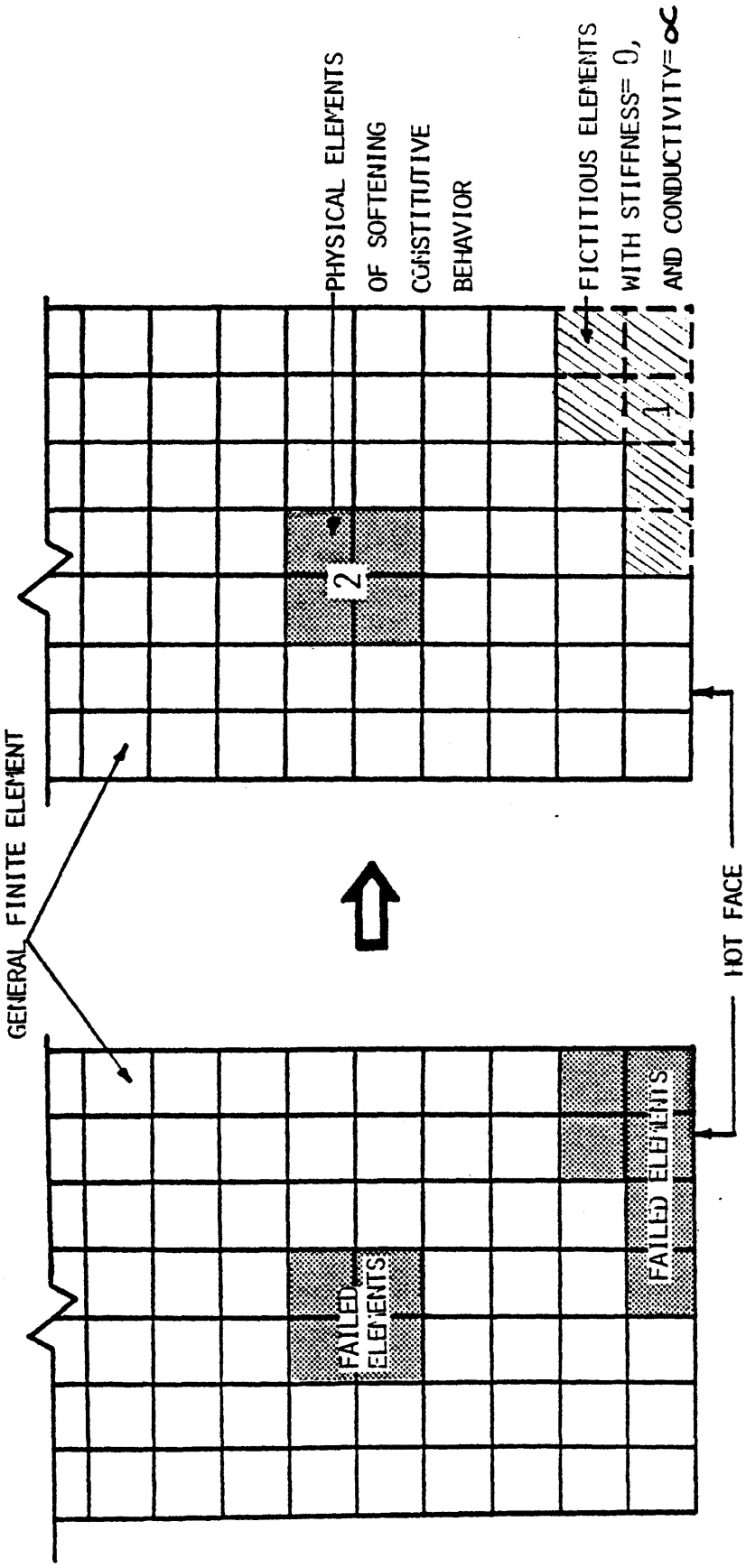

Figure 5.19 Finite Element Modeling of Failure Zone

CHAPTER 6

LINING BEHAVIOR IN TRANSIENT HEATING PROCESS

§6.1 INTRODUCTION

Thermal attack and corrosion attack are two major destructive factors to the refractory linings in slagging gasifiers. The long-term corrosion behavior of the slag-refractory systems was studied in Chapter 4. In this chapter the thermomechanical behavior of the refractory linings in high-temperature gasification environments is studied. Emphasis is on the thermomechanical behavior of the linings in transient heating process. During this process the linings experience most severe structural condition, due to the high temperature gradient through the linings, the resulting high stresses, and the less effective stress relaxation due to creep. Such a severe condition may result in the cracking/crushing and spalling of the lining materials, failure of the joint materials, and accordingly, the loss of integrity of the lining systems (Fig. 6.1).

Conceptually, the abovementioned damages in a lining system during the transient heating process can be minimized if a proper design is achieved and an optimal operating scheme is adopted. With these in mind, the primary objective of this chapter is to assess the effects of various governing design variables and operational schemes on the thermomechanical behavior of refractory lining systems in slagging

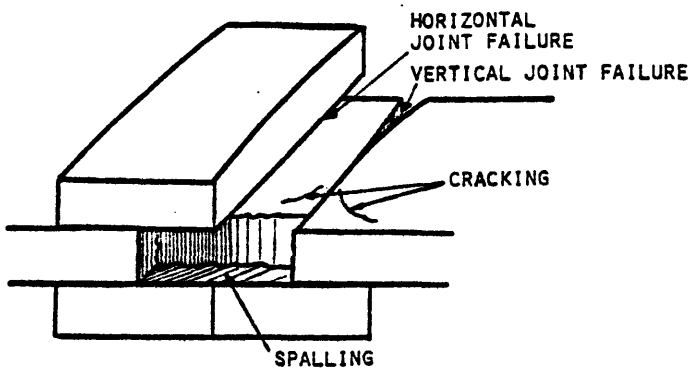

Figure 6.1 Potential Failure Modes in a Lining System

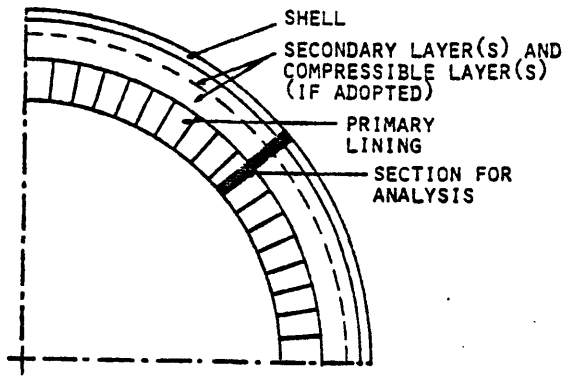

Figure 6.2 Schematic of a Refractory Lining System

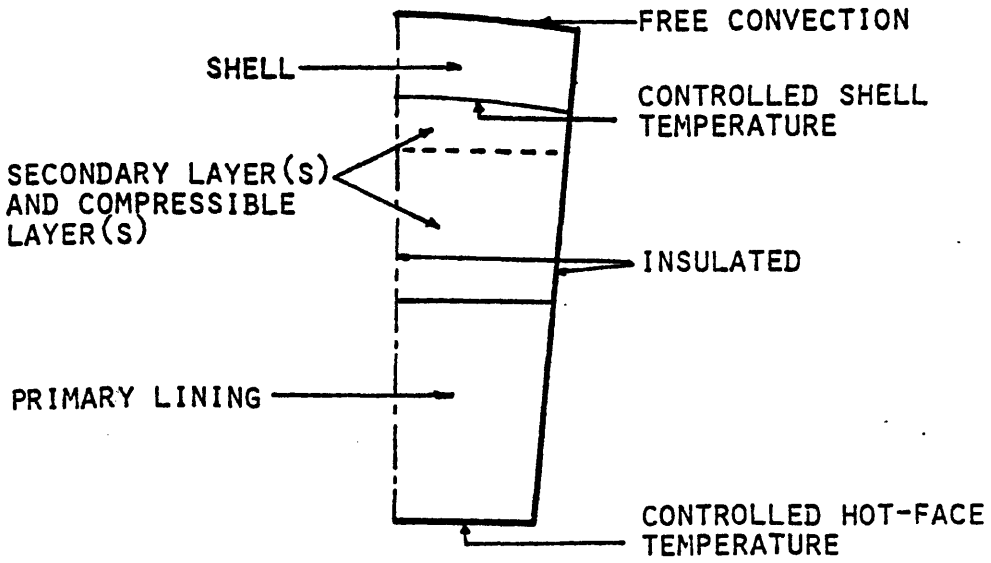

Figure 6.3 Boundary Conditions for Half-Brick (Shaded Zone in Fig. 6.2) used in the Analysis

gasification environments. Parameter studies, which include various lining configurations, heating rates, and holding periods, are performed with the use of the developed analysis capability presented in Chapter 5. Results from these parameter studies, combined with those results and observations from Chapters 3 and 4, will be used in the next chapter toward the determination of a conceptually reliable design and operation schedule for the refractory linings in slagging gasifiers.

§6.1.1 Assumptions

For the analyses in this chapter, some general assumptions are made. They are summarized as follows:

(1) The overall configuration of the refractory lining systems is taken as a composite cylindrical wall which is composed of a number of layers (Fig. 6.2). The outer radius for these linings is taken to be 108".

(2) The arrangement of the refractory bricks is assumed to be circumferentially symmetrical. In this case only half of the brick (shaded area in Fig. 6.2) with the symmetry boundary conditions (Fig. 6.3) needs to be modeled for the analyses.

(3) Temperature variation in the axial (z) direction is assumed negligible, since the temperature gradient along the axis of the gasifier vessel is insignificant.

(4) Based on the assumption (3), adoption of a two-dimensional (2-D) representation for the heat-transfer and stress analyses is considered adequate. However, the effect of stresses in the third (z) direction is accounted in the following way. In the stress analysis, a generalized 2-D plain strain condition with zero total

end force in the z-direction is adopted. When the predicted stress in the z-direction exceeds the tensile bonding strength of the motar, a partial failure of the horizontal joint in the vertical direction is identified (Fig. 6.2). For the region of the failed joint, plain stress condition is assumed. With this assumption shear stresses on the z-x and z-y planes are neglected.

(5) The effects of the cooling system is assumed important only in the heat transfer analysis in the way it controls the shell temperature; however, it is assumed that the cooling system has no structural contribution to the lining system and is not included in the stress analysis.

(6) Mortar thickness is taken to be 1/16" .

(7) In the analysis the heating rate of the hot face is controlled. The hot face heating rate is taken as a parameter for various heating schedules adopted.

(8) An active cooling system is adopted in controlling the shell temperature. Although the shell temperature should be controlled at low levels (say, 150^{o}F) during operating period (steady state), in the transient heat-up process the allowable maximum shell temperature can be higher (say, up to 600^{o}F) for reducing confining stress to the linings (see §6.3).

(9) Shrinkage of bricks and mortar at elevated temperatures is assumed insignificant [9].

(10) Operating pressure is taken to be atmospheric pressure.

§6.1.2 Materials and Lining Configurations

Although both 90% Al_2O_3 and 80% Cr_2O_3 refractory bricks have been considered to be the candidate materials for the primary lining (the lining which is exposed directly to the gasification environment), in the present analyses the 90% Al_2O_3 brick only is used. This is because more material data for this brick needed for the thermomechanical analysis was available. For the secondary and the back-up linings, SiC brick and 50% Al_2O_3 insulating castable (or various other compressible materials) are adopted, respectively. The thermophysical and mechanical behavior and the associated material models of the abovementioned materials were presented in Chapter 3. A compatible mortar for 90% Al_2O_3-mortar interface is assumed to have a constant bonding strength of 1000 psi in pure tension. The ratio of thermal conductivity to the product of density and specific heat of steel is taken to be 84.0 in^2/hr [88].

The lining configurations considered in the following analyses include various combinations of numbers of layers and materials. They are summarized in Table 6-1. Some of these configurations, which are shown by the first few analyses to be impractical, are eliminated in the further analyses.

§6.1.3 Operational Schemes

Different combinations of heating schemes on the hot face, and the cooling schemes in controlling the shell temperature by the cooling system are adopted (Fig. 6.4). For the heating process on the hot face, three sets of heating schemes are used:

Heating scheme (1): The hot face temperature is controlled at a constant heating rate (see Figs. 6.4a and

Lining Configuration	Case No.	Material A	B	C	D	Dimension (in) a	b	c	d	e	Remarks
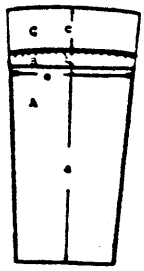	#1-1	AL	GA	SS		9.0	1.0	2.5		4.5	
	#1-2	AL	GA	SS		9.0	0.0	2.5		4.5	
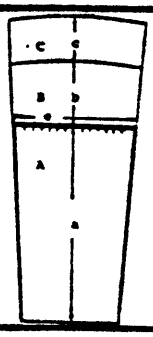	#2-1	AL	IC	SS		9.0	1.0	2.5		4.5	
	#2-2	AL	IC	SS		9.0	4.5	2.5		4.5	
	#2-3	AL	CM	SS		9.0	3.0	2.5		4.5	$E=1.x10^{5}$psi
	#2-4	AL	CM	SS		9.0	3.0	2.5		4.5	$E=1.x10^{4}$psi
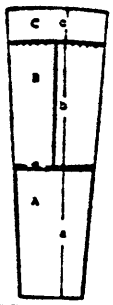	#3-1	AL	SC	SS		9.0	9.0	2.5		4.5	Perfect joint for SC layer
	#3-2	AL	SC	SS		9.0	9.0	2.5		4.5	Dry joint for SC layer
	#3-3	AL	SC	SS		9.0	4.5	2.5		4.5	Dry joint for SC layer
	#4-1	AL	SC	CM	SS	9.0	9.0	3.0	2.5	4.5	Perfect joint for SC layer $E = 1.x10^{5}$psi
	#4-2	AL	SC	CM	SS	9.0	9.0	3.0	2.5	4.5	Dry joint for SC layer $E = 1.x10^{5}$psi
	#4-3	AL	SC	CM	SS	9.0	9.0	3.0	2.5	4.5	Perfect joint for SC layer $E = 1.x10^{4}$psi
	#4-4	AL	SC	CM	SS	9.0	9.0	3.0	2.5	4.5	Dry joint for SC layer $E = 1.x10^{4}$psi

Material Index:
- AL : 90%Al_2O_3- 10%Cr_2O_3 Brick
- CM : Compressible Material
- GA : Gap
- IC : Insulating Castable
- SC : SiC Brick
- SS : Steel shell

Legend:
- : Cooling system
- : Joint Interface

E = Elastic modulus of Compressible Material

Table 6.1 Lining Configurations Used in the Analysis

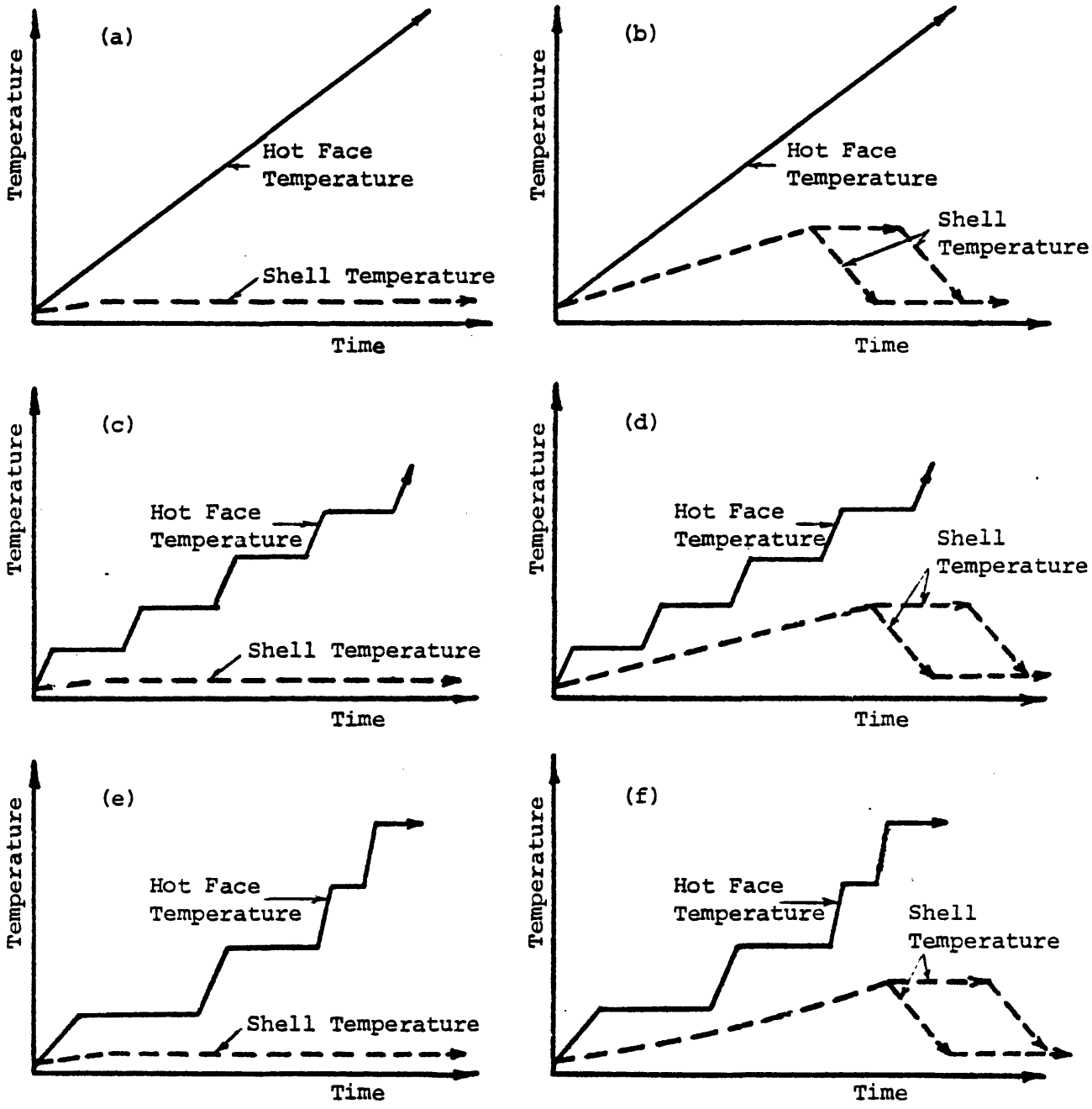

Figure 6.4 Hot-Face Heating Schemes and Cold-Face Cooling Schemes

6.4b). In the following studies, this rate is taken to be 50 or 150°F/hr.

Heating scheme (2): The hot face temperature is controlled by repeating a subset of the heating process which is composed of a period of constant heating rate (50 or 150°F/hr) and a period of holding temperature (see Figs. 6.4c and 6.4d).

Heating scheme (3): This scheme is the same as the heating scheme (2) except that the constant heating rate in an individual subset can be different from one subset to another (Figs. 6.4e and 6.4f). Also, the hold periods can be variable.

The two sets of cooling schemes are studied:

Cooling scheme (1): The cooling system is operated in a way that the shell temperature at any time does not exceed 150°F. If the shell temperature is lower than 150°F, the cooling system is not active (see Figs. 6.4a, 6.4c and 6.4e).

Cooling scheme (2): During the transient heating processes, the cooling system is not used until the shell temperature reaches a critical temperature (say, 600°F). After this critical temperature has been reached, the shell temperature is then controlled by the cooling system at various combinations of cooling rates (50 to 150°F/hr) until the shell temperature reaches 150°F. Then, shell temperature is kept at 150°F (Figs. 6.4b, 6.4d, and 6.4f).

The cooling system is located at a proper place such that it can perform the following two funtions:

(1) The shell temperature can be effectively controlled by the cooling system.

(2) The hot face temperature of the primary lining can be effectively reduced (from operating temperature) by the cooling system. This is important and desired in the design of the lining for the slagging gasifier since lower hot face temperature can result in less damage from corrosion attack to the linings (see Chapter 4). For this reason the cooling system may be located on the innermost face of all insulating layers if they are adopted (Table 6.1). Otherwise, the cooling system is located on the outer face of the lining system, or inner face of the vessel shell.

§6.1.4 Failure Modes

All analyses reported in this chapter were automatically stopped by the computer program whenever any of the following three destructive failure modes in the lining systems was detected during the heat-up process:

(1) Hot face spalling: When refractory material in the vicinity of the hot face is predicted to fail under certain combinations of stresses resulting in tensile strain in radial direction of the lining, the spalling is assumed to occur.

(2) Severe joint failure: When the length of joint failures along any mortar-refractory interface exceeds 2/3 of the original length of the joint, a "severe" joint failure is defined and the system is considered to be too slack (unstable).

(3) Yielding of steel: When the stress in the steel shell exceeds its yield stress (say, 34000 psi), the shell is assumed to be in an unsafe state.

§6.1.5 Organization

Sections 6.2 to 6.4 study the thermomechanical behavior of the linings with various configurations (single-layer and multiple-layer), material combinations, and heating schemes. For the primary linings shaped 90% Al_2O_3 refractory bricks with 9" thickness and 4.5" outer width is used. Adoption of a back-up lining or a secondary lining, and their thicknessess are taken as parameters for the study. Finally, a summary of the findings for these analysis is presented in section 6.5.

§6.2 HEATING SCHEME (1)

This section studies the thermomechanical behavior of the linings with the heating scheme (1); namely, a constant heating rate is imposed on the hot face. This heating rate is taken to be either 50°F/hr or 150°F/hr for the present study. Both of the cooling schemes defined in §6.1.3 are used and all the lining configurations shown in Table 6.1 are studied.

§6.2.1 Heating Rate = 50°F/hr

A constant heating rate of 50°F/hr is adopted first for studying the thermomechanical behavior of various linings. By using the finite element analysis capability developed in Chapter 5, those cases listed in Table 6.1 with various lining geometries and material combinatinos are studied. Table 6.2 summarizes the failure conditions (mode, time, and hot face temperature) associated with each case. It can be seen that under this heating scheme no lining configuration in Table 6.1 can sustain a hot face temperature over 1000°F without failure. However, the results from these analyses can offer information which can be used as a basis for improving lining configuration or operational scheme. Furthermore, the results can also be used to eliminate some impractical lining configurations for further study.

Single-layer lining systems (C-1 to C-4) are not ideal for slagging gasifiers. If the lining system is not in contact with the vessel shell (C-1, C-2), it experiences severe joint failure which would make the system loose or unstable. Moreover, these significant joint failures would yield ways to gas penetration through the linings and result in the corrosion attack of gases to the vessel shell. Such a joint-failure process and the resulting lining behavior is dependent on the joint properties (strength, stiffness). On the other hand, if the linings are in perfect contact with the vessel shell (C-3, C-4), although the length of the joint failure can be generally reduced, the confining stress contributed from the shell stiffness leads to a significant compressive hoop-stress on the hot face of the linings. This can cause material failure and spalling problem on the hot face. The abovementioned two types of systems can be improved if some compressible materials (layers)

Simulation No.	Lining Configuration	Hot-Face Heating Rate(^{o}F)	Cold-face Cooling Scheme	Failure Mode	Failure Time(hr)/ Failure Hot-Face Temperature(^{o}F)	Remarks
C-1	#1-1	50	1	2	4.0/277	
C-2	#1-1	50	2	2	13.5/742	
C-3	#1-2	50	1	1	14.5/802	3.1" Joint Failure
C-4	#1-2	50	2	1	16.5/902	4.2" Joint Failure
C-5	#2-1	50	1	3	10.0/577	
C-6	#2-1	50	2	3	11.0/627	
C-7	#2-2	50	1	3	9.0/527	0.39" Concrete Crashed
C-8	#2-2	50	2	3	9.5/552	0.39" Concrete Crashed
C-9	#2-3	50	1	1	15.5/852	0.5" Joint Failure
C-10	#2-3	50	2	1	15.0/827	0.5" Joint Failure
C-11	#2-4	50	1	1	16.5/902	0.5" Joint Failure
C-12	#2-4	50	2	1	17.5/952	0.5" Joint Failure
C-13	#3-1	50	1	1	15.0/827	
C-14	#3-1	50	2	1	15.0/827	
C-15	#3-2	50	1	1	15.0/827	0.5" Joint Failure
C-16	#3-2	50	2	1	15.0/827	0.5" Joint Failure
C-17	#3-3	50	1	1	13.5/752	
C-18	#3-3	50	2	1	13.5/752	
C-19	#4-1	50	1	1	13.0/727	
C-20	#4-1	50	2	1	13.0/727	
C-21	#4-2	50	1	1	15.0/827	
C-22	#4-2	50	2	1	15.0/827	
C-23	#4-3	50	1	1	13.5/752	
C-24	#4-3	50	2	1	13.5/752	
C-25	#4-4	50	1	1	14.0/777	
C-26	#4-4	50	2	1	14.0/777	

Note: (1) Length of joint failure is measured from the outer face of primary lining.
(2) Depth of crashed zone in concrete layer is measured from the outer face of the layer.
(3) Failure modes : Mode 1 : Hot-face spalling
Mode 2 : Sever joint failure
Mode 3 : Steel yieling

Table 6.2 Predicted Failures for the Cases Studied (Constant Heating Rate = 50^{o}F/hr)

are located between such primary lining and the vessel shell to release a part of the confining stress [3,92]. At the same time, these compressible layers should still offer certain confining effects on the primary linings to prevent severe joint failure.

Several lining systems composed of primary lining and either an insulating concrete layer or a compressible layer (with various stiffness) have been studied (C-3 to C-6). Elastic model has been used for the constitutive behavior of the compressible materials, and the Young's modulus (E) for the materials is taken to be a parameter for the study. The values 1×10^5 psi and 1×10^4 psi are chosen for E , while the Poisson's ratio of these materials is taken to be 0.2 The analysis results (see Table 6.2) show that the general stability of the linings with compressible layers (C-5 to C-12) is generally improved from those without compressible layers (C-1 to C-4). However, failure (spalling) still occurs in the linings adopting compressible layers, due to high stresses near the hot faces. Also shown in the results is the tendency of releasing hot face compressive stress by adopting compressible layers.

Secondary linings are commonly adopted in the lining design to provide a second level of protection to the shell from the thermal and corrosion attacks [3], and usually taken as permanent components in the lining systems. To maintain the effectiveness of the cooling system on reducing hot-face temperature, and to decrease the potential of slag penetration, dense materials with high thermal conductivity should be adopted. In the present study, SiC bricks are chosen for the secondary linings, when they are adopted.

Cases C-13 to C-26 study the thermomechanical behavior of the linings composed of a primary lining and a secondary lining, with or without a compressible layer. Generally speaking, adopting a secondary lining increases the confining stress to the primary lining due to the increase of lining thickness, if the external (outer) radius of the lining system is fixed. In the present heating scheme, it is found that the adoption of either the cooling scheme (1) or the scheme (2) makes no difference in the thermomechnical behavior of any of these linings, since shell temperatures in these cases are lower than 150°F before failure occurs. It is also found that the adoption of a dry joint for SiC layer slightly increases the failure time from that using a perfect joint; however, joint opening over dry joint interface can yield a way for gas penetrations, which may then result in corrosion attack to the shells. It is also found that, if perfect joint is assumed for SiC layers, the elastic modulus of the compressible layers has little effect on the lining behavior.

The stress and temperature distributions in the primary linings, accompanied with the directions of maximum principle stress, for the abovementioned cases (C-1 to C-26) at certain intermediate steps are shown in Figs. 6.5 to 6.30.

The analyses on the cases studied in this section do not yield any lining configuration or operational scheme which is ideal for the design or operations of the lining during heating process, however, following findings from the analyses point out certain directions for the search of such an optimal design or operational scheme:

(1) There are two major sources which cause stress in the primary

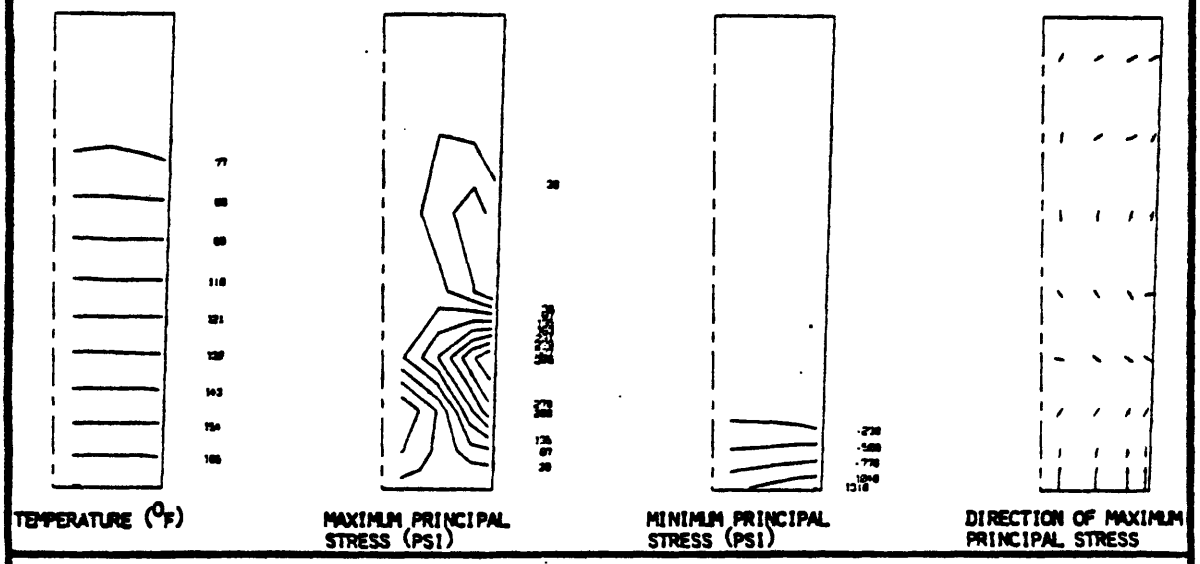

Figure 6.5 Temperature and Stress Distributions (Simulation No. C-1, Time = 2.0 hr, Hot-Face Temperature = 177°F)

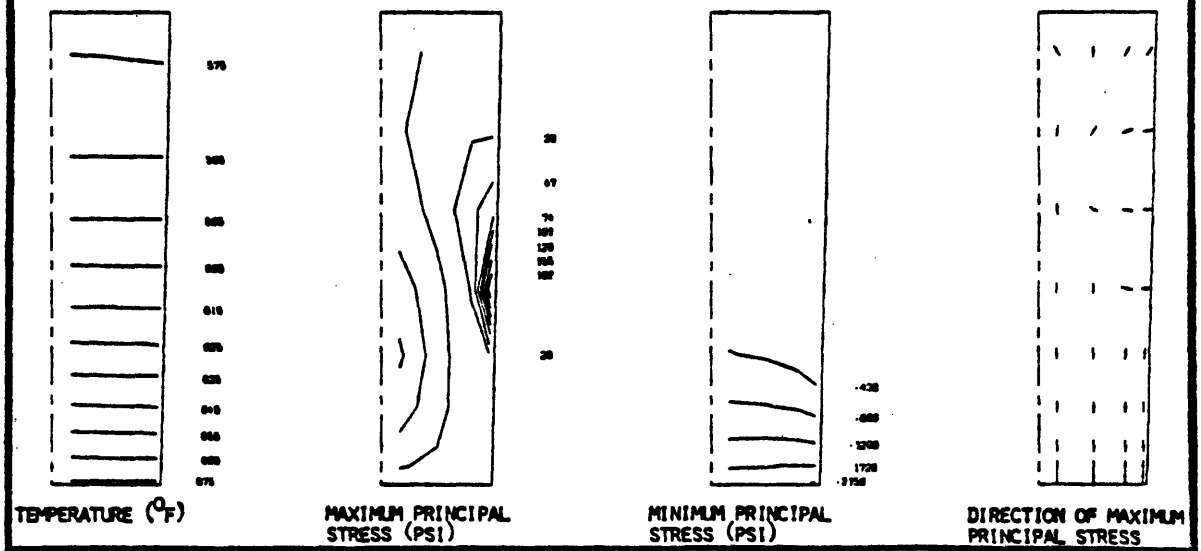

Figure 6.6 Temperature and Stress Distributions (Simulation No. C-2, Time = 12.0 hr, Hot-Face Temperature = 677°F)

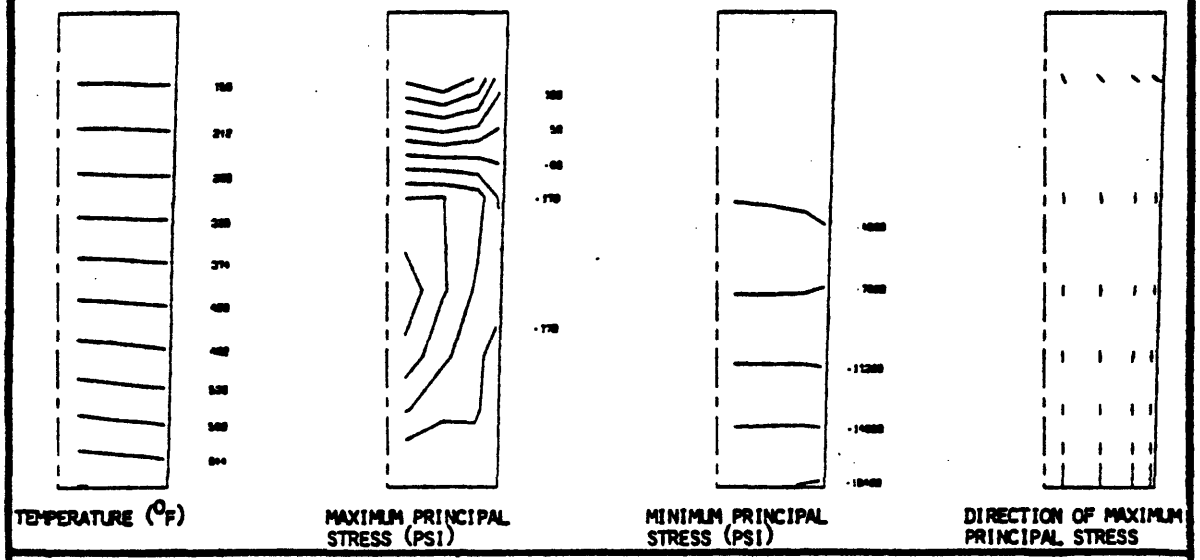

Figure 6.7 Temperature and Stress Distributions (Simulation No. C-3, Time = 12.0 hr, Hot-Face Temperature = 677°F)

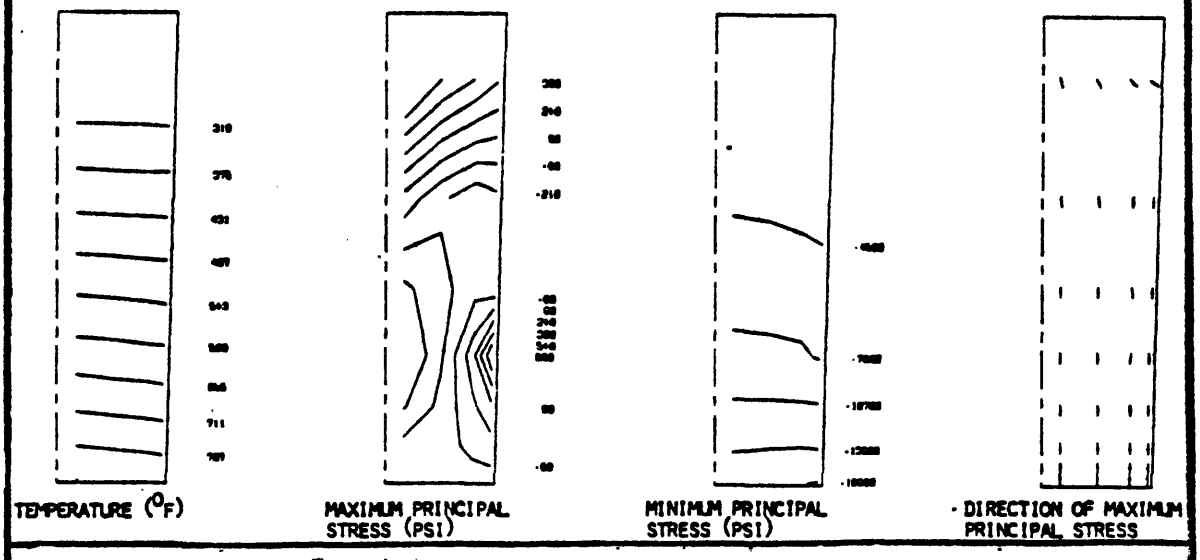

Figure 6.8 Temperature and Stress Distributions (Simulation No. C-4, Time = 15.0 hr, Hot-Face Temperature = 827°F)

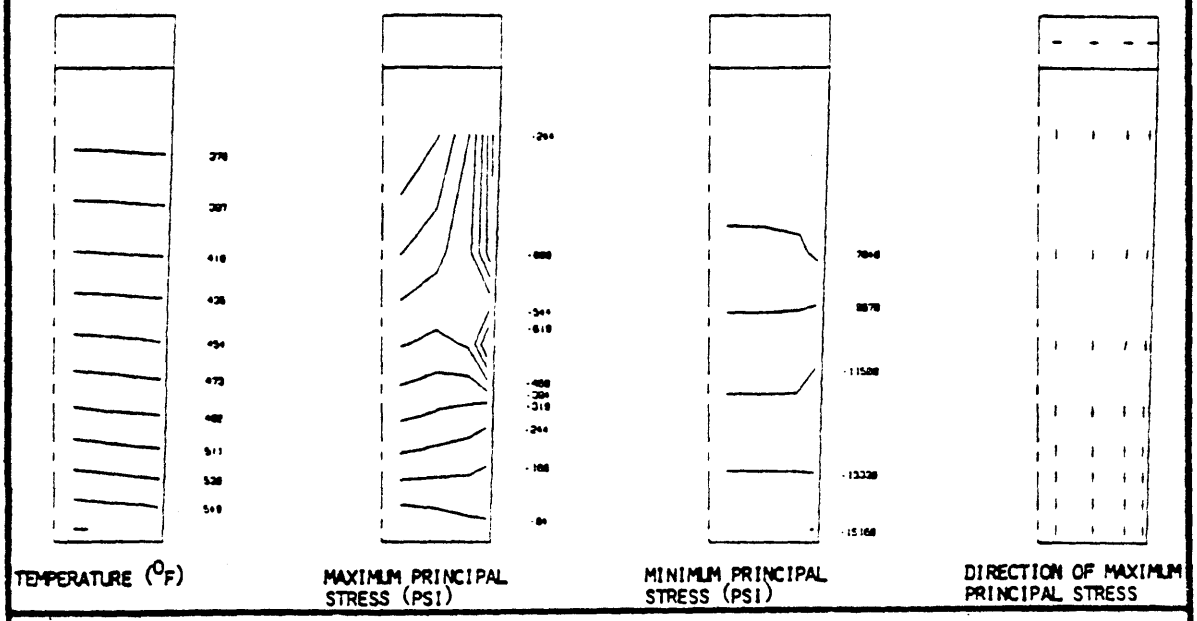

Figure 6.9 Temperature and Stress Distributions (Simulation No. C-5, Time = 10.0 hr, Hot-Face Temperature = 577°F)

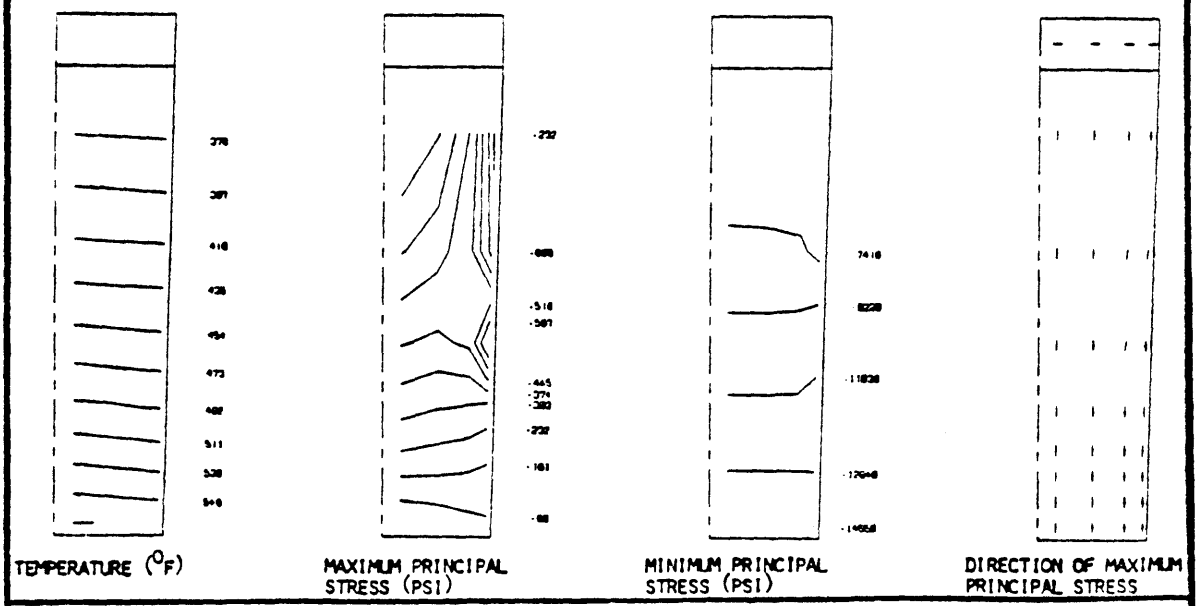

Figure 6.10 Temperature and Stress Distributions (Simulation No. C-6, Time = 10.0 hr, Hot-Face Temperature = 577°F)

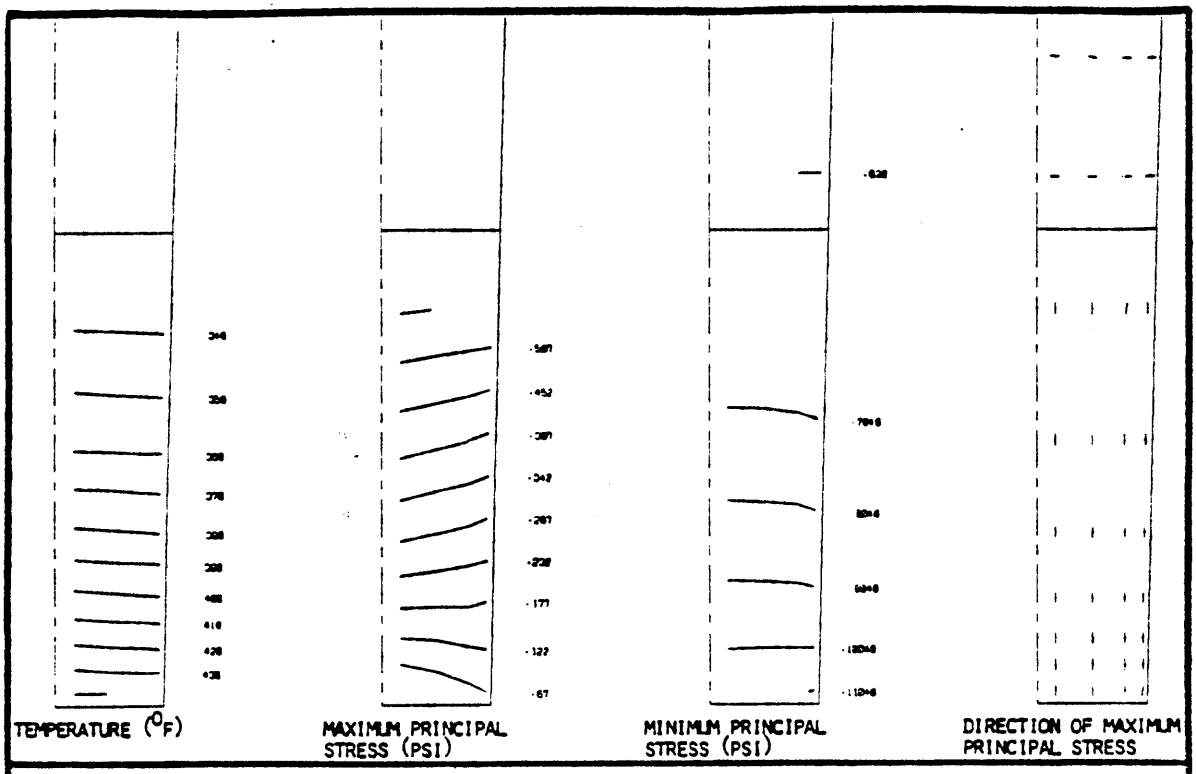

Figure 6.11 Temperature and Stress Distributions (Simulation No. C-7, Time = 7.5 hr, Hot-Face Temperature = 452°F)

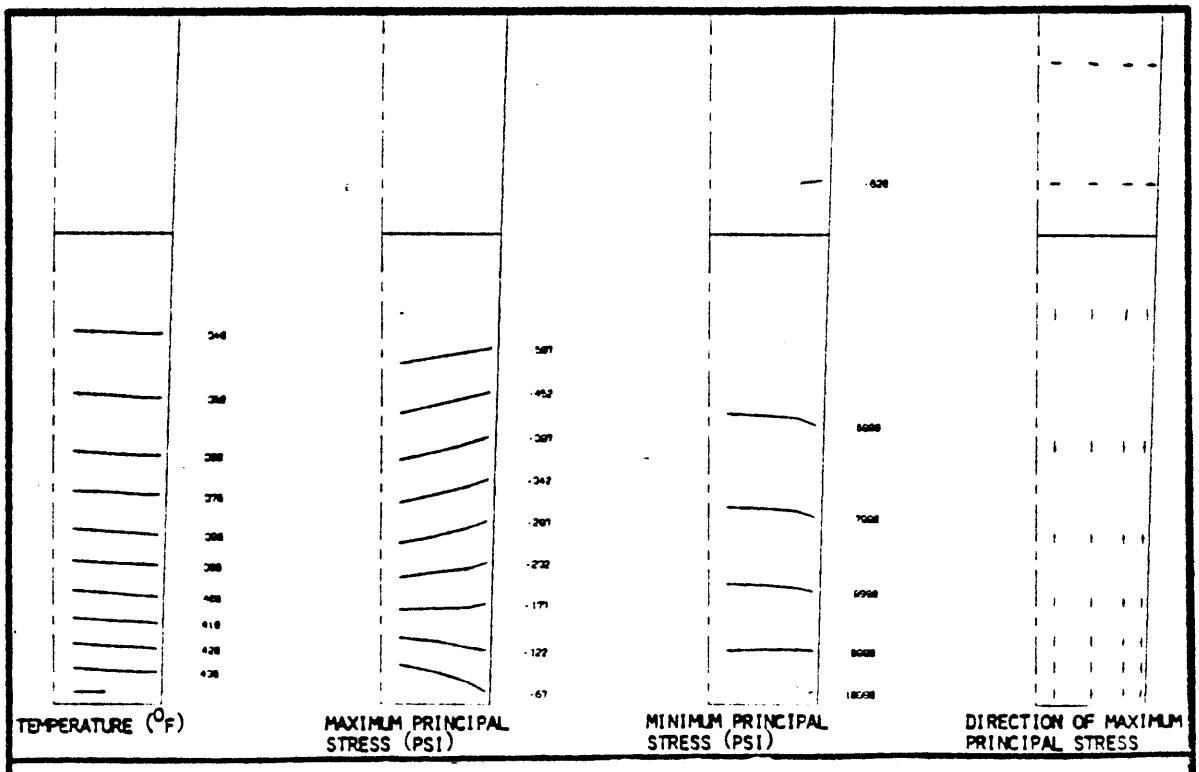

Figure 6.12 Temperature and Stress Distributions (Simulation No. C-8, Time = 7.5 hr, Hot-Face Temperature = 452°F)

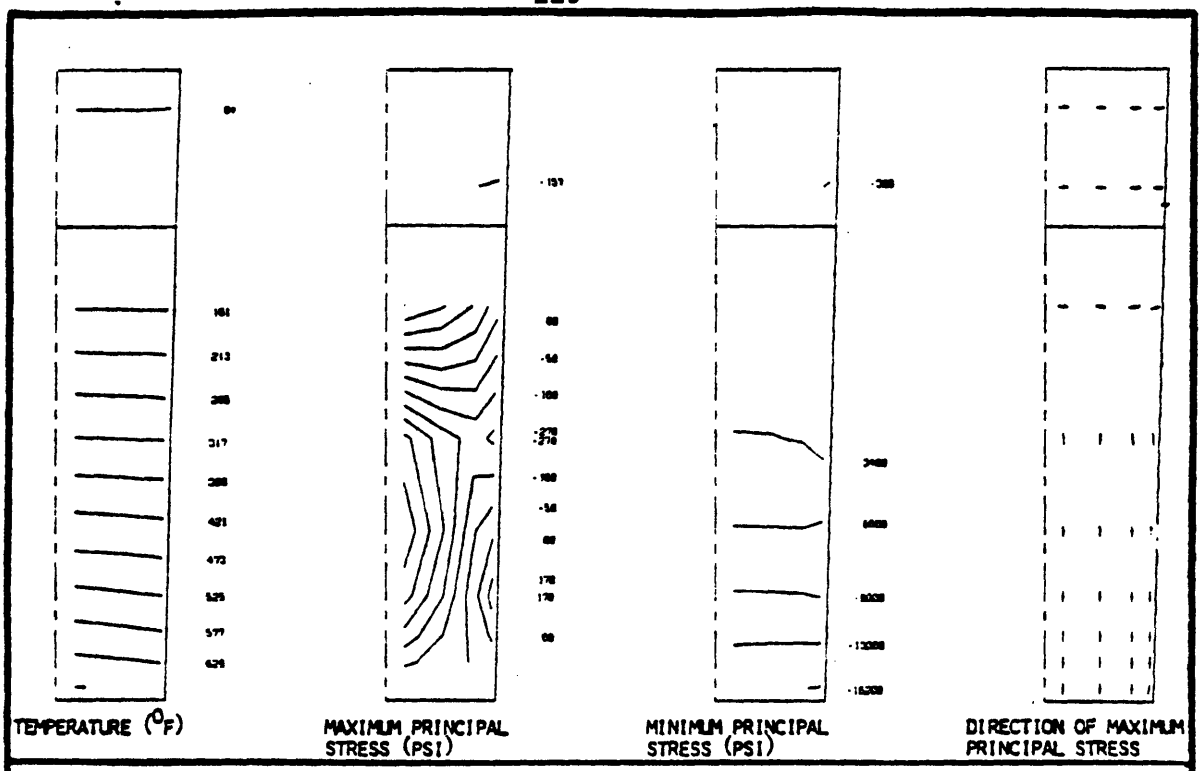

Figure 6.13 Temperature and Stress Distributions (Simulation No. C-9, Time = 12.5 hr, Hot-Face Temperature = 702°F)

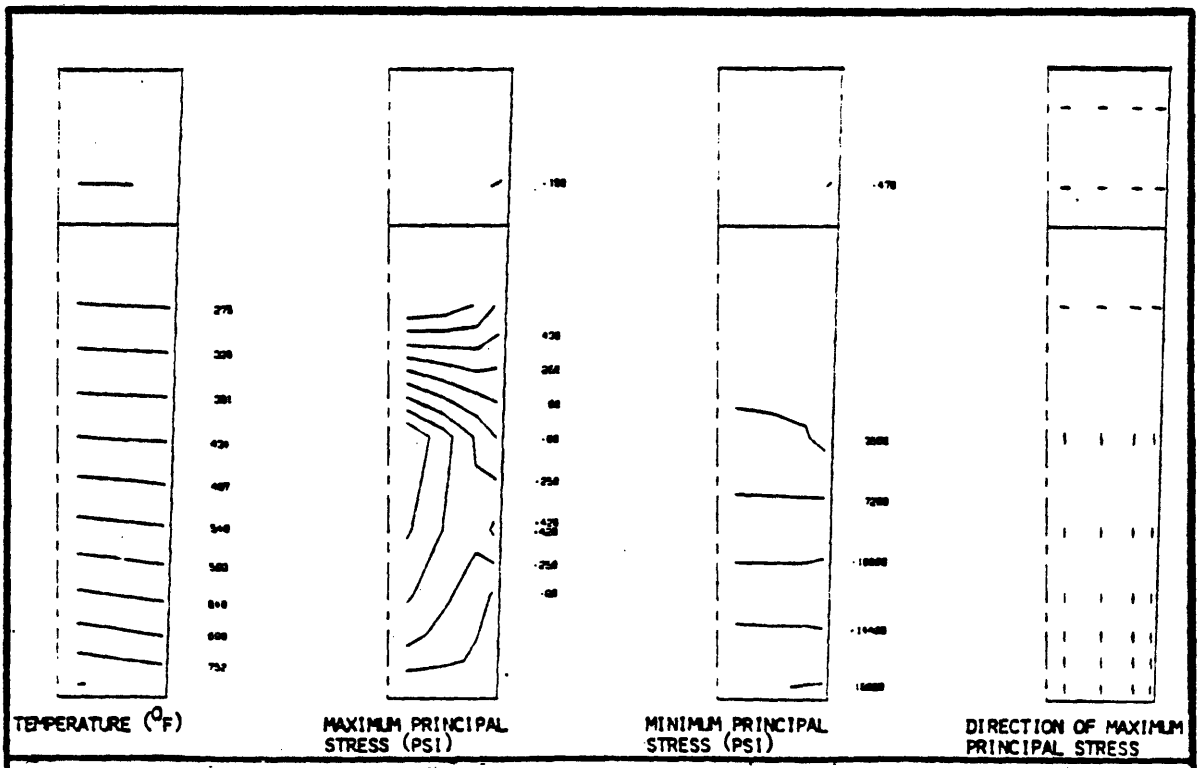

Figure 6.14 Temperature and Stress Distributions (Simulation No. C-10, Time = 12.5 hr, Hot-Face Temperature = 702°F)

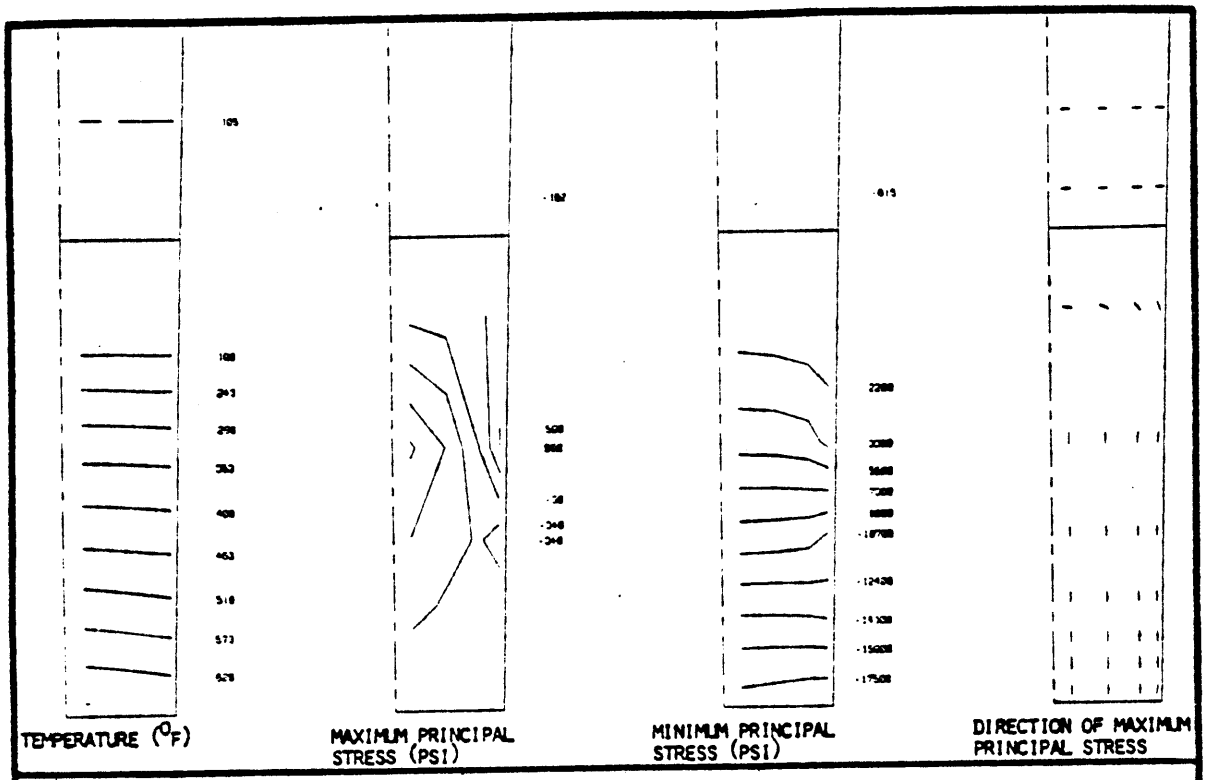

Figure 6.15 Temperature and Stress Distributions (Simulation No. C-11, Time = 10.0 hr, Hot-Face Temperature = 677°F)

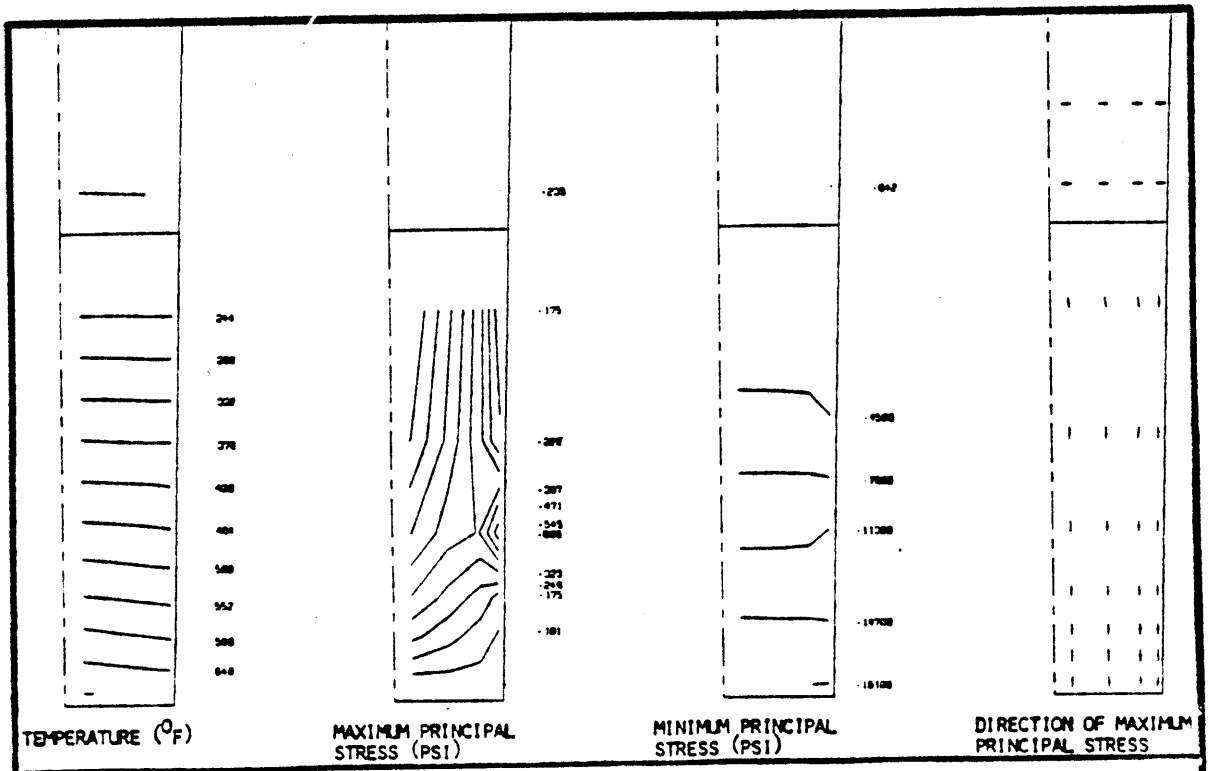

Figure 6.16 Temperature and Stress Distributions (Simulation No. C-12, Time = 15.0 hr, Hot-Face Temperature = 827°F)

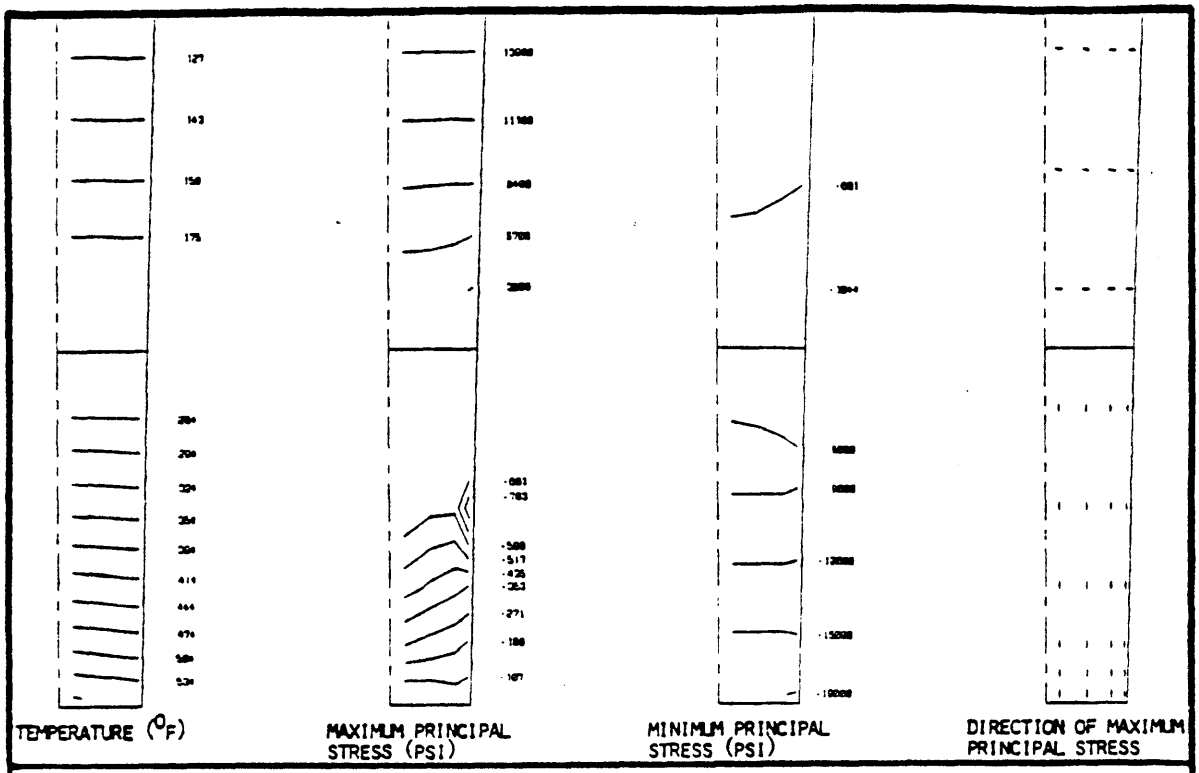

Figure 6.17 Temperature and Stress Distributions (Simulation No. C-13, Time = 10.0 hr, Hot-Face Temperature = 577°F)

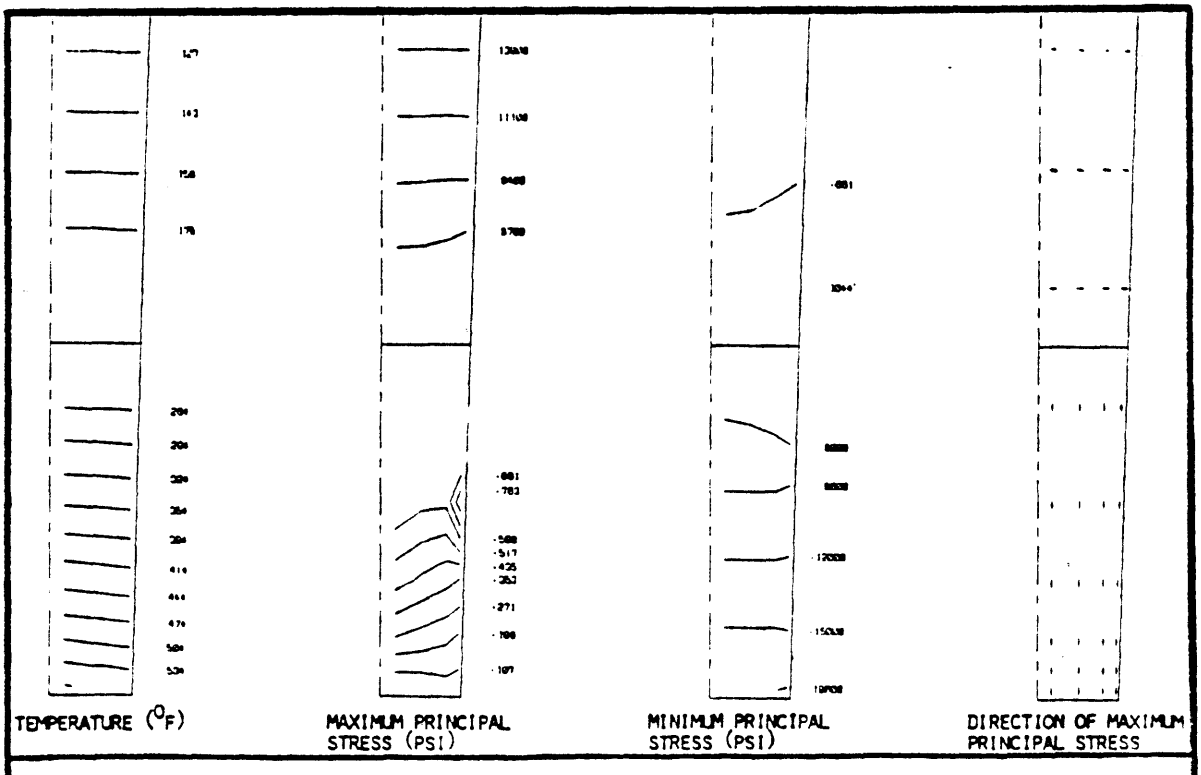

Figure 6.18 Temperature and Stress Distributions (Simulation No. C-14, Time = 10.0 hr, Hot-Face Temperature = 577°F)

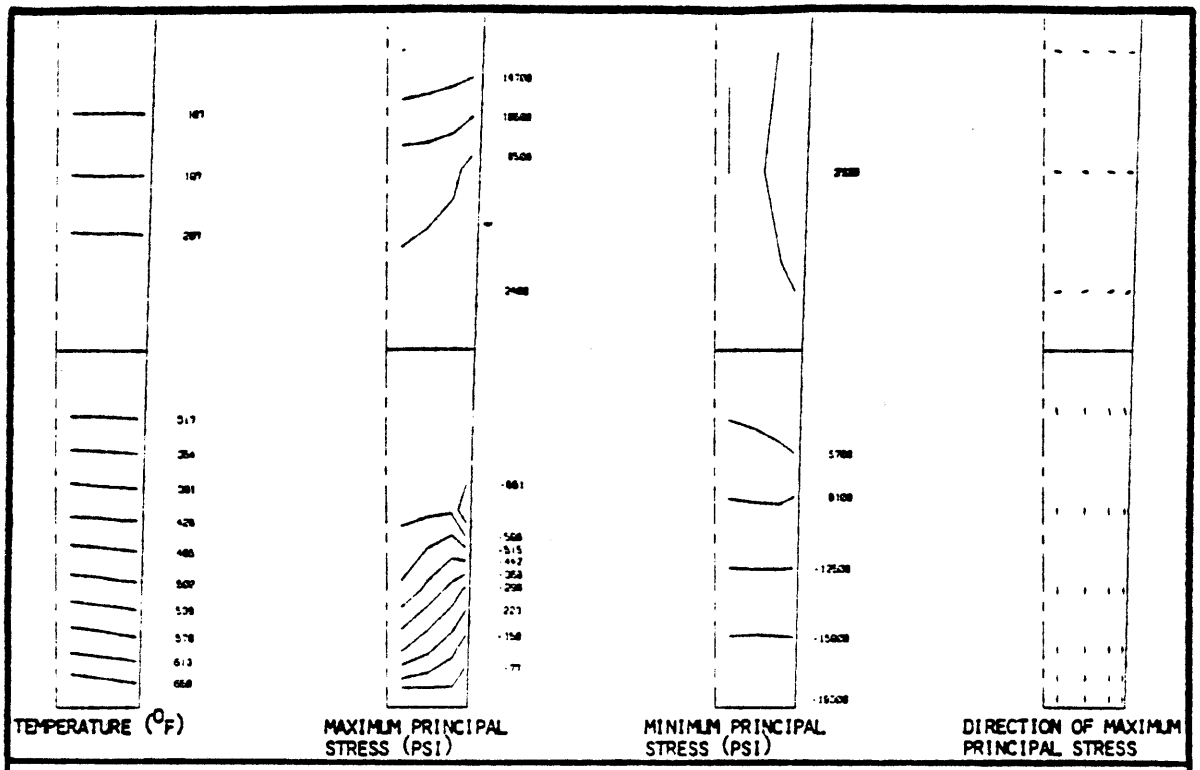

Figure 6.19 Temperature and Stress Distributions (Simulation No. C-15, Time = 12.5 hr, Hot-Face Temperature = 702°F)

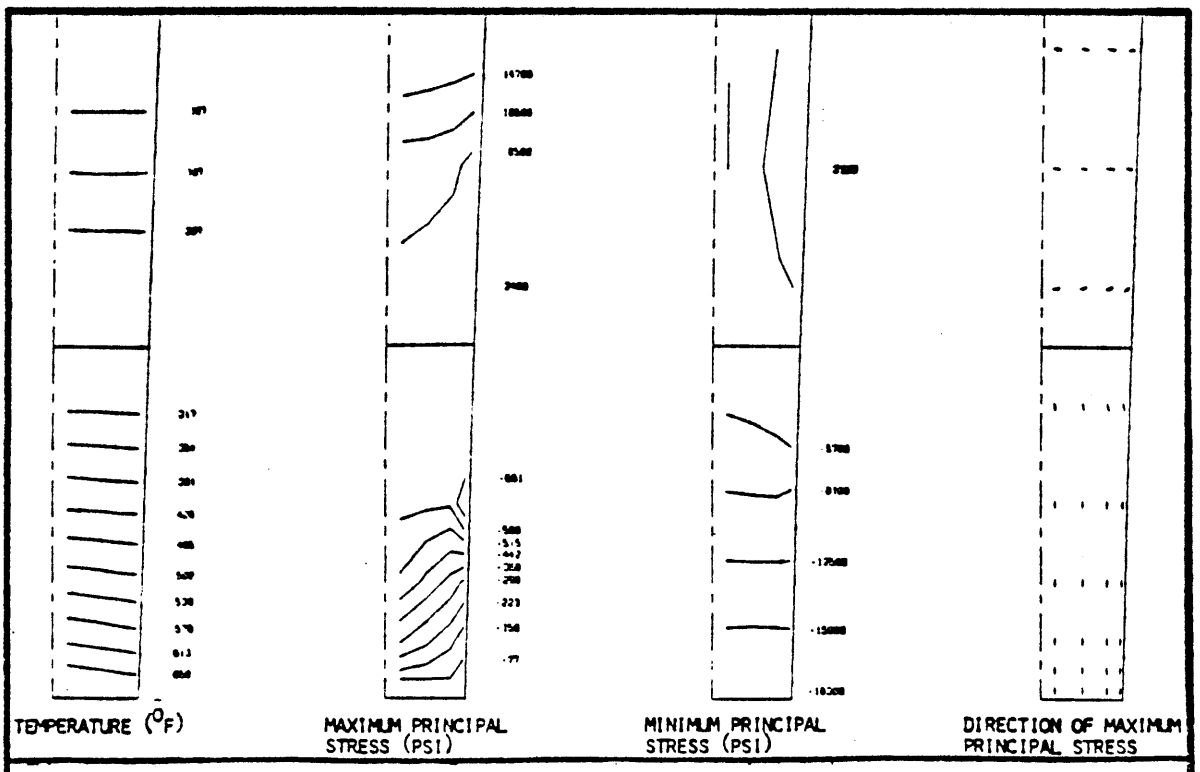

Figure 6.20 Temperature and Stress Distributions (Simulation No. C-16, Time = 12.5 hr, Hot-Face Temperature = 702°F)

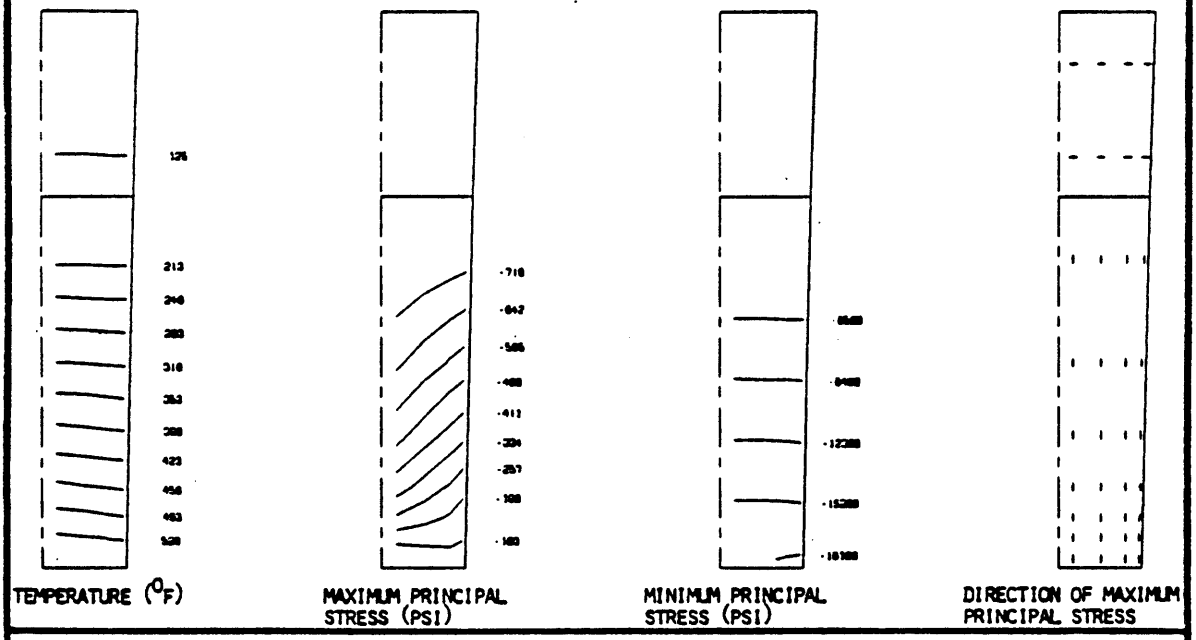

Figure 6.21 Temperature and Stress Distributions (Simulation No. C-17, Time = 10.0 hr, Hot-Face Temperature = 577°F)

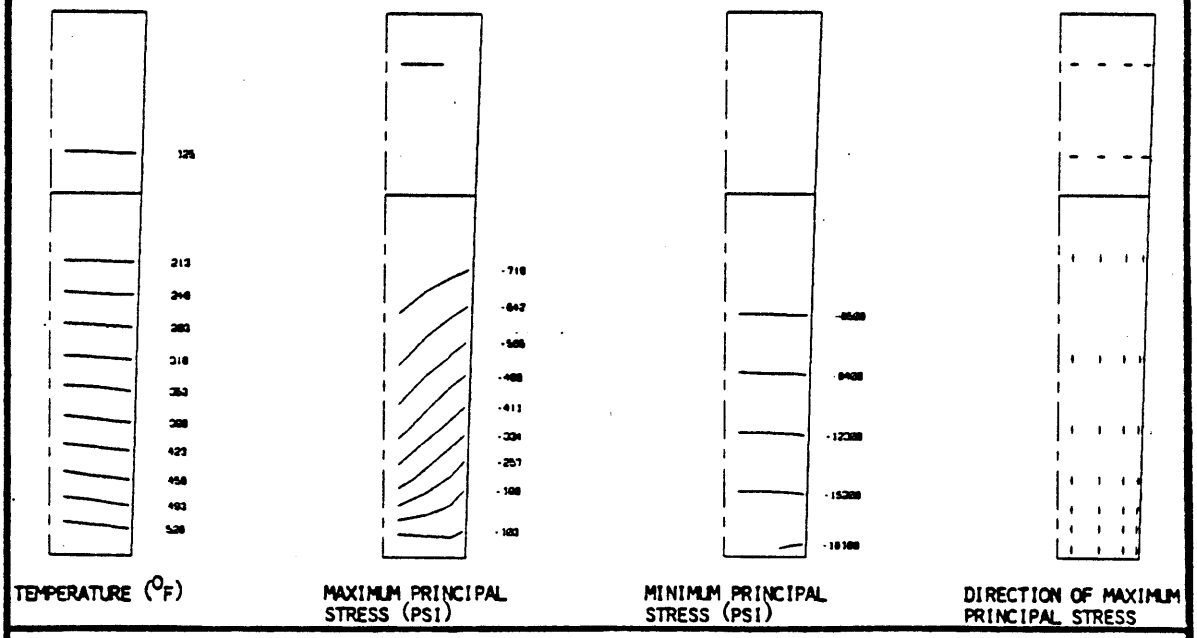

Figure 6.22 Temperature and Stress Distributions (Simulation No. C-18, Time = 10.0 hr, Hot-Face Temperature = 577°F)

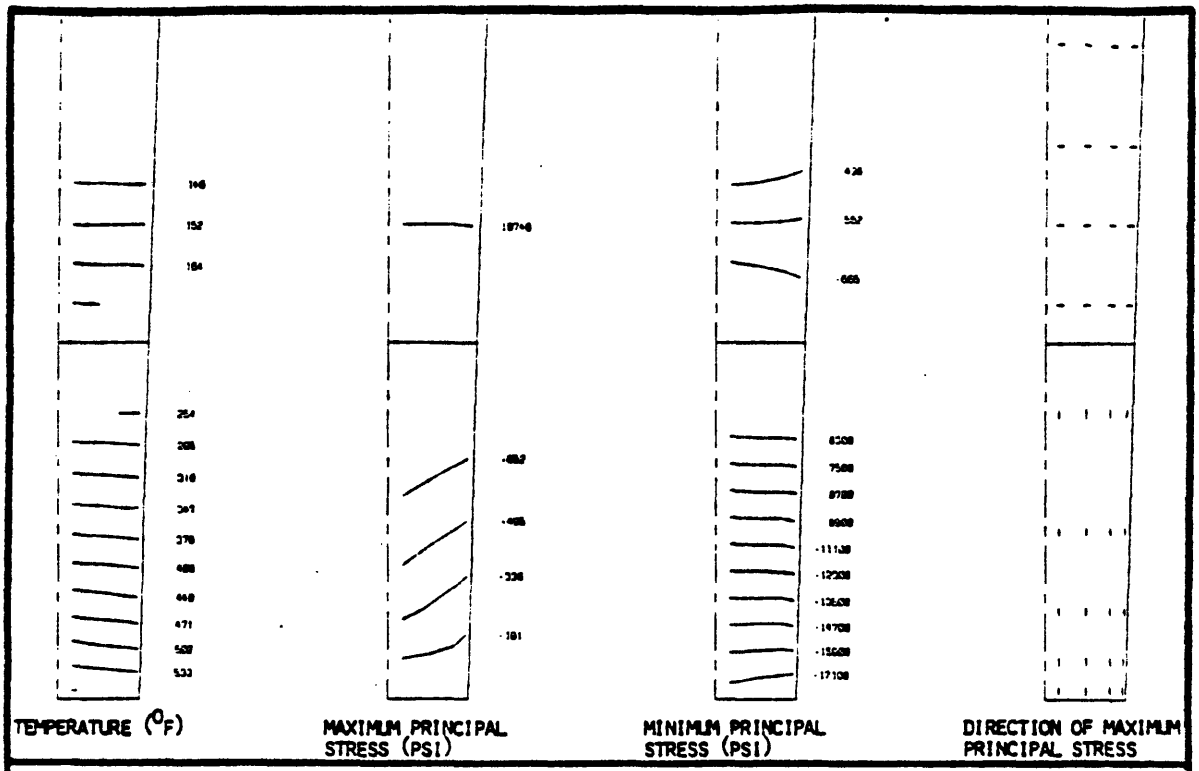

Figure 6.23 Temperature and Stress Distributions (Simulation No. C-19, Time = 10.0 hr, Hot-Face Temperature = 577°F)

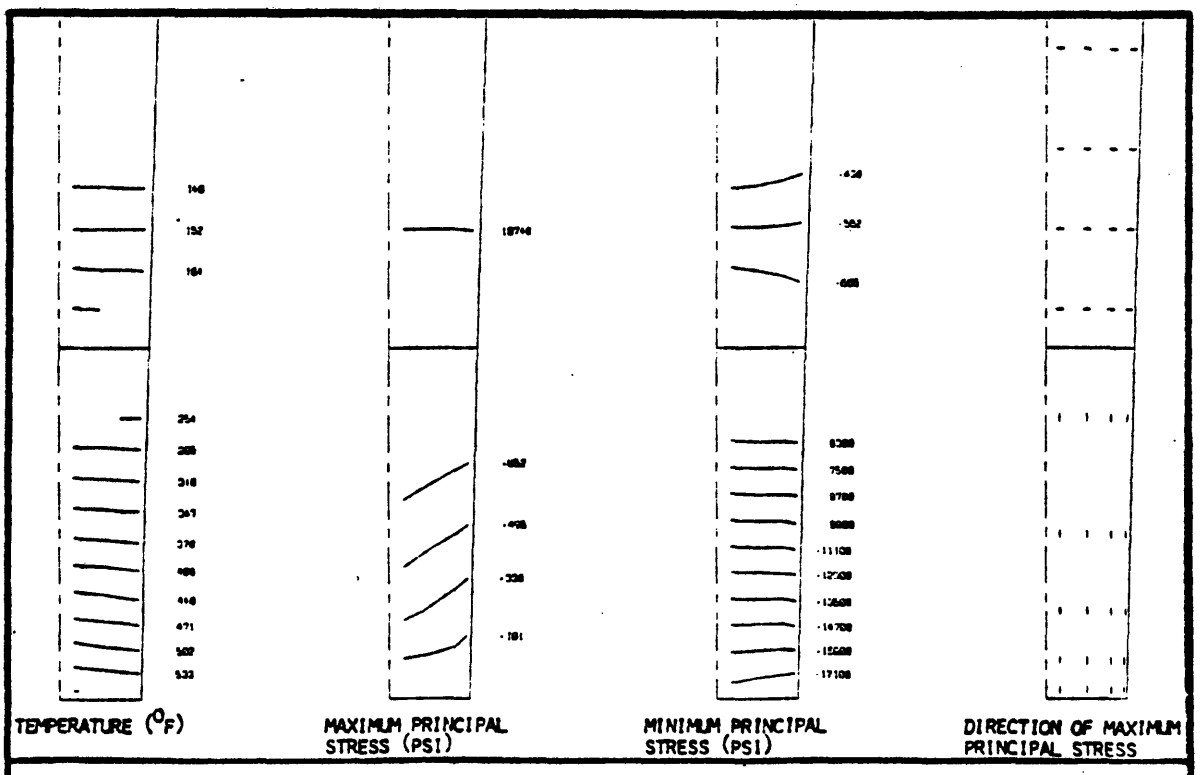

Figure 6.24 Temperature and Stress Distributions (Simulation No. C-20, Time = 10.0 hr, Hot-Face Temperature = 577°F)

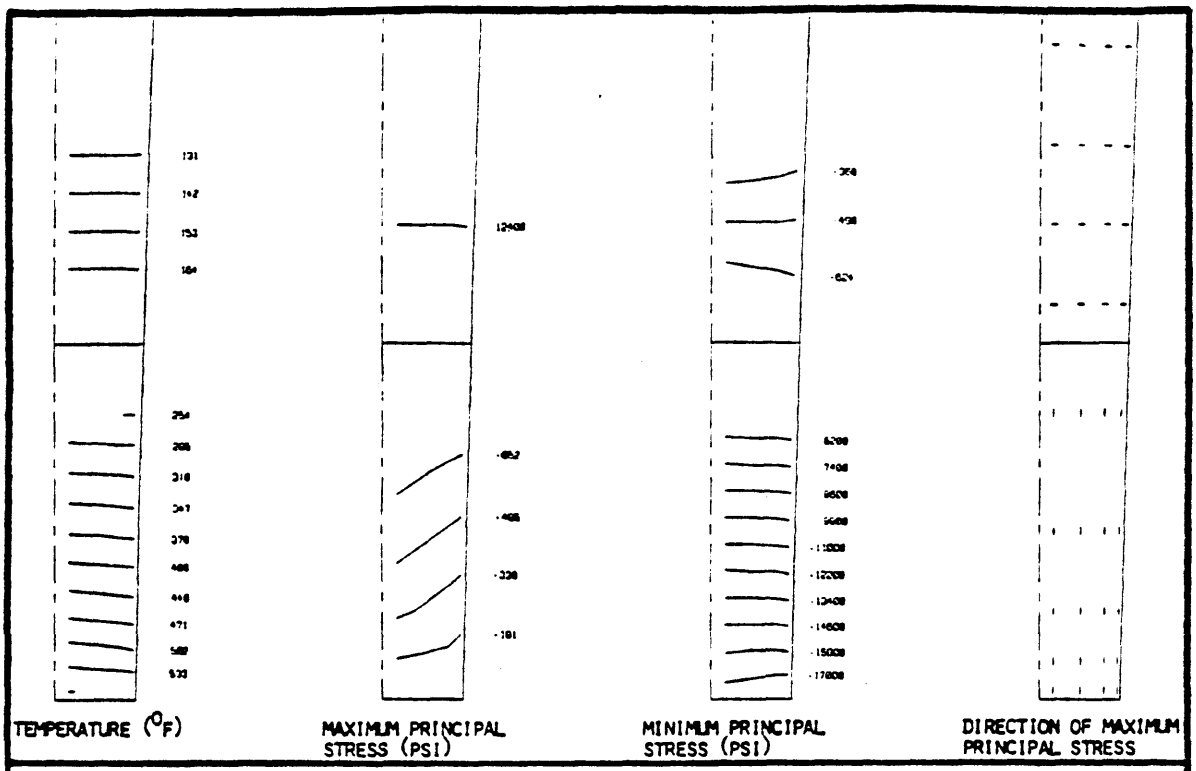

Figure 6.25 Temperature and Stress Distributions (Simulation No. C-21, Time = 10.0 hr, Hot-Face Temperature = 577°F)

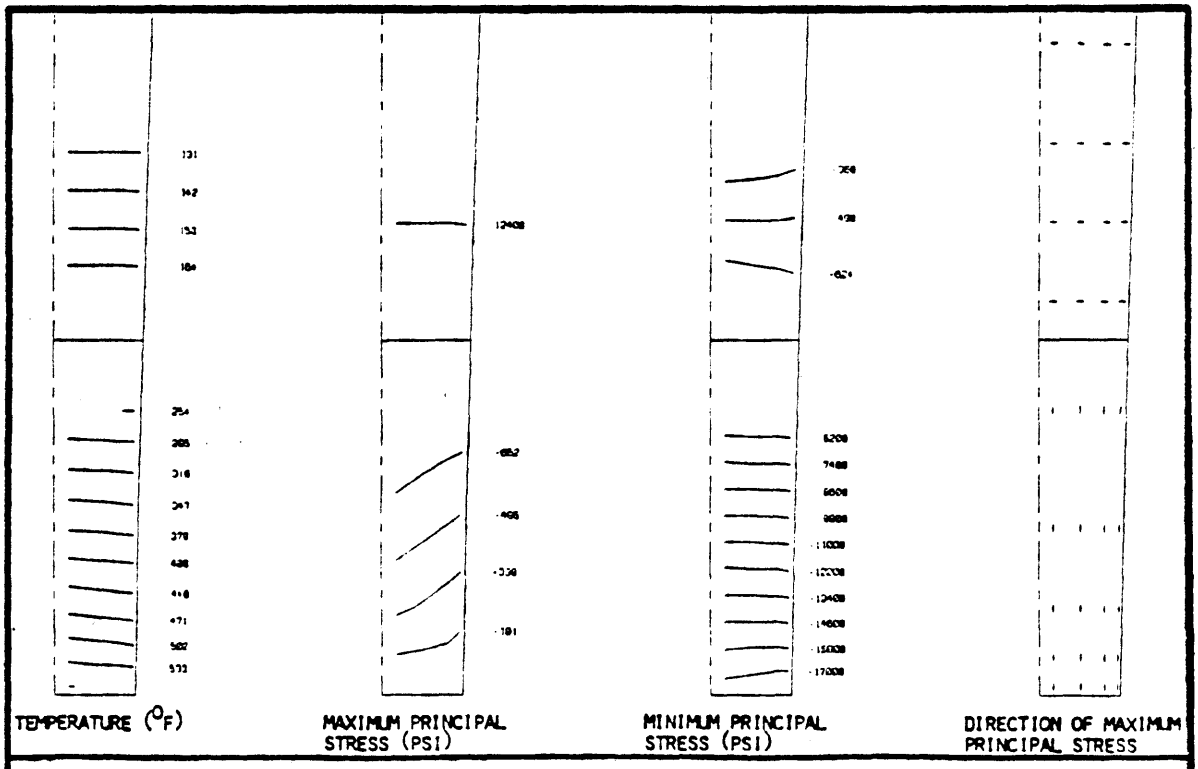

Figure 6.26 Temperature and Stress Distributions (Simulation No. C-22, Time = 10.0 hr, Hot-Face Temperature = 577°F)

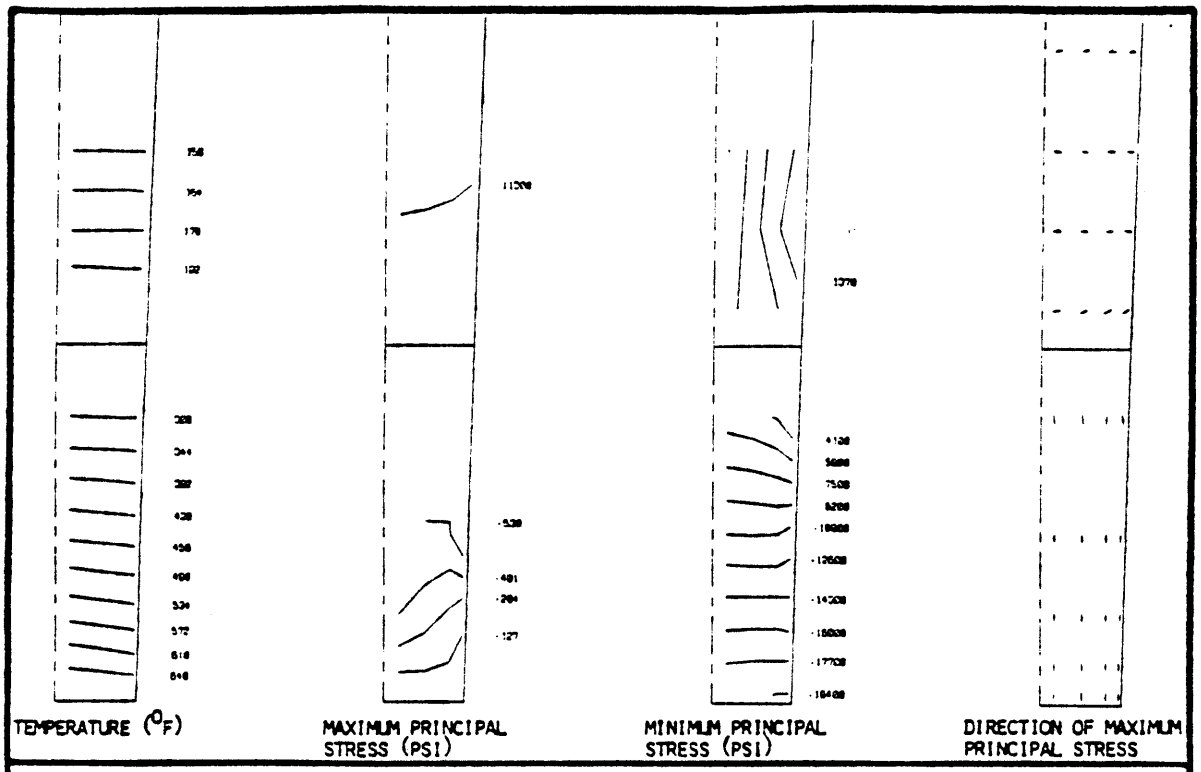

Figure 6.27 Temperature and Stress Distributions (Simulation No. C-23, Time = 12.5 hr, Hot-Face Temperature = 702°F)

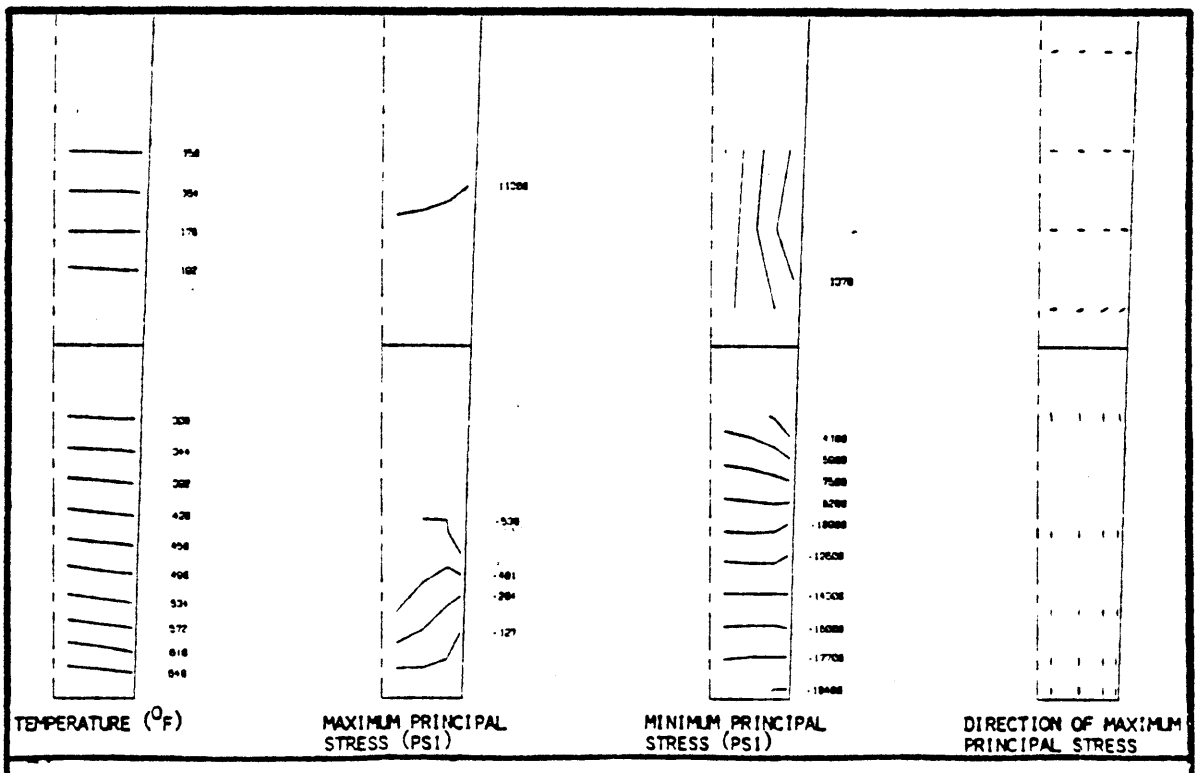

Figure 6.28 Temperature and Stress Distributions (Simulation No. C-24, Time = 12.5 hr, Hot-Face Temperature = 702°F)

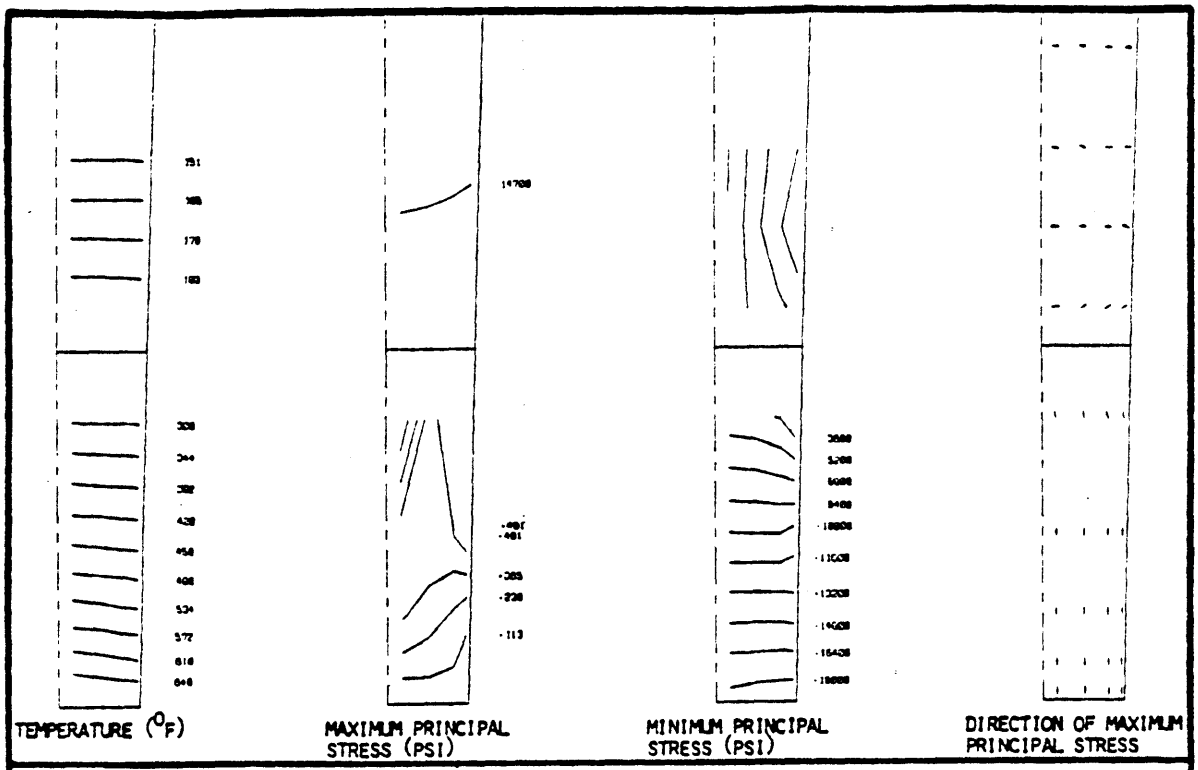

Figure 6.29 Temperature and Stress Distributions (Simulation No. C-25, Time = 12.5 hr, Hot-Face Temperature = 702°F)

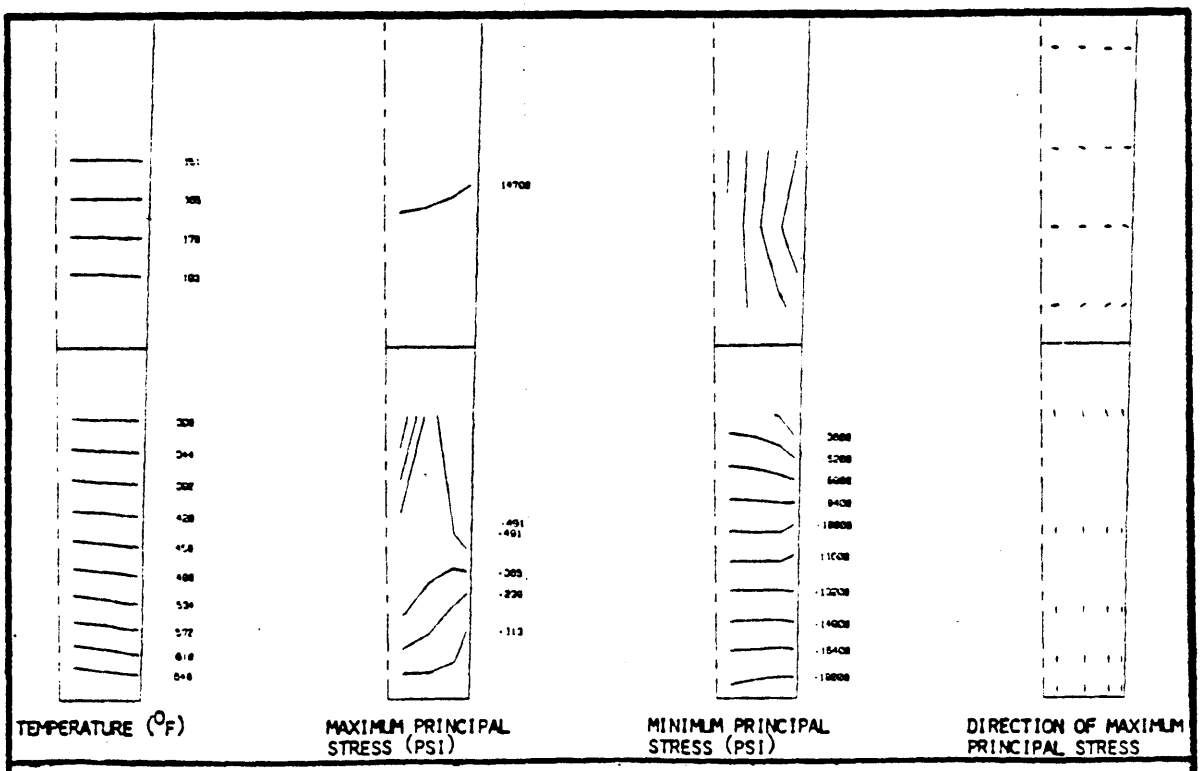

Figure 6.30 Temperature and Stress Distributions (Simulation No. C-26, Time = 12.5 hr, Hot-Face Temperature = 702°F)

linings: (A) temperature gradient and (B) radial confinement (e.g. the effect of shell). The temperature gradient through the lining thickness can result in compressive stress on the hot face and tensile stress on the cold face, if the lining is not confined. The radial confining structure can result in additional compressive stresses in the lining through the confining against expansion of the lining at elevated temperatures. The final stress distribution in the lining is then contributed from both sources.

(2) The use of a slow heating rate can generally reduce the temperature gradient in the lining. However, for the same hot face temperature, the overall temperature in the lining is higher for lower heating rate which can cause more compressive stresses in the lining due to the confining effects. A more efficient way to release the hot-face compressive stress is to allow expansion of the confining structures (e.g. shell) by, for example, adopting the cooling scheme (2) and a holding period.

(3) It seems that the ways to reduce stresses from both temperature gradient and confining effects are to

(A) use a slow heating rate,

(B) adopt cooling scheme (2), and

(C) adopt a holding period during heating process (heating scheme (2) or (3))

The purpose of adopting (B) and (C) is to increase the temperature of the confining structures such that the confining effects can be reduced through the expansion of the structures.

6.2.2 Heating Rate = 150 ^{o}F/hr

The linings listed in Table 6.1 are now subjected to the heating scheme (1) with the heating rate of 150^{o}F/hr. As found in §6.2.1, none of these linings can sustain the hot face temperature over 1000^{o}F without failure. In Table 6.3 the failure conditions (mode, time, and hot face temperature) of these cases are summarized.

Increasing hot-face heating rate from 50 to 150^{o}F/hr increases the temperature gradient through the lining and results in the increase of the critical stresses induced by temperature gradients; however, if the lining is confined, for the same hot-face temperature the increase of the heating rate generally reduces the total expansion of the lining and results in less stresses induced by the confining layers. Accordingly, the choice of a low or high heating rate for a lining system, from the thermomechanical point of view, will depend on the magnitude of resulting critical stress conditions in the system; the lower stresses are preferred. In fact, the analysis results show that in those highly confined lining systems (C-47 to C-56) the increase of heating rate gives higher hot face temperatures at failures, compared with the same systems with lower heating rate.

It is noted that, although the use of a higher heating rate during the heat-up process can result in less compressive stress (on the hot face) in some lining systems and reduce the chance of a hot-face spalling, the lower heating rate may still be desired for extracting moisture in the gasifier and to stabilize the moisture-contained materials without causing cracking, especially in the low hot-face temperature (<1000^{o}F) range. However, a high heating rate may be adopted for high hot-face temperature range during the heat-up process,

Simulation No.	Lining Configuration	Hot-Face Heating Rate(^{o}F/hr)	Cold-Face Cooling Scheme	Failure Mode	Failure Time(hr)/ Failure Hot-Face Temperature(^{o}F)	Remarks
C-31	#1-1	150	1	2	1.2/257	
C-32	#1-1	150	2	2	1.4/287	
C-33	#1-2	150	1	1	5.8/947	2.8" Joint Failure
C-34	#1-2	150	2	1	6.0/977	2.8" Joint Failure
C-35	#2-1	150	1	3	4.0/677	
C-36	#2-1	150	2	3	4.2/703	
C-37	#2-2	150	1	3	3.8/647	
C-38	#2-2	150	2	3	3.8/647	
C-39	#2-3	150	1	1	5.0/827	0.5" Joint Failure
C-40	#2-3	150	2	1	5.0/827	0.5" Joint Failure
C-41	#2-4	150	1	1	5.8/947	0.5" Joint Failure
C-42	#2-4	150	2	1	5.6/917	0.5" Joint Failure
C-43	#3-1	150	1	1	4.2/707	
C-44	#3-1	150	2	1	4.2/707	
C-45	#3-2	150	1	1	5.2/857	0.5" Joint Failure
C-46	#3-2	150	2	1	5.0/827	0.5" Joint Failure
C-47	#3-3	150	1	1	4.4/737	
C-48	#3-3	150	2	1	4.4/737	
C-49	#4-1	150	1	1	4.6/767	
C-50	#4-1	150	2	1	4.6/767	
C-51	#4-2	150	1	1	4.8/797	
C-52	#4-2	150	2	1	4.8/797	
C-53	#4-3	150	1	1	5.0/827	
C-54	#4-3	150	2	1	5.0/827	
C-55	#4-4	150	1	1	4.6/767	
C-56	#4-4	150	2	1	4.6/767	

Note: (1) Length of joint failure is measured from the outer face of primary lining.
(2) Failure modes : Mode 1 : Hot-face spalling
Mode 2 : Severe joint failure
Mode 3 : Steel yielding

Table 6.3 Predicted Failures for the Cases Studied (Constant Heating Rate = 150^{o}F/hr)

especially when creep is significantly developed (see §6.4).

The patterns of stress distributions, temperature distributions, and failure modes of the cases studied in this section is similar to those of the associated cases described in §6.2.1. Hence, no additional figures are provided or further discussion given associated with these cases.

§ 6.3 HEATING SCHEME (2)

With the heating scheme (2) the hot face of the linings is heated by repeating a subset of the heating schedule which is composed of a constant heating period and a hold period (Fig. 6.4). Based on the analysis results and discussions in the previous sections (§6.2), the emphasis with the following analyses is on two practical lining configurations:

Case CH-1: A 9" 90% $A\ell_2O_3$ primary lining, with a 3" back-up compressible layer (same as C-12). The Young's modulus (E) for the material used in compressible layer is taken to be a parameter: the values of $1x10^5$ psi and $1x10^4$ psi are chosen for E in these studies. The cooling scheme (2) is used for the system due to its capability in reducing confining stress.

Case CH-2: A 9" 90% $A\ell_2O_3$ primary lining, with a 6" SiC-brick compressible layer and a 3" compressible layer. Perfect joints are assumed over the interfaces between the bricks. Previous analyses showed that in such a system the lining behavior is not sensitive to the E value for the specific compressible layer; $E = 1 \times 10^5$ psi is adopted for the present study .

Considering the requirement of a low heating rate in the low (hot-face) temperature range, 50°F/hr is adopted for the heating rate during the constant heating period. The interfaces between the two layers are assumed perfectly in contact if the normal stress over the interface is compression, and open if the stress is tension. The previously separated two layers may be contacted again if the gap between two adjacent faces of the two layers reduces to zero.

The case CH-1 is studied first. Fig. 6.31 shows the histories of the hot-face temperature and the shell temperature. Fig. 6.32 gives the maximum tensile-stress history in the shell, with E = $1x10^5$ psi or E = $1x10^4$ psi. Fig. 6.33 gives the maximum compressive-stress histories in the compressible layers, with E = $1x0^5$ psi or E = $1x10^4$ psi.

It can be seen that, when E = $1x10^5$ psi is adopted for the compressible layers, the confining stress is so high that the spalling occurs on the hot face during the heat-up; when the Young's modulus E is reduced to $1x10^4$ psi, the hot-face compressive stress can be reduced to a level that spalling does not occur before any significant creep developes. Once the creep becomes significant in the near field of the hot face, it can effectively reduce the compressive stress on the hot face, and the location of the maximum compressive stress moves away from the hot face. The evolution of the stresses, in conjunction with the associated temperature distributions for the case CH-1 (E=$1x10^4$ psi) is presented in Figs. 6.34 to 6.39 which show the results at selected intermediate steps during the heat-up. High compressive stresses (see Fig. 6.38) which are in the direction approximately parallel to and in some distance behind the hot face, and which are maintained for a long

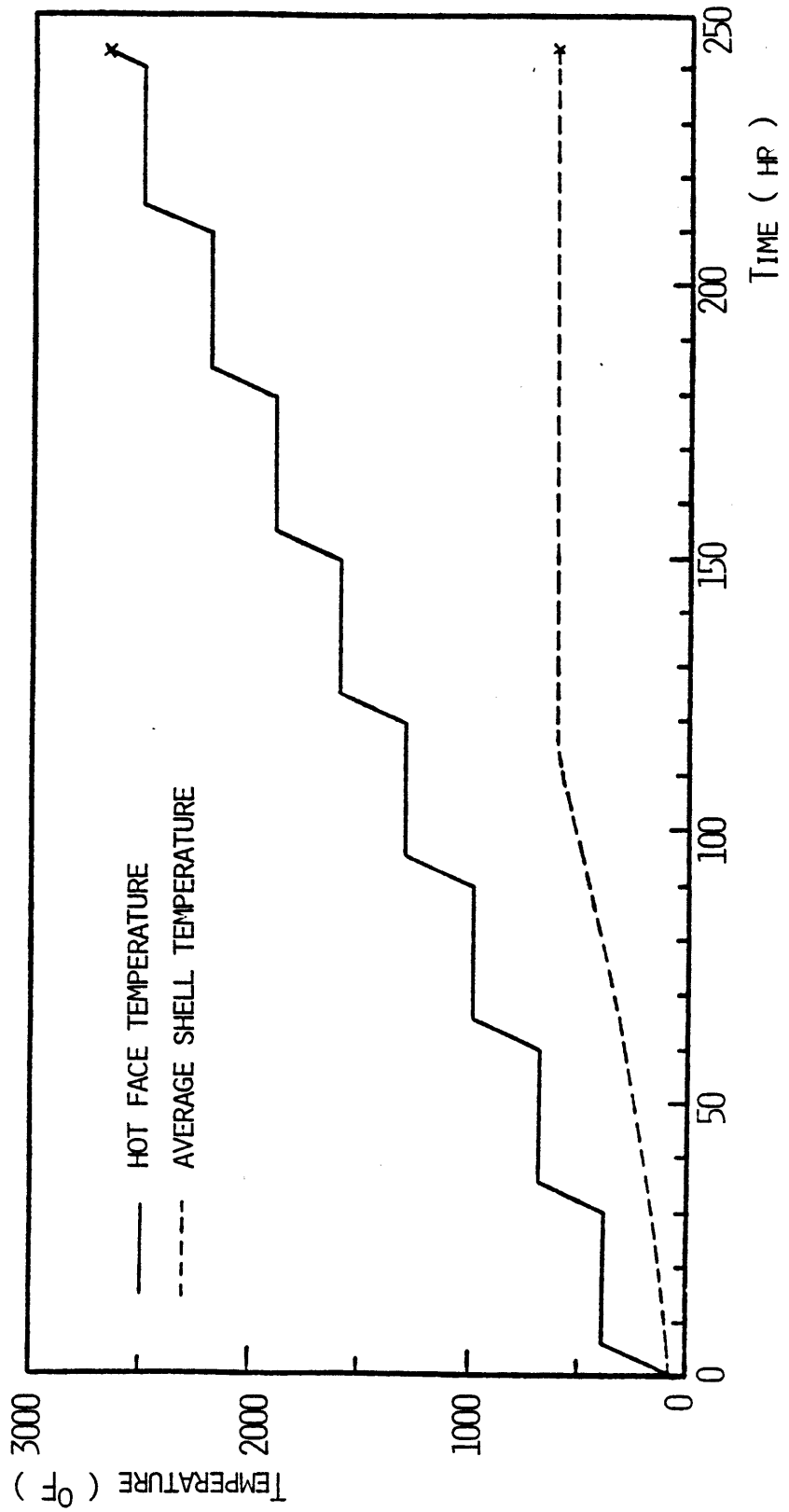

Figure 6.31 Temperature Histories (Case CH-1)

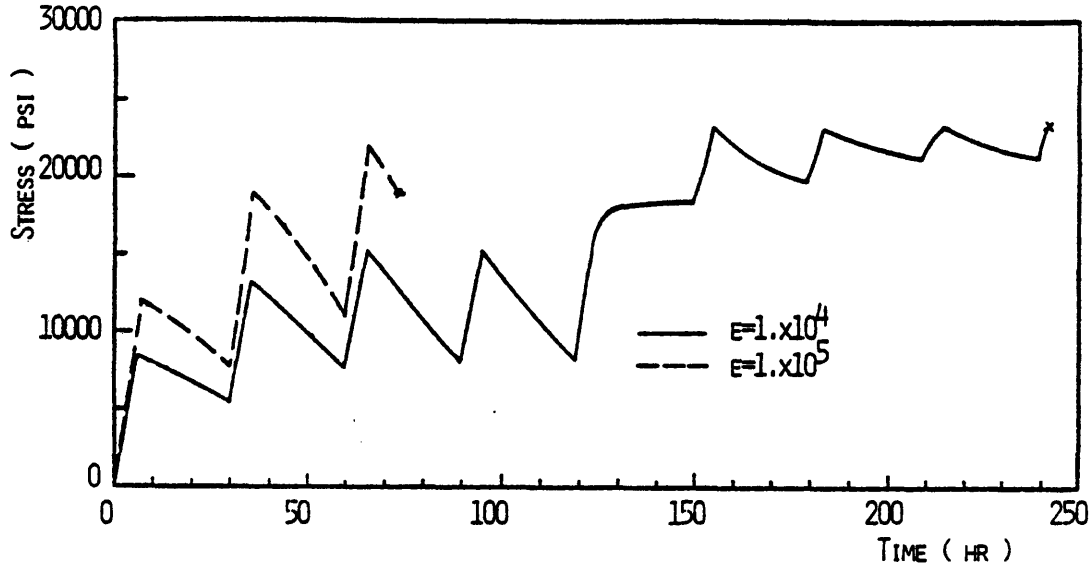

Figure 6.32 Histories of Maximum Tensile Stress in Steel Shell (Case CH-1)

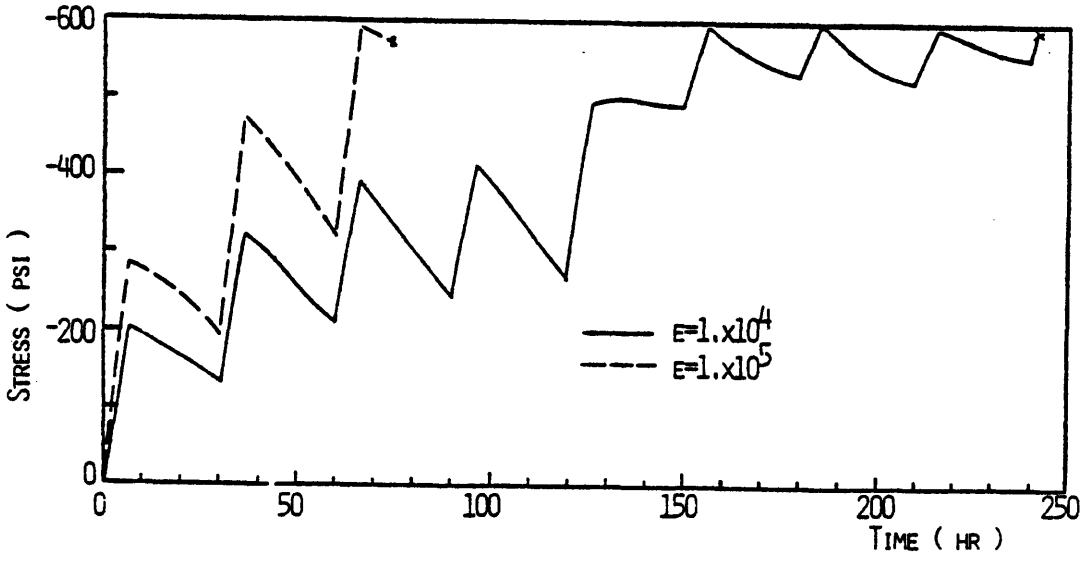

Figure 6.33 Histories of Maximum Compressive Stress in Compressible Layer (Case CH-1)

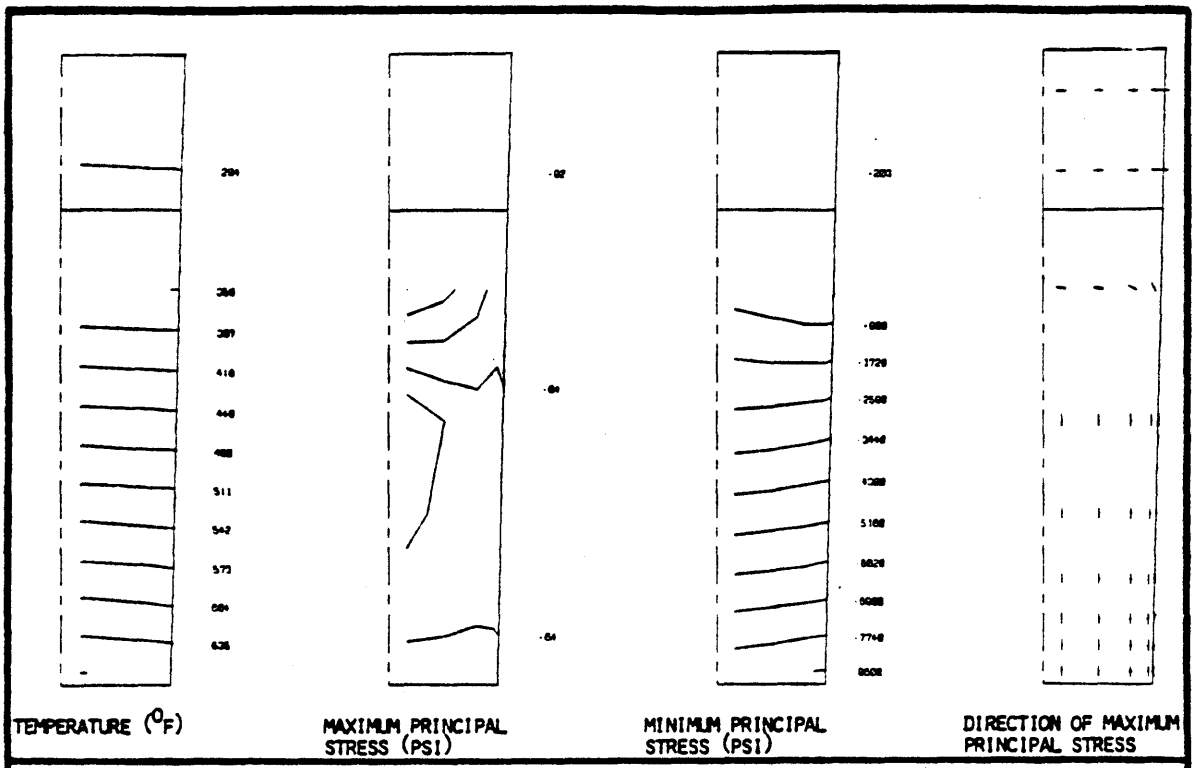

Figure 6.34 Temperature and Stress Distributions (Simulation No. CH-1, Time = 60.0 hr, Hot-Face Temperature = 677°F)

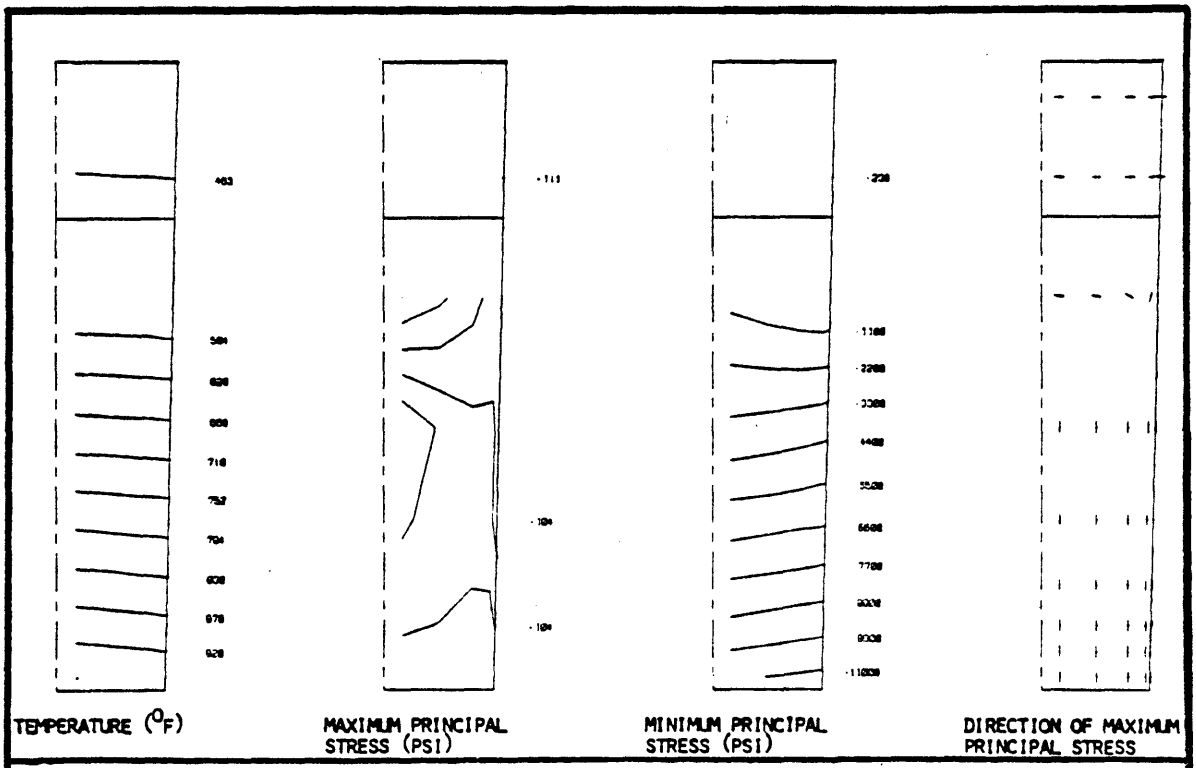

Figure 6.35 Temperature and Stress Distributions (Simulation No. CH-1, Time = 90.0 hr, Hot-Face Temperature = 977°F)

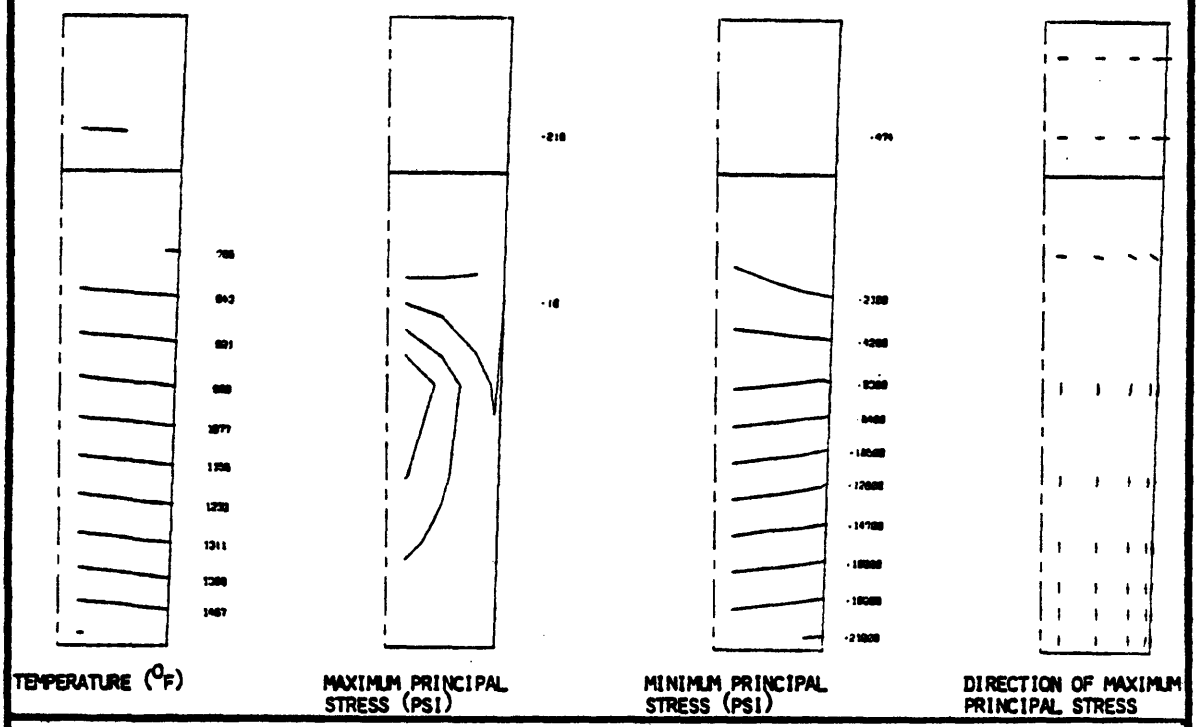

Figure 6.36 Temperature and Stress Distributions (Simulation No. CH-1, Time = 123.0 hr, Hot-Face Temperature = 1427°F)

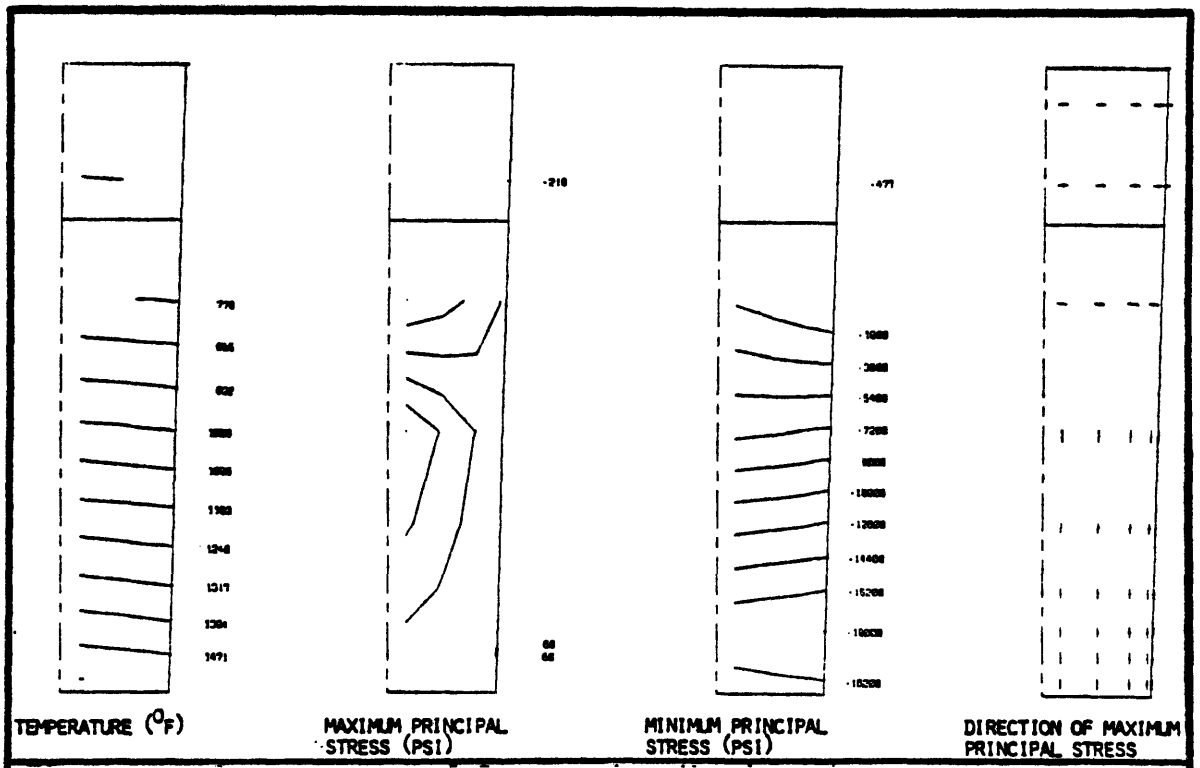

Figure 6.37 Temperature and Stress Distributions (Simulation No. CH-1, Time = 150.0 hr, Hot-Face Temperature = 1577°F)

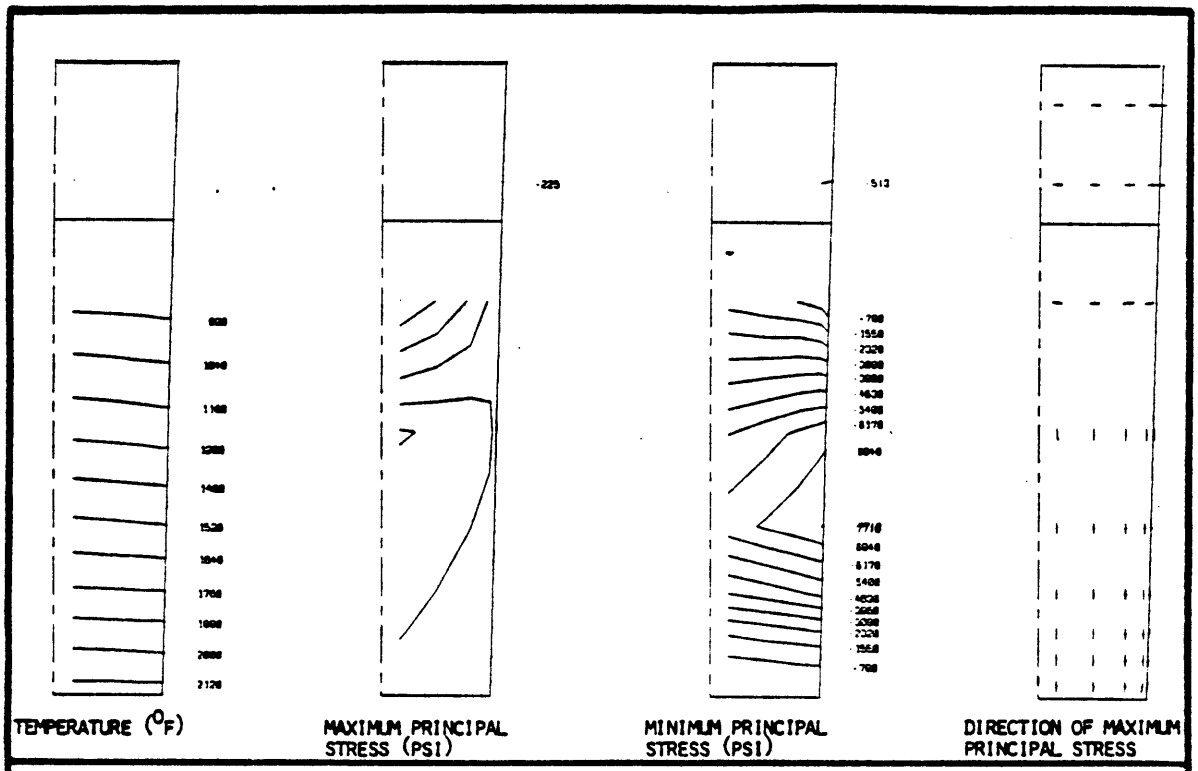

Figure 6.38 Temperature and Stress Distributions (Simulation No. CH-1, Time = 210.0 hr, Hot-Face Temperature = 2177°F)

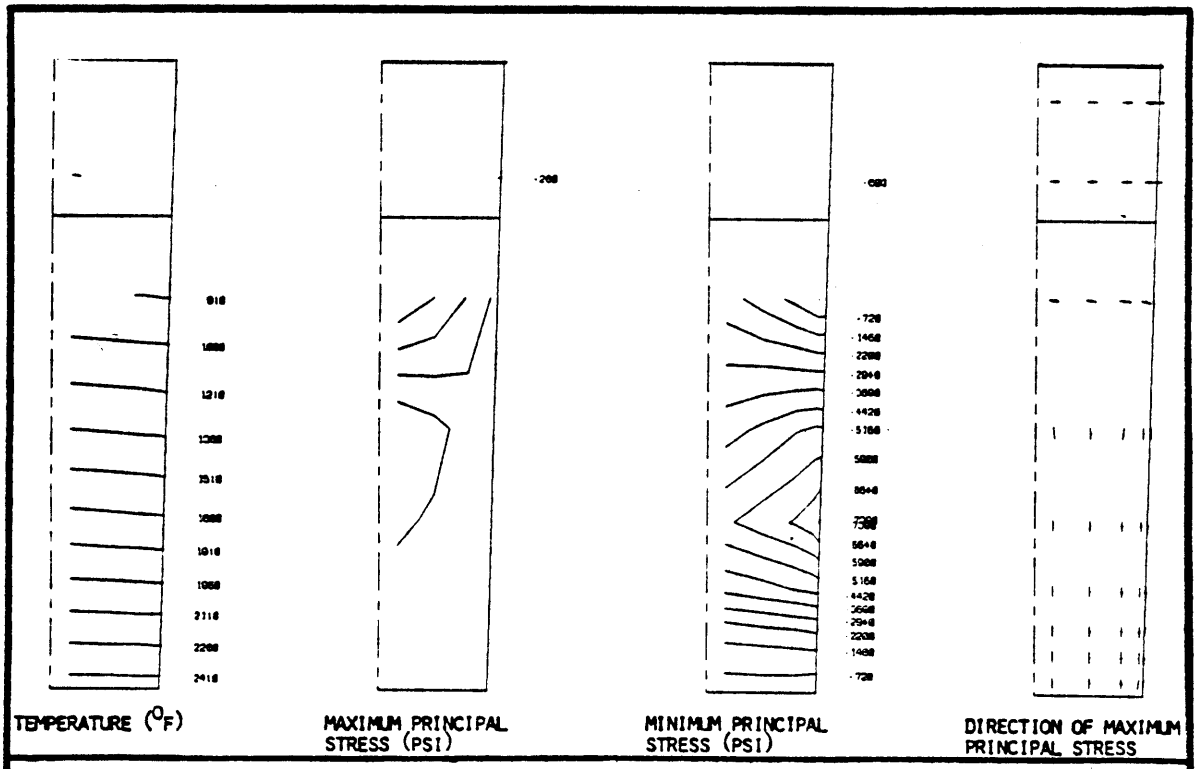

Figure 6.39 Temperature and Stress Distributions (Simulation No. CH-1, Time = 216.0 hr, Hot-Face Temperature = 2477°F)

period of time during the operation period, can cause creep rupture resulting in the formation of cracks (approximately parallel to and behind the hot face) in the linings.

When the hot face temperature exceeds the critical temperature of slag penetration T_c, the portion of the lining from the hot face is penetrated by the slag (see Chapter 4). At elevated temperatures considerable reduction in the strength of the refractories caused by slag penetration, creates a weak zone next to the hot face. This weak zone is prone to fail and spall in excessive compressive hoop stress. In fact, for the case CH-1 with $E = 1x10^4$ psi, T_c is assumed to be 2650°F and the analysis ends when the hot face temperature exceeds T_c, due to the occurrence of spalling. For the safety of the linings adopting 90% Al_2O_3 refractory, the hot face temperature should be controlled to be lower than T_c during the heat-up process and at least during the initial stage of the operating period.

The required strength of the compressible materials is of interest. For the case CH-1 adopting $E = 1x10^4$ psi, the maximum compressive stress in the compressive layer is approximately 600 psi (Fig. 6.33). The compressive strength of the compressible materials should be higher than this stress. It is noticed that for a typical compressible material with E at the order of $1x10^4$ psi, the compressive strength can be quite low. Failure of the compressible materials in compression may result in a significant opening between the primary lining and the shell. However, the use of a high stiffness compresssive material (e.g. $E = 1x10^5$ psi) can result in a high confining stress which may cause the spalling problem. Hence, the trade-off between the material strength and the stiffness of the compressible layers should be studied. If the solution

can not be obtained for a certain lining system, redesign of the lining configurations would be necessary.

The case CH-2 which adopts the cooling scheme (2) is studied next. In this system the primary lining ($A\ell_2O_3$) layer is highly confined by the SiC layer (due to the relatively low thermal expansion of the layer) and the shell, resulting in high compressive stresses near the hot face. In fact, spalling occurs at the hot face temperature of 877°F due to such high stress. Fig. 6.40 shows the histories of the hot-face temperature and average shell temperature. Fig. 6.41 gives the histories of maximum tensile stress in the SiC layer and in the shell. The relative thermal expansion between layers has significant effects on the lining behavior. It is found that the shell stress drops to zero after 51 hr. This is the result of the separation between the shell and the compressible layer. Fig. 6.42 gives the history of the maximum compressive stress in the compressible layer. Also separation is found between the compressive layer and the SiC layer, indicated by the zero stress in the compressible layer. Such separations between the layers, which are caused by the low thermal expansion of the SiC material, should be avoided in the design. One way to solve this problem is to use the cooling scheme (1) by which the shell and the compressible layers may expand less than the SiC layer does. However, the analysis results show that the adopting of the cooling scheme (1) increases the hot-face compression and accelerates the spalling process (see Figs. 6.40 to 6.42)

Studies on the abovementioned two cases of the linings and those cases in section 6.2 reveal the difficulty in finding an optimal operational scheme to simultaneously eliminate all types of undesired

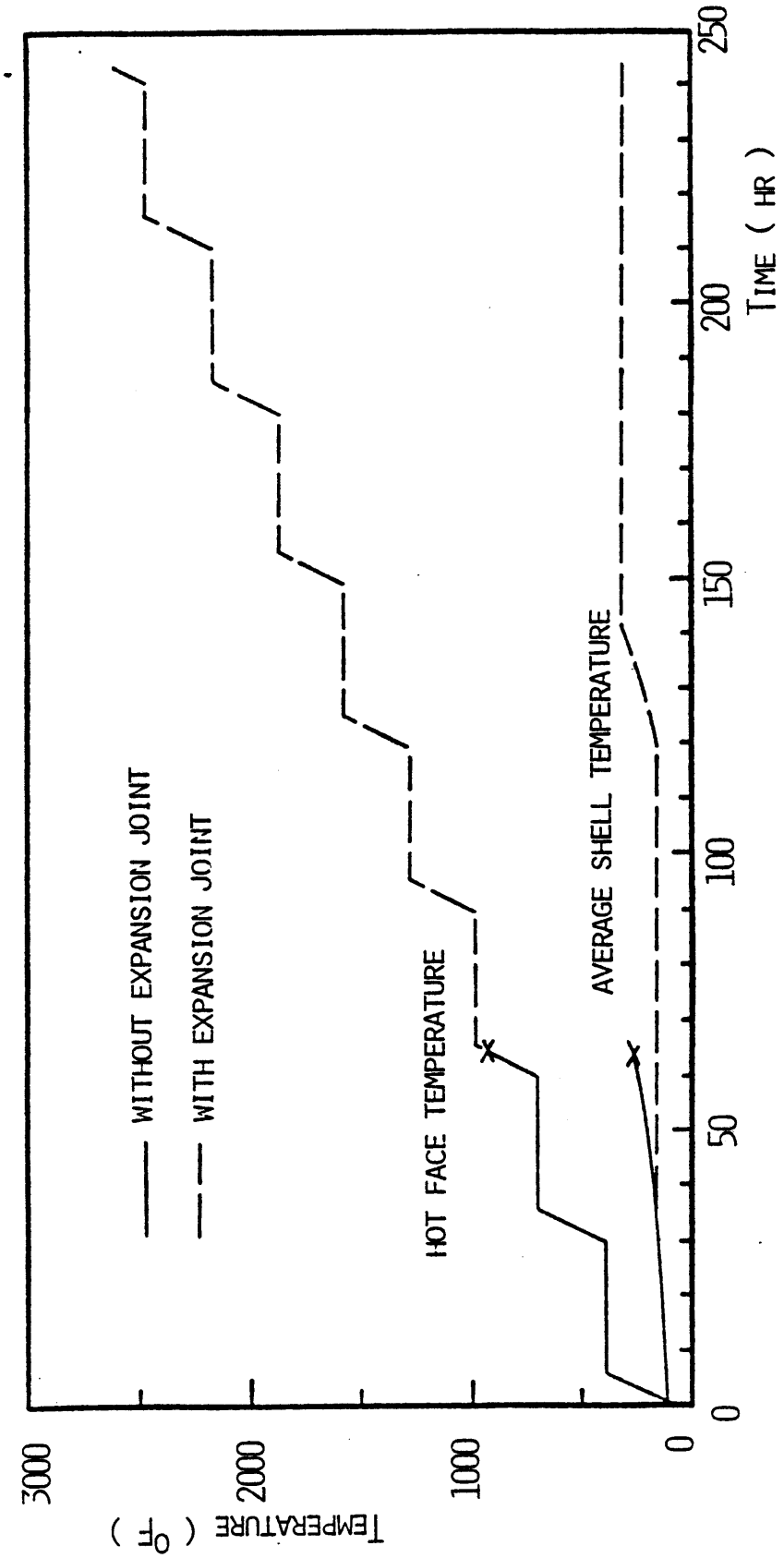

Figure 6.40 Temperature Histories (Case CH-2)

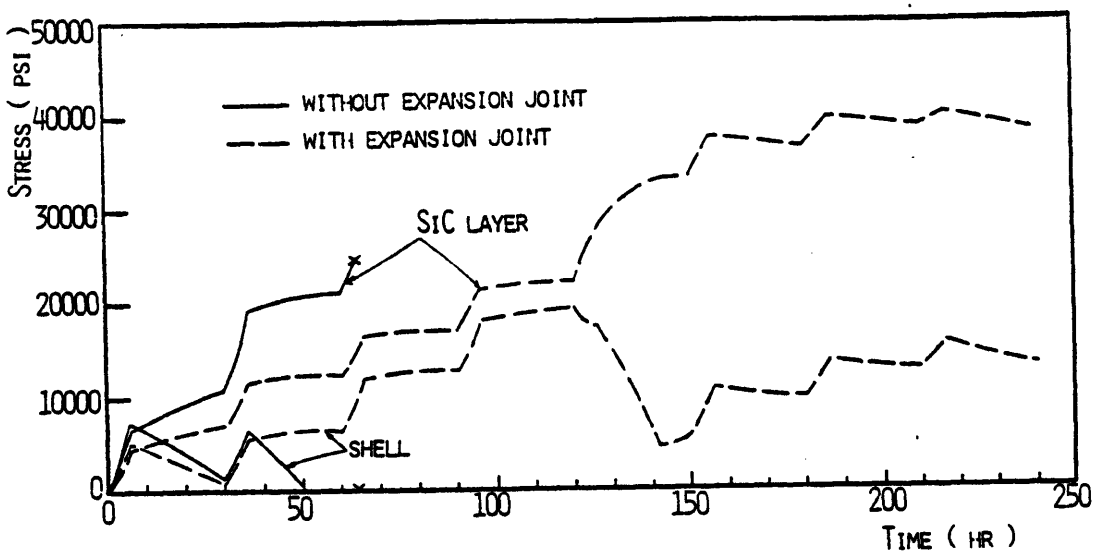

Figure 6.41 Histories of Maximum Tensile Stresses in Steel Shell and SiC Layer (Case CH-2)

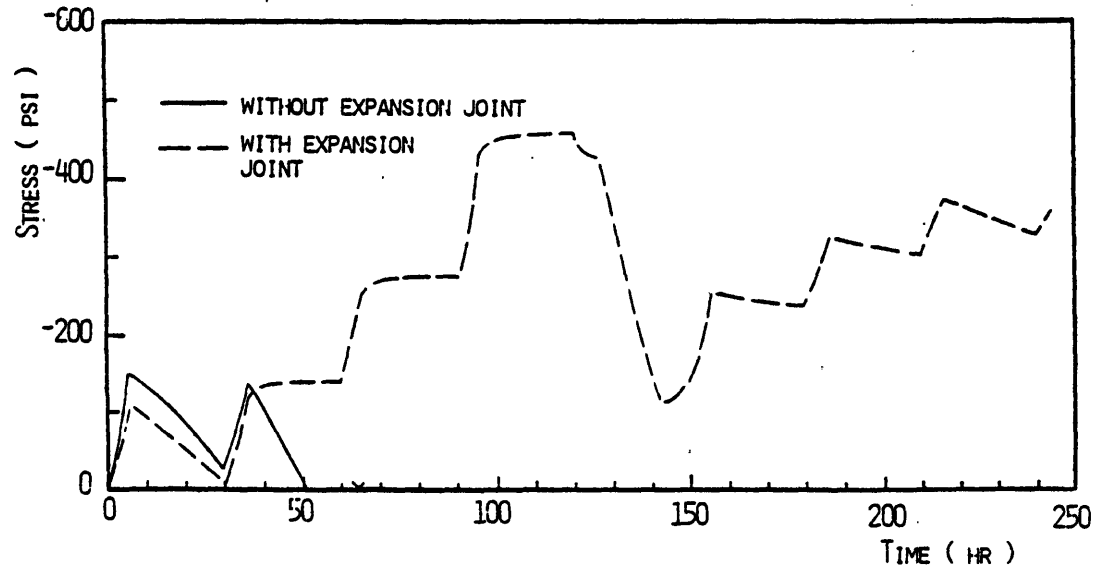

Figure 6.42 Histories of Maximum Compressive Stresses in Compressible Layer (Case CH-2)

failures. It can be seen from these studies that for most lining systems the improvement of lining safety during the heating process by adjusting the heating schedule may be somehow limited. Further adoption of special design features for the lining system seems necessary. One possibility of such a design is the adoption of expansion joints extending from the hot face (Fig. 6.43).

Expansion joints between the bricks allow a brick to expand without causing confining stress from the adjacent bricks over the joint interfaces. Locating such an expansion joint at the brick to brick interface, extending from the hot face (as shown in Fig. 6.43), can significantly reduce the hot-face compressive stress. On the other hand, the joint openings yield ways to gas penetration which may damage the vessel shell especially when the shell temperature is high. Based on these considerations, a proper design for the expansion joints should optimize the size (L) and the width (W) of the joints, by which the hot-face stresses can be reduced sufficiently while the joint can still be closed and tight enough during the operating periods to reduce the potential of gas penetration. These requirements can be achieved by choosing L and W in such a way that the joints are open during the low to intermediate hot-face temperature ranges to allow bricks to expand freely, and closed thereafter to assure tightness against gas penetration at higher hot-face temperature levels.

The effects of the use of an expansion joint are studied in the case CH-2. In this case study the joint length L is taken to be 3" and the joint opening at room temperature W is designed in a way that joint closes at hot face temperture 1000^{o}F. Based on the consideration of hot-gas corrosion the cooling scheme (1) is adopted when the joint is not

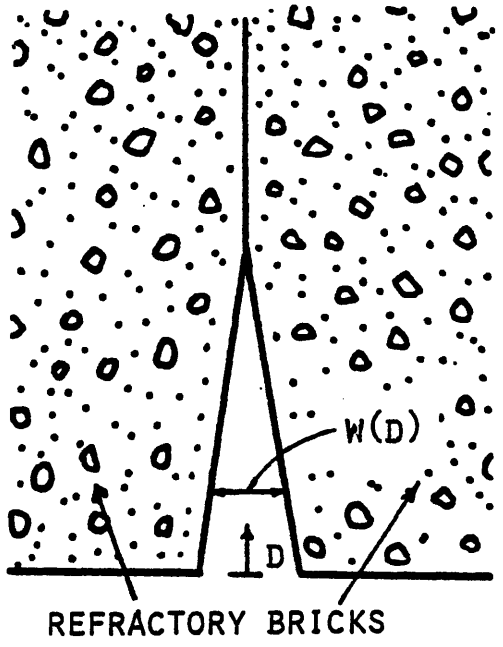

Figure 6.43 Expansion Joint Between Bricks

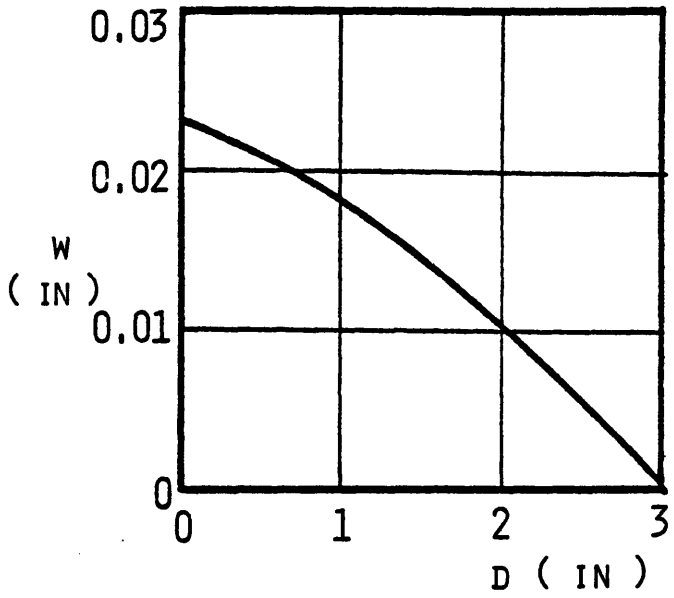

Figure 6.44 Width of Expansion Joint (Case CH-2)

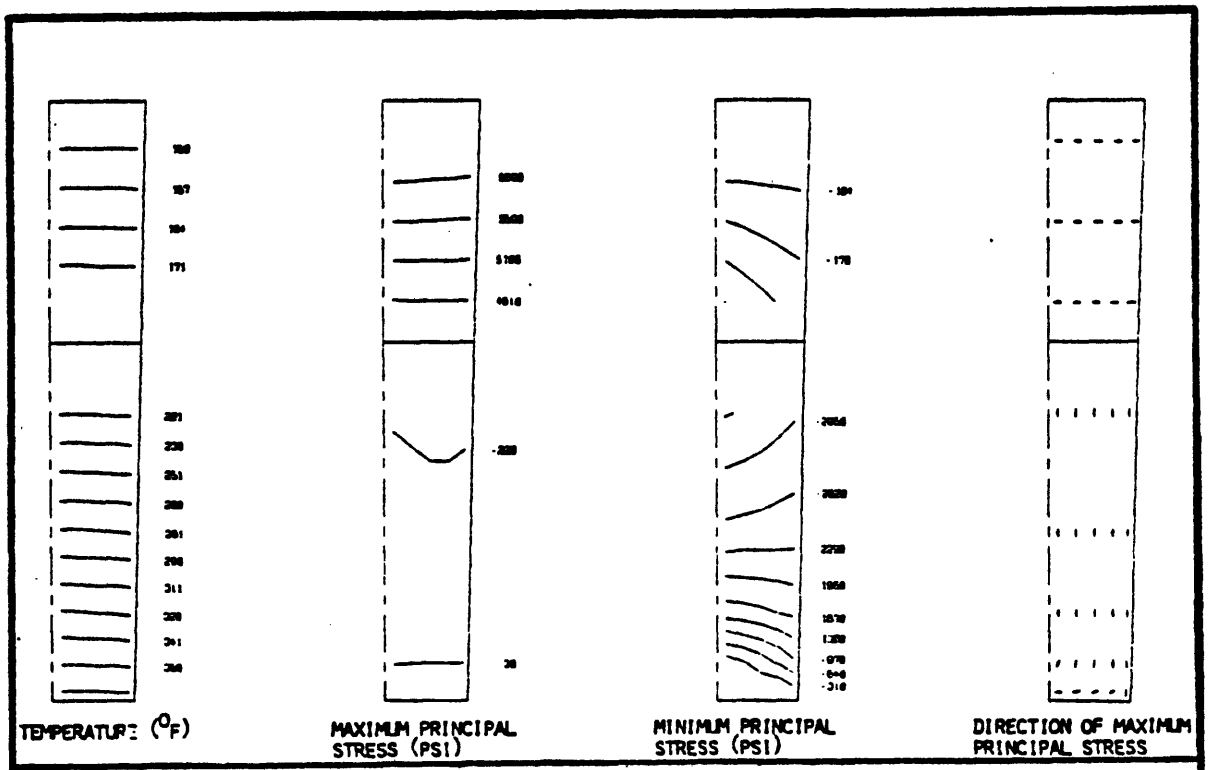

Figure 6.45 Temperature and Stress Distributions (Simulation No. CH-2, Time = 30.0 hr, Hot-Face Temperature = 377°F)

completely closed. The cooling scheme (2) may be adopted after the joint is closed, and, by adopting such a scheme, the separation between the layers should not occur. Fig. 6.40 shows the hot-face temperature and the shell-temperature histories by adopting the abovementioned schemes. To avoid the separation between layers, the maximum allowable shell temperature used for scheme (2) is chosen to be 300°F. The resulting maximum-tensile-stress history in steel shell and the maximum-compressive stress history in the compressible layer are shown in Figs. 6.41 and 6.42 Fig. 6.44 shows the required widths (W) for the expansion joint to close at 1000°F. The stress and temperature contours and principle stress directions through the primary lining at several time steps are shown in Figs. 6.45 to 6.51. It can be seen from the analysis results of this example that the adoption of expansion joints can effectively reduce the occurrence of severe failures during heat-up process.

6.4 HEATING SCHEME (3)

Although the adoption of the heating scheme (2) may not cause severe damage in a lining system, the generally required long heat-up period is not economical. The adoption of higher heating rate with shorter holding period should be considered, which can shorten the heat-up period without causing severe damage to the lining system. This alternative may be possible at high-temperature levels due to the effective stress relaxation at these levels.

Case studies are given with such high heating rate at high temperature levels. The lining configuration adopted in the case CH-2 (§6.3) with 9" Al_2O_3 primary lining, 6" SiC secondary lining and 3"

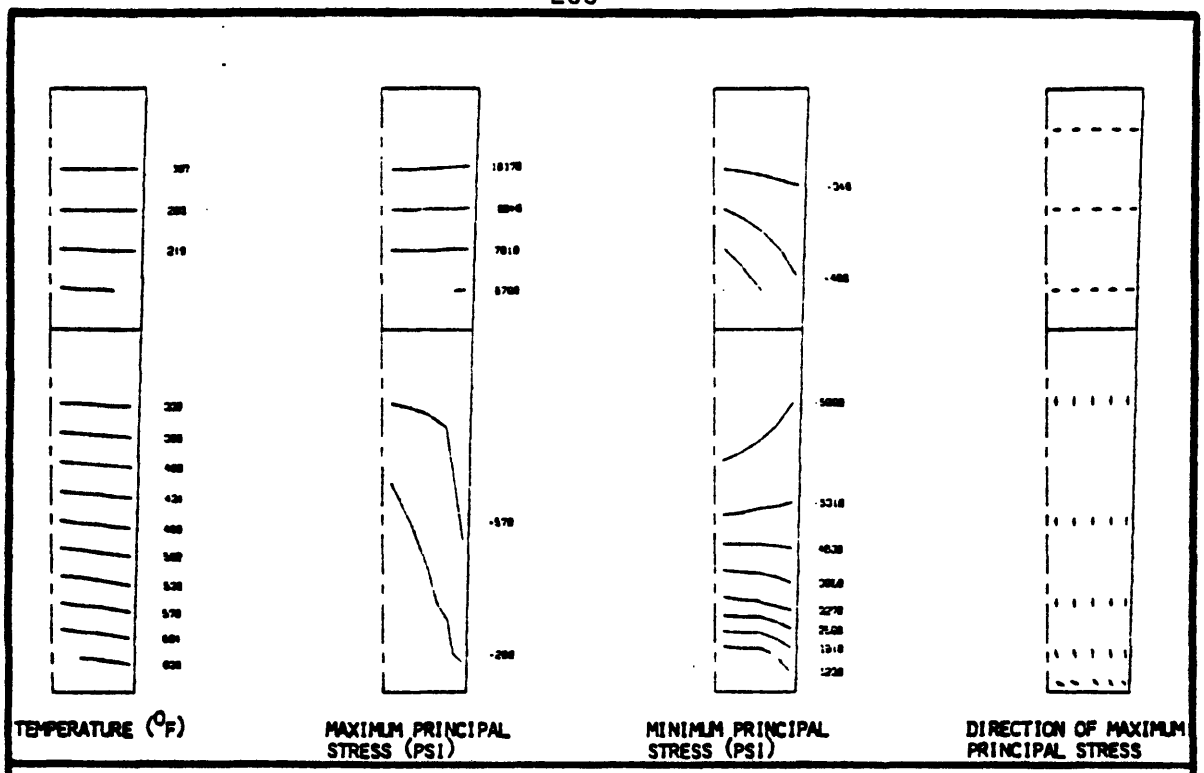

Figure 6.46 Temperature and Stress Distributions (Simulation No. CH-2, Time = 60.0 hr, Hot-Face Temperature = 677°F)

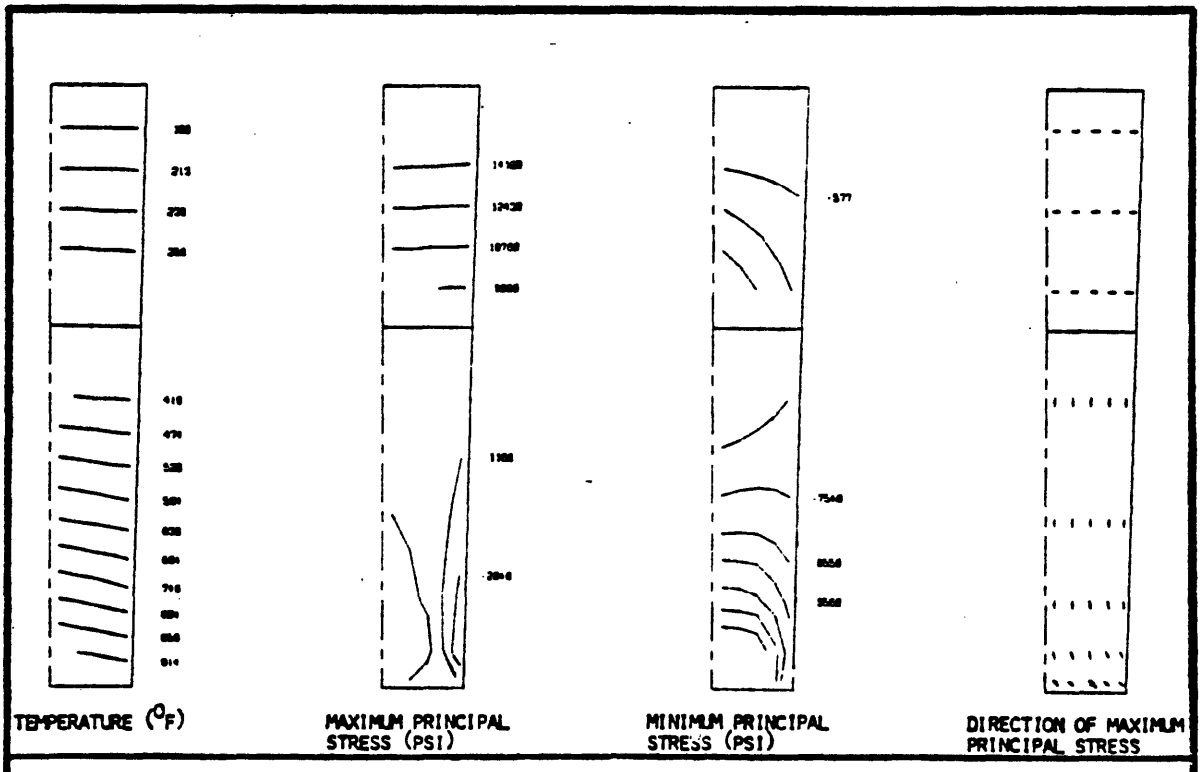

Figure 6.47 Temperature and Stress Distributions (Simulation No. CH-2, Time = 90.0 hr, Hot-Face Temperature = 977°F)

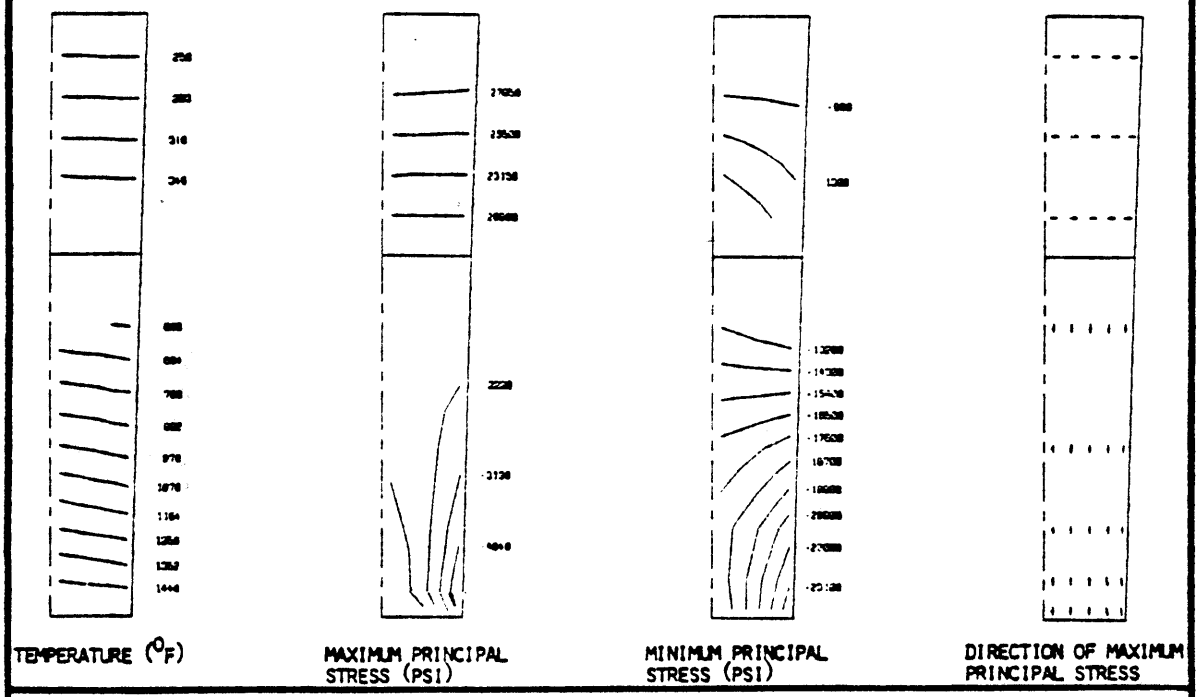

Figure 6.48 Temperature and Stress Distributions (Simulation No. CH-2, Time = 126.0 hr, Hot-Face Temperature = 1577°F)

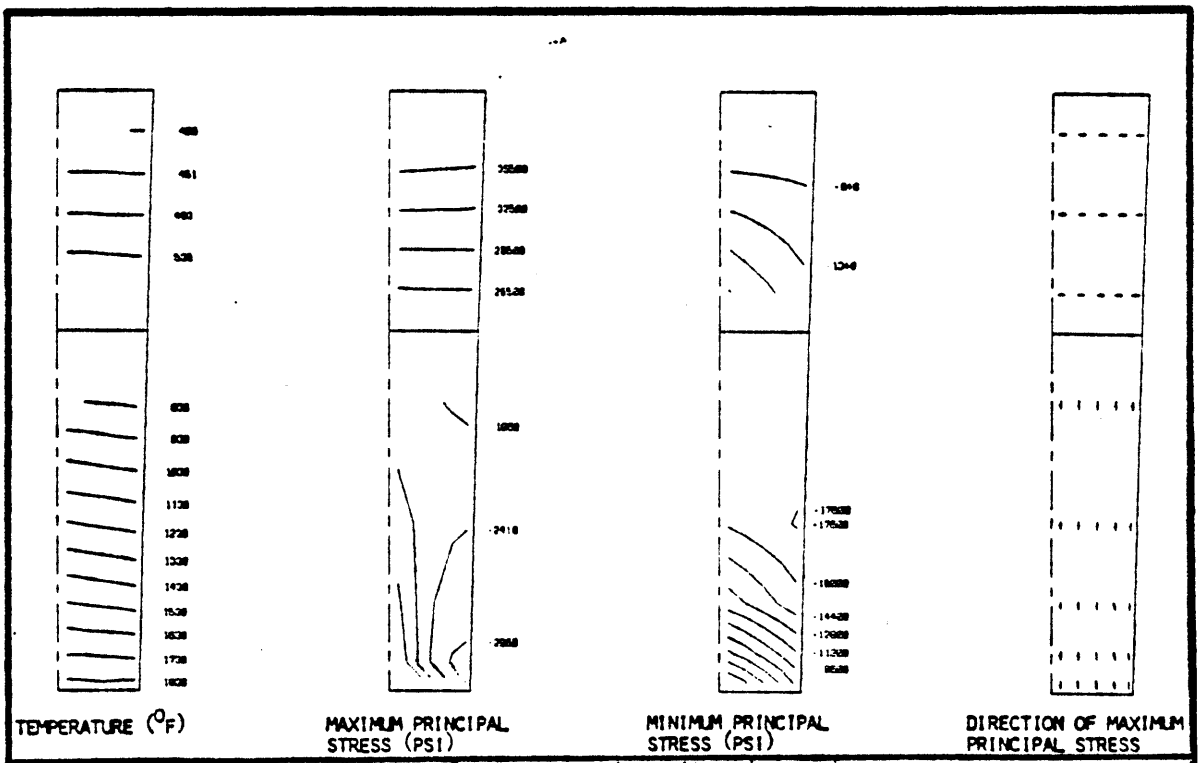

Figure 6.49 Temperature and Stress Distributions (Simulation No. CH-2, Time = 180.0 hr, Hot-Face Temperature = 1877°F)

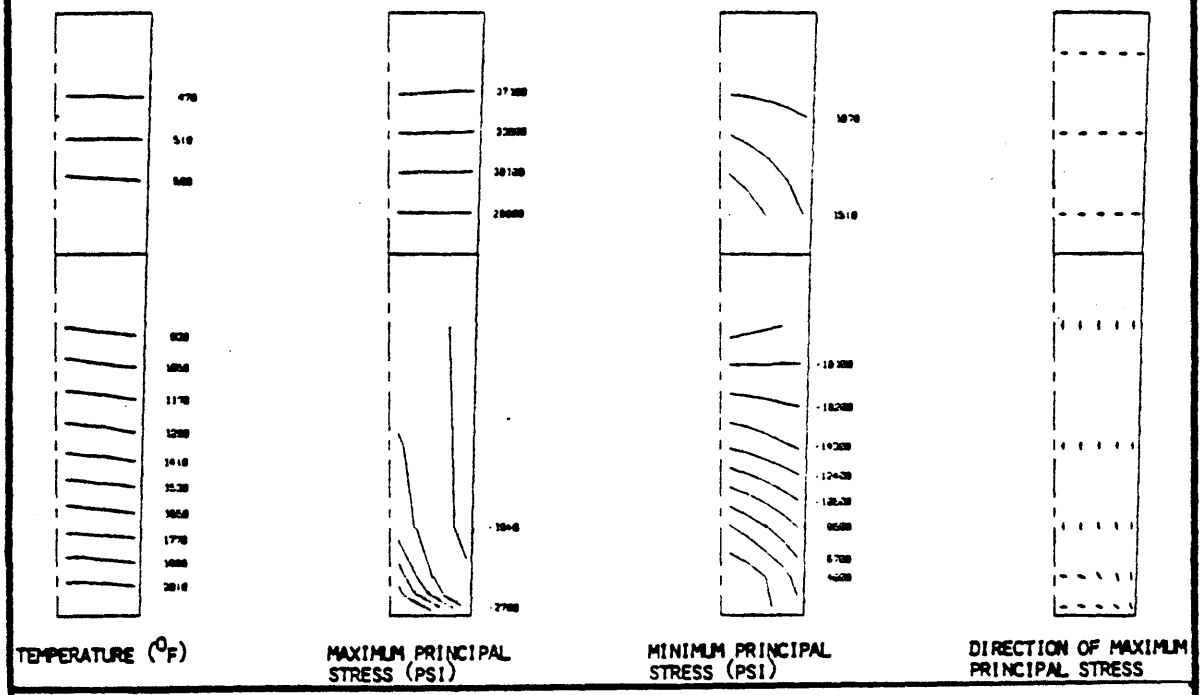

Figure 6.50 Temperature and Stress Distributions (Simulation No. CH-2, Time = 210.0 hr, Hot-Face Temperature = 2177°F)

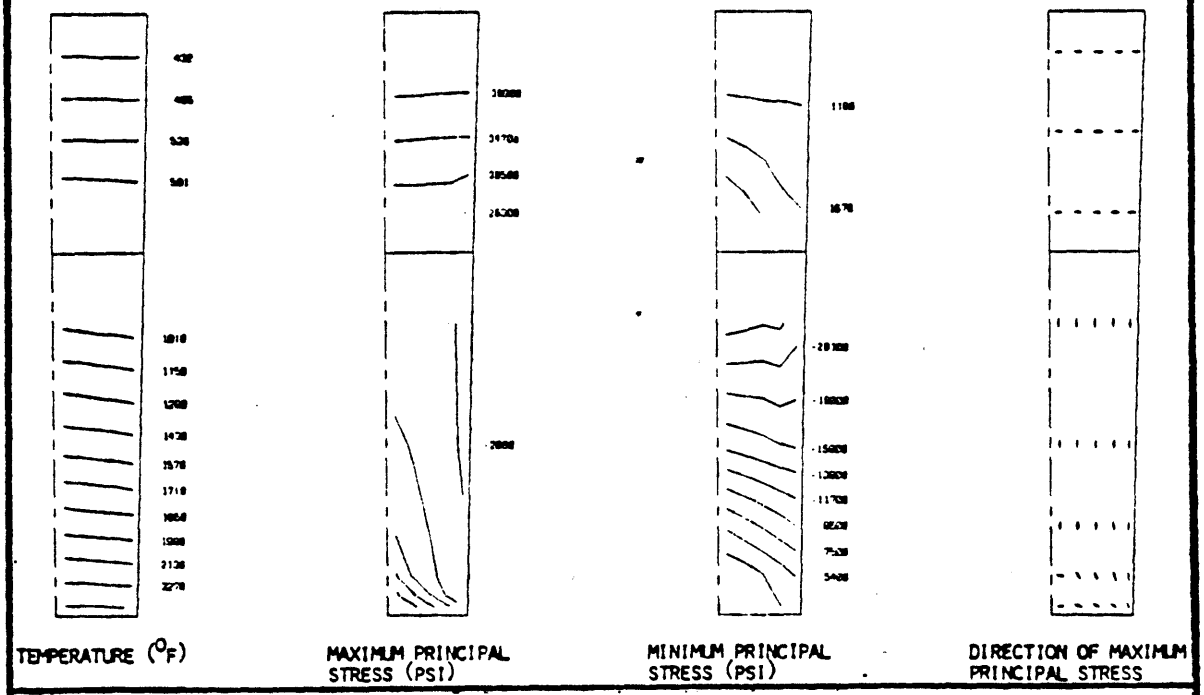

Figure 6.51 Temperature and Stress Distributions (Simulation No. CH-2, Time = 216.0 hr, Hot-Face Temperature = 2477°F)

compressible layer ($E=1x10^5$psi) is adopted for study. A 3" expansion joint extending from hot-face (Fig. 6.43) is adopted. This joint is designed to close at the hot-face temperature of 1000°F. Following four cases which adopt various heating schemes are studied (Fig. 6.52).

Case VH-1: The same heating scheme in case CH-2 is adopted until the hot-face temperature reaches 1877°F, and a constant heating rate of 50°F/hr is adopted thereafter.

Case VH-2: The same as case VH-1 except that the constant heating rate adopted after the hot-face temperature reaches 1877°F is 150°F/hr.

Case VH-3: The same heating scheme as in the case of CH-2 is adopted until the hot-face temperature reaches 1577°F, and a constant heating rate of 50°F/hr is adopted thereafter.

Case VH-4: The same as case VH-3 except that the constant heating rate adopted after hot-face temperature reaches 1577°F is 150°F/hr.

From the analyses, the hot-face and the shell temperature histories, the maximum stress histories in the SiC. layer and the shell, and the maximum compressive stress histories in the compressible layer are shown in Figs. 6.52 to 6.54. The stresses and temperature contours for these cases at high hot-face temperatures and certain time steps are shown in Figs. 6.55 to 6.58.

In these case studies, the adoption of a high heating rate does not cause damage in the primary lining during the heat-up period. Moreover, the critical stress states in shell and the compressible layer are generally reduced, when compared with that in the Case CH-2; however, the

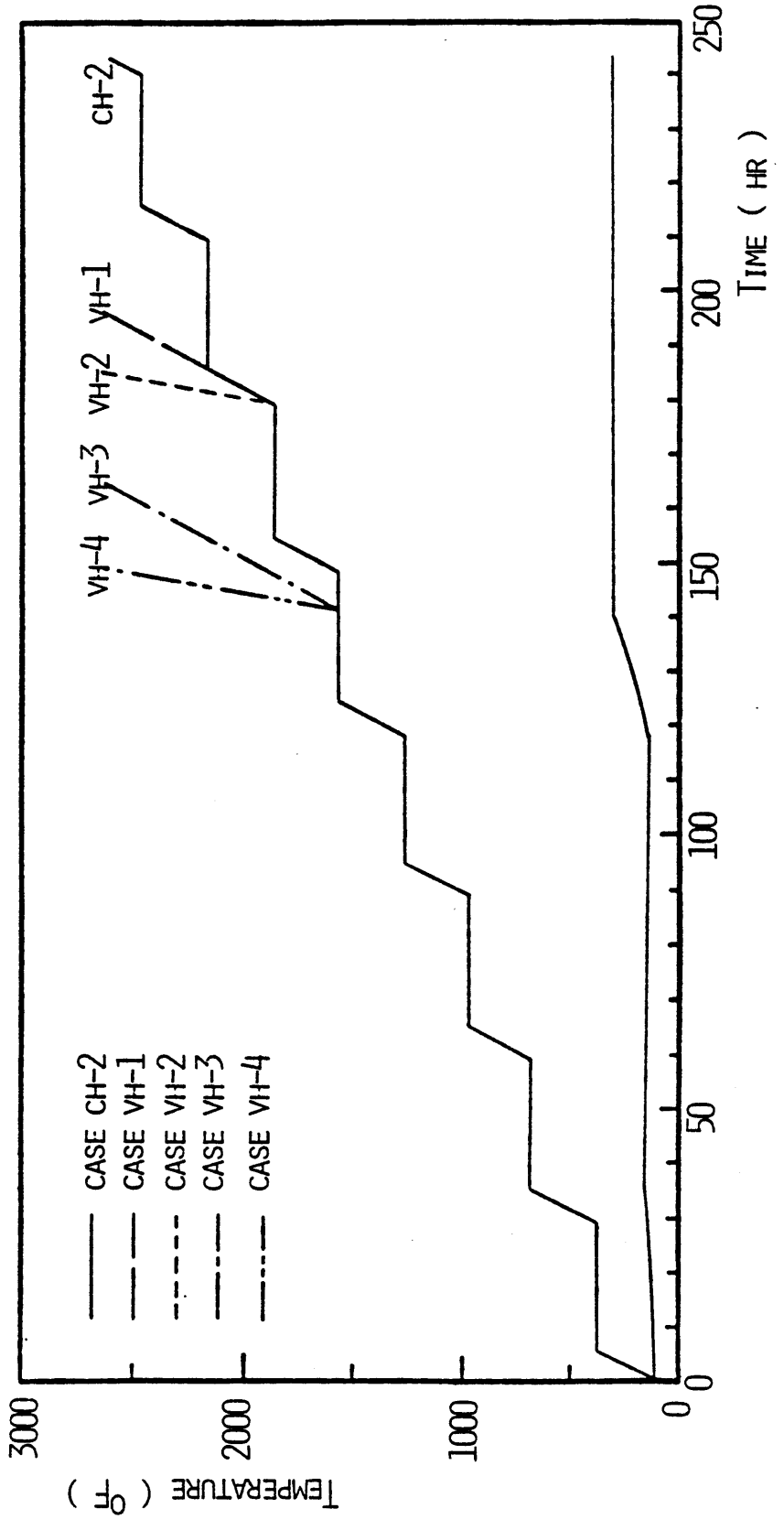

Figure 6.52 Temperature Histories (Cases VH-1 ~ VH-4)

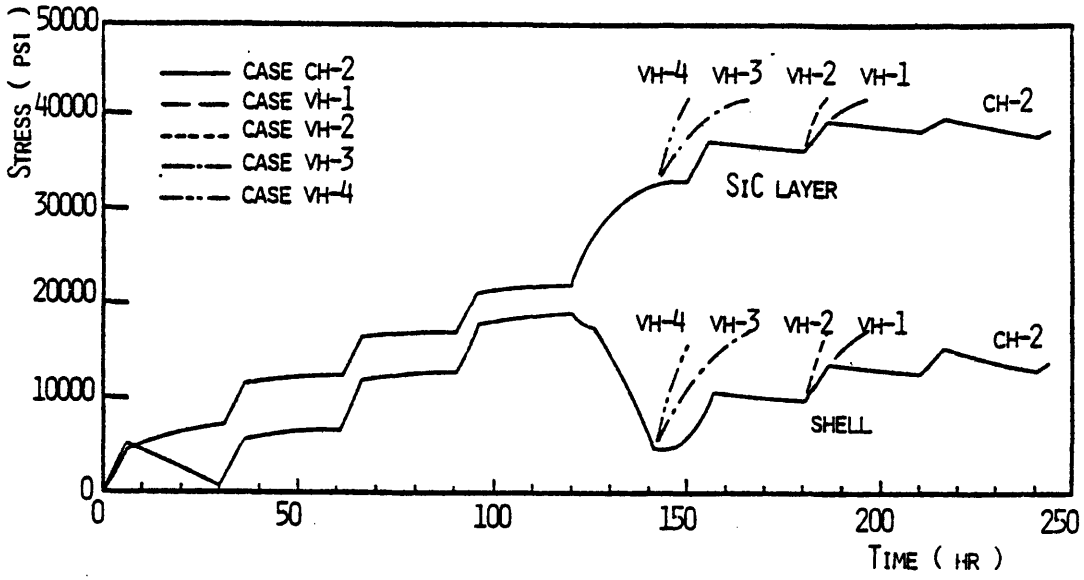

Figure 6.53 Histories of Maximum Tensile Stresses in Steel Shell and SiC Layer (Cases VH-1 ~ VH-4)

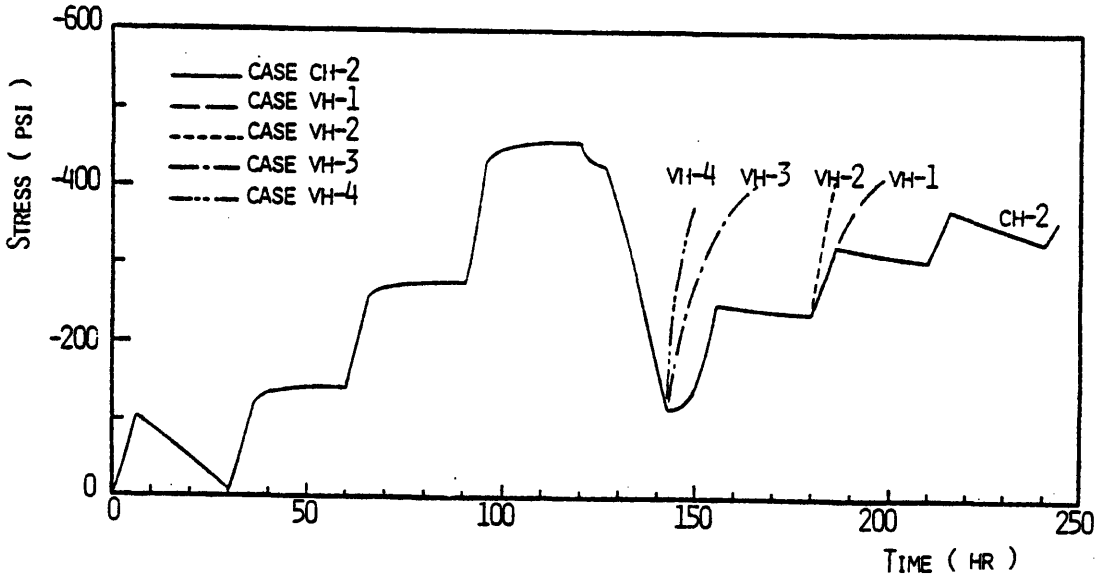

Figure 6.54 Histories of Maximum Compressive Stresses in Compressible Layer (Cases VH-1 ~ VH-4)

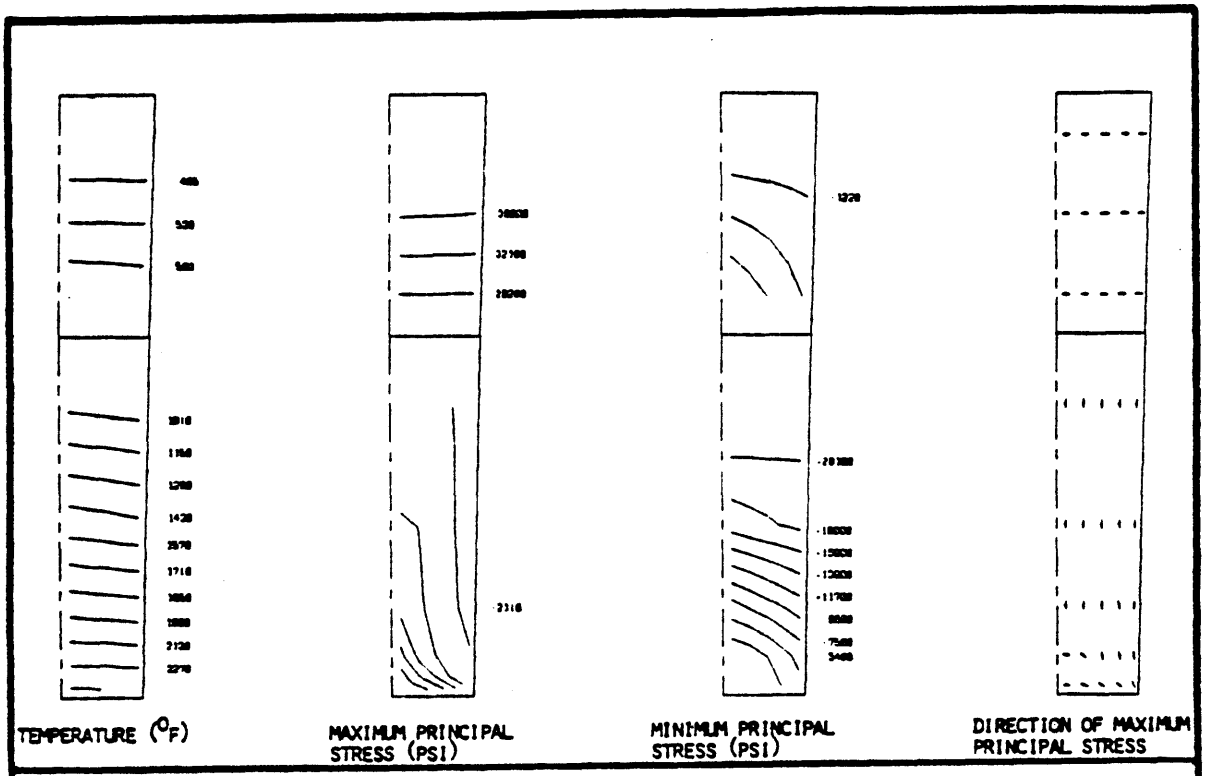

Figure 6.55 Temperature and Stress Distributions (Simulation No. VH-1, Time = 192.0 hr, Hot-Face Temperature = 2477°F)

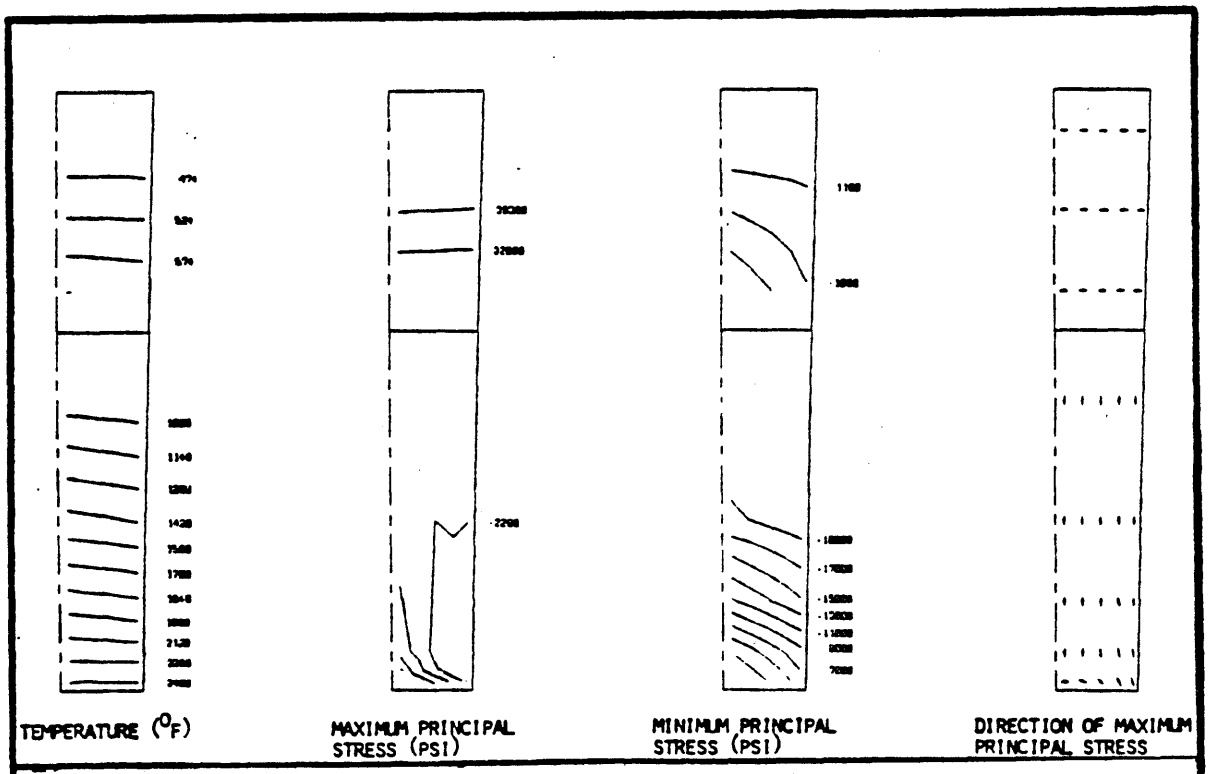

Figure 6.56 Temperature and Stress Distributions (Simulation No. VH-2, Time = 184.0 hr, Hot-Face Temprature = 2477°F)

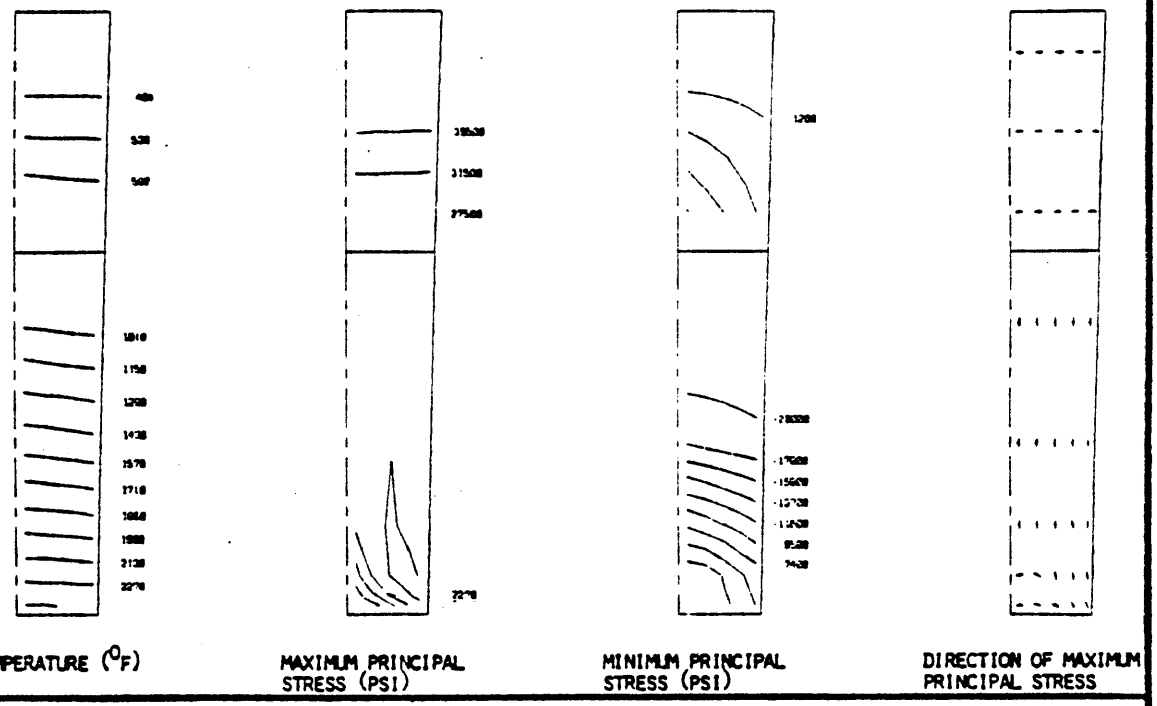

Figure 6.57 Temperature and Stress Distributions (Simulation No. VH-3, Time = 160.0 hr, Hot-Face Temperature = 2477°F)

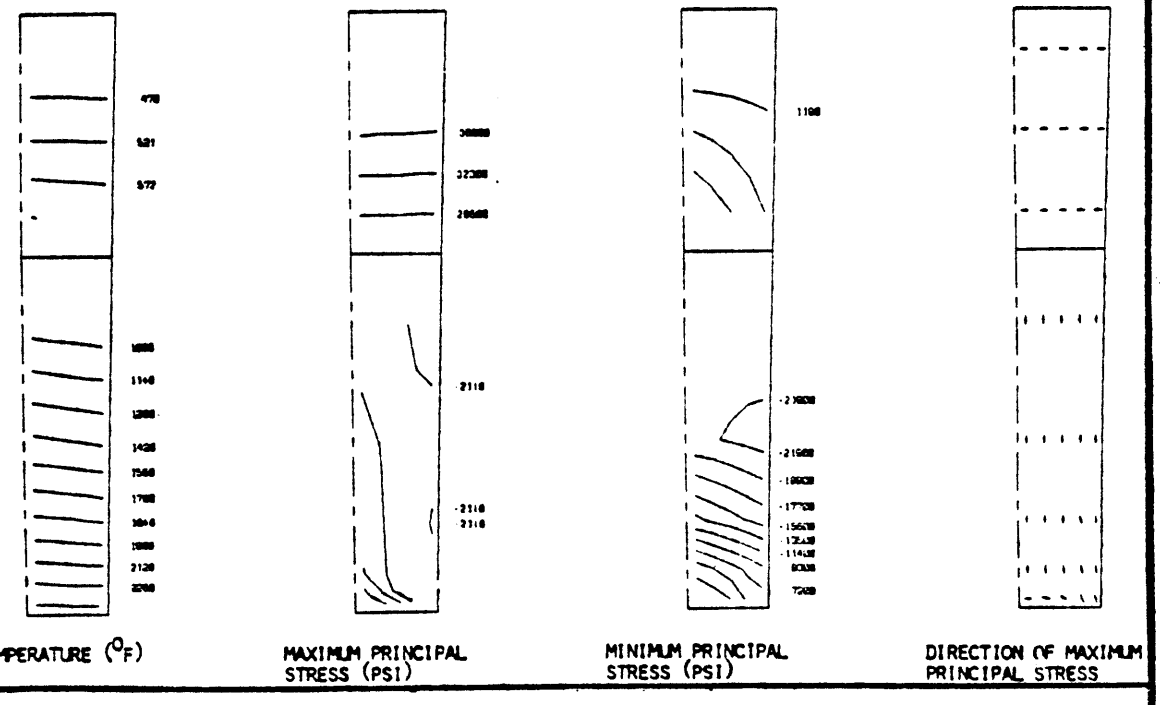

Figure 6.58 Temperature and Stress Distributions (Simulation No. VH-4, Time = 148.0 hr, Hot-Face Temperature = 2477°F)

critical compressive stresses in SiC layers during this period are generally increased, which may result in the tensile failure (cracking) in the SiC layers and the problem of slag penetration.

§6.5 SUMMARY

The determination of proper design and operational schemes for a lining in slagging gasifiers is a challenging problem to the designers. High operating temperatures, high temperature gradients along the lining thickness, and the generally existing interaction between the components of the linings result in a very complex lining behavior in slagging gasification environments.

In this chapter extensive parameter studies have been performed to assess the effects of various design and operational parameters on the thermomechanical behavior of refractory-brick linings during the heat-up process. These parameters include different lining configurations, combinations of lining materials, and operational schemes.

Important findings from these analysis combining the above-mentioned various parameters are summarized as follows:

(1) Stress distributions in the primary lining is generally controlled by the two major sources: (a) temperature gradient through the lining, and (b) confining stress from the shell or the secondary lining. The analyses indicate trade-offs in stress magnitudes produced by the effects from these two sources. That is for a given hot face temperature less thermal gradients would result in a decreased hot face compressive stresses from this source while higher stresses are produced from the confinement effect.

(2) The single-layer lining systems are not ideal for the slagging gasifier. If the linings are not in contact with the vessel shell, the linings experience a severe joint failure due to the high temperature gradient along the lining thickness; on the other hand, if the linings are contacted with the shell, the spalling problem occurs near the hot face of the linings due to the high confining stress from the shell.

(3) The compressible layer is found to be very effective in reducing the confining stress. Proper stiffness and strength of the compressible material to be adopted for a specific lining system can be determined through the analyses. The specific material satisfying such stiffness/strength requirements can then be identified. If the material with those required properties is not available, redesign of the system may be needed.

(4) An expansion joint extending from the hot face can significantly reduce the hot face compression resulting in a better structural system which would be less susceptible to damages from the heating process. Optimal size and widths of the expansion joint should be determined, by which the hot face stresses can be reduced sufficiently while the joint can still be tight enough to reduce the potential of gas penetration during operating periods.

(5) The thermal expansion characterisitcs of the lining materials and the shell material is very important to the lining behavior. For example, in a multiple-layer lining system, if

the primary lining has much higher coefficient of thermal expansion than outer secondary layers or shell, high confining stress from the secondary linings or shell to the primary linings results, which may cause hot-face spalling problems in primary lining or tensile failure in secondary linings or shell. On the other hand, if the primary lining has much lower coefficient of thermal expansion than secondary layers or shell, the separation between the layers may occur, which results in a loose lining system. A proper material combinations for the lining systems should be determined to avoid these two extremes.

(6) With respect to heating schedule, the adoption of low heating rate in low-intermediate hot-face temperature range is required to stabilize lining materials. This schedule is also found helpful to heat up a gasifier without causing severe damage in the associated lining system. For high temperature levels significant creep strain can develop in releasing stresses, and the heating schedules adopting high heating rates can be used.

(7) The adoption of higher controlled temperature on the shell for the heat-up period than that for the operating period (steady state) may allow the confining structures to expand sufficiently in reducing confining stress to the primary lining. However, this allowable maximum shell temperature for heat-up should be limited to a certain value, below which the separation between the shell and the linings will not occur.

CHAPTER 7

DESIGN AND OPERATIONAL RECOMMENDATIONS

Materials in the lining systems for slagging gasifiers face severe operational environments. The operating temperatures are high with simultaneous presence of highly corrosive slags and gases in the system. Adequate designs to ensure safety and integrity of these lining systems cannot be based on empirical methods and simplified linear material assumptions. Moreover, improper operational control of the linings would result in severe damage in the linings due to thermal and corrosion attacks.

Based on the results from the simulation and parameter study on the corrosion behavior (Chapter 4) and the thermomechanical behavior (Chapter 6) of the linings, the following guidelines are provided for the design with respect to material selection, lining configuration and the operation of the refractory lining systems in slagging gasifiers.

§ 7.1 DESIGN

Design recommendations with respect to the material selection and the determination of lining configurations are given below.

§7.1.1 Material Selection

(1) The selection of proper materials for the linings in the slagging gasifiers should be based on the consideration of material resistance to both corrosion and thermal attacks. With respect to the corrosion attack, designers should choose optimal materials which satisfactorily perform against corrosion due to the coal slags and the operational gases during gasification process, and serve for a required period of time before replacement. With respect to the thermal attack, in addition to the study of some fundamental properties of a single brick (e.g. initial Young's modulus, modulus of rupture, and thermal-shock properties), designers should develop an understanding of the behavior of brick systems and other components in a lining system. Such a behavioral understanding can be achieved through an accurate predictive analysis capability, and, based on this behavioral understanding, the designers can prevent unwanted failure in the system and in each individual component.

(2) Within the scope of work performed in this study on high-Al_2O_3 and high-Cr_2O_3 refractories, it is found that the high Cr_2O_3 refractories generally provide better corrosion resistance than high-Al_2O_3 refractories. For the linings with hot-face temperature above 2600°F, the high Al_2O_3 refractories experience severe mass loss within short periods of time due to slag corrosion, while the high-Cr_2O_3 refractories can sustain a hot-face temperature up to 2800°F with acceptable corrosion rate. However, the high Cr_2O_3 refractories are

relatively expensive and have less thermal-shock resistance than the high-Al_2O_3 refractories. The adoption of the high-Al_2O_3 refractories may still be considered, with a trade-off in loosing a certain extent the process efficiency within acceptable levels, such as the descrease in operating temperature, pressure, or gas velocity. Final selection of specific lining material(s) should be based on an economic analysis to evaluate the total cost/benefit of each gasification process with different lining materials and operating conditions.

(3) Material selection for the resistance to thermal attack requires a thorough behavioral understanding of a lining system in the high-temperature gasification environments. Such a behavioral understanding can be achieved by a thermomechanical analysis capability in studying the lining behavior. For the accuracy of such analysis, data on the following material properties should be obtained and implemented in the associated material models:

(a) Time independent constitutive behavior at different temperature level, including stress-strain curve and strength of materials in general loads, and post-failure behavior;

(b) Creep behavior in different temperature levels, including the material response and rupture time in general loads;

(c) Thermophysical properties in heating cycles, including thermal conductivity, density, specific heat, and coefficient of thermal expansion; and

(d) Effects of slag penetration on the abovementioned behaviors.

(4) Spalling process, which results from the combined effects of slag penetration and erosion, plays an important role in the determination of the lining life. A better control in reducing either spalling rate or amount of mass in each spalling can effectively lengthen the lining life, in both a deterministic and a probabilistic sense. With respect to design, such a control may be achieved in various ways. Examples are the chemical treatment to the refractories to reduce the potential of slag penetration resulting in the deterioration of material properties, or adding appropriate radial reinforcement to refractory linings in reducing spalling rate.

§7.1.2 Lining Configuration

(1) A critical stress state in the lining as a result of a thermal attack emerges during the heat-up period when high temperature qradients occur which are accompanied by high confining stresses, and insufficient stress relaxation due to creep. During the heat-up period stress distributions in the primary (working) lining is generally controlled by the two major sources: (a) temperature gradient through the lining, and (b) confining stress from the shell or the secondary lining. The analyses indicate trade-offs in stress magnitudes produced by the effects from these two sources. That is, for a given hot face temperature less thermal gradients would result in decreased hot face compressive stresses from this source

while higher stresses are produced from the confinement effect. Considering the complexities in material and lining system behaviors, a design procedure for the optimal lining configuration should be based on a thermomechanical analysis which has the capability to predict the abovementioned behavior accurately. Through such analysis and parameter studies, the optimal lining configuration in a given gasification environment can then be determined, resulting in minimal or no damage during the heating process.

(2) Single-layer lining system is not ideal for the lining in high temperature gasification environments. If the lining is not in contact with vessel shell, it can expericence severe joint failure; on the other hand, if the lining is in contact with the vessel shell, high confining stress resulting in high hot face compressive hoop stress can occur, which may cause spalling problems.

(3) The use of a compressible layer is found to be very effective in reducing the confining stress to primary (working) lining. Proper combinations of the stiffness and strength of the compressible material to be adopted for a specific lining system can be determined through the thermomechanical analysis. The specific material satisfying such stiffness and strength requirements should be identified. If the material with those required properities is not available, redesign of the system may be needed.

(4) An expansion joint extending from the hot face can significantly reduce the hot face compression resulting in a better structural system which would be less susceptible to damages from the heating process. Optimal size and width of the expansion joint should be determined, by which the hot face stresses can be reduced sufficiently while the joint can still be tight enough to reduce the potential of gas penetration during operating periods.

(5) In a multiple-layer lining system, the relative thermal expansion behavior between layers has significant effects on stress distribution in the linings. It is preferred that the coefficients of thermal expansion of these layers increase from the inner layer toward the outer layer, such that the confining stress over the interfaces between layers can be reduced.

§ 7.2 OPERATION

(1) For lining systems with different lining designs the operational schedules leading to minimal damage in each system during heat-up and operating period may be different depending on the lining material behavior and the system behavior. Hence, for a certain lining system with a given configuration, thermomechanical analysis with various heating schemes and corrosion analysis with various process conditions should be performed, and the optimal operational conditions should be adopted to assure the required performance of the lining during its design life time.

(2) In a slagging gasifier the long-term lining behavior in such a corrosive environment is sensitive to the operating conditions, such as operating temperature, pressure, and gas velocity. Reducing operating temperature, which results in a lower temperature on the hot face of the lining, can effectively reduce corrosion rate of the lining by slag attack. When operating temperature is fixed, reducing gas pressure and velocity, which can reduce the coefficient of the hot face convection, can also reduce the hot-face temperature and, accordingly, the corrosion rate. Again, the determination of optimal combination of lining materials, operating conditions and lining life should be based on a rational economic analysis.

(3) Adoption of a cooling system on the cold (outer) face of the lining or on the shell can reduce the hot-face temperature and may result in a steady layer of slag to form on the hot face. This layer can protect the lining from the potential corrosion attack during the operating period.

(4) During the heat-up process slow heating rate (say, 50°F/hr) , in conjuction with holding periods, is desired, at least for low to intermediate temperature (say, < 1500°F) levels. The adoption of such a slow heating rate and hold periods is required to dry up the moisture-containing lining materials without causing severe cracking. This slow heating rate and holding period is also needed to achieve a less critical stress state in the lining during heat-up. On the other hand, such a heating scheme results in a long period of time for heat-up. A feasible solution in

shortening this heat-up period is to adopt high heating rate (say, 150°F/hr) for high hot-face temperature range (say, >1500°F) with shorter hold period, which would not cause severe damage in the linings.

(5) During the operating period the low shell temperature (say, < 200°F) controlled by the cooling system is needed, which can reduce the activity of gas corrosion on the shell and help a steady layer of slag to form on the hot face of the lining. However, such a low shell temperature can result in high temperature gradient and confining stress in the lining during transient heat-up process and, accordingly, may cause failure in the linings. It is suggested that a higher maximum allowable temperature (say, 200°F-600°F) be adopted for the shell during transient heat-up process to reduce the critical stress state in the linings, especially at low to intermediate hot-face temperature levels when the stress relaxation in the lining is not significant. However, the shell temperature should still be controlled at low level (<200°F) during operating period for minimizing the long-term corrosion.

CHAPTER 8

SUMMARY, CONCLUSIONS AND RECOMMENDATIONS FOR FUTURE RESEARCH

§8.1 SUMMARY

High-temperature gasification process in converting coal into a suitable and economic gaseous fuel is an emerging new technology with unique material requirements. The gasification takes place in refractory lined vessels where structurally severe environments exist with corrosive slags and gases, and high operating temperatures. Optimal design of safe and economical lining systems for slagging gasifiers requires a fundamental understanding of the thermomechanical and corrosion behavior of brick-mortar systems in high-temperature and highly corrosive environments.

The objective of this work is to study the behavior of refractory brick lined coal gasification vessels under transient temperature loadings and long-term corrosion attack. Material models, including cyclic multiaxial nonlinear constitutive law, temperature dependent heat conduction model and temperature dependent creep law, are developed for refractories, and implemented in a finite element program for predicting the stress and strain distributions in the brick-mortar linings during heating process. Parameter studies on the

linings with various lining configurations, material combinations, and operational schemes are performed. A corrosion model is proposed to study the long-term behavior of the refractory linings in corrosive environments. Based on such studies of the transient thermomechanical and long-term corrosion behavior of the refractory linings, recommendations for design and optimum operational schemes of the linings are given.

The thermophysical and thermomechanical behavior of candidate refractories for the linings in slagging gasifiers is complex. The thermophysical properties (thermal conductivity, density, specific heat, and coefficient of thermal expansion) are nonlinearly dependent on temperature, in general. Thermal conductivity of the materials can be affected by slag penetration and stress-induced cracking, which results in an anisotropic behavior in conductivity even when the initial material conductivity may be isotropic.

The thermomechanical behavior of refractory materials is generally temperature and time dependent. With respect to the time effects, the thermomechanical behavior can be conveniently divided into two categories: time-independent constitutive behavior and creep (time-dependent) behavior. The time-independent response of the material to external loads is generally nonlinear and involves plastic deformation, stress path and damage dependent material moduli, and post-failure softening behavior. Test data in characterizing such a complex behavior for candidate materials is insufficient and more experimental work is needed to provide a thorough behavioral understanding of the material response to general loads.

The creep of candidate materials under loads is significant at high temperature levels, which generally results in a visco-plastic type of deformation. Such a creep behavior can affect the stress distributions in a lining system at high operating temperatures by releasing local stresses with time.

Slag penetration into refractories can change the chemical and mechanical properties of the refractories. Penetrated slags cause microcracking in the refractories, and, consequently, reduce the strength and stiffness of the refractories. Such a deterioration process may result in spalling problems in the high thermal stress and highly erosive gasification conditions. Mechanical properties of slag penetrated refractories are not well understood and further research on this aspect is needed.

Corrosion of refractory linings in slagging gasification environments is primarily contributed by the dissolution process and the spalling process of the refractory in slags and gases. The dissolution process is a chemical process by which the refractory is gradually dissolved in a slag composite, while the spalling process primarily results from sequential deterioration processes including slag penetration, material degradation in strength, stress-induced microcracking, and severe erosion by slags and gases. The results of such corrosion process are the progressive loss of the materials with time from the hot face of the linings and, accordingly, the loss of required performance of the linings.

In this study a simple corrosion model is proposed to predict the long-term corrosion behavior of the linings in slagging gasifiers.

This model incorporates the coupling effects between different mechanisms (e.g., dissolution, penetration, and erosion) of corrosion process and the variation of temperature through the linings. In conjunction with the short-term experimental results on corrosion and spalling, and physical findings, the model permits evaluation of the long-term corrosion behavior of the linings. Special features of this model are (1) the capability to extrapolate the results of the short-term corrosion tests on materials at certain temperature levels to the long-term lining behavior taking into account the progression of events involving the interaction between temperature variation, corrosion rate, and lining thickness, and (2) the capability to include the discrete-type spalling process into the overall corrosion behavior.

By using the developed corrosion model, the long-term corrosion behavior of the linings adopting 90% Al_2O_3 or 80% Cr_2O_3 refractories are studied. Through the parameter studies, the relative importance of material dissolution rate, spalling rate, and operating conditions are assessed. Furthermore, a study of the effects of uncertainty in dissolution and spalling processes on the long-term corrosion behavior is performed. The results from these studies provide the designers with a background on the basis of which optimization of operating conditions, and proper design and control of the lining systems may be achieved.

A simple quantification of the proposed corrosion model is made. This model can predict the long-term lining corrosion behavior with an acceptable accuracy, and can be adopted for design purposes.

For performing thermomechanical analyses, material models for the refractories and an analysis methodology using finite elements are developed. In material modeling, polynomial representations of temperature dependent thermophysical properties, including thermal conductivity, density, specific heat and coefficient of thermal expansion, are obtained by data fitting. Time, temperature and load history dependent constitutive models of the candidate materials are developed. These models are then implemented in a generalized finite element program in predicting the thermomechanical behavior of refractory linings in gasification environments. The finite element program includes special features to model the joint behavior (failure), and the refractory spalling process, to modify the local conductivity due to stress-induced cracking and to adjust the material properties of the refractories for slag penetration.

Extensive parameter studies of the thermomechanical behavior of refractory linings in transient heating process, with various configurations and material combinations, and under various operational schemes, are performed. Lining systems with different designs (configurations, materials, etc.) may behave differently and encounter different structural problems even under the same operational scheme. Consequently, optimum operational schemes resulting in minimal or no damage to a lining system, can be different from one system to another.

The developed methodology presented in this report provides a systematic way to study and understand the behavior of the lining during critical structural stages; namely, the thermomechanical

behavior during heat-up process, and the long-term corrosion behavior. By adopting this methodology, the optimal design and operation for a lining system in slagging gasification environments can be determined.

§8.2 CONCLUSIONS

Based on the results from the analytical/numerical analyses performed in this work, the following conclusions are drawn:

(1) The developed general methodology incoporating material models, structural models, corrosion models and finite element analysis capability provides a powerful and unique tool for the transient thermomechanical and long-term corrosion analyses of refractory lining systems. This methodology, with appropriate modification, can be expanded to study the behavior of general ceramic-type structures in elevated-temperature and corrosive environments.

(2) Under the same operating conditions, the lining with 80% Cr_2O_3 refractory material has relatively high resistance to corrosion attack than that with 90% Al_2O_3 and can satisfy the generally accepted lining life (~ 2 years) before replacement. However, within an acceptable range, certain modifications in operating conditions, such as reducing operating temperature, pressure, or gas speed, which can result in a lower hot face temperature of the lining, would improve the corrosion resistance of the lining with 90% Al_2O_3 refractory. The high-Al_2O_3 refractories are relatively

inexpensive compared to high-Cr_2O_3 refractories; however less efficient gasification conditions are generally obtained to ensure the required life of the linings adopting high-Al_2O_3 refractories. Such tradeoffs should be considered in adopting various lining materials and operating conditions and in a cost/benefit analysis for selecting a specific gasification system.

(3) Spalling process and its uncertain nature affects significantly the long-term behavior of a lining in corrosive environment. Analysis results show that with a lower value of the coefficient of hot-face heat convection, a lower spalling rate and a less depth of slag penetration, the lining life can be effectively improved. Such a control of corrosion process may be achieved through optimizing the gas velocity and the size of particles entrained in gases and slags, or by special (chemical or structural) treatments to the refractory bricks.

(4) Damage from the thermal attack to the refractory lining is primarily due to the high thermal gradients and resulting confining stresses introduced in the lining during heat-up. Large differences in temperatures between the inner (hot) and outer (cool) faces of the linings, and large thermal expansion occurring at high temperatures introduce high thermal stresses in the linings. This may result in the disintegration of the lining system in the forms of joint

failure, and cracking and spalling of the bricks. This problem is more severe during the transient heating process when stress relaxation due to creep is less compared to that during the steady state operation. Reduction of the damage in a lining system from the thermal attack can be achieved through an optimum structural design and assessment of a proper operational scheme, i.e., heating schedule. For this purpose a thorough understanding of the thermomechanical material behavior in transient heating process is needed.

(5) The adoption of compressible layers between steel shell and refractory linings, and introduction of expansion joints extending from the hot face are helpful for the lining safety. The compressible layer can generally release a portion of the confining stress introduced from the shell to the linings, and the expansion joint can relieve hot face stress and reduce the occurrence of cracking and spalling. Determination of the required strength and stiffness of compressive materials can be obtained through analysis; the associated materials satisfying such requirements can then be identified. The size and width of expansion joints should be determined such that sufficient stresses can be released by the adoption of the joints; the joints should be closed and tight enough at high operating-termperature levels to prevent hot-gases from penetrating through the linings.

(6) For the primary (working) linings in most of the lining systems, the damage in the linings during heat-up period can be reduced by adopting a slow heating rate (say, 50°F/hr), and a higher maximum shell temperature (say, 600°F) than that required during the operation period (say, <200°F). Thus, the critical stress induced from the temperature gradient is reduced while allowing the confining structures to expand and release the associated confining stress to the primary linings. High heating rates (say, 150°F/hr) may be adopted for high hot-face temperature levels (say, >1500°F), which would not cause severe damage in the lining systems.

(7) The penetration of slags into the linings can considerably reduce the strength and stiffness of the refractories. This material deterioration due to slag penetration may cause cracking and spalling problems on the hot face of linings, especially when high hoop compressive stress exists near the hot face. A control and behavioral understanding of such a deterioration process is needed.

§8.3 RECOMMENDATIONS FOR FUTURE RESEARCH

The numerical analysis capability developed in the present work for the thermomechanical analysis of mortar-brick systems is a powerful tool to predict stress and strain distributions, cracking and deterioration. Optimal designs of these systems may be achieved by the use of such capabilities. Although the methodology developed is

general and valid for brittle-type materials, due to unavailability of the material data for short-term loadings, the present research included applications to high-alumina bricks only. Even for the high alumina brick, the material data is not complete. Also, further tests on high alumina bricks are needed to verify existing data and to provide additional information as necessary. More work on the experimental characterization of the material behavior for candidate materials is needed in constructing relevant material models to be implemented in predictive capabilities.

The use of high-Cr_2O_3 refractory materials seems advantageous in that their resistance to corrosion is higher; but these materials have lower resistance to high temperature attacks, when compared to high-Al_2O_3 materials. At present the thermomechanical properties of the high-Cr_2O_3 materials are not established, and thus, the study of the system behavior of the lining adopting such materials cannot be made. Hence, experiments to determine the thermomechanical properties of these materials followed by the analytical studies in characterizing the lining system behavior are necessary.

With respect to the long-term reliability of the lining systems, large scale corrosion-test facilities which can simulate both the dissolution and spalling processes are needed. By using the results from these tests, the long-term reliability and the uncertainty in the depletion process of the linings can be assessed.

REFERENCES

REFERENCES

1. M. Adams, and G. Sines, "Determination of Biaxial Compressive Strength of a Sintered Alumina Ceramic," Journal of the American Ceramic Society, Vol. 59, No. 7-8, 1976.

2. J. Armitt, et al., "The Spalling of Steam-Grown Oxide from Superheater and Reheater Tube Sheets," EPRI Report, FP-686, 1978.

3. P. Artelt, "Refractories for Oxygen Steel-Making in Germany," British Ceramic Society Transactions and Journal, Vol. 74, No. 3, 1975.

4. Babcock & Wilcox Experimental Report, 1983.

5. E. B. Backensto, and J. W. Sjoberg, "Iso-Corrosion Rate Curves for High Temperature Hydrogen-Hydrogen Sulfide," Corrosion, Vol. 15, 1959.

6. W. T. Bakker, and J. Stringer, "Materials for Coal Gasification Combined Cycle Power Plants," Sixth Annual Conference on Material for Coal Conversion and Utilization, October 1981.

7. W. T. Bakker, S. L. Darling, and W. C. Coons, "Refractory and Coal Slag Experience in the Combustion Engineering Gasification Process Development Unit," Seventh Annual Conference on Materials for Coal Conversion and Utlization, November 1982.

8. K. J. Bathe, Finite Element Procedure in Engineering Analysis. Prentice-Hall, Inc., 1982.

9. Z. P. Bazant, et al., "Normal and Refractory Concrete for LMFBR Applications; Volume 2: Evaluation of Concretes for LMFBR Appilcations." EPRI Report NP-2437, 1982.

10. J. R. Benjamin, and C. A. Cornell, Probability, Statistics, and Decision for Civil Engineers, McGraw Hill Book Company, 1970.

11. F. C. Bock, "An Exponential Lining-Wear Model for Slagging Gasifiers," IITRI Report No. M6043-4(AR), 1979.

12. J. T. Boyle, and J. Spence, Stress Analysis for Creep, Butterworth & Co. Ltd., 1983.

13. J. Boow, "Desirable Physical and Chemical Properties of Refractories Resistant to Corrosion by Coal Ash Slags," Journal of Australian Ceramic Society, Vol. 5, 1969.

14. E. R. Broadfield, "Refractory Lining for the Cyclone Combustion Chamber of a Power Plant Boiler," Refractories Journal, Vol. 45, 1969.

15. L. J. Broutman, and R. H. Cornish, "Effect of Polyaxial Stress on Failure Strength of Alumina Ceramics," Journal of the American Ceramic Society, Vol. 48, No. 10, 1965.

16. P. P. Budnikov, The Technology of Ceramics and Refractories, MIT Press, 1964.

17. T. S. Busby, "Corrosion Tets as a Planning Tool in Furnace Design," British Ceramic Society Transactions and Journal, Vol. 75, No. 1, 1976.

18. O. Buyukozturk, "Stress-Strain Response and Fracture of A Model of Concrete in Biaxial Loading," Ph.D. Thesis, Cornell Unversity, 1970.

19. O. Buyukozturk, and T. M. Tseng, "Thermomechanical behavior of Refractory Concrete Linings," Journal of the American Ceramic Society, Vol. 65, No. 6, 1982.

20. O. Buyukozturk, and T. M. Tseng, "Heat Conduction Through Layered Refractory Linings," Journal of Engineering Mechanics Division, ASCE, Vol. 109, No. 4, 1983.

21. W. R. Cannon, and O. D. Sherby, "Creep Behavior and Grain-Boundary Sliding in Polycrystalline $A\ell_2O_3$," Journal of the Americal Ceramic Society, Vol. 60, No. 1-2, 1977.

22. R. M. Cannon, W. H. Rhodes, and A. H. Heuer, "Plastic Deformation of Fine-Grained Alumina I, Interface-Controlled Diffusional Creep," Journal of the American Ceramic Society, Vol. 63, No. 1-2, 1980.

23. L. Cedolin, Y. R. J. Crutzen, and S. Dei Pole, "Triaxial Stress-Strain Relationship for Concrete," Journal of Engineering Mechanics Division, ASCE, Vol. 103, EM3, Proc. Paper 12969, 1977.

24. K. J. Chen, et al., "Thermal Expansion of Aluminosilicate Refractory Brick," Bulletin of the American Ceramic Society, Vol. 61, No. 8, 1982.

25. W. F. Chen, Plasticity in Reinforced Concrete, McGraw-Hill Book Company, 1982.

26. B. Clavaud, "Hot Mechanical Properties of Refractories - Compressive Strength," British Ceramic Society Transactions and Journal, No. 5, 1976.

27. N. Claussen, J. Steeb, and R. F. Pabst, "Effect of Induced Microcracking on the Fracture Toughness of Ceramics," Bulletin of the American Ceramic Society, Vol. 56, No. 6, 1977.

28. W. S. Coblenz, "Elastic Moduli of Boron-Doped Silicon Carbide," Journal of the American Ceramic Society, Vol. 58, No. 11-12, 1975.

29. A. R. Cooper, "Kinetics of Refractory Corrosion," Ceramic Engineering and Science Proceedings, Vol. 2, American Ceramic Society, 1981.

30. B. R. Cooper, and W. A. Ellingson, Ed., The Science and Technology of Coal and Coal Utilization, Plenum Press, 1984.

31. M. S. Crowley, "Hydrogen-silca Reactions in Refractories," Bulletin of the American Ceramic Society, Vol. 46, No. 7, 1967.

32. M. S. Crowley, "Refractory Problems in Coal Gasification Reactors," Bulletin of the American Ceramic Society, Vol. 54, No. 12, 1975.

33. C. S. Desai, and J. F. Abel, Introduction to the Finite Element Methods, Van Norstrand Reinhold Co., 1971.

34. D. R. Diercks, S. Greenberg, and G. Bandyopadhyay, "Corrosion and Thermal-Shock Studies on Slagging Coal Gasifier Refractories," Seventh Annual Conference on Material for Coal Conversion and Utilization, November, 1982.

35. M. N. Fardis, B. Alibe, and J. L. Tassoulas, "Monotonic and Cyclic Constitutive Law for Concrete," Journal of the Engineering Mechanics Division, ASCE, Vol. 109, No. EM2, Proc. Paper 17871, April 1983.

36. K. Endell, R. Fehling, and R. Kley, "Influence of Fluidity, Hydrodynamic Characteristics, and Solvent Action of Slag on the Destruction of Refractories at High Temperatures," Journal of the American Ceramic Society, Vol. 22, 1939.

37. W. N. Findley, J. S. Lai, and K. Onaran, Creep and Relaxation of Nonlinear Viscoelastic Materials, North-Holland Publishing Company, 1976.

38. R. F. Firestone, "Refractory Test Facility," Sixth Annual Conference on Material for Coal Conversion and Utilization, October 1981.

39. H. F. Folk, and W. C. Bohling, "High Temperature Strength of High Alumina Refractories," Bulletin of the American Ceramic Society, Vol. 47, No. 6, 1968.

40. E. R. Fuller, Jr., C. R. Robins, and A. Lobe, "Steam Degradation of Calcium Alumina Refractories," Bulletin of the American Ceramic Society, Vol. 55, 1976.

41. K. H. Gerstle, et al., "Behavior of Concrete under Multiaxial Stress States," Journal of Engineering Mechanics Division, ASCE, Vol. 106, EM6, Proc. Paper 15945, 1980.

42. V. Gilbert, "Rotary Slag Testing of Basic Refractories," Bulletin of the American Ceramic Society, Vol. 55, NO. 7, 1976.

43. M. J. Greaves, and D. McKee, "Design, Engineering and Evaluation of Refractory Liners for Slagging Gasifiers," IITRI Report No. M6043-4(AR), 1979.

44. S. J. Green, and S. R. Swanson, "Static Constitutive Relations for Concrete," Technical Report No. AFWL-TR-72-2, Terra-Tec, Inc., Salt Lake City, Utah, 1973.

45. S. Greenberg, "Corrosion of Refractories for Slagging Gasifiers," Fossil Energy Material Program Review Meeting, Tennessee, 1983.

46. A. H. Heuer, N. J. Tighe, and R. M. Cannon, "Plastic Deformation of Fine-Grained Alumina II, Basal Slip and Nonaccommodated Grain-Boundary Sliding," Journal of the American Ceramic Society, Vol. 63, No. 1-2, 1980.

47. M. Kachanov, "Continuum Model of Medium with Cracks," Journal of Engineering Mechanics Division, ASCE, Vol. 106, EM5, Proc. Paper 15750, 1980.

48. I. D. Karsan, and J. O. Jirsa, "Behavior of Concrete under Compressive Loadings," Journal of Engineering Structural Division, ASCE, Vol. 95, ST12, Proc. Paper 6935, 1969.

49. C. R. Kennedy, "Coal Slag-Refractory Compatibility Studies," Ceramic Engineering and Science Proceedings: Vol. 2, American Ceramic Society, 1981.

50. C. R. Kennedy, "Selection of Refractories for Slagging Coal Conversion Systems," Sixth Annual Conference on Material for Coal Conversion and Utilization, October 1981.

51. C. R. Kennedy, "Compatibility of Water-Cooled Chromina-Containing Refractories with a High Iron Oxide Acidic Coal-Ash Slag at 1575°C," Journal of Materials for Energy Systems, December, 1981.

52. M. D. Kotsovos, and J. B. Newman, "A Mathematical Description of the Deformational Behavior of Concrete under Complex Loading," Magazine of Concrete Research, Vol. 31, No. 107, 1979.

53. M. D. Kotsovos, and J. B. Newman, "A Mathematical Description of the Deformational Behavior of Concrete Under Generalized Stress Beyond ultimate Strength," ACI Journal, Vol. 77, No. 5, 1980.

54. M. D. Kotsovos, "Concrete - A Brittle Fracture Material," to appear in Material and Structures, RILEM, 1984.

55. D. Krajcinovic, and G. U. Fonseka, "The Continuous Damage Theory of Brittle Materials: Part 1 - General Theory; Part 2 - Uniaxial and Plane Response Models," Journal of Applied Mechanics, Vol. 48, 1981.

56. H. Kupfer, H. K. Hilsdorf, and H. Rusch, "Behavior of Concrete Under Biaxial Stresses," ACI Journal, Vol. 66, No. 8, 1969.

57. A. M. Law, and W. D. Kelton, Simulation Modeling and Analysis, McGraw Hill Book, Inc., 1982.

58. J. C. Maxwell, A Treatise on Electricity and Magnetism, Third Edition, Vol. 1, Dover, 1954.

59. T. D. McGee, "Laboratory Slag Tests," Ceramic Engineering and Science Proceedings: Vol. 2, American Ceramic Society, 1981.

60. T. D. McGee, "High Temperature Creep of Refractories for Coal Processing Vessels," U. S. Dept. of Energy, Fossil Energy Advanced Research and Technology Development Reports, ONRL/FMP-83/3-5, 1983, ONRL/RMP-84/1, 1984.

61. F. H. Norton, Refractories, 4th Edition, McGraw-Hill Book Company, 1968.

62. Norton Company Report, December, 1981.

63. E. A. Nelson, "Action of Hydrogen on Steel at High Temperature and High Pressures," Welding Research Council Bulletin, No. 145, 1969.

64. P. Nowacki, Ed., Coal Gasification Process, Noyes Data Corporation, 1981.

65. H. L. Oh, K. P. L. Oh, S. Vaidyanathun, and I. Finnie, "On the Shaping of Brittle Solids by Erosion and Ultrasonic Cutting," U. S. National Bureau of Standards, Special Publication 348, 1970.

66. H. M. Ondik, B. W. Christ, and A. Perloff, "Construction Material for Coal Conversion: Performance and Properties Data," U. S. National Bureau of Standards, Special Publication 642, 1982.

67. M. N. Ozisik, Heat Transfer, John Wiley & Sons, 1980.

68. G. C. Padgett, J. A. Cox, and J. F. Clements, "Stress/Strain Behavior of Refractory Materials at High Temperature," British Ceramic Society Transactions and Jounal, Vol. 68, No. 2, 1969.

69. H. Perry, "The Gasification of Coal," Scientific American, Vol. 230, No. 3, 1974.

70. P. J. Pike, O. Buyukozturk, and J. J. Connor, "Thermomechanical Analysis of Refractory Concrete Lined Coal Gasification Vessels," MIT Report No. R80-2, 1982.

71. S. S. Rao, The Finite Element Method in Engineering, Pergamon Press, Inc., 1982.

72. W. M. Rohsenow and J. P. Hartnett, Ed., Handbook of Heat Transfer, McGraw-Hill Book, Inc., 1973.

73. R. Y. Rubinstein, Simulation and the Monte Carlo Method, John Wiley & Sons, 1981.

74. E. Ruh, and J. S. McDowell, "Thermal Conductivity of Refractory Brick," Journal of the American Ceramic Society, Vol. 45, No. 2, 1962.

75. E. Ruh, and W. Wallace, "Thermal Expansion of Refractory Brick," Bulletin of the American Ceramic Society, Vol. 42, No. 2, 1963.

76. B. N. Samaddar, W. D. Kingery, and A. R. Cooper, Jr., "Dissolution in Ceramic Systems: II, Dissolution of Alumina, Mullite, Anorthite, and Silica in a Calcium-Aluminum-Silicate Slag," Journal of the American Ceramic Society, Vol. 47, No. 5, 1964.

77. R. Scavuzzo, et al., "Simple Formulation of Concrete Response to Multiaxial Load Cycles," Proceedings of the Internaional Conference on Constitutive Laws for Engineering Materials: Theory and Application, 1983.

78. G. Schickert, and H. Winkler, "Results of Tests Concerning Strength and Strain of Concrete Subjected to Multiaxial Compressive Stress," Deutscher Ausschuss fur Stahlbeton, Heft 277, Wilhelm Ernst & Sohn, Berlin, 1977.

79. M. S. Seltzer, "High Temperature Creep of Silcon-Base Compounds," Bulletin of the American Ceramic Society, Vol. 56, No. 4, 1977.

80. D. K. Shetty, A. R. Rosenfield, W. H. Duckworth, and P. R. Held, "A Biaxial-Flexure Test for Evaluating Ceramic Stength," Journal of the American Ceramic Society, Vol. 66, No. 1, 1983.

81. D. C. Spooner, and J. W. Dougill, "A Quantitative Assessment of Damage Sustained in Concrete during Compressive Loading," Magazine of Concrete Research, Vol. 27, No. 92, 1975.

82. J. Sweeney, and M. Cross, "Analysis the Stress Response of Commercial Refractory Structures in Service at High Temperature: I. A Simple Model of Viscoelastic Stress Response," British Ceramic Society Transactions and Journal, Vol. 81, No. 1, 1982.

83. J. Sweeney, and M. Cross, "Analysis the Stress Response of Commercial Refractory Structures in Service at High Temperature: II. A Thermal Stress Model for Refractory Structures," British Ceramic Society Transactions and Journal, Vol. 81, No. 1, 1982.

84. S. P. Timoshenko an J. N. Goodier, Theory of Elasticity, Third Edition, McGraw-Hill Book, Inc., 1970.

85. N. L. Torti, J. W. Lucek, N. I. Prille, and D. P. Reed, "Silicon Carbide Ceramics for Coal Conversion Applications," Seventh Annual Conference on Material for Coal Conversion and Utilizaiton, November 1982.

86. Y. S. Touloukian, et al., Thermal Conductivity, IFI/Plenum, 1970.

87. G. G. Trantina, and H. G. deLorenzi, "Design Methodology for Ceramic Structures," Journal of Engineering for Power, Tran. ASME, Paper No. 77-GT-49, 1977.

88. T. M. Tseng, "Thermomechanical Behavior of Refractory Concrete-Lined Vessels," MIT Report No. R82-44, 1982.

89. M. E. Washburn, and R. K. Bart, "Thermal Conductivity of Silicon Carbide Refractory," Bulletin of the American Ceramic Socieity, Vol. 44, No. 7, 1965.

90. M. E. Washburn, "Rotating Sample Slag Test for Refractories," Seventh Annual Conference on Material for Coal Conversion and Utilization, November 1982.

91. S. M. Wiederhorn, "Erosion Behavior of Ceramics," U. S. Dept. of Energy Report, CONF-751194, 1975.

92. G. M. Workman, "Development of Refractory Linings for Handling Molten Iron," British Ceramic Society Transactions and Journal, Vol. 73, No. 7, 1974.

93. O. C. Zienkiewicz, The Finite Element Method, Third Edition, McGraw-Hill Book Company, 1977.

APPENDIX

A.1 APPENDIX I : PROGRAM " SRLT "

A.1.1 List of Progrm

```
C       THIS PROGRAM (1) CALCULATES THE HOT FACE TEMPERATURE (TH) AS
C                        FUNCTION OF LINING THICKNESS (Y),
C                    (2) CALCULATES THE PENETRATION DEPTH (DP) AS
C                        FUNCTION OF LINING THICKNESS (Y), AND
C                    (3) CALCULATES THE RESIDUAL THICKNESS (THIK) AS
C                        FUNCTION OF TIME (TIME).
C       ************************************************************
C       ************************************************************
C       **                  PROGRAM PARAMETERS:                   **
C       **                                                        **
C       **       IOPT     =1, DO TASK  (1)                      **
C       **                =2, DO TASKS (1) & (2)                **
C       **       IU       =Ø, SKIP TASK (3)                     **
C       **                =1, DO TASK (3), DETERMINISTICALLY    **
C       **                =2, DO TASK (3), BY SIMULATION        **
C       **                =3, DO TASK (3), BY SIMULATION AND PRINT OUT
C       **                    STISTICAL RESULTS                 **
C       **       IPR1     =Ø, NO PRINT-OUT FOR TASK 1           **
C       **                =1, PRINT OUT RESULTS OF TASK 1       **
C       **       IPR2     =Ø, NO PRINT-OUT FOR TASK 2           **
C       **                =1, PRINT OUT RESULTS OF TASK 2       **
C       **       IPR3     =Ø, NO PRINT-OUT FOR TASK 3           **
C       **                =1, PRINT OUT RESULTS OF TASK 3       **
C       **       ICORR    =1, EXPONENTIAL CORROSION RATE OF TEMPERATURE
C       **                =2, LINEAR CORROSION RATE  OF TEMPERATURE
C       **                      (NOT USED IN THIS VERSION)      **
C       **                =3, RESERVED                          **
C       **       AA,AM    =PARAMETER(MEAN) OF CORROSION RATE (IN)
C       **       BB       =PARAMETER OF COSSION RATE      (F)   **
C       **       CV       =COEFFICIENT OF CONVECTION (BTU/HR-IN**2-F)
C       **       CD       =THERMAL CONDUCTIVITY (BTU/HR-IN-F)   **
C       **       IDIS     =INDEX FOR DISTRIBUTION OF OCCURENCE TIME
C       **       IDISA    =INDEX FOR DISTRIBUTION OF VARIABLE "A"
C       **       IX       =INITIAL INPUT FOR RANDOM DATA GENERATION
C       **       NSIM     =NO. OF SIMULATION (=1 FOR IU=1)      **
C       **       NTH      =NO. OF DIVISION USED FOR THICKNESS (TASK (1))
C       **       NY       =NO. OF DIV OF THICKNESS IN TASK(1)&(2)
C       **       R        =OUTER RADIUS OF THE LINING(IN)       **
C       **       TCRI     =CRITICAL TEMPERATURE FOR SLAG PENETRATION (F)
C       **       TE1      =TEMPERATURE IN THE GASIFER (F)       **
C       **       TE2      =TEMPERATURE AT THE OUTER FACE OF LINING (F)
C       **       TINI     =TIME INTERVAL (HR)                   **
C       **       TREF     =REFERENCE TIME IN DISSOLUTION MODEL (K)
C       **       TL       =DESIGN LIFE TIME (HR)                **
C       **       VA       =STAD. DIVI. OF VARIABLE "A" (IN)     **
C       **       YINI     =INITIAL LINING THICKNESS (IN)        **
C       **       YMAX     =MAXIMUM LINING THICKNESS IN TASK (1)&(2) (IN)
C       **       YMIN     =MINIMUM LINING THICKNESS IN TASK (1)&(2) (IN)
C       **       YPAR1,2  =PARAMETERS FOR DISTRIBUTION OF OCCURENCE TIME
C       **                                                      **
C       ************************************************************
C       ************************************************************
```

```
      DOUBLE PRECISION B3,C1,C2,RESULT
      DIMENSION C1(2000),C2(2000)
      COMMON/ONE/IOPT,NY,IU,YMAX,YMIN,YINI,DP(2000),
     *  TH(2000),Y(2000)
      COMMON/CONI/CV(4),CD(4)
      COMMON/SIMU/ICORR,AA,BB,TREF,TINT,TL,THIK(2000),
     *  TIME(2000),TSPA(500),NSTEP

C     READ CONTROL INDEX
      READ(5,*) IOPT,IU
      WRITE(6,901) IOPT,IU
C     READ PRINTOUT INDEX FOR EACH TASK
      READ(5,*) IPR1,IPR2,IPR3
C     READ DATA FOR TASK (1)&(2)
      READ(5,*) R,YMAX,YMIN,NY,TE1,TE2
      WRITE(6,903) R,YMAX,YMIN,NY,TE1,TE2

      NLOOP=2
      TICR=1.

      IF(IOPT.EQ.2) THEN
      READ(5,*) TCRI
      WRITE(6,904) TCRI
      END IF
      READ(5,*) (CV(I),I=1,4)
      WRITE(6,905) (CV(I),I=1,4)
      READ(5,*) (CD(I),I=1,4)
      WRITE(6,906) (CD(I),I=1,4)

C     READ DATA FOR TASK (3)
      IF (IU.EQ.0) GO TO 5
      READ(5,*) ICORR
      WRITE(6,902) ICORR
      READ(5,*) YINI,TINT,TL
      WRITE(6,907) YINI,TINT,TL
      IF(IU.EQ.1) NSIM=1
      IF(IU.GE.2) READ(5,*) NSIM
      WRITE(6,908) NSIM
      IF(IU.EQ.1) THEN
      READ(5,*) YPAR1,YPAR2,AM,BB,TREF
      WRITE(6,909) YPAR1,YPAR2,AM,BB,TREF
      END IF
      IF(IU.GE.2) THEN
      READ(5,*) IX,IDIS,YPAR1,YPAR2,IDISA,AM,BB,TREF
      WRITE(6,909) YPAR1,YPAR2,AM,BB,TREF
      READ(5,*) VA
      WRITE(6,910) VA
      END IF
```

```
C       ****************************************
C       TASK (1)
C       ****************************************
5       TRY=TE2
        CALL CONI(1,TE2,RESULT)
        B1=RESULT
        DIV=(YMAX-YMIN)/FLOAT(NY)
        NSLOOP=(TE1-TE2)/TICR+1.
        DO 2Ø JJ=1,NY+1
        YY=DIV*FLOAT(JJ-1)+YMIN
        Y(JJ)=YY
        DO 1Ø II=1,NSLOOP
        CALL CONI(2,TRY,RESULT)
        CH=RESULT
        C11=(TRY-TE1)*CH*(R-YY)
        CALL CONI(1,TRY,RESULT)
        B2=RESULT
        C12=(B1-B2)/LOG(R/(R-YY))
        IF(C11.GE.C12) GO TO 15
1Ø      TRY=TRY+TICR
        WRITE(6,915)YY
        GO TO 999

15      TSRY=TRY-TICR
        TSICR=TICR
        DO 16 II=1,NLOOP
        TSICR=TSICR/1Ø.
        DO 17 III=1,1Ø
        TSRY=TSRY+TSICR
        CALL CONI(2,TSRY,RESULT)
        CH=RESULT
        C11=(TSRY-TE1)*CH*(R-YY)
        CALL CONI(1,TSRY,RESULT)
        B2=RESULT
        C12=(B1-B2)/LOG(R/(R-YY))
        IF(C11.GE.C12) GO TO 18
17      CONTINUE
18      TSRY=TSRY-TSICR
16      CONTINUE
        TH(JJ)=TSRY
        C1(JJ)=C11
        C2(JJ)=B2-C11*LOG(R-YY)
2Ø      CONTINUE

C       ****************************************
C       TASK (2)
C       ****************************************
        IF(IOPT.NE.2) GO TO 12Ø
        CALL CONI(1,TCRI,RESULT)
        B3=RESULT
        DO 11Ø JJ=1,NY+1
        IF(TH(JJ).LT.TCRI)THEN
        DP(JJ)=Ø.
        ELSE
        DP(JJ)=EXP((B3-C2(JJ))/C1(JJ))-R+Y(JJ)
```

```
        END IF
        IF(DP(JJ).LT.Ø.) DP(JJ)=Ø.
11Ø     CONTINUE

12Ø     IF(IPR1.EQ.Ø.AND.IPR2.EQ.Ø) GO TO 16Ø
        NPP=(NY+1)/1Ø+1
        WRITE(6,919)
        DO 15Ø II=1,NPP
        WRITE(6,92Ø)
        JS=1Ø*(II-1)+1
        JE=1Ø*II
        WRITE(6,921) (Y(J),J=JS,JE)
        IF(IPR1.EQ.1)WRITE(6,922) (TH(J),J=JS,JE)
        IF(IOPT.EQ.2.AND.IPR2.EQ.1)
     *  WRITE(6,923) (DP(J),J=JS,JE)
15Ø     CONTINUE

C       ****************************************
C       TASK (3)
C       ****************************************
16Ø     IF(IU.EQ.Ø) GO TO 999
        NRPP=1ØØØØØØØ
        DO 28Ø JJ=1,NSIM
        IF(IOPT.NE.2) GO TO 25Ø
C       GENERATING SPALLING TIME
C       CONSTANT OCCOURAENCE TIME  =YPAR1
        NSTEP=Ø
        IF(IU.EQ.1) THEN
        NSTEP=TL/YPAR1
        DO 21Ø I=1,NSTEP
21Ø     TSPA(I)=YPAR1*FLOAT(I)
        ELSE
C       RANDOM OCCOURANCE WITH PARAMETERS YPAR1,YPAR2
        TOTAL=Ø.
        I=Ø
22Ø     I=I+1
        IF(I.GT.5ØØØ) THEN
        WRITE(6,925)
        GO TO 999
        END IF

        CALL RAND(IX,RN)
        CALL RVG(IDIS,YPAR1,YPAR2,RN,RESULT)
        TOTAL=TOTAL+RESULT
        TSPA(I)=TOTAL
        IF(TOTAL.LT.TL) GO TO 22Ø
        NSTEP=I
        END IF

        IF(IPR3.EQ.Ø) GO TO 25Ø
        WRITE(6,93Ø) JJ
        NPP=NSTEP/1Ø+1
        DO 23Ø II=1,NPP
        WRITE(6,92Ø)
        JS=1Ø*(II-1)+1
```

```
      JE=10*II
      WRITE(6,926)(J,J=JS,JE)
      WRITE(6,927)(TSPA(J),J=JS,JE)
230   CONTINUE

250   IF(IU.EQ.1) AA=AM
      IF(IU.GE.2) THEN
      CALL RAND(IX,RN)
      CALL RVG(IDISA,AM,VA,RN,RESULT)
      AA=RESULT
      END IF

      CALL THICK(NPOINT)

      IF(NPOINT.LT.NRPP) NRPP=NPOINT
      WRITE(1) (THIK(J),J=1,NPOINT)

      IF(IPR3.EQ.0) GO TO 280
      NPP=NPOINT/10+1
      WRITE(6,933) AA
      DO 260 II=1,NPP
      WRITE(6,920)
      JS=10*(II-1)+1
      JE=10*II
      WRITE(6,931)(TIME(J),J=JS,JE)
      WRITE(6,932)(THIK(J),J=JS,JE)
260   CONTINUE
280   CONTINUE
890   WRITE(6,934)NRPP
C     ****************************************
C     OUTPUT SPECIFICATION
C     ****************************************
901   FORMAT(1X,'IOPT     =',I10/
     *       1X,'IU       =',I10)
902   FORMAT(1X,'ICORR    =',I10)
903   FORMAT(1X,'INNER RADIUS              =',F15.8,'IN'/
     *       1X,'MAX. LINING THICKNESS     =',F15.8,'IN'/
     *       1X,'MIN. LINING THICKNESS     =',F15.8,'IN'/
     *       1X,'NO. OF DIVISON            =',I10/
     *       1X,'OPERATING TEMPERATURE     =',F15.8,' F'/
     *       1X,'TEMPERATURE AT COLD FACE=',F15.8,' F')
904   FORMAT(1X,'TEMP. FOR SALG PENETRAT.=',F15.8,' F')
905   FORMAT(1X,'COEF. OF CONVECTION      ='/
     *       10X,E10.4,'+(',E10.4,'T)+(',E10.4,'T**2)+(',
     *           E10.4,'T**3)')
906   FORMAT(1X,'THERMAL CONDUCTIVITY     ='/
     *       10X,E10.4,'+(',E10.4,'T)+(',E10.4,'T**2)+(',
     *           E10.4,'T**3)')
907   FORMAT(1X,'INITIAL THICKNESS        =',F15.8,'IN'/
     *       1X,'TIME INTERVAL            =',F15.8,'HR'/
     *       1X,'DESIGN LIFE TIME         =',F15.8,'HR')
908   FORMAT(1X,'NO. OF SIMULATION        =',I10//)
909   FORMAT(1X,'PARAMERER 1              =',E15.10/
     *       1X,'PARAMETER 2              =',E15.10/
     *       1X,'AA                       =',E15.10/
```

```
     *         1X,'BB                          =',E15.10/
     *         1X,'REFERENCE TEMPERATURE       =',E15.10)
910       FORMAT(1X,'VARIANCE OF "A"            =',F15.10//)
915       FORMAT(1X,'SEARCH OF  TEMP. DEVERGE AT',F15.8)
919       FORMAT(////1X,120('*')/
     *    1X,'HOT FACE TEMPERATURE AND PENETRATION DEPTH'/
     *    1X,120('*')//)
920       FORMAT(1X,120('-'))
921       FORMAT(1X,'THICKNESS          ',10F10.4)
922       FORMAT(1X,'H.F.TEMPERATURE    ',10F10.2)
923       FORMAT(1X,'PENE. DEPTH        ',10F10.4)
925       FORMAT(//1X,'SPALLING OCCURS TOO OFTEN')
926       FORMAT(1X,'NO. OF SPALLING    ',10I10)
927       FORMAT(1X,'TIME OF SPALLING   ',10F10.2)
930       FORMAT(////1X,120('*')/
     *              1X'RESULT OF SIMULATION',I10/
     *              1X,120('*')//)
931       FORMAT(1X,'TIME               ',10F10.2)
932       FORMAT(1X,'RESID. THICKNESS   ',10F10.4)
933       FORMAT(//1X,'AA=',E15.6//)
934       FORMAT(//1X,'MAX. NO. OF COMPLETED',
     *    ' SIMULATION POINT=',I10//)
999       STOP
          END



          SUBROUTINE CONI(IND,X,Y)
          DOUBLE PRECISION X,Y
          COMMON/CONI/CV(4),CD(4)
          IF(IND.EQ.1) THEN
          Y=(((0.25*CD(4)*X+CD(3)/3.)*X+0.5*CD(2))*X+CD(1))*X
          ELSE
          Y=((CV(4)*X+CV(3))*X+CV(2))*X+CV(1)
          END IF
          RETURN
          END



          SUBROUTINE RAND(IX,RN)
          INTEGER A,P,IX,B15,B16,XHI,XALO,LEFTLO,FHI,K
          DATA A,B15,B16,P/16807,32768,65536,2147483647/
          XHI=IX/B16
          XALO=(IX-XHI*B16)*A
          LEFTLO=XALO/B16
          FHI=XHI*A+LEFTLO
          K=FHI/B15
          IX=(((XALO-LEFTLO*B16)-P)+(FHI-K*B15)*B16)+K
          IF(IX.LT.0)IX=IX+P
          RN=FLOAT(IX)*4.656612875E-10
          RETURN
          END
```

```
      SUBROUTINE RVG(INDEX,YPA1,YPA2,X,Y)
C     X: RANDOM DATA FROM UNIFORM-DISTRIBUTION GENERATOR
C     INDEX=1 ,Y:POISSON   DISTRIBUTION
C     INDEX=2 ,Y:NORMAL    DISTRIBUTION
C     INDEX=3 ,Y:UNIFORM   DISTRIBUITON
      GO TO (100,200,300)INDEX

100   Y=-YPA1*LOG(1.-X)
      GO TO 900

200   Z=SQRT(-LOG(X**2))
      Y1=(0.010328*Z+0.802853)*Z+2.515517
      Y2=((0.001308*Z+0.189269)*Z+1.432788)*Z+1.
      Y=(Z-Y1/Y2)*YPA2+YPA1
      GO TO 900

300   Y=X*(YPA1-YPA2)+YPA2

900   RETURN
      END




      SUBROUTINE THICK(NPPPP)
      COMMON/ONE/IOPT,NY,IU,YMAX,YMIN,YINI,DP(2000),
     * TH(2000),Y(2000)
      COMMON/SIMU/ICORR,AA,BB,TREF,TINT,TL,THIK(2000),
     * TIME(2000),TSPA(500),NSTEP
      ISTOP=0
      NINT=TL/TINT
      THIK(1)=YINI
      TIME(1)=0.
      IF(YINI.LT.YMIN.OR.YINI.GT.YMAX) THEN
      WRITE(6,901)
      GO TO 999
      END IF
      DO 10 II=1,NY
      IIJ=NY-II+1
10    IF(YINI.GT.Y(IIJ)) GO TO 20
20    SLOPE=(YINI-Y(IIJ))/(Y(IIJ+1)-Y(IIJ))
      IF(IOPT.EQ.2)XPD=DP(IIJ)+SLOPE*(DP(IIJ+1)-DP(IIJ))
      XHT=TH(IIJ)+SLOPE*(TH(IIJ+1)-TH(IIJ))
      ISTAR=II
      ICOUNT=1
      DO 100 JJ=2,NINT+1
      TIME(JJ)=TINT*FLOAT(JJ-1)
      IF(ICORR.EQ.1) THEN
C     ONLY EXPONENTIAL DISSOLUTION MODEL IS USED IN THIS VERSION
      XHHT=(XHT+459.67)*5./9.
      FAC1=-AA*EXP(-BB*(1./XHHT-1./TREF))*TINT
      END IF
```

```
      FAC2=Ø.
      IF(IOPT.EQ.2) THEN
      ISPA=Ø
      IF(ICOUNT.GT.NSTEP) GO TO 3Ø
      IF(TIME(JJ).GT.TSPA(ICOUNT))THEN
      FAC2=-XPD
      ISPA=1
      ICOUNT=ICOUNT+1
      END IF
      END IF

3Ø    THIK(JJ)=THIK(JJ-1)+FAC1+FAC2
      THH=THIK(JJ)
      IF(THH.LT.YMIN) GO TO 999
      DO 4Ø II=ISTAR,NY
      IIJ=NY-II+1
4Ø    IF(THH.GT.Y(IIJ)) GO TO 5Ø
5Ø    SLOPE=(THH-Y(IIJ))/(Y(IIJ+1)-Y(IIJ))
      XHT=TH(IIJ)+SLOPE*(TH(IIJ+1)-TH(IIJ))
      ISTAR=II
      IF(IOPT.EQ.2) THEN
      IF(ISPA.EQ.1) THEN
      RXPD=DP(IIJ)+SLOPE*(DP(IIJ+1)-DP(IIJ))
      ELSE
      RXPD=RXPD+FAC1
      PXPD=DP(IIJ)+SLOPE*(DP(IIJ+1)-DP(IIJ))
      XPD=MAX(RXPD,PXPD)
      END IF
      END IF
1ØØ   CONTINUE
9Ø1   FORMAT(1X'THICKNESS RANGE IS NOT ENOUGTH')
999   NPPPP=JJ-1
      RETURN
      END
```

A.1.2 Example of Input File

```
2 1                                          : IOPT,IU
1 1 1                                        : IPR1,IPR2,IPR3
108. 9.Ø 6.5 25Ø 3ØØØ. 15Ø.                 : R,YMAX,YMIN,NY,TE1,TE2
28ØØ.                                        : TCRI
1.Ø Ø. Ø. Ø.                                 : CV
Ø.273 -Ø.324E-4 Ø.562E-8 Ø.145E-12           : CD
1                                            : ICORR
9. 24. 3ØØØ.                                 : YINI,TINT,TL
1ØØØ. Ø. 2.36E-4 437ØØ. 1813.                : YPAR1,YPAR2,AM,BB,TREF
```

A.1.3 Example of Output File

```
IOPT     =          2
IU       =          1
INNER RADIUS              =    108.00000000IN
MAX. LINING THICKNESS     =      9.00000000IN
MIN. LINING THICKNESS     =      6.50000000IN
NO. OF DIVISON            =        250
OPERATING TEMPERATURE     =   3000.00000000 F
TEMPERATURE AT COLD FACE=     150.00000000 F
TEMP. FOR SALG PENETRAT.=    2800.00000000 F
COEF. OF CONVECTION       =
        0.1000E+01+(0.0000E+00T)+(0.0000E+00T**2)+(0.0000E+00T**3)
THERMAL CONDUCTIVITY      =
        0.2730E+00+(-.3240E-04T)+(0.5620E-08T**2)+(0.1450E-12T**3)
ICORR    =          1
INITIAL THICKNESS         =      9.00000000IN
TIME INTERVAL             =     24.00000000HR
DESIGN LIFE TIME          =   3000.00000000HR
NO. OF SIMULATION         =            1


PARAMERER 1               =.1000000000E+04
PARAMETER 2               =.0000000000E+00
AA                        =.2360000071E-03
BB                        =.4370000000E+05
REFERENCE TEMPERATURE     =.1813000000E+04
```

****

HOT FACE TEMPERATURE AND PENETRATION DEPTH

****

THICKNESS	6.5000	6.5100	6.5200	6.5300	6.5400	6.5500	6.5600	6.5700	6.5800	6.5900
H.F.TEMPERATURE	2894.93	2895.08	2895.23	2895.38	2895.53	2895.68	2895.83	2895.97	2896.12	2896.27
PENE. DEPTH	0.2078	0.2084	0.2090	0.2097	0.2103	0.2109	0.2116	0.2121	0.2128	0.2134
THICKNESS	6.6000	6.6100	6.6200	6.6300	6.6400	6.6500	6.6600	6.6700	6.6800	6.6900
H.F.TEMPERATURE	2896.42	2896.56	2896.71	2896.85	2897.00	2897.14	2897.29	2897.43	2897.57	2897.72
PENE. DEPTH	0.2140	0.2147	0.2153	0.2159	0.2166	0.2172	0.2178	0.2184	0.2191	0.2197
THICKNESS	6.7000	6.7100	6.7200	6.7300	6.7400	6.7500	6.7600	6.7700	6.7800	6.7900
H.F.TEMPERATURE	2897.86	2898.00	2898.14	2898.28	2898.43	2898.57	2898.71	2898.84	2898.98	2899.12
PENE. DEPTH	0.2204	0.2210	0.2216	0.2222	0.2229	0.2235	0.2241	0.2247	0.2253	0.2259
THICKNESS	6.8000	6.8100	6.8200	6.8300	6.8400	6.8500	6.8600	6.8700	6.8800	6.8900
H.F.TEMPERATURE	2899.26	2899.40	2899.54	2899.67	2899.81	2899.95	2900.08	2900.22	2900.36	2900.49
PENE. DEPTH	0.2266	0.2272	0.2278	0.2284	0.2291	0.2298	0.2303	0.2310	0.2316	0.2322
THICKNESS	6.9000	6.9100	6.9200	6.9300	6.9400	6.9500	6.9600	6.9700	6.9800	6.9900
H.F.TEMPERATURE	2900.63	2900.76	2900.89	2901.03	2901.16	2901.29	2901.43	2901.56	2901.69	2901.82
PENE. DEPTH	0.2329	0.2335	0.2341	0.2348	0.2354	0.2360	0.2367	0.2373	0.2379	0.2386

PENE. DEPTH	0.3201	0.3207	0.3213	0.3219	0.3225	0.3231	0.3238	0.3244	0.3250	0.3256
THICKNESS	8.4000	8.4100	8.4200	8.4300	8.4400	8.4500	8.4600	8.4700	8.4800	8.4900
H.F.TEMPERATURE	2917.28	2917.37	2917.46	2917.55	2917.64	2917.73	2917.82	2917.91	2918.00	2918.09
PENE. DEPTH	0.3262	0.3269	0.3275	0.3281	0.3287	0.3293	0.3299	0.3306	0.3312	0.3318
THICKNESS	8.5000	8.5100	8.5200	8.5300	8.5400	8.5500	8.5600	8.5700	8.5800	8.5900
H.F.TEMPERATURE	2918.18	2918.27	2918.36	2918.45	2918.54	2918.63	2918.71	2918.80	2918.89	2918.98
PENE. DEPTH	0.3324	0.3331	0.3336	0.3342	0.3349	0.3355	0.3361	0.3367	0.3373	0.3380
THICKNESS	8.6000	8.6100	8.6200	8.6300	8.6400	8.6500	8.6600	8.6700	8.6800	8.6900
H.F.TEMPERATURE	2919.07	2919.15	2919.24	2919.33	2919.42	2919.50	2919.59	2919.67	2919.76	2919.85
PENE. DEPTH	0.3386	0.3392	0.3398	0.3404	0.3411	0.3417	0.3423	0.3429	0.3435	0.3442
THICKNESS	8.7000	8.7100	8.7200	8.7300	8.7400	8.7500	8.7600	8.7700	8.7800	8.7900
H.F.TEMPERATURE	2919.93	2920.02	2920.10	2920.19	2920.27	2920.36	2920.44	2920.53	2920.61	2920.69
PENE. DEPTH	0.3447	0.3454	0.3459	0.3466	0.3472	0.3479	0.3484	0.3491	0.3496	0.3502
THICKNESS	8.8000	8.8100	8.8200	8.8300	8.8400	8.8500	8.8600	8.8700	8.8800	8.8900
H.F.TEMPERATURE	2920.78	2920.86	2920.94	2921.03	2921.11	2921.19	2921.28	2921.36	2921.44	2921.52
PENE. DEPTH	0.3509	0.3515	0.3521	0.3527	0.3533	0.3540	0.3546	0.3553	0.3558	0.3564
THICKNESS	8.9000	8.9100	8.9200	8.9300	8.9400	8.9500	8.9600	8.9700	8.9800	8.9900
H.F.TEMPERATURE	2921.61	2921.69	2921.77	2921.85	2921.93	2922.01	2922.09	2922.18	2922.26	2922.34
PENE. DEPTH	0.3570	0.3577	0.3583	0.3588	0.3595	0.3601	0.3607	0.3614	0.3620	0.3626
THICKNESS	9.0000	0.0000	0.0000	0.0000	0.0000	0.0000	0.0000	0.0000	0.0000	0.0000
H.F.TEMPERATURE	2922.42	0.00	0.00	0.00	0.00	0.00	0.00	0.00	0.00	0.00
PENE. DEPTH	0.3632	0.0000	0.0000	0.0000	0.0000	0.0000	0.0000	0.0000	0.0000	0.0000

****

RESULT OF SIMULATION 1

****

NO. OF SPALLING	1	2	3	4	5	6	7	8	9	10
TIME OF SPALLING	1000.00	2000.00	3000.00	0.00	0.00	0.00	0.00	0.00	0.00	0.00

AA= 0.236000E-03

TIME	0.00	24.00	48.00	72.00	96.00	120.00	144.00	168.00	192.00	216.00
RESID. THICKNESS	9.0000	8.9868	8.9736	8.9604	8.9473	8.9341	8.9210	8.9078	8.8947	8.8816
TIME	240.00	264.00	288.00	312.00	336.00	360.00	384.00	408.00	432.00	456.00
RESID. THICKNESS	8.8685	8.8554	8.8423	8.8292	8.8161	8.8031	8.7900	8.7770	8.7639	8.7509
TIME	480.00	504.00	528.00	552.00	576.00	600.00	624.00	648.00	672.00	696.00
RESID. THICKNESS	8.7379	8.7249	8.7119	8.6989	8.6860	8.6730	8.6600	8.6471	8.6342	8.6212

THICKNESS	7.0000	7.0100	7.0200	7.0300	7.0400	7.0500	7.0600	7.0700	7.0800	7.0900
H.F.TEMPERATURE	2901.95	2902.08	2902.21	2902.34	2902.47	2902.60	2902.73	2902.86	2902.98	2903.11
PENE. DEPTH	0.2391	0.2398	0.2404	0.2410	0.2416	0.2423	0.2429	0.2435	0.2441	0.2448
THICKNESS	7.1000	7.1100	7.1200	7.1300	7.1400	7.1500	7.1600	7.1700	7.1800	7.1900
H.F.TEMPERATURE	2903.24	2903.37	2903.49	2903.62	2903.75	2903.87	2904.00	2904.12	2904.25	2904.37
PENE. DEPTH	0.2454	0.2460	0.2467	0.2473	0.2479	0.2485	0.2492	0.2498	0.2504	0.2510
THICKNESS	7.2000	7.2100	7.2200	7.2300	7.2400	7.2500	7.2600	7.2700	7.2800	7.2900
H.F.TEMPERATURE	2904.49	2904.62	2904.74	2904.86	2904.99	2905.11	2905.23	2905.35	2905.47	2905.59
PENE. DEPTH	0.2517	0.2523	0.2529	0.2536	0.2542	0.2548	0.2554	0.2560	0.2566	0.2573
THICKNESS	7.3000	7.3100	7.3200	7.3300	7.3400	7.3500	7.3600	7.3700	7.3800	7.3900
H.F.TEMPERATURE	2905.72	2905.84	2905.96	2906.08	2906.20	2906.31	2906.43	2906.55	2906.67	2906.79
PENE. DEPTH	0.2579	0.2586	0.2592	0.2598	0.2604	0.2610	0.2617	0.2623	0.2629	0.2636
THICKNESS	7.4000	7.4100	7.4200	7.4300	7.4400	7.4500	7.4600	7.4700	7.4800	7.4900
H.F.TEMPERATURE	2906.90	2907.02	2907.14	2907.26	2907.37	2907.49	2907.60	2907.72	2907.83	2907.95
PENE. DEPTH	0.2641	0.2648	0.2654	0.2661	0.2666	0.2673	0.2679	0.2685	0.2691	0.2697
THICKNESS	7.5000	7.5100	7.5200	7.5300	7.5400	7.5500	7.5600	7.5700	7.5800	7.5900
H.F.TEMPERATURE	2908.06	2908.18	2908.29	2908.40	2908.52	2908.63	2908.74	2908.86	2908.97	2909.08
PENE. DEPTH	0.2704	0.2711	0.2716	0.2722	0.2729	0.2735	0.2741	0.2748	0.2753	0.2760
THICKNESS	7.6000	7.6100	7.6200	7.6300	7.6400	7.6500	7.6600	7.6700	7.6800	7.6900
H.F.TEMPERATURE	2909.19	2909.30	2909.41	2909.52	2909.63	2909.74	2909.85	2909.96	2910.07	2910.18
PENE. DEPTH	0.2766	0.2772	0.2778	0.2785	0.2791	0.2797	0.2803	0.2810	0.2816	0.2822
THICKNESS	7.7000	7.7100	7.7200	7.7300	7.7400	7.7500	7.7600	7.7700	7.7800	7.7900
H.F.TEMPERATURE	2910.29	2910.40	2910.51	2910.62	2910.72	2910.83	2910.94	2911.05	2911.15	2911.26
PENE. DEPTH	0.2828	0.2835	0.2841	0.2847	0.2853	0.2859	0.2866	0.2872	0.2878	0.2884
THICKNESS	7.8000	7.8100	7.8200	7.8300	7.8400	7.8500	7.8600	7.8700	7.8800	7.8900
H.F.TEMPERATURE	2911.36	2911.47	2911.57	2911.68	2911.78	2911.89	2911.99	2912.10	2912.20	2912.31
PENE. DEPTH	0.2890	0.2897	0.2903	0.2909	0.2916	0.2922	0.2928	0.2934	0.2940	0.2947
THICKNESS	7.9000	7.9100	7.9200	7.9300	7.9400	7.9500	7.9600	7.9700	7.9800	7.9900
H.F.TEMPERATURE	2912.41	2912.51	2912.62	2912.72	2912.82	2912.92	2913.03	2913.13	2913.23	2913.33
PENE. DEPTH	0.2953	0.2959	0.2966	0.2971	0.2978	0.2983	0.2990	0.2996	0.3002	0.3009
THICKNESS	8.0000	8.0100	8.0200	8.0300	8.0400	8.0500	8.0600	8.0700	8.0800	8.0900
H.F.TEMPERATURE	2913.43	2913.53	2913.63	2913.73	2913.83	2913.93	2914.03	2914.13	2914.23	2914.33
PENE. DEPTH	0.3015	0.3021	0.3027	0.3034	0.3039	0.3046	0.3052	0.3058	0.3064	0.3071
THICKNESS	8.1000	8.1100	8.1200	8.1300	8.1400	8.1500	8.1600	8.1700	8.1800	8.1900
H.F.TEMPERATURE	2914.43	2914.52	2914.62	2914.72	2914.82	2914.91	2915.01	2915.11	2915.21	2915.30
PENE. DEPTH	0.3077	0.3083	0.3089	0.3095	0.3102	0.3107	0.3114	0.3120	0.3127	0.3132
THICKNESS	8.2000	8.2100	8.2200	8.2300	8.2400	8.2500	8.2600	8.2700	8.2800	8.2900
H.F.TEMPERATURE	2915.40	2915.49	2915.59	2915.69	2915.78	2915.88	2915.97	2916.07	2916.16	2916.25
PENE. DEPTH	0.3139	0.3144	0.3151	0.3158	0.3163	0.3170	0.3176	0.3182	0.3189	0.3194
THICKNESS	8.3000	8.3100	8.3200	8.3300	8.3400	8.3500	8.3600	8.3700	8.3800	8.3900
H.F.TEMPERATURE	2916.35	2916.44	2916.54	2916.63	2916.72	2916.81	2916.91	2917.00	2917.09	2917.18

TIME	720.00	744.00	768.00	792.00	816.00	840.00	864.00	888.00	912.00	936.00
RESID. THICKNESS	8.6083	8.5954	8.5825	8.5696	8.5568	8.5439	8.5311	8.5182	8.5054	8.4926
TIME	960.00	984.00	1008.00	1032.00	1056.00	1080.00	1104.00	1128.00	1152.00	1176.00
RESID. THICKNESS	8.4798	8.4670	8.1238	8.1113	8.0988	8.0863	8.0738	8.0613	8.0489	8.0364
TIME	1200.00	1224.00	1248.00	1272.00	1296.00	1320.00	1344.00	1368.00	1392.00	1416.00
RESID. THICKNESS	8.0240	8.0116	7.9991	7.9867	7.9743	7.9620	7.9496	7.9372	7.9249	7.9125
TIME	1440.00	1464.00	1488.00	1512.00	1536.00	1560.00	1584.00	1608.00	1632.00	1656.00
RESID. THICKNESS	7.9002	7.8879	7.8756	7.8633	7.8510	7.8387	7.8265	7.8142	7.8020	7.7898
TIME	1680.00	1704.00	1728.00	1752.00	1776.00	1800.00	1824.00	1848.00	1872.00	1896.00
RESID. THICKNESS	7.7775	7.7653	7.7531	7.7409	7.7288	7.7166	7.7045	7.6923	7.6802	7.6681
TIME	1920.00	1944.00	1968.00	1992.00	2016.00	2040.00	2064.00	2088.00	2112.00	2136.00
RESID. THICKNESS	7.6560	7.6439	7.6318	7.6197	7.3298	7.3180	7.3063	7.2945	7.2827	7.2710
TIME	2160.00	2184.00	2208.00	2232.00	2256.00	2280.00	2304.00	2328.00	2352.00	2376.00
RESID. THICKNESS	7.2593	7.2475	7.2358	7.2241	7.2125	7.2008	7.1891	7.1775	7.1658	7.1542
TIME	2400.00	2424.00	2448.00	2472.00	2496.00	2520.00	2544.00	2568.00	2592.00	2616.00
RESID. THICKNESS	7.1426	7.1310	7.1194	7.1078	7.0963	7.0847	7.0732	7.0616	7.0501	7.0386
TIME	2640.00	2664.00	2688.00	2712.00	2736.00	2760.00	2784.00	2808.00	2832.00	2856.00
RESID. THICKNESS	7.0271	7.0156	7.0042	6.9927	6.9813	6.9698	6.9584	6.9470	6.9356	6.9242
TIME	2880.00	2904.00	2928.00	2952.00	2976.00	3000.00	0.00	0.00	0.00	0.00
RESID. THICKNESS	6.9128	6.9015	6.8901	6.8788	6.8675	6.8561	0.0000	0.0000	0.0000	0.0000

A.2 APPENDIX II: PROGRAM " PARL "

A.2.1 List of Program

```
C     ****************************************************************
C     ****************************************************************
C     **      THIS PROGRAM PERFORMS STATISTICAL ANALYSES USING THE  **
C     **      DATA GENERATED FROM PROGRAM "SRLT"                    **
C     **                                                            **
C     **      INPUT VARIABLES:                                      **
C     **      NSIM    =NO. OF SIMULATION                            **
C     **      NRPP    =MAX. NO. OF COMPLETED SIMULATION DATA        **
C     **      TINT    =TIME INTERVAL                                **
C     **      NDIVD   =NO. OF DIVISION FOR P.D.F.                   **
C     **      DSPAC   =TIMES OF STANDARD DEV. FOR P.D.F.            **
C     **      NPOP    =OPTION FOR PRINT OUT                         **
C     **              =1,PRINT AT EACH "NPRINT" STEPS               **
C     **              =2,PRINT AT STEP NPST(NPRINT)                 **
C     ****************************************************************
C     ****************************************************************

      DIMENSION DATA(10000),DIST(2,1000),TIME(10000),
     *  NPST(10000)

      READ(5,*)NSIM,NRPP,TINT,NDIVD,DSPAC,NPOP
      IF(NPOP.EQ.1) READ(5,*)NPRINT
      IF(NPOP.EQ.2) THEN
      READ(5,*) NPRINT
      READ(5,*)(NPST(II),II=1,NPRINT)
      END IF
      NPRI=1
      DO 50 KK=1,NRPP
50    TIME(KK)=TINT*FLOAT(KK-1)
      NN=0
      DO 200 KK=2,NRPP
      REWIND 1
      NN=NN+1
      IF(NPOP.EQ.1) THEN
      IF(KK.NE.(NPRI*NPRINT+1)) GO TO 200
      NPRI=NPRI+1
      END IF
      IF(NPOP.EQ.2) THEN
      IF(KK.NE.NPST(NPRI)) GO TO 200
      NPRI=NPRI+1
      END IF
      ICOUNT=0
      RMEAN=0.
      RVAR=0.
      DO 100 II=1,NSIM
      ICOUNT=ICOUNT+1
      CALL REDT(NN,A)

      DATA(ICOUNT)=A
      RMEAN=RMEAN+A
100   RVAR=RVAR+A**2
```

```
C       CALCULATE MEAN AND VARIANCE
        RMEAN=RMEAN/FLOAT(NSIM)
        RVAR=RVAR/FLOAT(NSIM)-RMEAN**2
        FAC1=DSPAC*SQRT(RVAR)
        DMIN=RMEAN-FAC1
        DIV=2.*FAC1/FLOAT(NDIVD)
        DO 120 JJ=1,NDIVD
120     DIST(2,JJ)=0.
        DO 150 II=1,NSIM
        DO 130 JJ=1,NDIVD
        CC=DATA(II)
        CMIN=DMIN+DIV*FLOAT(JJ-1)
        CMAX=DMIN+DIV*FLOAT(JJ)
        IF(CC.LT.CMAX.AND.CC.GT.CMIN) THEN
        DIST(2,JJ)=DIST(2,JJ)+1.0
        GO TO 150
        END IF
130     CONTINUE
150     CONTINUE
        DO 160 JJ=1,NDIVD
        DIST(1,JJ)=DMIN+DIV*(FLOAT(JJ)-0.5)
160     DIST(2,JJ)=DIST(2,JJ-1)+DIST(2,JJ)/FLOAT(NSIM)

C       CALL QPICTR
        WRITE(6,930)TIME(KK),RMEAN,RVAR
        NPP=NDIVD/10+1
        DO 180 II=1,NPP
        WRITE(6,920)
        JS=10*(II-1)+1
        JE=10*II
        WRITE(6,931)(DIST(1,J),J=JS,JE)
        WRITE(6,932)(DIST(2,J),J=JS,JE)
180     CONTINUE
200     CONTINUE
920     FORMAT(1X,120('-'))
930     FORMAT(///1X,120('*')/
     *  1X,'TIME=',F10.2,'  MEAN THICKNESS=',F10.6,
     *  1X,'  VARIANCE OF THICKNESS=',F10.6/1X,120('*')//)
931     FORMAT(1X,'THICKNESS=',10F10.6)
932     FORMAT(1X,'C.D.F.    =',10F10.6)
        STOP
        END



        SUBROUTINE REDT(MM,A)
        DIMENSION DUMMY(10000)
        READ(1)(DUMMY(I),I=1,MM),A
        RETURN
        END
```

A.3 - APPENDIX III: 2-D FINITE ELEMENT HEAT TRANSFER ANALYSIS USING TRIANGULAR ELEMENT

The two dimensional heat transfer problem (without heat generation) in x-y coordinate system is in finding temperature distribution $T(x,y)$ which minimizes the functional

$$\pi = \iint_{\Omega} \left[k_x \left(\frac{\partial T}{\partial x}\right)^2 + k_y \left(\frac{\partial T}{\partial y}\right)^2 + 2\rho C_p \frac{\partial T}{\partial t} T\right] d\Omega + \int_{\Gamma_2} h(T-T_\infty)^2 \, d\Gamma \qquad (A.3.1)$$

where k_x, k_y = conductivity in x and y directions, respectively,

ρ = density of the material,

C_p = specific heat of the material,

h = heat transfer coefficient on Γ_2

T_α = ambient temperature

Ω = domain of the body, and

Γ_2 = boundary on which the convective heat loss is specified;

and satisfies the boundary conditions

$$T = \overline{T}(x,y) \quad \text{on} \quad \Gamma_1 \qquad (A.3.2)$$

where $\overline{T}$ = prescribed temperature on Γ_1, and

Γ_1 = boundary on which temperature is specified.

The solution domain Ω is idealized with E triangle elements, as shown in Fig. A-3.2, with three nodes (i,j,k) each. If a linear variation of temperature in one element, say m^{th} element, is assumed,

the temperature in the element can be approximated by its value at nodes through the interpolation functions $[\underset{\sim}{N}]^m$, i.e.:

$$T^m(x,y) = [N(x,y)]^m \underset{\sim}{T}_n^m \qquad (A.3.3)$$

(1×1) (1×3) (3×1)

where

$$[N(x,y)]^m = [(a_i+xb_i+yc_i)/2A_m \ (a_j+xb_j+yc_j)/2A_m \ (a_k+xb_k+yc_k)/2A_m]^m$$

$$= [N_i(x,y) \ \ N_j(x,y) \ \ N_k(x,y)]^m$$

$$\underset{\sim}{T}_n^m = \begin{bmatrix} T_i \\ T_j \\ T_k \end{bmatrix}^m$$

A_m = area of the triangle;

$a_i = x_jy_k - x_ky_j$

$a_j = x_ky_i - x_iy_k$

$a_k = x_iy_j - x_jy_i$

$b_i = y_i - y_k$

$b_j = y_k - y_i$

$b_k = y_i - y_j$

$c_i = x_k - x_j$

$c_j = x_i - x_k$

$c_k = x_j - x_i$

and T_i, T_j, T_k = temperature at nodes i , j , and k .

The derivative of T with respect to x and y can be also related to $\underset{-n}{T}$

$$\begin{bmatrix} \frac{\partial T}{\partial x} \\ \frac{\partial T}{\partial y} \end{bmatrix}^m = \begin{bmatrix} [\frac{\partial N}{\partial x}] \\ [\frac{\partial N}{\partial y}] \end{bmatrix}^m \underset{\sim n}{T}^m = \underline{B}^m \underset{\sim n}{T}^m \qquad (A.3.4)$$

where $$[\frac{\partial N}{\partial x}] = \begin{bmatrix} \frac{\partial N_i}{\partial x} & \frac{\partial N_j}{\partial x} & \frac{\partial N_k}{\partial x} \end{bmatrix} = \frac{1}{2A_m} [b_i \; b_j \; b_k]$$

and $$[\frac{\partial N}{\partial y}] = \begin{bmatrix} \frac{\partial N_i}{\partial y} & \frac{\partial N_j}{\partial y} & \frac{\partial N_k}{\partial y} \end{bmatrix} = \frac{1}{2A_m} [c_i \; c_j \; c_k]$$

Then the minimization of Eq. A-3.1 can be represented in a matrix form as [71]

$$\underline{C} \dot{\underset{\sim}{T}} + \underline{k_s} \underset{\sim}{T} = \underset{\sim}{P} \qquad (A.3.5)$$

where

$\underline{C}$ = system assemblage of heat capacity matrix

$$= \sum_{m=1}^{E} [\underline{C}]^m$$

$$[\underline{C}]^m = [C_{\ell p}]^m$$

$$= [\iint_{\Omega^m} \rho c \, N_\ell \, N_p \, d\,\Omega]$$

$$= \frac{(\rho c)_m \, A_m}{12} \begin{bmatrix} 2 & 1 & 1 \\ 1 & 2 & 1 \\ 1 & 1 & 2 \end{bmatrix}$$

$\underline{k}_s$ = system assemblage of heat conductivity matrix

$$= \sum_{m=1}^{E} ([K_s^m]_1 + [K_s^m]_2)$$

$$[K_s^m]_1 = [k^m \ell_p]_1$$

$$= \frac{1}{4A_m} \underset{\sim}{B}^{m'} \underline{D} \underset{\sim}{B}^m$$

$\underline{D}$ = material conductivity matrix

$$= \begin{bmatrix} k_x & 0 \\ 0 & k_y \end{bmatrix} \qquad \text{(A.3.6)}$$

$$[K_s^m]_2 = \frac{h}{6} (L_{ij}\Delta_{ij} + L_{jk}\Delta_{jk} + L_{ki}\Delta_{ki}) \cdot$$

$$\begin{bmatrix} 2 & 1 & 1 \\ 1 & 2 & 1 \\ 1 & 1 & 2 \end{bmatrix} \cdot \begin{bmatrix} \Delta_i & 0 & 0 \\ 0 & \Delta_j & 0 \\ 0 & 0 & \Delta_k \end{bmatrix}$$

L_{ab} = length of the edge ab , (a,b = i,j,k)

$$\Delta_{ab} = \begin{cases} 1 , & \text{if ab is the convection boundary} \\ 0 , & \text{otherwise} \end{cases} \quad (a,b = i,j,k)$$

$$\Delta_a = \begin{cases} 1 , & \text{if node "a" lies on the convection boundary} \\ 0 , & \text{otherwise} \end{cases} \quad (a = i,j,k)$$

$\underset{\sim}{P}$ = heat supply vector

$$= \sum_{m=1}^{E} \underset{\sim}{p}^{m}$$

$$\underset{\sim}{p}^{m} = h\, T_{\infty}\, (L_{ij}\Delta_{ij} + L_{jk}\Delta_{jk} + L_{ki}\Delta_{ki}) \begin{bmatrix} \Delta_i \\ \Delta_j \\ \Delta_k \end{bmatrix}$$

A.4 APPENDIX IV: DESCRIPTION OF PROGRAM "TARL"

Program TARL (Thermomechanical Analysis of Refractory Linings) is a computer program in FORTRAN for the generalized two-dimensional, transient heat-transfer and stress analyses. This program incorporates several special features for the analysis of lining systems with refractory/brittle materials. These special features include a time-independent, damage-type constitutive model for the cracked media, a model for the behavior over joint interface, the capability to modify the material properties and boundary conditions due to slag penetration, spalling and joint failure, and the capability to detect lining failure.

The input to the program includes:

(1) Number and location of element nodes which define the geometry of the interested field problem;

(2) Number of material types and associated material properties with each material;

(3) Number of elements and the associated nodes and material type of each element;

(4) Initial conditions (displacement and temperature) at each node;

(5) Generalized load patterns (force, displacement and temperature) and number of steps repeating each pattern; and

(6) Selected time steps for printing stress/temperature states at each integration points and plotting stress/temperature contours through the linings.

The output from the program includes:

(1) Stress states at each integration point at predetermined time steps;

(2) Temperatures at each integration point at predetermined time steps;

(3) Principle stress contours and the directions of maximum principle stress through the linings at predetermined time steps; and

(4) Temperature contours through the linings at predetermined time steps.